Ph.D. Dissertation
in Physics

High power impulse magnetron sputtering of tungsten and zirconium: An ionization region model study

Swetha Suresh Babu

March 2025

FACULTY OF PHYSICAL SCIENCES

High power impulse magnetron sputtering of tungsten and zirconium: An ionization region model study

Swetha Suresh Babu

Dissertation submitted in partial fulfillment of a
Philosophiae Doctor degree in Physics

Ph.D. Committee
Jón Tómas Guðmundsson (Chair)
Daniel Lundin
Snorri Þorgeir Ingvarsson

Opponents
Claudia Lazzaroni
Tomáš Kozák

Faculty of Physical Sciences
School of Engineering and Natural Sciences
University of Iceland
Reykjavik, March 2025

High power impulse magnetron sputtering of tungsten and zirconium: An ionization region model study

(High power impulse magnetron sputtering of tungsten and zirconium)

Dissertation submitted in partial fulfillment of a *Ph.D.* degree in Physics

Copyright © 2025 Swetha Suresh Babu
All rights reserved

Faculty of Physical Sciences
School of Engineering and Natural Sciences
University of Iceland
Dunhaga 5
IS-107 Reykjavik
Iceland

Telephone: 525-4000

Bibliographic information:
Swetha Suresh Babu, 2025, *High power impulse magnetron sputtering of tungsten and zirconium: An ionization region model study*, Ph.D. Dissertation, Faculty of Physical Sciences, University of Iceland, 122 pp.

Author ORCID: https://orcid.org/0000-0001-5360-5562
ISBN: ISBN 978-9935-9826-3-6

Printing: Háskólaprent, Fálkagata 2, 107 Reykjavik
Reykjavik, Iceland, March 2025

Abstract

The plasma dynamics of high power impulse magnetron sputtering (HiPIMS) discharges with a tungsten and zirconium targets are studied by applying the ionization region model (IRM). The IRM effectively captures the temporal variations of the species densities as well as the electron energy, providing insights into key discharge parameters such as ionization and back-attraction probabilities and the working gas rarefaction processes. When operating with tungsten target the discharge current at the cathode target surface is composed of both argon and tungsten ions and the argon ions precede the tungsten ions. The investigations reveal that for tungsten target, an initial peak in the discharge current waveform is primarily due to argon ion bombardment, transitioning to dominance by tungsten ions as the discharge progresses. The model illustrates how tungsten ions increasingly contribute to the discharge current at higher cathode voltages, effectively leading to higher discharge current densities, highlighting increase in the ionization probability and decrease in the back-attraction probability correlating with voltage increases. The ionized flux fraction F_{flux} is estimated to be in the range from 7 % for peak current density of 0.33 A/cm^2, and increase to 34 % at 0.73 A/cm^2, increasing with increased discharge voltage. In case of zirconium target, roughly 2/3 of the discharge current at the cathode target surface is carried by Ar^+ ions while only about 1/3 is carried by Zr^+ ions. For discharges with zirconium target, the study presents experimental validations where the ionized flux fraction varies significantly, ranging from 25% to 59%, increasing with higher peak discharge current density. Using the IRM, the substantial contribution of electron impact ionization in promoting working gas rarefaction is observed, a critical factor in these discharges, especially pronounced at lower pressures and higher discharge current densities. Additionally, comparisons with experimental data using Thomson scattering and optical emission spectrometry for discharges with tungsten target show that while the IRM slightly underestimates electron density and overestimates the electron temperature, it reliably predicts the overall trends of these parameters. Collectively, these findings underscore that the ionization region model is very effective at predicting the complex behaviors seen in HiPIMS discharges, and its predictions match well with what is observed in experiments. For HiPIMS discharges with both tungsten and zirconium targets, there are significant contributions from both argon ions and metal ions. This indicates that with both tungsten and zirconium targets the discharges operate on combination of working gas and self-sputter recycling.

Ágrip

Kvik hegðun rafgass í háaflspúlsuðum segulspætum (HiPIMS) með þungsteins og sirkon skotmörkum eru rannsökuð með því að beita jónunarsvæðislíkani (IRM). Jónunarsvæðislíkanið fangar vel breytingar í þéttleika agna með tíma, sem og orku rafeinda, sem gefur okkur innsýn í helstu kennistærðir afhleðslunnar eins og líkur jónunnar og líkur á því að jónir séu dregnar til baka að skotmarkinu, sem og fall í þéttleika vinnugassins. Niðurstöðurnar sýna að fyrir þungsteinsskotmark, að upphafstoppurinn í afhleðslustraumnum er að mestu borinn af argon jónum, og samsetning straumsins breytist síðan í það að þungteins jónir verða ráðandi hleðsluberi síðar í púlsinum. Líkanniðurstöðurnar sýna hvernig þungsteinsjónirnar leggja meira til afhleðslustraumsins þegar spennan á bakskaut afhleðslunnar er aukin, sem í raun eykur strauminn um afhleðsluna, og dregur fram hvernig jónunarlíkur aukast og bakdráttarlíkum falla með hækkandi bakskautsspennu. Þegar skotmarkið er þungsteinn þá samanstendur straumurinn um afhleðsluna af bæði argon- og þungsteinsjónum, og argon jónirnar birtast á undan þungsteinsjónunum. Hlutfall jóna í flæði agna F_{flux} er metið vera á bilinu 7 % fyrir hámarks straumþéttleika 0.33 A/cm^2 og hækkar í 34 % við 0.73 A/cm^2, og þetta hlutfall eykst með aukinn bakskautsspennu. Fyrir sirkon skotmark, er um það bil 2/3 af straumnum um afhleðsluna við yfirborð skotmarksins borinn af Ar^+ jónum á meðan um 1/3 er borinn af Zr^+ jónum. Fyrir afhleðslur með sirkon skotmarki, sýnir rannsóknin, sem er staðfest með tilraunum, að hlutfall jóna í flæðinu breytist all verulega, fer frá 25% upp í 59%, hækkar með hækkandi hámarks straumþéttleika um afhleðsluna. Með því að beita IRM, sést glögglega mikilvægt hlutverk jónunar argons með árekstri við rafeindir í því að valda þrýstingslækkun vinnugassins, í þessum afhleðslum, einkum við lágan gasþrýsting og háan straumþéttleika. Þessu til viðbótar, þá sést með samanburði við tilraunaniðurstöður, sem fengnar voru með mælingu á Thomson dreifingu, og mælingu á ljósútgeislun, frá afhleðslum með þungsteinsskotmark að þrátt fyrir að IRM gefi of lág gildi á rafeindaþéttleika og gefi of há gildi fyrir rafeindahitastig, þá segir það fyrir um hegðan þessara stærða sem fall af tíma. Þegar á allt er litið, þá sýna þessar niðurstöður að meðalrúmmálslíkanið er er mjög notadrjúgt í að segja fyrir um þá flóknu hegðun sem finna má í HiPIMS afhleðslum, og að þær forspár falla vel að því sem hefur sést í tilraunum. Fyrir HiPIMS afhleðslur, með bæði þungsteins og sirkon skotmörk, er verulegt framlag til straums um afhleðslunnar frá bæði argon og málmjónum. Þetta þýðir að bæði þungsteins og sirkon afhleðslur gera út á bæði endurvinnslu jóna vinnugassins og jóna sjálf-spætunar.

Dedication

To the One who makes all things possible.

Table of Contents

List of Figures xi

List of Tables xiii

List of Publications xv

Abbreviations xvii

Acknowledgements xxi

1 Introduction 1
- 1.1 High power impulse magnetron sputtering 2
- 1.2 Ionization region model 2
- 1.3 Outline 3

2 The magnetron sputtering discharge 7
- 2.1 High power impulse magnetron sputtering 9
- 2.2 Advantages and drawbacks of HiPIMS 9
- 2.3 History of modeling HiPIMS 11
- 2.4 Tungsten and zirconium 13

3 The Ionization Region Model 15
- 3.1 Particle Balance 16
  - 3.1.1 Sputtering 17
  - 3.1.2 Ion particle balance 17
  - 3.1.3 The kick out effect 18
  - 3.1.4 Electron balance 19
- 3.2 Power Balance 20
  - 3.2.1 Collisional energy loss 21
  - 3.2.2 Modeled discharge current 21
  - 3.2.3 Generalized recycling model 22
- 3.3 Internal discharge parameters 23
- 3.4 Updating the ionization region model for new target materials in HiPIMS . 24
  - 3.4.1 Reaction rate 25
  - 3.4.2 Secondary electron emission yield 25
  - 3.4.3 Sputter yield 26
  - 3.4.4 Parameters to lock the model 27

4 Results from the model 29
- 4.1 Experimental apparatus and method 29
  - 4.1.1 Tungsten 29

4.1.2 Zirconium . . . 30
4.2 Fitting with IRM . . . 31
4.3 Species densities . . . 33
4.3.1 Neutral Densities . . . 33
4.3.2 Charged Particle Densities . . . 34
4.4 Current composition . . . 35
4.5 Electron behavior . . . 36
4.6 Internal discharge parameters . . . 36
4.7 Normalised deposition rate . . . 37
4.8 The potential drop across the IR . . . 39
4.9 Ionized flux fraction . . . 40
4.10 Gas rarefaction . . . 40
4.11 Sputter-rate-normalized deposition rate . . . 41

5 Summary of Papers **45**
5.1 Paper I: Modeling of high power impulse magnetron sputtering discharges with tungsten target . . . 45
5.2 Paper II: High power impulse magnetron sputtering of tungsten: a comparison of experimental and modeling results . . . 46
5.3 Paper III: High power impulse magnetron sputtering of a zirconium target . . . 48
5.4 Paper IV: On working gas rarefaction in high power impulse magnetron sputtering . . . 50

6 Conclusions **51**

Paper I **53**

Paper II **68**

Paper III **79**

Paper IV **93**

List of Figures

2.1 A schematic of the magnetron sputtering discharge 8
2.2 Timeline showing the evolution of the sputtering technology and magnetron sputtering. 8
2.3 A schematic of the HiPIMS set up. 10
3.1 A schematic showing the dimensions of the assumed ionization region . . . 15
3.2 The magnetic field topology and the geometry of the ionization region . . . 15
3.3 Collisional energy loss 21
4.1 Experimental depiction of the temporal changes in discharge voltage and current 30
4.2 A fitting map and discharge current curve for tungsten 32
4.3 A fitting map and discharge current curve for zirconium 32
4.4 The temporal evolution of the neutral particle densities for tungsten and zirconium 33
4.5 Temporal evolution of charged particle densities for tungsten and zirconium 34
4.6 Temporal evolution of the current composition of tungsten and zirconium . 35
4.7 The temporal evolution of the (a) electron density (b) electron temperature of tungsten 36
4.8 Ionization probability α_t and the back-attraction probability $\beta_{t,pulse}$ and β_t of tungsten 37
4.9 Deposition rate comparisson 38
4.10 The measured normalized deposition rate versus the peak discharge current density for a zirconium target 38
4.11 The fractional potential drop over the IR 39
4.12 Ionized flux fraction 40
4.13 Gas rarefaction of tungsten 41
4.14 The sputter-rate-normalized deposition rate F_{sput} versus the measured normalized deposition rate F_{dep} 43
5.1 The temporal evolution of various species Ar^0, Ar^+, W^0, and W^+ from OES and IRM 46
5.2 Discharge current composition for zirconium target 48
5.3 The fractional contribution of the various processes to working gas rarefaction within the ionization region versus self-sputter yield 50

List of Tables

3.1 Input parameters in model 25
3.2 The reactions and rate coefficients of tungsten and zirconium 26
3.3 The parameters of the model 27

List of Publications

Paper I: **Swetha Suresh Babu**, Martin Rudolph, Daniel Lundin, Tetsuhide Shimizu, Joel Fischer, Michael A. Raadu, Nils Brenning and Jon Tomas Gudmundsson, Modeling of high power impulse magnetron sputtering discharges with tungsten target. *Plasma Sources Science and Technology*, **31**(6) (2022) 065009 `https://iopscience.iop.org/article/10.1088/1361-6595/ac774a`

Paper II: **Swetha Suresh Babu**, Martin Rudolph, Peter John Ryan, Joel Fischer, Daniel Lundin, James W. Bradley and Jon Tomas Gudmundsson, High power impulse magnetron sputtering of tungsten: a comparison of experimental and modelling results . *Plasma Sources Science and Technology*, **32**(3) (2023) 034003 `https://iopscience.iop.org/article/10.1088/1361-6595/acc12f/pdf`

Paper III: **Swetha Suresh Babu**, Joel Fischer, Kateryna Barynova, Martin Rudolph, Daniel Lundin, Jon Tomas Gudmundsson, High power impulse magnetron sputtering of a zirconium target. *Journal of Vacuum Science and Technology A*, **42**(4) (2024) 043007 `https://doi.org/10.1116/6.0003647`

Paper IV: Kateryna Barynova, Martin Rudolph, **Swetha Suresh Babu**, Joel Fischer, Daniel Lundin, Michael A Raadu, Nils Brenning, and Jon Tomas Gudmundsson, On working gas rarefaction in high power impulse magnetron sputtering *Plasma Sources Science and Technology* **33**(6) (2024) 065010 `https://iopscience.iop.org/article/10.1088/1361-6595/ad53fe`

My contributions to papers I, II and III is that upon receiving the experimental data, it was curated and supplemented with additional data. I added the reaction sets for tungsten and zirconium to the model and executed the simulations, and then analyzed and interpreted the results. For Paper IV I provided input for the manuscript by contributing simulation results and supplementary data, supporting the interpretation of the findings.

Conference presentations:

Conference I:	**Swetha Suresh Babu**, Martin Rudolph, Daniel Lundin, Tetsuhide Shimizu, Joel Fischer, Michael A. Raadu, Nils Brenning and Jon Tomas Gudmundsson, Modeling of high power impulse magnetron sputtering discharges with tungsten target, poster presentation at the 18th International Conference on Plasma Surface Engineering (PSE2022), Erfurt, Germany, September 12 – 15, 2022.
Conference II:	**Swetha Suresh Babu**, M. Rudolph, D. Lundin, T. Shimizu, J. Fischer, J. W. Bradley, J. T. Gudmundsson, Modeling of high power impulse magnetron sputtering discharges with tungsten target, oral presentation at the 49th International Conference on Metallurgical Coatings and Thin Films (ICMCTF 2023), San Diego, California, May 21 – 26, 2023.
Conference III:	**Swetha Suresh Babu**, Joel Fischer, Kateryna Barynova, Martin Rudolph, Daniel Lundin, and Jon Tomas Gudmundsson. High power impulse magnetron sputtering of zirconium and tungsten target, a poster presentation at HiPIMS Today 2024, March 11 – 13, 2024.

Abbreviations

CVD Chemical vapor deposition

PVD Physical vapor deposition

IPVD Ionized physical vapour deposition

IRM Ionization region model

HiPIMS High power impulse magnetron sputtering

dcMS Direct current magnetron sputtering

rfMS Radio frequency magnetron sputtering

IR Ionization region

SH Sheath

BP Bulk plasma

DR Diffusion region

AP Anode plasma

OES Optical emission spectrometry

QCM Quartz crystal micro-balance

EEDF Electron Energy Distribution Function

Variables, superscripts and subscripts

Ar	Argon atom in ground state
$\mathbf{Ar}^{\mathrm{m}}$	Argon atom in metastable state
$\mathbf{Ar}^{+}$	Singly ionized argon ion
$\mathbf{Ar}^{2+}$	Doubly ionized argon ion
$\mathbf{Ar}^{\mathrm{W}}$	Warm argon atom in ground state
$\mathbf{Ar}^{\mathrm{H}}$	Hot argon atom in ground state
$\mathbf{e}^{\mathrm{H}}$	Hot electron
$\mathbf{e}^{\mathrm{C}}$	Cold electron
W	Tungsten atom in ground state
$\mathbf{W}^{+}$	Singly ionized tungsten ion
$\mathbf{W}^{2+}$	Doubly ionized tungsten ion
Zr	Zirconium atom in ground state
$\mathbf{Zr}^{+}$	Singly ionized zirconium ion
$\mathbf{Zr}^{2+}$	Doubly ionized zirconium ion
$Y_i(\mathscr{E}_{\mathrm{i}})$	Sputter yield
$\gamma_{\mathbf{see}}$	Secondary electron emission yield coefficient
S_{RT}	Surface area of the racetrack
$\mathscr{E}_{\mathrm{c}}$	Collisional energy loss per electron-ion pair
$\Gamma_{\mathbf{tn}}^{\mathbf{DR}}$	Target neutral fluxes out of the ionization region to the diffusion region
$\Gamma_{\mathbf{sput}}$	Sputtered flux
α_{t}	Ionization probability
β_{t}	Back-attraction probability
$\beta_{\mathrm{t,pulse}}$	Back-attraction probability during pulse
F_{sput}	Sputter-rate-normalized deposition rate
F_{flux}	Ionized flux fraction
r	Electron recapture probability
$\mathscr{V}_{\mathrm{IR}}$	Total volume of the ionization region
V_{D}	Discharge voltage
I_{D}	Discharge current
V_{IR}	The potential across the ionization region

Acknowledgements

Words cannot express my gratitude to my supervisor, Prof. Jón Tómas Guðmundsson, whose expertise, and his patience added considerably to my graduate experience. I am grateful for his guidance throughout this research and his valuable comments and his help with writing papers. Beyond academia, his encouragement and mentorship have been a source of motivation, and I sincerely appreciate the time and effort he has dedicated to my growth as a researcher.

I am very thankful to the doctoral committee, Dr. Daniel Lundin and Prof. Snorri Þorgeir Ingvarsson for their assistance at all levels of the research project.

I must thank our weekly Skype meetings members, especially Dr. Martin Rudolph, who helped me with the code in the beginning of this research and who is always ready to help, and Prof. Tiberiu Minea, Dr. Michael A. Raadu, Dr. Hamid Hajihoseini and Joel Fischer whose assistance was always given willingly and efficiently. Your contributions and suggestions have been crucial to the success of my work.

To my family, whose endless support and love have always been my strength, I am forever in your debt. Thank you for believing in me more than I sometimes did in myself.

I am grateful to all my friends, my personal cheer squad, both in Iceland and in India, for moral support, laughter, long conversations, and everything in between.

Finally, I thank myself for not giving up during the difficult times. This journey has tested my limits, and I am proud to have persevered, learned, and grown. And I thank God for providing me the strength to persevere through this journey.

1 Introduction

Thin film deposition refers to the process of depositing layers of material onto a substrate. Thin films and coatings, ranging from fractions of a nanometer to several micrometers thick, are crucial components of many modern technologies. The intriguing part of thin films is the interplay between the properties of the thin films and the substrate. Thin films are broadly used to enhance material properties such as optical, electrical, magnetic, chemical, or mechanical characteristics (Ohring, 2002). The deposition method influences the thin film properties and the interplay between the thin film and the substrate.

Thin films hold great technological significance, and there is a great deal of research and development being conducted on synthesis methods. There are number of deposition methods applied for this purpose. Broadly thin film deposition methods are categorized into chemical vapor deposition (CVD) (Snyders et al., 2023) and physical vapor deposition (PVD) (Gudmundsson et al., 2022) methods. In the CVD processes the initial source material is gas-vapour and it is therefore a chemical process, while in the PVD processes the source material is typically a solid (can also be liquid) and the atoms are released by physical means. PVD methods can therefore be applied to deposit thin films of a wide range of materials onto different substrates.

Physical vapor deposition methods, encompasses methods where material released from a solid source condenses onto a substrate. One such technique is sputter deposition, a PVD method employing ion bombardment to dislodge the material from a solid target for deposition. The target, typically plate or disk-shaped, serves as the source of the film forming material. The method involves bombarding the target material with particles from a plasma discharge or a focused ion beam. The incoming particles dislodge target atoms into typically a vacuum chamber, with a portion of the atoms depositing onto the substrate, thus contributing to thin film growth. One such sputter based deposition technique is magnetron sputtering (Kelly and Arnell, 2000; Gudmundsson, 2020). These are often driven by a direct current (dc) source or a radio frequency (rf) sinusoidal generator. The dc magnetron sputtering discharge has proven to be a highly successful and important PVD method that is widely used. However, it has a drawback of low ionization of the sputtered species, as ionized flux of the film forming material is known to be beneficial for the deposited film properties (Petrov et al., 2003). To overcome this limitation and to further customize the film properties while retaining the advantages of PVD methods, ionized PVD (IPVD) methods (Helmersson et al., 2006), such as high power impulse magnetron sputtering (HiPIMS) (Gudmundsson et al., 2012), can be employed. Then high power pulses are applied to the cathode target. IPVD can also be achieved by adding a secondary discharge between the target and the substrate, often an inductively coupled discharge (Rossnagel and Hopwood, 1994; Hopwood, 1998). In IPVD a significant proportion of the sputtered species is ionized as they travel from the target surface to the substrate.

1.1 High power impulse magnetron sputtering

In the realm of material science and surface engineering, high power impulse magnetron sputtering (HiPIMS) continues to stand out due to its ability to deposit thin films with superior properties (Lundin and Sarakinos, 2012). Unlike dc magnetron sputtering, which applies a constant voltage to the target (cathode), in HiPIMS, the voltage is applied to the target (cathode) in pulses as the HiPIMS technique is based on pulsing the power to the cathode target at low frequency while keeping the duty cycle short (Gudmundsson et al., 2012). HiPIMS has been successfully developed for over two decades and has been demonstrated to show increased the level of ionization of the sputtered species compared to dcMS (Kouznetsov et al., 1999; Fischer et al., 2023; Lundin et al., 2015; Hajihoseini et al., 2019). With HiPIMS, it is possible to utilize significantly higher peak power without altering the average power output by shortening the duty cycle. Typically, the peak power exceeds the time-averaged power by two orders of magnitude. The primary advantage of the HiPIMS process over other existing PVD methods lies in its ability to generate a highly ionized flux of the species responsible for film formation toward the substrate (Bohlmark et al., 2006; Hajihoseini et al., 2019). Applying short and intense power pulses to the magnetron target can result in electron densities reaching up to 10^{19} m^{-3} near the target (Gudmundsson et al., 2002; Bohlmark et al., 2005). Consequently, this increases the likelihood of ionization for both the background or working gas and, maybe of more importance, the sputtered neutral flux. Pulsing at high peak power density has been shown to result in an ionized density fraction at the substrate position exceeding 90%, with variations depending on the target material and process parameters (Bohlmark et al., 2005). A major drawback of the HiPIMS technique is that the deposition rate is generally found to be lower than in a conventional dcMS discharge operated at the same average power (Samuelsson et al., 2010). Much effort has been put into understanding the cause of this decrease and to increase the ionization in HiPIMS and reduce the difference in deposition rate compared to dcMS. This encapsulates the essence of the studies contribution to both theoretical and practical aspects of magnetron sputtering technology, emphasizing the ongoing need for model improvement and experimental verification.

1.2 Ionization region model

Computational models have become increasingly important and serve as valuable tools for studying processes that are challenging or time-consuming to measure and validate experimentally (Minea et al., 2020). The model used in this study is the ionization region model (IRM), which has been in continuous development for over a decade (Raadu et al., 2011; Huo et al., 2017; Barynova et al., 2024) and has successfully led to significantly improved understanding of the operation and processes of pulsed magnetron sputtering discharges.

The ionization region model (IRM), is a time-dependent and volume-averaged plasma chemical model designed to simulate the ionization region within a HiPIMS discharge. The volume surrounding the cathode target, where a static magnetic field confines the electrons and creates a luminous plasma (Antunes et al., 2023), is known as the ionization region. The model is limited to the ionization region, and it is capable of calculating the fluxes of particles that enter and exit the region. With the model, it also becomes possible to track the temporal evolution of each of the species that constitute the discharge. This includes monitoring both neutrals and ions of the target material and the working gas, alongside the electron population

within the discharge. The IRM can provide valuable information about the probability of sputtered species being ionized, as well as the fraction of the flux that is ionized, and the probability that the ionized sputtered species return to the cathode target. The dependence of these parameters on operating parameters such as working gas pressure, pulse length, peak power density and the geometry of the system can help researchers to better understand the behavior of ions within the plasma, and can be used to optimize the HiPIMS process for various applications. In the past, the IRM has proven to be an effective tool for modeling discharges with aluminium (Huo et al., 2017), titanium (Stancu et al., 2015; Gudmundsson et al., 2015), graphite (Eliasson et al., 2021) and copper (Gudmundsson et al., 2022) targets. Furthermore, the reactive HiPIMS discharge in Ar/O_2 mixture with the titanium target has been modeled (Gudmundsson et al., 2016; Lundin et al., 2017). In this work, we add zirconium (Paper III) (Suresh Babu et al., 2024) and tungsten (Papers I and II) (Suresh Babu et al., 2022, 2023) to the elements investigated by the IRM. The IRM has been applied to study working gas rarefaction in a discharge with aluminum target (Huo et al., 2012) and with number of target materials ((Paper IV) (Barynova et al., 2024), and the mechanism for energizing the electrons (Huo et al., 2013), the effect of shortening the pulse length (Rudolph et al., 2020), and ion recycling (Gudmundsson et al., 2016; Brenning et al., 2017). The results obtained from these models have been found to be in good agreement with the values obtained from actual measurements (Rudolph et al., 2021; Stancu et al., 2015). This suggests that the IRM is a reliable and accurate method for predicting the behavior of these materials under real discharge conditions.

One focus of our modeling is on the physical mechanisms that we regard as most important for determining the deposition rate in HiPIMS, namely the ionization degree of metal flux species, the reason for and extent of ion attraction back to the target, the factors that influence the gas rarefaction, and how the externally controllable parameters influence the internal physics of relevance for these mechanisms.

1.3 Outline

The structure of this thesis is organized as follows:

Chapter 1 introduces the fundamental concepts of thin film processing, high power impulse magnetron sputtering (HiPIMS), and the ionization region model (IRM), providing a comprehensive overview of the background and objectives of the study.

Chapter 2 delves into the specifics of magnetron sputtering discharge, detailing the physics and operational principles behind sputtering processes, with a focus on HiPIMS as the chosen deposition method.

Chapter 3 presents an in-depth exploration of the ionization region model (IRM), outlining the necessary parameters to initiate the modeling such as initial discharge conditions, rate coefficients, adding new target materials, discharge geometries, as well as working gas temperature and pressure.

Chapter 4 reports the results generated by the model, examining the behavior of plasma species and comparing modeled predictions to experimental data to assess the accuracy of the IRM in capturing the dynamics of the HiPIMS discharge.

Chapter 5 provides a summary of the study, highlighting the key findings and discussing the implications of the results.

Chapter 6 concludes the thesis, highlighting the primary contributions, limitations of the current model, and potential directions for future research in the field of thin film deposition using HiPIMS.

2 The magnetron sputtering discharge

Sputtering is a physical vapor deposition (PVD) technique used to deposit thin films onto a substrate (Ohring, 2002). Sputtering is the release of a target atom due to momentum exchange between energetic species and atoms within the target. Specifically, magnetron sputtering is recognized as one of the most successful approaches utilized for industrial PVD processes. In the practice of magnetron sputtering, the process begins by igniting a plasma discharge within a sputtering chamber, and the acceleration of ions from the plasma discharge towards a solid target, which typically is in the form of a disk or a plate serving as the source of the film-forming material. To induce the plasma discharge, the chamber is pumped to vacuum and filled with a working gas, which is most often a noble gas, to a specific pressure, after which a negative voltage of typically several hundred volts is applied to the target (cathode) across the cathode dark space or the cathode sheath. The applied voltage creates an electric field that accelerates positive ions towards the target. The ion bombardment dislodges the target atoms, and some are released from the target. Upon ion bombardment of the target, secondary electrons are also emitted. These electrons are accelerated to high energy by the cathode potential. Subsequently, some of these electrons are trapped by the magnetic field of the magnetron assembly, where they excite and ionize the working gas, which usually is argon.

The magnetic field is typically maintained by permanent magnets. For a circular disk shaped targets two concentric magnets are placed behind the target, one center magnet and another with opposite polarity along the outer circumference. If the inner and outer magnets are of the same strength the magnetron assembly is said to be balanced. An important variation in magnetron assembly designs is the unbalanced magnetron, which is distinguished by its partially open magnetic field loops around the target. Unbalanced magnetron assembly is achieved by inner and outer magnets of unequal strength. If the outer magnet is stronger than the center magnet not all the field lines are closed on the target surface. This configuration allows some electrons to escape the magnetic confinement near the target, facilitating plasma formation further away from the target. This, in turn, enhances the efficiency of ion transport to the substrate (Lundin, 2010; Window and Savvides, 1986).

Within the plasma itself, distinct regions are defined based on the dominant physical phenomena occurring in each. These regions include the anode plasma, the bulk plasma, the ionization region, and the cathode sheath, as displayed in Figure 2.1. The sheath (SH) is defined by a large charge imbalance, where the density of positive ions is at least twice that of the electron density. The ionization region (IR) is where the majority of the ionization occurs. In the bulk plasma (BP), also referred to as the diffusion region (DR), the primary process involves the transport of species from the IR across the magnetic field lines towards the anode plasma (AP). Finally, in the anode plasma, the electric circuit is closed by the electron flux reaching the anode (substrate or chamber walls) (Huo et al., 2017; Brenning et al., 2008). The ionization region is the region of interest in this current work and will be explored further through to the computational modeling approach used.

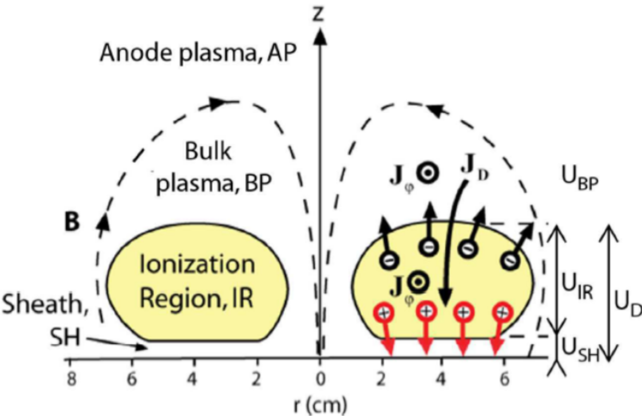

Figure 2.1. A schematic of the magnetron sputtering discharge, showing the sheath (SH), the ionization region (IR), the bulk plasma (BP), and the anode plasma (AP). Reprinted from Huo et al. (2013). ©IOP Publishing. Reproduced with permission. All rights reserved.

Magnetron sputtering typically employs direct current (dc), referred to as dcMS (direct current magnetron sputtering). While dcMS is a cost-effective and straightforward method for depositing metal films, it falls short in ionizing the sputtered species effectively. In a dcMS discharge, the film-forming material predominantly consists of neutral species, and the few ions that do bombard the substrate are typically ions of the working gas. Also, the ions that bombard the cathode target are ions of the working gas. For many applications, achieving a higher ionization in the film-forming material is highly desirable.

The timeline in Figure 2.2 highlights the significant milestones in the development of sputtering technology, which eventually led to magnetron sputtering. This figure illustrate the evolution of magnetron sputtering technology from its inception in the mid-19th century to its major advancements in the 20th century. Starting from basic sputter deposition, innovations like cylindrical and planar magnetron sputtering, and the advanced HiPIMS technique have played critical roles in making magnetron sputtering a key technology for thin film deposition across scientific and industrial domains.

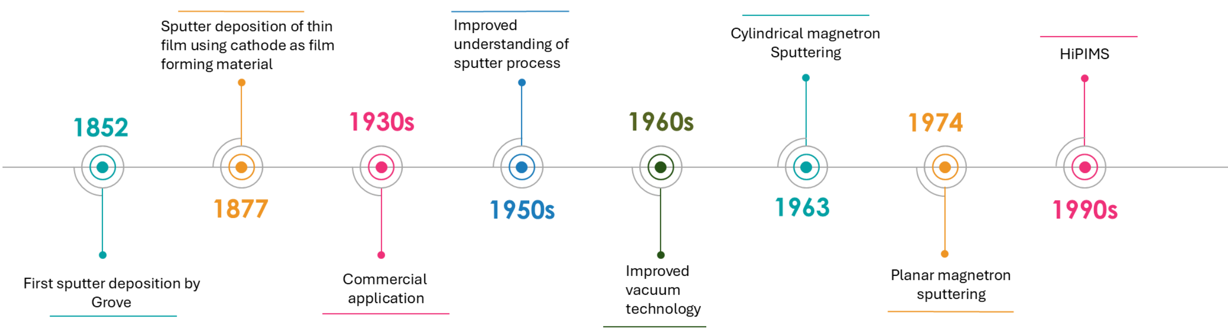

Figure 2.2. Timeline showing the evolution of the sputtering technology and magnetron sputtering.

2.1 High power impulse magnetron sputtering

High power impulse magnetron sputtering (HiPIMS) is an ionized physical vapor deposition technique that builds upon the magnetron sputtering principles. The foremost reason for employing the HiPIMS technique is that it permits turning a conventional magnetron sputtering discharge into a source of ions of the sputtered material. HiPIMS became noticed by the seminal work of Kouznetsov et al. (1999). This work followed development that had been carried out at Moscow State Engineering and Physics Institute (MEPhI) (Mozgrin, 1994; Mozgrin et al., 1995; Fetisov et al., 1999), and the High Current Electronics Institute in Tomsk (Bugaev et al., 1996, 2001) in the 1990s.

The key to achieve IPVD is high electron density and short ionization mean free path for the sputtered species. The principle of the HiPIMS technique is to focus the applied power into highly energetic pulses to create a high-density plasma. In a standard dcMS setup, a constant voltage is applied to the cathode (target) to initiate and sustain the plasma discharge, while in HiPIMS, the voltage is delivered in pulses, which enables the application of larger voltage, often in excess of several hundred volts, which then results in achieving higher peak discharge current densities (Gudmundsson, 2020). For instance, while direct current magnetron sputtering (dcMS) is typically operated in the discharge current density range 4 – 60 mA/cm^2 (Waits, 1978), high power impulse magnetron sputtering (HiPIMS) can reach a peak discharge current density of upto 1 – 10 A/cm^2, all while maintaining the same average power at the cathode (target) (Lundin, 2010). The average power supplied to the magnetron sputtering discharge is however limited by the target cooling. To put the thermal load of the target under control, HiPIMS has to be operated at low frequency (10 – 5000 Hz) and low duty cycle (less than 2 %) (Gudmundsson et al., 2012). When a short and intense power pulse is applied to the magnetron target, it can result in high electron densities of up to 10^{19} m^{-3} in the vicinity of the target (Bohlmark et al., 2005; Gudmundsson et al., 2009), i.e. 2 – 4 orders of magnitude higher densities than for dcMS. Such plasma densities reduce the mean free path for ionization of the sputtered species to a distance to less than a cm, i.e. the dimensions of the intense plasma close to the target, while the corresponding figure for dcMS can be several tens of cm (Gudmundsson, 2010). As a result, the probability of ionization of both the background gas and the sputtered neutral flux increases, leading to ionized density levels of over 90% at the substrate.

2.2 Advantages and drawbacks of HiPIMS

The primary advantage of the HiPIMS technique lies in its ability to convert existing magnetron sputtering systems into ionized magnetron sputtering with minimal modifications.

The HiPIMS technique harnesses the power of highly energetic pulses to create a high-density plasma, leading to a significant ion flux towards the substrate. This high ion flux directed toward the substrate promotes adatom surface diffusion processes during film growth (Alami et al., 2009) and may lead to renucleation (Ehiasarian et al., 2004) and knock-on effects. As a result, HiPIMS deposited films become a notably dense and exhibit smooth surface (Sarakinos et al., 2010). Moreover, research indicates that the utilization of HiPIMS, as opposed to dcMS, results in a film mass density increase ranging from 6 – 30% for various target materials (Alami et al., 2009; DeKoven et al., 2003; Konstantinidis et al., 2007; Samuelsson et al., 2010).

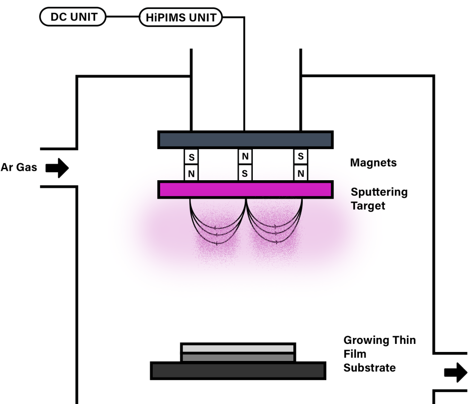

Figure 2.3. A schematic of the HiPIMS set up. A dc power supply feeds a pulser unit, that delivers high power pulses to the cathode target.

The HiPIMS process allows for the customization of thin film properties, including improved crystallinity (Alami et al., 2005), the achievement of low surface roughness (Sarakinos et al., 2010; Magnus et al., 2011), enhanced substrate adhesion (Ehiasarian et al., 2007), lower electrical resistivity (Magnus et al., 2012; Cemin et al., 2016), and increased film hardness (Paulitsch et al., 2010).

The primary drawback of the HiPIMS technique is its significantly lower deposition rate compared to dcMS when operated at the same average power (Helmersson et al., 2006; Sarakinos et al., 2010). Typically, HiPIMS achieves only 15 – 40 % of the deposition efficiencies measured in (Åmin^{-1}/Wcm^{-2}) that dcMS does (Helmersson et al., 2006; Samuelsson et al., 2010). Moreover, deposition rates in HiPIMS are generally expected to be between 30 – 80 % of those achieved by conventional magnetron sputtering under equivalent power conditions. A major factor contributing to this reduced efficiency and the decrease in deposition rate is the ion back-attraction, where sputtered atoms are ionized near the cathode target and are drawn back to the cathode (Christie, 2005), thus not contributing to the film growth. This occurs due to the magnetic field confinement and the extended cathode potential drop. This phenomenon often results in a lower self-sputtering yield—where the target material is bombarded by ions of the same element—compared to the yield achieved with argon ion sputtering. Other causes have been suggested like the non-linear energy dependence of the sputter yields (Emmerlich et al., 2008).

In such scenarios, unless a sputtered atom ionized within this plasma potential gradient has sufficient kinetic energy to overcome it and reach the substrate, it will be drawn back to the target, leading to self-sputtering and further loss of material available for deposition. This effect of self-sputtering in HiPIMS, when compared to the dominant argon ion sputtering in conventional methods, highlights the significant impact of this mechanism on the deposition process.

2.3 History of modeling HiPIMS

An overview on modeling of the pulsed magnetron sputtering discharge was given by Minea et al. (2020). Various modeling approaches have been taken to study the magnetron sputtering discharge and in particular the HiPIMS discharge.

Among the first numerical models developed was the Monte Carlo simulations, by Metropolis and Ulam (1949) and Metropolis et al. (1953). This approach has been widely used to track a large set of test particles, simulating their interactions within the plasma discharge to determine the electron energy distribution function (EEDF) and other discharge properties when combined with particle-in-cell simulations. An example of using Monte Carlo simulations to explore the magnetron sputtering discharge is the work of Sheridan et al. (1990) which explored how electron confinement allows magnetron sputtering discharges to operate at lower working gas pressures than similar unmagnetized discharges.

The fundamental concept of particle-in-cell Monte Carlo collision (PIC/MCC) simulations (Birdsall, 1991) is to use hundreds of thousands of computer-simulated particles (superparticles or macroparticles) to represent a much larger number of real particles, with densities typically ranging from 10^{14} to 10^{18} m^{-3}. The approach of this method helps to overcome some limitations of the Monte Carlo method, but they face challenges in modeling the HiPIMS discharge due to the high electron density and the high densities of target material atoms and ions. The detailed spatial and temporal resolution required for HiPIMS makes these simulations unsolvable in a reasonable timeframe. However, there have been a number of attempts to utilize PIC/MCC simulations to study the HiPIMS discharge (Minea et al., 2014; Revel et al., 2018).

The Direct Simulation Monte Carlo (DSMC) method, based on the Monte Carlo approach, is used to simulate interactions between target material species and neutral gas atoms, such as in rarefied gas flows (Bird, 1994). While DSMC is slower and more complex to implement compared to the Monte Carlo Collision (MCC) approach, it provides accurate results when sufficient macroparticles are used in each computational cell, with time steps constrained by particle velocity and grid size. Often the DSMC method is applied only on the neutral species (Kadlec, 2007; Kozák and Lazar, 2018). However, recent efforts to model the HiPIMS discharge have included the transport of ions as well (Kozák, 2023).

Christie's (Christie, 2005) material pathway model was developed to explain the observed decrease in deposition rates compared to conventional dc magnetron sputtering (dcMS). This method was subsequently extended by Vlček and Burcalová (2010), who incorporated ionization within the plasma bulk (DR) and an energy balance equation for the secondary electrons to determine the probability of ions returning to the target. The material pathway model exclusively concentrates on the trajectories of atoms sputtered from the target.

The ionization region model (IRM), a time-dependent global model, stands out as the most validated tool for studying plasma dynamics during high power impulse magnetron sputtering (HiPIMS) pulses and their afterglow phases. Originally described by Raadu et al. (2011), the IRM has undergone significant enhancements over the past decade. Concurrently, IRM was applied to a discharge operated with argon as the working gas and Al target to study gas rarefaction Raadu et al. (2011), refill processes (Huo et al., 2012), to explain the reason behind loss in deposition rate (Brenning et al., 2012), the electron heating mechanism (Huo et al., 2013) and the onset of self-sputtering (Huo et al., 2014).

Meanwhile, another ionization region model was developed by Kozák and Pajdarová (2011) for HiPIMS discharges based on a well-established method of dividing the plasma volume according to the typical spatial structure of magnetron discharges. The model introduces several key features like the inclusion of fast (secondary) electrons and fast sputtered target material atoms, the addition of a calculated potential drop near the target, and a self-consistent calculation of the target current, plasma species densities, and deposition characteristics. While the model simplifies the spatial details of the discharge, it retains all the essential processes, enabling it to provide qualitatively accurate time evolutions of the discharge characteristics.

The detailed kinetics of argon metastable species was implemented to the IRM with titanium targets by Stancu et al. (2015) and has been compared with the experimental results. This was succeeded by a study of metastable argon atoms and how stepwise ionization impacts the HiPIMS discharges, as outlined by Gudmundsson et al. (2015). The IRM has been adapted to also handle reactive Ar/O_2 discharges using titanium target by adding reaction set and surface processes for oxygen (Gudmundsson et al., 2016; Lundin et al., 2017). More modifications concerning the treatment of the afterglow (Rudolph et al., 2020) and updated reaction rates (Rudolph et al., 2021) have been made, as well as a modification to the term that describes the kick-out by the sputtered species and contributes to working gas rarefaction as discussed by Barynova et al. (2024). This last modification was needed to analyze and compare the contributions from electron impact ionization and kick-out by sputtered species and fast argon atoms to working gas rarefaction. This part discusses only the evolution and features of IRM, while the detailed implementation and associated code will be addressed in Chapter 3.

The IRM has proven to be an effective tool for modeling discharges with aluminium (Huo et al., 2017), titanium (Stancu et al., 2015; Gudmundsson et al., 2015), graphite (Eliasson et al., 2021) and copper (Gudmundsson et al., 2022), tungsten (Suresh Babu et al., 2022, 2023) and zirconium (Suresh Babu et al., 2024) targets.

Earlier an ionization region model was developed for a reactive HiPIMS discharge and applied to study a discharge with tungsten target in argon-oxygen atmosphere, to better understand the effects of key parameters, including voltage pulse length, oxygen partial pressure and pulse-averaged target power density on the discharge operation (Rezek et al., 2021). Similar to the ionization region model, this model utilizes inputs such as the experimental geometry, current and voltage waveforms, argon and oxygen flow rates or partial pressures, ion return probabilities, and material parameters including densities, sticking coefficients, sputtering yields, and implantation profiles. This model's main features are that it tracks the ionization of sputtered atoms and oxygen dissociation in the plasma, based on electron density and temperature. It accounts for oxygen dissociation and varying sticking coefficients for atoms and molecules. The model includes oxygen chemisorption on the target and its implantation into the target. Furthermore, it considers the return and implantation of ionized sputtered atoms onto the target surface and the subsurface layers of the target.

In a recent study Vavassori et al. (2023) explored a HiPIMS discharge with tungsten target through a combination of modeling and experiments to investigate the plasma behavior under varying magnetic field conditions (40 mT and 60 mT at the target surface). The findings revealed that an increase in magnetic field strength enhanced the degree of self-sputtering recycling. This stronger recycling effect with a higher magnetic field led to higher sputtered ion fraction in the plasma discharge, making these ions more likely to be attracted back to the

target.

2.4 Tungsten and zirconium

Tungsten (W) is a refractory metal, commonly found in the A2 bcc structure. It has the highest melting point among elemental metals (3695 K) and the lowest thermal expansion coefficient (4.5×10^{-6} K^{-1}), along with low electrical resistivity. Tungsten's ability to withstand extreme temperatures makes it a prime candidate for high-temperature environments, such as thermonuclear fusion reactors. It is a leading material for divertor targets in these reactors due to its thermal shock resistance and low vapor pressure. Its machinability and resistance to sputtering by hydrogen and helium ions further highlight its suitability for harsh conditions. In microelectronics, tungsten is commonly used for metallization, serving as interconnects, contact plugs, and diffusion barriers. These advantages make it an exceptional material for a range of advanced coating applications.

Tungsten thin films deposited via dcMS and HiPIMS exhibit two phases: the equilibrium $\alpha-$W (A2 bcc) and the metastable $\beta-$W (A15 cubic). HiPIMS-deposited films have better density, smaller grains, and stronger adhesion (Engwall et al., 2019; Roychowdhury et al., 2020; Shimizu et al., 2021). They also feature enhanced properties such as smoother surfaces, greater hardness, and higher Young's modulus (Engwall et al., 2019; Velicu et al., 2018, 2017). In some cases, these improvements were amplified by adding a toroidal-shaped permanent magnet in front of the cathode target to generate an external magnetic field (Velicu et al., 2017).

Zirconium (Zr) is a group-IV transition metal that typically forms a hexagonal close-packed (hcp) structure (α-Zr) at room temperature and atmospheric pressure. At 1136 K, it undergoes a martensitic transformation into a body-centered cubic (bcc) structure (β-Zr phase) (Schnell and Albers, 2006). It boasts a high melting point, excellent thermal conductivity, low thermal expansion, and strong mechanical properties. Additionally, zirconium has a low neutron scattering cross-section and high solubility for oxygen and hydrogen, making it suitable for use in the nuclear industry (Olander, 1976; Coleman, 2022).

Zirconium thin films with an α-Zr structure have been produced via dc magnetron sputtering (Chakraborty et al., 2008; Pilloud et al., 2005; Fankhauser et al., 2016) asymmetric bipolar pulsed magnetron sputtering (Singh et al., 2011, 2014) and HiPIMS (Luo et al., 2019; Kuo et al., 2021). Notably, Fankhauser et al. (2016) used dc magnetron sputtering to deposit epitaxial Zr thin films on Al_2O_3(0001). With HiPIMS at substrate temperatures ranging from 300 to 873 K (Kuo et al., 2021), zirconium films are predominantly polycrystalline and display a [0 0 0 1] texture, while crystallite size increases with higher substrate temperatures. Kuo et al. (2021) found that adjusting the pulse width and substrate bias during HiPIMS could produce films with a [1 0 $\bar{1}$ 1] texture when longer pulse lengths and synchronized bias are applied. The HiPIMS technique enhances the inherent qualities of zirconium, leading to superior performance in demanding environments.

3 The Ionization Region Model

The ionization region model (IRM) of a high power impulse magnetron sputtering discharge is a time-dependent volume-averaged plasma chemistry model that provides the temporal variation of the various species densities and the electron energy. It is a semi-empirical model that requires experimentally determined discharge voltage and current waveforms, the working gas pressure, the target material and its dimensions, and the dimensions of the ionization region, as input.

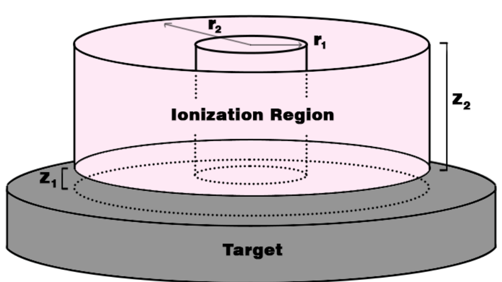

Figure 3.1. A schematic showing the dimensions of the assumed ionization region. The ionization region is defined as an annular cylinder of inner radius r_1 and outer radius r_2 resulting in racetrack width of $w_{RT} = r_2 - r_1$ located above the racetrack, and extends from z_1 to z_2 axially away from the target surface.

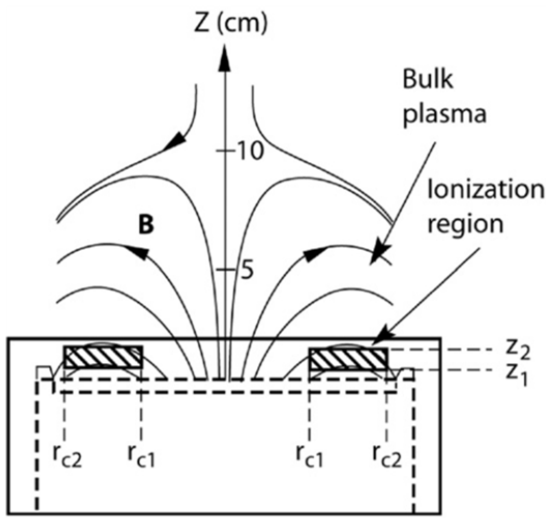

Figure 3.2. The magnetic field topology and the geometry of the ionization region. Reprinted from Raadu et al. (2011) ©IOP Publishing. Reproduced with permission. All rights reserved.

The IRM, initially described by Raadu et al. (2011), has been under constant development for the past 15 years. The IRM is derived from an attempt to model the HiPIMS discharge with a time-dependent volume averaged global model that covered the entire discharge chamber (Gudmundsson, 2006, 2008), which in turn was based on time-dependent global models of the plasma chemistry of a high density low pressure pulsed inductively coupled discharge (Ashida et al., 1995). The main features of the original IRM were summarized by Huo (2013) and Huo et al. (2017). The IRM only covers the target and the ionization region, which is defined as an annular cylinder of width $w_{\mathrm{RT}} = r_2 - r_1$ positioned above the racetrack, and a length $L = z_2 - z_1$, extending from z_1 to z_2 axially away from the target surface, as shown in Figure 3.1. Figure 3.2 shows the magnetic field topology and the geometry of the ionization region. In the IRM, the temporal development of the heavy species densities (neutrals and ions) and electron temperature is defined by a set of ordinary differential equations (Raadu et al., 2011; Huo et al., 2017). In addition, the electron density is found by applying the quasi-neutrality condition. The details of the IRM, including the reaction rates for the various surface and volume processes that are taken into account, are summarized by Huo et al. (2017). More recent modifications concerning the treatment of the afterglow (Rudolph et al., 2020) and updated reaction rates (Rudolph et al., 2021) have been made, as well as a modification to the term that describes the kick-out by the sputtered species and contributes to working gas rarefaction as discussed by Barynova et al. (2024). This last modification was needed to analyze and compare the contributions from electron impact ionization and kick-out to working gas rarefaction.

In this current work, tungsten and zirconium are added to the reaction set of the IRM as target materials. This chapter of the thesis examines the requirements for running the IRM, the parameters involved and provides a detailed explanation of the formulas essential for interpreting the outputs obtained from the model.

3.1 Particle Balance

Each heavy species in the plasma is governed by a particle balance equation. In our analysis, we focus on the following species: For the working gas, argon, we account for its ground state Ar, ion states, Ar^+ and Ar^{2+}, and a metastable state, Ar^{m}. The two metastable states are combined to give one effective metastable level. Additionally, we include warm argon atoms Ar^{W}, which are ground state argon atoms that were embedded in the target and subsequently released during operation. The warm population Ar^{W}, which is assumed to have an energy similar to the thermal energy of the target surface, with about 0.1 eV ($\sim$ 1000 K) (Anders et al., 2012), is due to argon ions that penetrate the target surface, and then slowly diffuse back as atoms. The hot argon atoms Ar^{H} population represents reflected argon atoms at the target (Yamamura and Ishida, 1995; Rudolph et al., 2018). They are assumed to have an average energy of 2 eV (Raadu et al., 2011). For tungsten, we consider ground state tungsten atoms W, and the tungsten ions W^+ and W^{2+} and for zirconium we consider the ground state zirconium atoms Zr, and the zirconium ions Zr^+ and Zr^{2+}.

The particle balance is the main mechanism modeled by the IRM and is governed by the general equation for each species X

$$\frac{dn^{(X)}}{dt} = \sum_i R^{(X)}_{\mathrm{Generation},i} - \sum_j R^{(X)}_{\mathrm{Loss},j} \tag{1}$$

The change of a species' particle density over time depends on the reaction rates $R^{(X)}_{\mathrm{Generation},i}$ and $R^{(X)}_{\mathrm{Loss},j}$ that describe all the generation and loss processes involving species X within the IR (Huo et al., 2017; Huo, 2013).

Each volume reaction rate, R_j for a given reaction j is calculated as the product of the densities of the reactants and the rate coefficient k_j of the reaction, where $n_{\mathrm{reactant},i}$ is the density of the i:th reactant and k_j is the rate coefficient of the reaction,

$$R_j = k_j \times \prod_i n_{\mathrm{reactant},i}. \tag{2}$$

As an example, the particle balance for the metal ion M^+ is written

$$\begin{aligned}\frac{\mathrm{d}n_{\mathrm{M}^+}}{\mathrm{d}t} = & \underbrace{k^{\mathrm{c}}_{\mathrm{iz,M}} n_{\mathrm{e}} n_{\mathrm{M}} + k^{\mathrm{h}}_{\mathrm{iz,M}} n_{\mathrm{e}} n_{\mathrm{M}}}_{\text{electron impact ionization}} + \underbrace{k_{\mathrm{P,iz}} n_{\mathrm{Ar^m}} n_{\mathrm{M}}}_{\text{Penning ionization}} + \underbrace{k_{\mathrm{chexc,1}} n_{\mathrm{M}} n_{\mathrm{Ar}^+} + k_{\mathrm{chexc,2}} n_{\mathrm{M}^{2+}} n_{\mathrm{Ar}}}_{\text{charge exchange}} \\ & - \underbrace{k^{\mathrm{c}}_{\mathrm{iz,M}^+} n_{\mathrm{e}} n_{\mathrm{M}^+} - k^{\mathrm{h}}_{\mathrm{iz,M}^+} n_{\mathrm{e}} n_{\mathrm{M}^+}}_{\text{electron impact ionization to create } \mathrm{M}^{2+}} - \underbrace{\frac{\Gamma^{\mathrm{RT}}_{\mathrm{M}^+} + \Gamma^{\mathrm{BP}}_{\mathrm{M}^+}(S_{\mathrm{IR}} - S_{\mathrm{RT}})}{\mathscr{V}_{\mathrm{IR}}}}_{\text{ion flux out of the ionization region}}\end{aligned} \tag{3}$$

where $k^{\mathrm{c}}_{\mathrm{iz,M}}$ and $k^{\mathrm{h}}_{\mathrm{iz,M}}$ are the rate coefficients for electron impact ionization of the M atom by cold and hot electrons, respectively, $k_{\mathrm{P,iz}}$ is the rate coefficient for Penning ionization, $k^{\mathrm{c}}_{\mathrm{iz,M}^+}$ and $k^{\mathrm{h}}_{\mathrm{iz,M}^+}$ are the rate coefficients for electron impact ionization of the M^+ ion by cold and hot electrons, respectively, and $k_{\mathrm{chexc,1}}$ and $k_{\mathrm{chexc,2}}$ are rate coefficients for charge exchange. The last term of Eq. (3) describes the metal ion flux out of the IR, towards the racetrack and the bulk plasma (BP).

3.1.1 Sputtering

The rate at which neutrals are sputtered off the target $R_{n,\mathrm{sputt}}$, is calculated as

$$R_{n,\mathrm{sputt}} = \frac{\sum_i \Gamma^{\mathrm{RT}}_i S_{\mathrm{RT}} Y_i(\mathscr{E}_{\mathrm{i}})}{\mathscr{V}_{\mathrm{IR}}} \tag{4}$$

From this relation we see that the rate of sputtered neutrals released from the target is a function of the incoming flux of ions i to the target racetrack Γ^{RT}_i , the surface area of the racetrack S_{RT}, the energy dependent sputter yield of the bombarding ion $Y_i(\mathscr{E}_{\mathrm{i}})$, and the total volume of the IR, $\mathscr{V}_{\mathrm{IR}}$.

3.1.2 Ion particle balance

The ion flux for ion i towards the racetrack is calculated using

$$\Gamma^{\mathrm{RT}}_i = \beta_i n_i \sqrt{\frac{q_i V_{\mathrm{IR}}}{m_i}} \tag{5}$$

where n_i is the density of ion species i, q_i is the ion charge, V_{IR} is the potential drop over the IR, m_i is the ion mass and β_i is the back-attraction probability of ions. The parameter β_i is an important fitting parameter to the IRM.

3.1.3 The kick out effect

In the early versions of the IRM, the gas rarefaction by the effect of the sputter wind was implemented as an argon kick-out term by collisions with fast sputtered particles coming from the target. For each of the neutrals Y of the working gas, including the metastable states, the particle balance includes a loss term

$$R_{n,\text{kick-out}} = \frac{1}{2}\frac{v_{\text{ran},X}}{L}F_{\text{coll}}\frac{m_X \sum_i n_{X,i}}{m_Y \sum_i n_{Y,i}}n_Y \tag{6}$$

where X here stands for the species sputtered off the target and their ions, singly and doubly ionized. The sum is taken over all the states of that sputtered species. A multiplication of the flux reductions by the mass ratio $m_\mathrm{X}/m_\mathrm{Y}$ accounts for the conservation of momentum. Eq. (6) represents the kick-out term that was used when modeling the discharge with tungsten targets (Suresh Babu et al., 2022, 2023) and in these studies only the sputtered tungsten atom contributed to kick-out of argon atoms.

For the study of the working gas rarefaction (Paper IV) (Barynova et al., 2024), the kick-out term was significantly revised in the IRM code from our earlier studies (Raadu et al., 2011; Huo et al., 2012, 2017). For the revised derivation of a kick-out term, we denote the kicking-out species by an X, and those that are kicked-out by a Y. Here, X = {M, $\mathrm{Ar^H}$}, where M stands for the target atoms, and Y = {$\mathrm{Ar^C}$, Ar(4s[3/2]$_2$), Ar(4s'[1/2]$_0$)}. In the model, we assume that a collision of a species X with a species Y leads to the instantaneous loss of species Y from the IR. This is acceptable if two conditions are met: (i) The momentum of species X is always higher than the average momentum of the cold Ar species (species Y) at an assumed working gas temperature of 500 K. The lightest target atom studied here, carbon, has the mass $M = 12M_\mathrm{p}$, where M_p is the proton mass, and an ejection energy $\mathscr{E}_\text{ejection} = \frac{1}{2}\mathscr{E}_\text{cohesive}$ = 3.7 eV (Eliasson et al., 2021). This yields a momentum of 10^{-22} kg m/s which is higher than the momentum of an average argon species at T_g = 500 K which is $\sim 10^{-23}$ kg m/s. We therefore consider the first condition to be fulfilled. (ii) The length of a HiPIMS pulse is longer than the typical loss time of species Y out of the IR after the collision. For example, a collision in the middle of the IR with a typical height $h = 2$ cm and a post-collision velocity of $v = 1000$ m/s, results in a loss of species Y within $t = h/2v = 10$ μs. The pulse lengths of the HiPIMS discharges investigated in this study are longer by a factor of 4 to 20, which is why the assumed instantaneous loss is an acceptable assumption. We neglect that this assumption underestimates the momentary argon density. This approximation of instant loss of species from the IR is therefore acceptable for the discharges studied in this work. Furthermore, for collisions between $\mathrm{Ar^H}$ and $\mathrm{Ar^C}$, we neglect the effect that head-on collisions would simply result in the exhange of velocity vectors with no net change in the argon density in the IR. Collisions under an angle result in both particles to be lost out of the IR. As collisions under an angle are much more probable compared to head-on collisions, also this is an acceptable assumption.

For each species X, we assume that there is a certain probability for these particles to collide with particles of the species Y. This is given by

$$F_{\mathrm{coll,X\to Y}} = 1 - \exp(-L/\lambda_{\mathrm{X\to Y}}), \tag{7}$$

where L is the height of the IR and the mean free path $\lambda_{\mathrm{X\to Y}}$ of a species X in a background

gas composed of species Y is given by

$$\lambda_{\mathrm{X}\to\mathrm{Y}} = \frac{1}{\sigma_{\mathrm{X}\to\mathrm{Y}} n_{\mathrm{Y}}}. \tag{8}$$

where the cross sections $\sigma_{\mathrm{X}\to\mathrm{Y}}$ are the momentum transfer cross sections for each pair of X and Y, and n_{Y} is the density of species Y.

Note that $F_{\mathrm{coll,X}\to\mathrm{Y}}$ is the fraction of the momentum carried by the sputtered species that is transferred to the kicked-out species Y. We can therefore link the sputter flux $\Gamma_{\mathrm{sputter}}$ (in m^{-2} s^{-1}) to the kick-out flux $\Gamma_{\mathrm{kickout}}$ out of the IR by

$$R_{\mathrm{kickout,X}\to\mathrm{Y}} = F_{\mathrm{coll,X}\to\mathrm{Y}} \Gamma_{\mathrm{sputter,X}} \frac{S_{\mathrm{RT}}}{\mathscr{V}_{\mathrm{IR}}} = \Gamma_{\mathrm{kickout}} \frac{S_{\mathrm{DR}}}{\mathscr{V}_{\mathrm{IR}}}, \tag{9}$$

where S_{RT} is the surface area of the IR facing the racetrack, and S_{DR} is the surface area of the IR facing the diffusion region (Raadu et al., 2011). The sputtered flux is

$$\Gamma_{\mathrm{sputter,X}} = \sum_i \Gamma_i^{\mathrm{RT}} Y_i(\mathscr{E}_{\mathrm{i}}) \tag{10}$$

where $Y_i(\mathscr{E}_{\mathrm{i}})$ is the sputter yield for an ion species i bombarding the target. Note that Eq. (9) represents 6 equations, representing each pair (X,Y) of kicking-out species X and species Y that are kicked-out. Also, note that this model assumes that there is at most one collision between a sputtered species and a gas species. Based on the long mean free path of sputtered species in the IR compared to the typical height of the IR (see above), this is an acceptable assumption. This updated kick-out term is discussed in more detail by Barynova et al. (2024) and was used when modeling the discharge with zirconium target (Suresh Babu et al., 2024).

3.1.4 Electron balance

The electron energy distribution function (EEDF) facilitates the calculation of rate coefficients. In modeling these dynamics, the ionization region model (IRM) categorizes electrons into two distinct populations: the cold population $\mathrm{e^C}$ and the hot population $\mathrm{e^H}$. The majority of the electrons belong to the cold Maxwellian electron population, which therefore dictates the electron density and the effective electron temperature. For cold electrons originating from ionization processes within the plasma bulk, the typical energy range is assumed to be 1 to 7 eV, while for hot electrons, which are secondary electrons emitted from the cathode, the energy spans from 200 to 1000 eV. This categorization helps in understanding the behavior of electrons in the ionization region and the effects of their energy distribution on plasma processes and to calculate rate coefficients. The rate coefficients are calculated assuming a Maxwellian electron energy distribution function and fit in the range $T_{\mathrm{e}} = 1 - 7$ eV for cold electrons, and in the range 200 – 1000 eV for hot electrons. This assumption has been tested against a Boltzmann solver, showing a good agreement (Rudolph et al., 2021)

Regarding the particle balance, the IR closely adheres to the quasineutrality approximation, allowing the cold electron density to be accurately determined as

$$n_{\mathrm{ec}} = \sum_i Z_i n_{+,i} - \sum_j n_{-,j} - n_{\mathrm{eh}} \tag{11}$$

where Z_i is the charge state of the positive ion, n_{+i} is the density of the positive ion i, n_{-i} is the density of the negative ion i, and where the density of the hot electrons is obtained from

their effective electron temperature T_{eh} and their electron energy density p_{eh} is

$$n_{\mathrm{eh}} = \frac{p_{\mathrm{eh}}}{eT_{\mathrm{eh}}}. \tag{12}$$

Note that for the discharges modeled in this work there are no negative ions.

3.2 Power Balance

The power balance equates the power absorbed by the plasma electrons to power losses from various phenomena like elastic and inelastic collisions, de-excitation processes, and Penning ionization.

Employing two distinct electron populations impacts the system in two ways. This approach provides a more precise evaluation of cost of ionization based on electron energy. Introducing two electron populations, affects the various parameters: the degree of metal ionization, self-sputtering, and the cold electron temperature generally decrease, whereas gas rarefaction and plasma density increase. These changes can be attributed to the reduced energy required for ionization, enabled by the newly included hot electron population. Secondly, this model allows for the quantification of two primary electron heating mechanisms: the acceleration of secondary electrons across the cathode sheath and Ohmic heating within the IR. The power transferred to the electrons is characterized by

$$P_{\mathrm{e}} = P_{\mathrm{SH}} + P_{\mathrm{Ohm}} = I_{\mathrm{e,SH}} V_{\mathrm{SH}} + I_{\mathrm{e,IR}} V_{\mathrm{IR}} \tag{13}$$

where P_{e} is split up into sheath energization P_{SH} and Ohmic heating P_{Ohm} in the ionization region, which are composed of the split up electron current $I_{\mathrm{e,SH}}$ and $I_{\mathrm{e,IR}}$ through the sheath and the ionization region, and potential drop V_{SH} and V_{IR} over the sheath and the ionization region, respectively, as show in Figure 2.1. The two split-up powers will serve for the power balance equations respectively of the cold electron population and the hot electron population. The split potential drops are function of time and function of the discharge voltage V_{D} measured experimentally. They are defined as

$$V_{\mathrm{D}}(t) = V_{\mathrm{IR}}(t) + V_{\mathrm{SH}}(t) = f V_{\mathrm{D}}(t) + (1-f) V_{\mathrm{D}}(t) \tag{14}$$

where f is the fraction of the discharge potential that falls over the IR and it is taken as a fitting parameter in our model. Usually, around 90% of the voltage falls over the sheath ($f \approx 0.1$). As for the secondary electron current in the sheath, it is obtained from the model-calculated ion fluxes to the target:

$$I_{\mathrm{e,SH}}(t) = e \sum_i \Gamma_i^{\mathrm{RT}} S_{\mathrm{RT}} \gamma_{\mathrm{see},i} (1-r) \tag{15}$$

where we have introduced $\gamma_{\mathrm{see},i}$, which is the secondary electron emission yield due to ion bombardment, and the probability of the secondary electron successfully leaving the sheath, r, or the electron recapture probability. The term $\Gamma_i^{\mathrm{RT}} S_{\mathrm{RT}}$ gives the number of the ions i bombarding the target per unit time.

$$I_{\mathrm{e,IR}}(t) = \left\langle \frac{I_{\mathrm{e}}}{I_{\mathrm{D}}} \right\rangle I_{\mathrm{D}}(t). \tag{16}$$

and $\langle I_{\mathrm{e}}/I_{\mathrm{D}} \rangle$ is the volume average of the fraction of the discharge current in the IR carried by electrons.

3.2.1 Collisional energy loss

The collisional energy loss per electron-ion pair created is due to electron impact ionization, excitation and elastic scattering against neutral atoms. The collisional energy loss per electron-ion pair created $\mathscr{E}_{\mathrm{c}}$ can be calculated using the ionization rate coefficient of neutral ground state species X, $k_{iz}^{(X)}$, the excitation rate coefficients $k_{\mathrm{ex},i}^{(\mathrm{X})}$,

$$\mathscr{E}_{\mathrm{c}}^{(X)} = \mathscr{E}_{\mathrm{iz}}^{(X)} + \sum_i \mathscr{E}_{\mathrm{ex},i}^{(X)} \frac{k_{\mathrm{ex},i}^{(X)}}{k_{\mathrm{iz}}^{(X)}} + \frac{k_{\mathrm{el}}^{(X)}}{k_{\mathrm{iz}}^{(X)}} \frac{3m_e}{m^{(X)}} T_e \tag{17}$$

where $\mathscr{E}_{\mathrm{iz}}^{(\mathrm{X})}$ is the ionization energy of species X, $\mathscr{E}_{\mathrm{ex},i}^{(\mathrm{X})}$ is the excitation energy and the rate coefficient of the i:th excitation process of species X, $k_{\mathrm{el}}^{(\mathrm{X})}$ is the elastic scattering rate coefficient of species X, m_{e} is the electron mass and $m^{(X)}$ is the mass of species X. The collisional energy loss per electron–ion pair created, $\mathscr{E}_{\mathrm{c}}$, is shown in Figure 3.3 as a function of the electron temperature for the ground state tungsten and argon atoms, calculated assuming a Maxwellian electron energy distribution. We see that the collisional energy loss per electron–ion pair created is higher for argon atoms than the metal atoms.

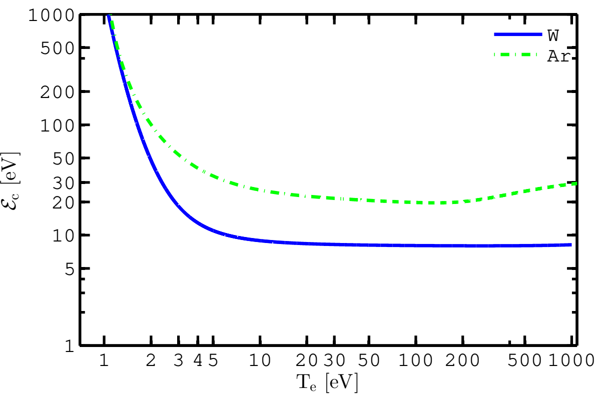

Figure 3.3. The collisional energy loss per electron–ion pair created, $\mathscr{E}_{\mathrm{c}}$, as a function of the electron temperature for the ground state tungsten and argon atoms, calculated assuming a Maxwellian electron energy distribution.

3.2.2 Modeled discharge current

Discharge current and voltage waveforms from a HiPIMS discharge and the geometry of the target is all that is needed as input to the IRM. Then the model will scan the parameter space defined by three parameters, (i) the back-attraction probability of ions $\beta_{\mathrm{t,pulse}}$, (ii) the fraction of the total discharge voltage falling over the IR, f, and (iii) the secondary electron recapture probability r, in an attempt to recreate the input current as closely as possible. The region within the (f, $\beta_{\mathrm{t,pulse}}$) parameter space that yields a good fit is relatively broad. To further constrain the model, we use the measured ionized flux fraction F_{flux}, when available as suggested by Butler et al. (2018).

The IRM calculates the discharge current by the fluxes of charged particles just above the racetrack. The current is calculated as

$$I_{\mathrm{calc}} = e \sum_i Z_i \Gamma_i S_{\mathrm{RT}} \left(1 + (1-r)\gamma_{\mathrm{see},i}\right) \tag{18}$$

where $\gamma_{\mathrm{see},i}$ is the secondary electron emission yield due to bombardment by ion i, S_{RT} is the area of the racetrack, Γ_i is the flux of ion i and the sum is taken over all the positive ions.

3.2.3 Generalized recycling model

The generalized recycling model combines the processes of self-sputter (SS)-recycling and working gas recycling in HiPIMS discharges (Brenning et al., 2017; Anders et al., 2012) and can be used to explain the large discharge currents observed in HiPIMS operation. In the generalized recycling model it is assumed that a primary current acts as a seed that is amplified by both the self-sputter recycling process and the working gas recycling process. A primary current I_{prim} is defined as a current, which is composed entirely of the ions of the noble working gas, here Ar^+ ions, that have been ionized for the first time and then drawn to the target (the contribution from secondary electrons, is neglected in the model) (Brenning et al., 2017). This primary current is the dominating current in dc magnetron sputtering discharge operation. However, there is a maximum steady state supply rate of argon atoms from the surrounding gas reservoir (Huo et al., 2017). This current therefore has a critical upper limit that can be estimated using

$$I_{\mathrm{crit}} = S_{\mathrm{RT}} e p_{\mathrm{g}} \sqrt{\frac{1}{2\pi m_{\mathrm{g}} k_{\mathrm{B}} T_{\mathrm{g}}}} = S_{\mathrm{RT}} e n_{\mathrm{g}} \sqrt{\frac{k_{\mathrm{B}} T_{\mathrm{g}}}{2\pi m_{\mathrm{g}}}}, \quad (19)$$

where p_{g} is the working gas pressure, T_{g} is the working gas temperature, n_{g} is the working gas density and S_{RT} is the racetrack area. For a gas temperature of 300 K, this gives an estimate of the maximum available discharge current due to working gas ions that are ionized for the first time and drawn to the target given in practical units as

$$I_{\mathrm{crit}} \approx 0.38 p_{\mathrm{g}} S_{\mathrm{RT}} \quad (20)$$

where S_{RT} is the racetrack area in cm^2, and p_{g} is the working gas pressure in Pa and here we assume $S_{\mathrm{RT}} = 0.5 \times S_{\mathrm{T}}$.

For discharge currents I_{D} larger than I_{crit} there has to be some kind of recycling of atoms that leave the target, subsequently become ionized and then drawn back to the target (Brenning et al., 2017). Depending on the type of ion drawn to the target, this results in either self-sputter recycling or working gas-recycling.

The discharge current in a HiPIMS discharge is the sum of the primary current, and contributions from working gas recycling and self sputter recycling, which can be written (Brenning et al., 2017)

$$I_{\mathrm{D}} \approx I_{\mathrm{prim}} + I_{\mathrm{gas-recycle}} + I_{\mathrm{SS}}. \quad (21)$$

The discharge current can also be written as multiplication of the primary current I_{prim} that then acts as a seed (Brenning et al., 2017), which in steady states gives

$$I_{\mathrm{D}} \approx I_{\mathrm{prim}} \left(1 + \frac{\pi_{\mathrm{g}}}{1-\pi_{\mathrm{g}}}\right)\left(1 + \frac{Y_{\mathrm{g}}}{Y_{\mathrm{SS}}} \frac{\pi_{\mathrm{SS}}}{1-\pi_{\mathrm{SS}}}\right) \quad (22)$$

where the working gas-sputtering parameter is $\pi_{\mathrm{g}} = \alpha_{\mathrm{g}} \beta_{\mathrm{g,pulse}} \xi_{\mathrm{pulse}}$ and the self-sputter parameter is $\pi_{\mathrm{SS}} = \alpha_{\mathrm{t}} \beta_{\mathrm{t,pulse}} Y_{\mathrm{SS}}$ Here, $\xi_{\mathrm{pulse}} = 1$ is the fraction of the recombined Ar^+ ions at the target that is assumed to return during the pulse as hot argon atom, Ar^{H} or warm argon atom, Ar^{W}.

The above discussion and in particular Eq. (22) is derived assuming that the primary current is at its critical upper limit, and that each subsequent cycle adds another contribution to the the working gas and self-sputter recycling current and, assuming a large number of such recycling loops, which allows the use of the infinite sum $\sum_{n=1}^{\infty} a^n = a/(1-a)$ where $0 < a < 1$.

To verify the validity of this assumption the ion loss time based on average quantities was estimated. The complete sequence of events to reach equilibium involves developing both a working gas recycling loop and a target species recycling loop. They come in a sequence of two loops. The working gas recycling loop initiates with an event of argon ionization and involves three steps (i) Ar^+ ion acceleration to the target (i.e., back-attraction), (ii) return to the IR either as a hot or a warm argon atom, and (iii) ionization. Similarly, the self-sputter recycling loop starts with an event of metal atom ionization followed by (i) M^+ ion acceleration to the target, (ii) sputtering that creates a metal atom that enters the IR, and (iii) ionization of this atom. To estimate the time of step (i) we assume the average ion that ends up at the target was produced in the middle of the IR, at a distance $(z_2 - z_1)/2$ from the sheath edge, and that the potential difference from this position to the sheath edge is $V_{IR}/2$. The loss time in the IR for this average ion is under these assumptions (Huo et al., 2017)

$$t_{loss} = \frac{z_2 - z_1}{\sqrt{\frac{q_i V_{IR}}{m_i}}}. \tag{23}$$

which for for Ar^+ ion is $t_{loss} \sim 2\ \mu$s and for W^+ ions the loss time is $t_{loss} \sim 4\ \mu$s, using z_1 and z_2 assumed in the IRM. A different estimate is based on lateral imaging of a HiPIMS discharge by Anders et al. (2012). They assume the atoms to only travel about 1 – 3 mm away from the target surface before they are ionized (Anders, 2012). Similar estimates have been made by Held et al. (2023) in particular for titanium. This leads to estimates for the residence time for Nb^+ ions in the range 0.2 – 0.3 μs. Scaling this with the square root of the ion mass ratio yields 0.3 – 0.4 μs for W^+ ions. For steps (ii) and (iii) we separate the time into a transit time t_{trans} and an ionization time t_{ion}. The transit time is the extent of the IR divided by the typical speed in the z-direction. It is longer for warm than for hot Ar atoms. Here we use the notation $\langle t_{trans} \rangle$ for a suitable average. The transit time $\langle t_{trans} \rangle$ is roughly 7.5 μs and 40 μs for hot and warm argon atoms, respectively, and about 13 μs for sputtered tungsten with energy of 4.45 eV. The ionization time for an atom is $t_{ion} = 1/(n_e \times k_{ioniz})$. The ionization time is about 1.5 ms for argon and about 30 μs for tungsten. A returning argon atom from the target can either be ionized in transit through the IR, or pass through it and escape to the diffusion region (DR) and therefore the effective time for steps (ii) and (iii) can be approximated as the shorter of these: the time from target to ionization $t_{t,iz} = \min(\langle t_{trans} \rangle, t_{ion})$. The slower of the loops, the self-sputter recycling loop, takes under 17 μs to complete. Therefore, the use of Eq. (22) is justified.

3.3 Internal discharge parameters

The IRM provides information on two important internal discharge parameters. The target material ionization probability α_t describes the probability that a sputtered target neutral is ionized within the IR. It is given by the fraction of the sputtered flux that does not leave the IR as neutrals

$$\alpha_t = 1 - \frac{\int_T \Gamma_{tn}^{DR}\, dt}{\int_T \Gamma_{sput}\, dt} \tag{24}$$

where $\Gamma_{\rm tn}^{\rm DR}$ is the target neutrals flux out of the ionization region to the diffusion region and $\Gamma_{\rm sput}$ is sputtered flux.

Similarly, the target ion back-attraction probability $\beta_{\rm t}$, is given by the fraction of produced ions that do not leave the ionization region to the diffusion region

$$\beta_t = 1 - \frac{\int_T \Gamma_{\rm ti}^{\rm DR}\, dt}{\int_T \Gamma_{\rm sput}\, dt - \int_T \Gamma_{\rm tn}^{\rm DR}\, dt}. \tag{25}$$

The sputter-rate-normalized deposition rate $F_{\rm sput}$ and the ionized flux fraction $F_{\rm flux}$ can then be expressed as functions of the internal discharge parameters $\alpha_{\rm t}$ and $\beta_{\rm t}$

$$F_{\rm sput} = (1-\alpha_{\rm t}) + \left(\frac{\xi_{\rm ti}}{\xi_{\rm tn}}\right)\alpha_{\rm t}(1-\beta_{\rm t}) \tag{26}$$

where $\xi_{\rm ti}/\xi_{\rm tn}$ is evaluated at the position of the ion meter which is used to determine $F_{\rm flux}$. This expression reduces to a reduction in the deposition rate by a factor $1-\alpha_t\beta_t$,

$$F_{\rm sput} = 1 - \alpha_{\rm t}\beta_{\rm t} = \frac{\Gamma^{\rm DR}}{\Gamma_0} \tag{27}$$

for the special case when $\xi_{\rm ti} = \xi_{\rm tn}$. This is the ratio of the flux of sputtered species (ions and neutrals) out of the ionization region (IR) towards the diffusion region (DR) $\Gamma^{\rm DR}$ and the total flux of atoms sputtered from the target Γ_0 (atoms/s).

The ionized flux fraction at the substrate becomes

$$F_{\rm flux} = \left(1 + \frac{\xi_{\rm tn}}{\xi_{\rm ti}}\frac{1-\alpha_t}{\alpha_t(1-\beta_t)}\right)^{-1}. \tag{28}$$

The ionization probability $\alpha_{\rm t}$ and the back-attraction probability $\beta_{\rm t}$ can be written as a function of $F_{\rm sput}$ and $F_{\rm flux}$

$$\alpha_t = 1 - F_{\rm sput}(1 - F_{t,\rm flux}) \tag{29}$$

and

$$\beta_t = \frac{F_{\rm sput}F_{t,\rm flux}\left(1 - \frac{\xi_{\rm tn}}{\xi_{ti}}\right) - F_{\rm sput} + 1}{1 - F_{\rm sput}(1 - F_{t,\rm flux})} \tag{30}$$

3.4 Updating the ionization region model for new target materials in HiPIMS

To begin modeling of a discharge with new target element, the IRM must be updated with a reaction set, energy dependent secondary electron emission yield, sputter yields, the geometry, the pressure, the working gas, target species and discharge parameters specifically tailored for an argon-tungsten and argon-zirconium HiPIMS discharge. The measured current and voltage waveforms are then fit with three parameters to reproduce the measured discharge current curve. The input parameters used for modeling HiPIMS discharges with tungsten and zirconium target are listed in Table 3.3.

Table 3.1. The input parameters used for modeling of a HiPIMS discharges with tungsten and zirconium target.

Target Input	Tungsten (Suresh Babu et al., 2022)	Tungsten (Suresh Babu et al., 2023)	Zirconium (Suresh Babu et al., 2024)
Pressure (Pa)	1.0	1.6	0.5, 1
Target diameter (mm)	75	150	50
r_{c1}, r_{c2}, z_1, z_2 (mm)	8, 27, 2, 22	12, 57, 2, 33	6, 19, 2, 13
Pulse length (μs)	100	50, 100, 200	50, 100

3.4.1 Reaction rate

A sputtered target atom experiences many interactions on the way through the plasma discharge. These interaction are implemented in the reactions that a target atom may take part in are listed in Table 3.2. When entering the discharge target atom experiences electron impact excitation and ionization, charge transfer, and Penning ionization.

The plasma-chemical reactions are described by two sets of rate coefficients, one for the cold and the other set for the hot electron population. The cold electrons are created by ionization of argon and tungsten atoms, while the hot electrons are ion-induced secondary electrons, emitted from the target surface, and consequently accelerated across the cathode sheath Rudolph et al. (2021).

3.4.2 Secondary electron emission yield

When energetic electrons, ions, or neutrals strike a metallic surface, they can cause the emission of electrons, known as secondary electrons. The secondary electron emission coefficient $\gamma_{\rm see}$, quantifies the average number of secondary electrons emitted for each bombarding particle. This coefficient varies based on the target material, its surface conditions, the type of bombarding species, and their kinetic energy. In magnetron sputtering discharges, where the cathode target is maintained at a high negative potential, these secondary electrons are propelled away from the target surface, starting with an initial energy approximately equal to the target's potential. For bombarding ions with low kinetic energy, the secondary electron emission yield remains constant regardless of the particle's energy. Here, electron emission results from the transfer of potential energy from the incoming ion or atom to an electron within the target, as described in the studies by Abroyan et al. (1967) and Hagstrum (1954).

For the secondary electron emission yield due to bombardment by argon ions of a tungsten target, we use the value of 0.094, which is taken from the measurements of Hagstrum (1956), determined by averaging over all the values measured for ion bombarding energy in the range up to 1000 eV. In this ion energy range the electron emission is due to potential emission which appears to give roughly constant electron emission yield. For the tungsten ions bombarding the tungsten target the secondary electron emission yield is essentially zero. We neglect secondary electron emission due to bombardment of the target by W^{2+} ions.

For the secondary electron emission yield due to bombardment of a zirconium target by

Table 3.2. The reactions and rate coefficients used in the IRM for a discharge with argon as the working gas and tungsten and zirconium cathode target, including both hot and cold electrons. The rate coefficients are calculated assuming a Maxwellian electron energy distribution function and fit in the range $T_e = 1 - 7$ eV for cold electrons, and 200 – 1000 eV for hot electrons. The rate coefficients in the reaction set for argon are taken from earlier works (Eliasson et al., 2021; Rudolph et al., 2021).

	Reaction	Threshold [eV]	Rate coefficient [m^3/s]	electrons	Reference
(R1)	$e + Ar(3p^6) \longrightarrow Ar^+ + e + e$	15.76	$2.34 \times 10^{-14}\ T_e^{0.59}\ e^{-17.44/T_e}$	cold	(Gudmundsson and Thorsteinsson, 2007)
			$8 \times 10^{-14}\ T_e^{0.16}\ e^{-27.53/T_e}$		
(R2)	$e + Ar(3p^6) \longrightarrow Ar(4s[3/2]_2) + e$	11.548	$1.617 \times 10^{-14} T_e^{-0.8238} \exp(-14.1256/T_e)$	cold	(Alves, 2014)
			$1.1397 \times 10^{-22} T_e^2 - 1.8975 \times 10^{-19} T_e + 8.7910 \times 10^{-17}$	hot	
(R3)	$e + Ar(3p^6) \longrightarrow Ar(4s'[1/2]_0) + e$	11.723	$2.86 \times 10^{-15} T_e^{-0.8572} \exp(-14.6219/T_e)$	cold	(Alves, 2014)
			$1.8045 \times 10^{-23} T_e^2 - 2.9825 \times 10^{-20} T_e + 1.357 \times 10^{-17}$	hot	
(R4)	$e + Ar(4s[3/2]_2) \longrightarrow Ar(3p^6) + e$		$3.23 \times 10^{-15} T_e^{-0.8238} \exp(-2.578/T_e)$	cold	Detailed
			$(1.1397 \times 10^{-22} T_e^2 - 1.8975 \times 10^{-19} T_e + 8.7910 \times 10^{-17})/5$	hot	balancing
(R5)	$e + Ar(4s'[1/2]_0) \longrightarrow Ar(3p^6) + e$		$2.86 \times 10^{-15} T_e^{-0.8572} \exp(-2.8989/T_e)$	cold	Detailed
			$1.8045 \times 10^{-23} T_e^2 - 2.9825 \times 10^{-20} T_e + 1.357 \times 10^{-17}$	hot	balancing
(R6)	$e + Ar(4s'[1/2]_0) \longrightarrow Ar^+ + 2e$	4.21	$1.14356 \times 10^{-13} T_e^{0.2548} \exp(-4.4005/T_e)$	cold	(Dixon et al., 1973; Freund, 1987)
			$1.5213 \times 10^{-19} T_e^2 - 2.9599 \times 10^{-16} T_e + 1.8155 \times 10^{-13}$	hot	
(R7)	$e + Ar(4s[3/2]_2) \longrightarrow Ar^+ + 2e$	4.21	$1.14356 \times 10^{-13} T_e^{0.2548} \exp(-4.4005/T_e)$	cold	(Dixon et al., 1973; Freund, 1987)
			$1.5213 \times 10^{-19} T_e^2 - 2.9599 \times 10^{-16} T_e + 1.8155 \times 10^{-13}$	hot	
(R8)	$e + Ar^+ \longrightarrow Ar^{2+} + 2e$	27.63	$8.6365 \times 10^{-15} T_e^{0.6746} \exp(-24.3019/T_e)$	cold	(Müller et al., 1980)
			$5.22 \times 10^{-14} - 4.943 \times 10^{-17} T_e$	hot	[1]
(R9)	$e + Ar \longrightarrow Ar^{2+} + 3e$		-	cold	(Stephan et al., 1980)
			$6.169 \times 10^{-15} - 1.6316 \times 10^{-17} T_e$	hot	[2]
(R10)	$e + W \rightarrow W^+ + e$	7.864	$6.3966 \times 10^{-14} T_e^{0.4839} \exp(-8.221/T_e)$	cold	(Deutsch et al., 2001)
			$4.2507 \times 10^{-10} T_e^{-1.1791} \exp(-256.38/T_e)$	hot	
(R11)	$e + W^+ \rightarrow W^{2+} + e$	16.35	$1.446 \times 10^{-14} T_e^{0.7143} \exp(-14.5193/T_e)$	cold	(Montague and Harrison, 1984)
			$4.673 \times 10^{-10} T_e^{-1.3047} \exp(-273.55/T_e)$	hot	
(R12)	$Ar^+ + W \rightarrow Ar + W^+$		2×10^{-16}		(Rae and Tobin, 1988)
(R13)	$Ar(4s'[1/2]_0) + W \rightarrow Ar + W^+ + e$		5.3×10^{-15}		see text
(R14)	$Ar(4s[3/2]_2) + W \rightarrow Ar + W^+ + e$		5.3×10^{-15}		see text
(R15)	$e + Zr \rightarrow Zr^+ + e$	6.63	$1.69 \times 10^{-13} T_e^{0.171} \exp(-7.825/T_e)$	cold	(Deutsch et al., 2008)
			$3.04 \times 10^{-13} - 2.18 \times 10^{-16} \times T_e$	hot	
(R16)	$e + Zr^+ \rightarrow Zr^{2+} + e$	13.13	$3.06 \times 10^{-14} T_e^{0.042} \exp(-14.39/T_e)$	cold	
			$3.09 \times 10^{-14} - 2.21 \times 10^{-17} \times T_e$	hot	
(R17)	$Ar^+ + Zr \rightarrow Ar + Zr^+$		2×10^{-16}		(Rae and Tobin, 1988)
(R18)	$Ar(4s'[1/2]_0) + Zr \rightarrow Ar + Zr^+ + e$		5.3×10^{-15}		
(R19)	$Ar(4s[3/2]_2) + Zr \rightarrow Ar + Zr^+ + e$		5.3×10^{-15}		

argon ions, we use the fit given for clean metals developed by Phelps and Petrović (1999). For the zirconium ions bombarding the zirconium target the secondary electron emission yield is essentially zero. Furthermore, we neglect secondary electron emission due to the bombardment of the target by Zr^{2+} ions.

3.4.3 Sputter yield

The efficiency of the sputtering process is characterized by the sputter yield, denoted as $Y_i(\mathscr{E}_i)$. This yield represents the average number of atoms ejected from the target surface per incident ion. Sputter yield varies based on several factors including the energy and mass of the bombarding ion, the mass of the target atom, the angle at which the ion strikes the surface, and the surface binding energy of the target. The target atoms enter the discharge in one of two ways, either they get sputtered off the target by a bombarding target ion, or by a bombarding argon ion. As suggested by (Anders, 2010), the sputter yield for each ion i are approximated by the general form

$$Y_i = a\mathscr{E}_i^b \tag{31}$$

where $\mathscr{E}_i$ is the energy of the incoming ion and a and b are constants that depend on the ion target pair.

Matsunami et al. (1983) and Yamamura and Tawara (1996) provided multiple empirical formulas that describe the sputter yield in relation to the energy of ion bombardment, alongside data for different combinations of bombarding ions and target materials. These, empirical equations for sputter yields at normal incidence have been implemented in the TU Wien Sputter Yield Calculator (Schmid, 2024), which was used to estimate the sputter yield for argon ions bombarding the zirconium target as well as for self sputtering of zirconium. The fit to the calculated yield gives $a = 0.003538$ and $b = 0.7936$ for Ar^+ sputtering of zirconium and for self-sputtering of zirconium $a = 0.001896$ and $b = 0.9316$.

To calculate the sputter yield for a given impacting species on a given target, as a function of the energy of the incident particle, can also be calculated using computer codes such as TRIM (transport of ions in matter) (Biersack and Haggmark, 1980), SRIM (stopping and range of ions in matter) (Ziegler et al., 2008, 2010), and TRIDYN (A TRIM simulation code including dynamic composition changes) (Möller and Eckstein, 1984; Möller et al., 1988) are commonly used. For argon ions bombarding tungsten $a = 0.0429$ and $b = 0.521$, and for self-sputter of tungsten $a = 0.0066$ and $b = 0.770$ (Anders, 2010) derived from fits to the sputter yields calculated using the TRIM (TRansport of Ions in Matter) code (Biersack and Haggmark, 1980).

3.4.4 Parameters to lock the model

There are three fitting parameters essential to lock the IRM model. The main ones are: (i) the potential drop across the ionization region IR, V_{IR}, and (ii) the probability of back attraction of ions to the target $\beta_{t,pulse}$. These parameters are adjusted so that the current to the target calculated in the model best reproduces an experimentally determined discharge current. potential drop across the IR, V_{IR}. The third fitting parameter is (iii) the electron recapture probability r. For a metal target the electron recapture probability r, can be varied in the range $0.25 \leq r \leq 0.9$ without influencing the model output much. For the tungsten case here (Suresh Babu et al., 2022) , the electron recapture probability r has been set to $r = 0.5$ (Thornton, 1978). For the cases presented in zirconium (Suresh Babu et al., 2024), we assume $r = 0.7$, since it has been suggested by Buyle et al. (2004), based on a Monte Carlo model calculations, that the electron recapture probability is typically between 65% and 75% for a planar magnetron sputtering discharge. Note that for a metal target, the value of the electron recapture probability r does not influence the model results significantly.

Table 3.3. The fitting parameters to lock the model.

Fitting parameter	Explanation
V_{IR}	The potential drop across the ionization region IR.
$\beta_{t,pulse}$	The probability of back attraction of ions to the target.
r	The electron recapture probability.

4 Results from the model

The IRM was applied to study HiPIMS discharges operated with tungsten and zirconium targets. As mentioned earlier, IRM is a semi-emperical model and needs input from measured discharge voltage and current waveforms. Here, we study the temporal evolution of the particle densities in the investigated discharges. We also explore the internal discharge parameters and how they depend on the peak discharge current density and working gas pressure and make comparison with HiPIMS discharges with other target materials.

4.1 Experimental apparatus and method

4.1.1 Tungsten

The discharge voltage and current waveforms for a HiPIMS discharge employing a tungsten target in an argon environment were analyzed using the IRM. The discharge voltage and current waveforms for the HiPIMS discharges, were taken from two experimental campaigns. The first set of measurements were taken from a setup based around a planar circular unbalanced magnetron assembly, featuring a tungsten disk (99.999% pure) with a diameter of 75 mm and a thickness of 5 mm, serving as the cathode target. The argon working gas, of purity of 99.997%, was regulated at a constant flow rate of 100 sccm and a steady pressure of 1.0 Pa by adjusting the pumping speed through the main gate valve. The system employed unipolar HiPIMS pulses with a pulse length of 100 μs, delivered by a HiPSTER 1 pulsing unit powered by a 1 kW HiPSTER 1 – DCPSU DC power supply from Ionautics AB, Sweden, as detailed by Shimizu et al. (2021). The measurements were performed at Tokyo Metropolitan University, Tokyo, Japan. Our study extends Shimizu et al.'s initial findings by investigating four different HiPIMS discharges, where the discharge voltage was varied in the range — 500 V, 600 V, 700 V, and 800 V. The pulse repetition frequency was varied to maintain fixed average power across all cases. For each discharge voltage and current waveform pair the deposition rate was determined, while the ionized flux fraction was not measured. The model study of these discharges is discussed in Paper I (Suresh Babu et al., 2022).

The second set of experiments was conducted at the University of Liverpool, Liverpool, United Kingdom and the details of the experimental setup are given by Ryan et al. (2019) and Ryan (2019). The experiments took place in a custom-designed cylindrical vacuum chamber constructed from stainless steel, measuring 500 mm in height and 450 mm in diameter. The discharge process utilized a SINEX 3 pulser unit (Chemfilt Ionsputtering A.B., Sweden) for driving the discharge. A tungsten target with a diameter of 150 mm was installed on a VTech 150 series unbalanced magnetron assembly (Gencoa Ltd, United Kingdom). Argon gas, maintained at a pressure of 1.6 Pa, served as the working gas for the experiments. The pulses had durations of 50 μs, 100 μs, and 200 μs, with a consistent repetition frequency of 50 Hz across all three scenarios. An average discharge power $\langle P_{\mathrm{D}} \rangle$ of 400 W was sustained for each case. The discharge voltage and current waveforms for these settings are depicted

in Figure 4.1. Note that both the discharge voltage and the discharge current vary with time as the SINEX 3 pulser unit has a smaller storage capacitor compared to more modern pulser units (Hubička et al., 2020; Gudmundsson et al., 2022).

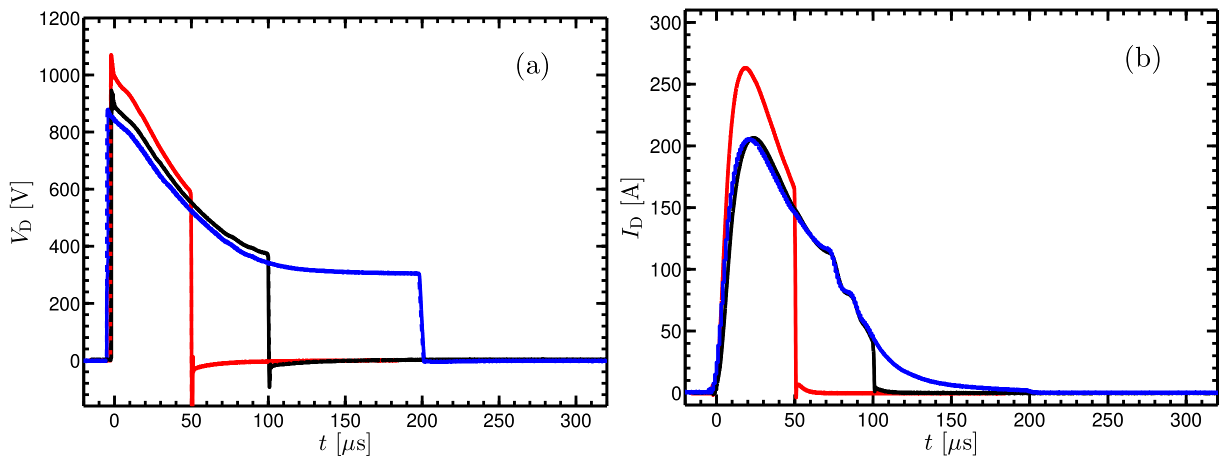

Figure 4.1. (a) The temporal evolution of the discharge (a) voltage $V_D(t)$ and (b) current $I_D(t)$. The argon working gas pressure was 1.6 Pa and the target was made of tungsten 150 mm in diameter.

Thomson scattering measurements were applied on the discharges to determine the temporal variation of the electron temperature and electron density. Also, time-resolved optical emission spectrometry (OES) measurements were performed in the magnetic trap region $r = 41$ mm, $z = 10$ mm) by Ryan (2019) to provide information on the species composition in the discharge. This involved measuring the temporal variation in the intensity of selected line emissions. The modeling of these three discharges and comparisson with experimentally determined discharge parameters are discussed in Paper II (Suresh Babu et al., 2023).

4.1.2 Zirconium

For a discharge with a zirconium target the setup utilized a 2-inch zirconium disk affixed to an unbalanced magnetron assembly. The base pressure was kept below 2×10^{-4} Pa using a turbomolecular pump supported by a roughing pump. The working gas pressure of either 0.5 or 1 Pa was achieved by controlling the argon gas flow. Voltage pulses were applied to the cathode target using a DC power supply in conjunction with a HiPSTER 6 pulsing unit from Ionautics AB, Sweden. These measurements were made at Linköping University, Linköping, Sweden.

The peak discharge current was held constant while the average discharge power, represented as $\langle P_D \rangle$, was maintained at 60 W by adjusting the repetition frequency. Pulse durations were consistently set to either 50 μs or 100 μs. For comparative purposes, measurements were also conducted under similar conditions using a DC magnetron sputtering (dcMS) system, with a discharge voltage of $V_{D,dcMS} = 255$ V at the same pressures and average power.

Flux parameters were assessed using an ion meter equipped with magnetic shielding, a grounded casing, and a quartz crystal micro-balance (QCM) sensor which can be biased to achieve charge selectivity. The ion meter is capable of measuring deposition rates from both ions and neutrals or exclusively from neutrals by adjusting the voltage on the biased top

electrode of the QCM. The design and operational principles of the ion meter, also known as a gridless QCM or m-QCM, are extensively detailed in other sources (Hubička et al., 2013; Kubart et al., 2014) . During the experiments, the ion meter was positioned at heights of 3, 4, 6, 8, and 10 cm above the racetrack region, oriented towards it. The modeling of the discharges with zirconium target are discussed in Paper III (Suresh Babu et al., 2024).

4.2 Fitting with IRM

The Ionization Region Model (IRM) is designed to simulate HiPIMS discharges by utilizing discharge current and voltage waveforms as input parameters to analyze plasma behavior and ionization dynamics. This model methodically explores a parameter space encompassing three critical variables: the ionized flux fraction (F_{flux}) (when available), the back-attraction probability of ions of the sputtered species during the pulse ($\beta_{\text{t,pulse}}$), the potential drop across the IR, (V_{IR}), as detailed in Eq. (14), and the electron recapture probability (r). The IRM's objective is to accurately replicate the input current waveform by calculating the fluxes of charged particles just above the racetrack.

A typical simulation using the ionization region model (IRM) may produce a variety of outputs, including the graphs depicted in Figure 4.2. During this specific simulation, the three fitting parameters were adjusted as follows: the back-attraction probability of ions ($\beta_{\text{t,pulse}}$) was varied between 0.3 and 0.99, the fraction of the total discharge voltage that drops across the ionized region $f = V_{\text{IR}}/V_{\text{D}}$ ranged from 0.05 to 0.2, while the electron recapture probability (r) was set at 0.5. Figure 4.2 presents two illustrative outputs from a simulation conducted using the ionization region model (IRM) for tungsten target (Suresh Babu et al., 2022). Figure 4.2 (a) shows results from an extensive scan of the parameter space, where the current fits are assessed based on their alignment with the experimentally measured current. Areas shaded in blue indicate a better fit. In this instance, the most accurate fits occurred when the fraction of the total discharge voltage across the ionized region (f) ranged from 0.5 to 0.15, and the back-attraction probability of ions ($\beta_{\text{t,pulse}}$) varied between 0.1 and 0.99. The overlay of white lines, annotated with black numerals, represents different values of the ionized flux fraction (F_{flux}). A white circle highlights the location of the best fit as achieved from estimating the mean square of error. Figure 4.2 (b) compares the discharge current waveform as measured experimentally against the fit produced by the IRM. The correspondence between the modeled and measured discharge currents demonstrates a high level of accuracy in the simulation outcomes. The figure of merit (FOM), shown in the Figure 4.3 (a) for zirconium target (Suresh Babu et al., 2024) with a color scale, is calculated as the weighted sum of square residuals normalized by the weighted total sum of squares (Gudmundsson et al., 2022). The regions on the fitting map where the modeled discharge current matches the experimental discharge current the best is shown as a yellow zone. This yellow zone indicates the combination of $f = V_{\text{IR}}/V_{\text{D}}$ and $\beta_{\text{t,pulse}}$ where the weighted square deviation of the discharge current is the smallest. The ionized flux fraction is shown as black contour lines in Figure 4.3 (a). As this yellow zone is large, an additional constraint from an experimentally determined quantity is necessary. This is done by using the measured ionized flux fraction to lock the model as suggested by Butler et al. (2018). In Figure 4.3 (a) we use the ionized flux fraction measured (45 %) at 10 cm from the target surface over the racetrack to lock the model. The measured discharge current waveform and the measured discharge voltage waveform are shown by solid lines in figure 4.3 (b). The resulting best fit determined by the IRM for the discharge current

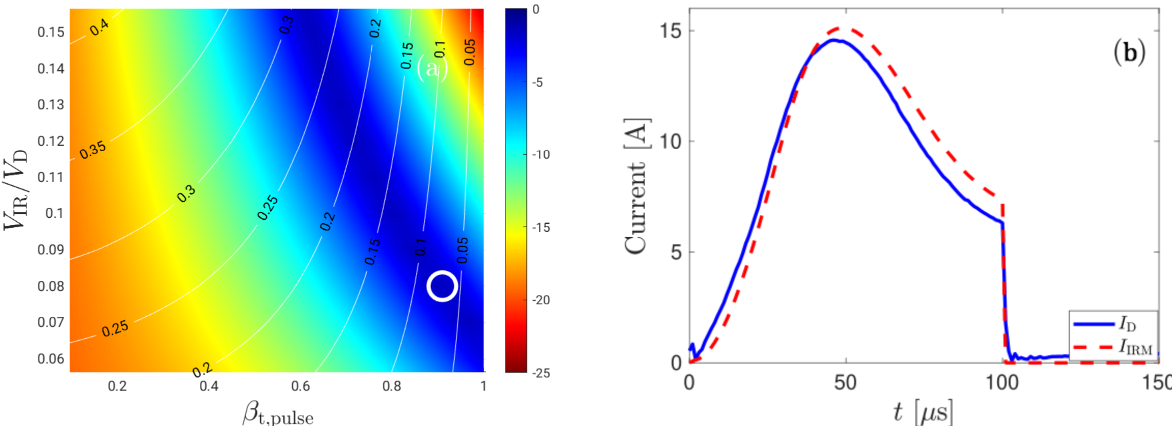

Figure 4.2. (a) The fitting maps showing $f = V_{IR}/V_D$ versus the back attraction probability $\beta_{t,pulse}$ for discharge voltage of 500 V and working gas pressure of 1.0 Pa, for a discharge with 75 mm diameter tungsten target. The white circles indicate where a well fitted current profile is observed. The white lines and the accompanying numbers indicate the ionized flux fraction (F_{flux}). (b) The measured temporal evolution of the discharge current (solid line) and the model fit (dashed line) for discharge voltage of 500 V for a discharge with 75 mm diameter tungsten target.

waveform and the measured ionized flux fraction is shown with a dot dashed line in figure 4.3 (b). The modeled discharge current matches the experimental discharge current very well.

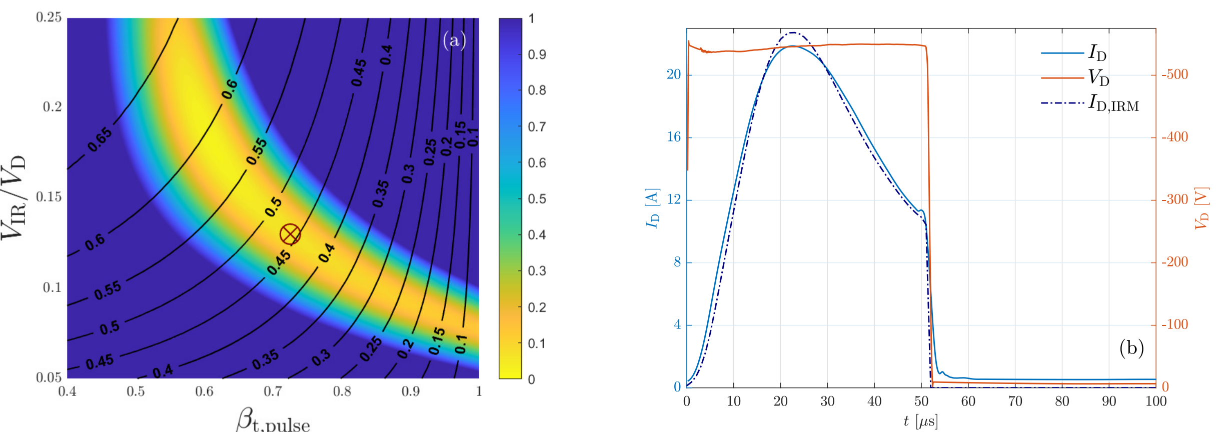

Figure 4.3. (a) The figure of merit (FOM) and the ionized flux fraction F_{flux}, displayed as a color map and contour lines, respectively, for a grid scan over $\beta_{t,pulse}$ and $f = V_{IR}/V_D$ for a 5.08 cm diameter zirconium target for a 50 µs long pulse, with peak discharge current density $J_{D,peak} = 1$ A/cm^2 and working gas pressure of 1 Pa. The parameter combination giving the best fit while meeting the F_{flux} constraint is highlighted with a red ×. (b) The measured temporal evolution of the cathode voltage (solid red line) and the discharge current (solid blue line) as well as the model fit (purple dash dot line) for the discharge current with a 5.08 cm diameter zirconium target, a 50 µs long pulse, a peak discharge current density $J_{D,peak} = 1$ A/cm^2, and working gas pressure of 1 Pa.

4.3 Species densities

The ionization region model (IRM) provides the temporal evolution of all particle densities in the HiPIMS discharges. This section continues the analysis from the previous discussions by examining how these species densities change over time for discharges with both tungsten and zirconium targets.

4.3.1 Neutral Densities

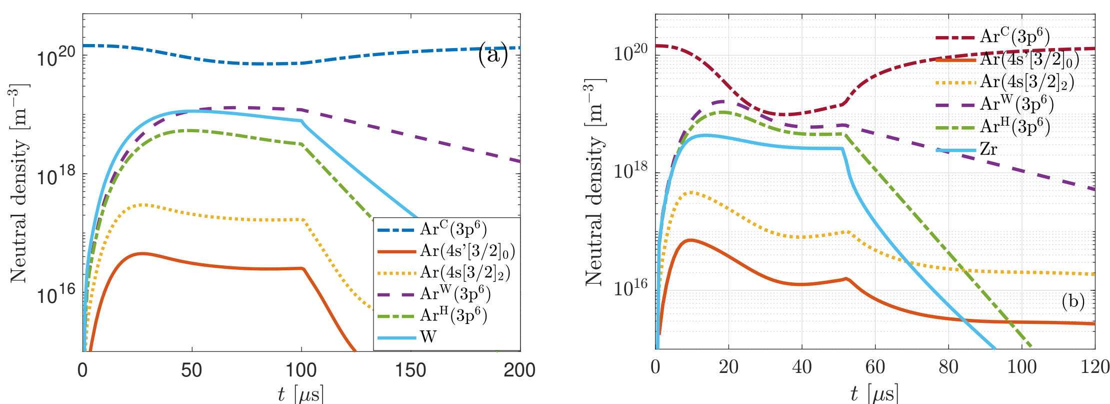

Figure 4.4. (a) The temporal evolution of the neutral particle densities for discharge voltage of 600 V for a discharge with 75 mm diameter tungsten target, $J_{\mathrm{D,peak}} = 0.54$ A/cm^2, and working gas pressure of 1.0 Pa. (b) The temporal evolution of the neutral particle densities for discharges with a 5.08 cm diameter zirconium target, 50 µs long pulse, with peak discharge current density $J_{\mathrm{D,peak}} = 1$ A/cm^2 and working gas pressure of 1 Pa.

Figure 4.4 (a) displays the temporal variation of neutral particle densities for a HiPIMS discharge in argon with tungsten target. Across different discharge voltages, the behavior of these densities remains consistent. The ground state working gas argon atoms dominate the discharge. Specifically, the cold argon ground state density (denoted $\mathrm{Ar^C(3p^6)}$) in Figure 4.4 (a) decreases during the pulse on time, reaching its lowest point at the end of the pulse, marking the occurrence of working gas rarefaction (Rossnagel, 1988). This phenomenon of working gas rarefaction, which is notably significant in HiPIMS discharges, has been well-documented through experimental evidence (Alami et al., 2006; Vlček et al., 2004; Vitelaru et al., 2012; Shimizu et al., 2021; Palmucci et al., 2013; Lundin et al., 2009).

Figure 4.4 (a) also illustrates that the density of tungsten atoms quickly rises at the beginning of the pulse and then stabilizes for the duration of the pulse. Following the pulse, when sputtering due to energetic ion bombardment ceases, the density of the ground state tungsten atoms initially drops sharply and then gradually declines. We also note a build up of warm and hot argon atoms during the pulse on period.

Figure 4.4 (b) shows the temporal evolution of the neutral particle densities for a HiPIMS discharge with zirconium target, which again illustrates the significant decrease in neutral argon density towards the end of the pulse. It is important to note that the total neutral argon density within the ionization region (IR) comprises the combined densities of cold, warm, and hot argon atoms in the ground state, along with those in the two metastable states. These

components enter the IR during the pulse and contribute to the rarefaction process. Thus, working gas rarefaction encompasses not just the decline in the density of cold argon atoms as shown in Figure 4.4 (b), but the overall reduction in total argon density.

4.3.2 Charged Particle Densities

Figure 4.5 (a) illustrates the temporal evolution of charged particle densities of tungsten target. Initially, Ar^+ ions dominate, but shortly after, W^+ ions take over and maintain dominance for the remainder of the pulse. The density of doubly charged W^{2+} ions remains consistently lower than that of Ar^+ ions, and the density of Ar^{2+} ions is significantly smaller. The temporal evolution of the charged particle densities in a HiPIMS discharge with zirconium target shown in Figure 4.5 (b) shows that the Ar^+ ions are persistently the dominant ion throughout the pulse-on period and the Zr^+ ion has always a smaller density. The densities of the doubly charged Zr^{2+} and Ar^{2+} ions are always more than an order of magnitude smaller than the density of the singly charged ions. For most of the pulse duration, the density of Ar^+ and Zr^+ ions surpasses the density of zirconium atoms.

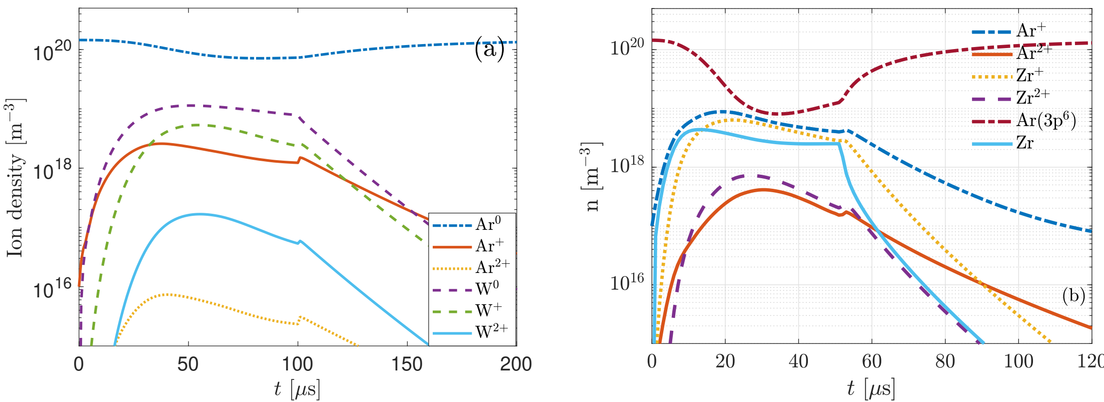

Figure 4.5. (a) The temporal evolution of the charged particle densities for discharge voltages of 600 V, for a discharge with 75 mm diameter tungsten target, $J_{D,peak} = 0.54$ A/cm^2, and working gas pressure of 1.0 Pa. In addition, we also show the total argon neutral density (ground state and excited states) [Ar^0] and the neutral tungsten density [W^0]. (b) The temporal evolution of the charged particle densities for a discharge with a 5.08 cm diameter zirconium target, 50 µs long pulse, with peak discharge current density $J_{D,peak} = 1$ A/cm^2 and working gas pressure of 1 Pa.

4.4 Current composition

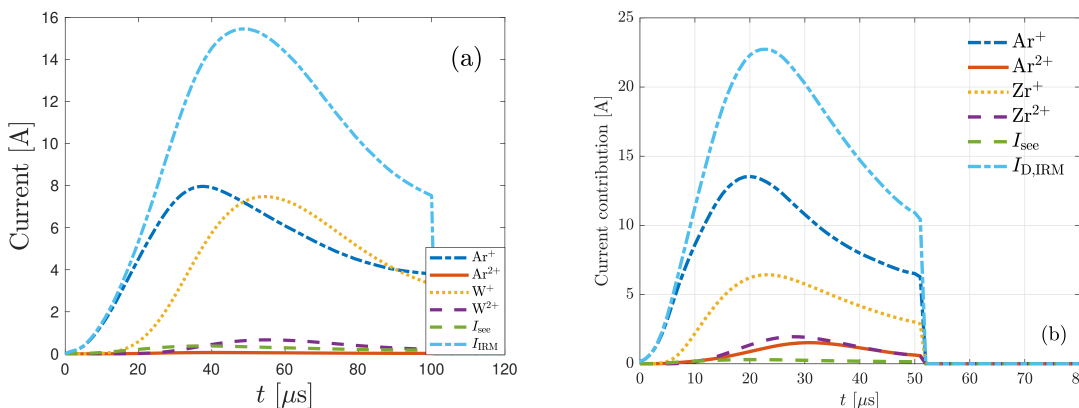

Figure 4.6. (a) The temporal evolution of the discharge current composition at the target surface for discharge voltages of 600 V for a discharge with 75 mm diameter tungsten target, $J_{D,peak} = 0.54$ A/cm^2, and working gas pressure of 1 Pa. (b) The temporal evolution of the discharge current composition at the target surface for a discharge with a 5.08 cm diameter zirconium target, for 50 µs long pulse, with peak discharge current density $J_{D,peak} = 1$ A/cm^2, and working gas pressure of 1 Pa.

Figure 4.6 (a) shows the discharge current composition at the target surfaces for a discharge with a tungsten target. Initially Ar^+ ions dominate, but as the the pulse continues, W^+ ions become the prevalent charged heavy species, especially as the initial peak of Ar^+ ions peak diminishes. This shift is more noticeable at higher discharge voltages, where the contribution of W^+ ions to the total discharge current at the target surface grows (Suresh Babu et al., 2022). Thus, at the onset of the pulse, the working gas ions strike the target, sputtering off metal atoms which are then ionized and drawn back to the target, creating a self-sputter recycling loop (Brenning et al., 2017). As a result, tungsten atoms and ions gradually take over some of the functions initially carried out by the working gas argon atoms and ions as the pulse progresses.

Figure 4.6 (b) shows the progression in the discharge current composition at the target surface for a discharge with a zirconium target over time. We see that roughly 2/3 of the discharge current is carried by Ar^+ ions while only 1/3 is carried by Zr^+ ions. The contributions from Ar^{2+} and Zr^{2+} ions, and secondary electron emission are comparatively minor. Given that both argon and zirconium ions play significant roles in the discharge current at the target surface, the discharge mechanism involves a mix of working gas recycling and self-sputter recycling (Brenning et al., 2017).

4.5 Electron behavior

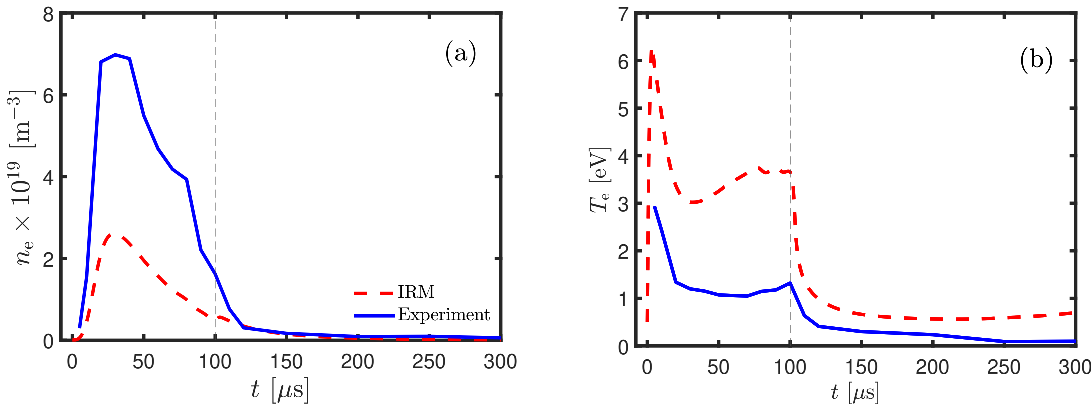

Figure 4.7. The temporal evolution of (a) the measured and calculated electron density (b) the measured and calculated electron temperature for pulse length of 100 µs for a discharge with argon working gas pressure of 1.6 Pa and 150 mm diameter tungsten target. The dashed vertical line indicates the termination of the pulse.

The measured temporal evolution of the electron density and electron temperature from the Thomson scattering measurements by Ryan et al. (2019) for tungsten target is shown in Figure 4.7 (a) and (b) respectively, in blue line. For the 100 μs long pulse the measured maximum electron density is $\sim 7 \times 10^{19}$ m^{-3} (Ryan et al., 2019). The measured temporal evolution of the electron density is compared to the calculated cold electron density in Figure 4.7 (a). Clearly, there is a discrepancy between the experimental and modeled electron density. The calculated electron density is always somewhat lower than the measured electron density. This discrepancy is up to a factor 4 during the peak for the 50 μs pulse length and somewhat smaller for 100 μs and 200 μs pulse length. In this thesis, only results for the 100 μs pulse length are presented, while the results for 50 μs and 200 μs pulse lengths are shown in Paper II (Suresh Babu et al., 2023). However, it should be taken into account that the IRM is a simple global model with densities averaged over the entire IR volume, which is here assumed to extend 33 mm away from the cathode target, while the measurement is taken 10 mm from the target surface. Therefore, if we assume the electron (and ion) density to decrease with distance from the target surface, it is expected that the model calculations yield a smaller electron density than what is measured close to the target surface.

Figure 4.7 (b) shows the temporal profiles of electron temperature within the magnetic trap for pulse lengths of 100 μs. The direct comparison of calculated and measured electron temperature shows a discrepancy. The calculated electron temperature is always significantly higher than the measured electron temperature. However, we point out that the features in the temporal evolution of the electron temperature are mostly captured by the model.

4.6 Internal discharge parameters

Figure 4.8 (a) shows the ionization probability and the back attraction probability versus the discharge voltage for HiPIMS discharges with tungsten target. In Figure 4.8 (a) we see that

the ionization probability α_t increases while the back-attraction probability $\beta_{t,pulse}$ decreases with increased discharge voltage. Earlier we have argued that the ionization probability depends only on the peak discharge current and increases with increased peak discharge current (Rudolph et al., 2022) and the decreasing back-attraction probability with increasing peak discharge current confirms the suggestion made earlier by Brenning et al. (2020, 2021).

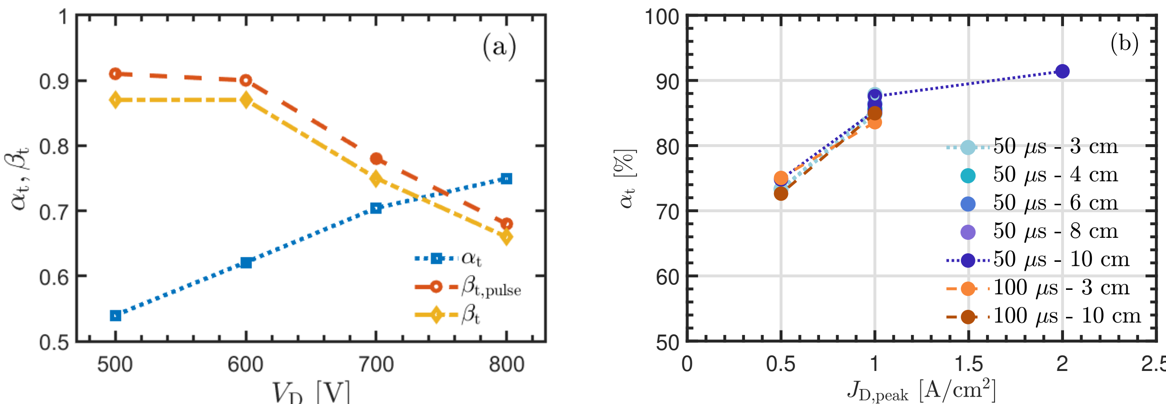

Figure 4.8. (a) The ionization probability α_t and the back-attraction probability $\beta_{t,pulse}$ and β_t versus the discharge voltage V_D, determined by the IRM for a discharge with 75 mm diameter tungsten target. (b) The ionization probability α_t versus the peak discharge current density for a discharge with a 50.8 mm diameter zirconium target and working gas pressure of 1 Pa.

Figure 4.8 (b) shows the ionization probability versus the peak discharge current density for HiPIMS discharges with zirconium target. For a zirconium target, as shown in Figure 4.8 (b) we see that the ionization probability α_t determined by the IRM, increases with increased peak discharge current density for a discharge with a 2 inch zirconium target for argon working gas pressure of 0.5 Pa (open circles) and 1 Pa (solid dots) and pulse length of 50 μs and 100 μs and the ionized flux fraction measured 3, 4, 6, 8, and 10 cm from the target surface.

That said, we see that ionization probability α_t increases as the discharge voltage V_D, and the peak discharge current density increase, for discharges with both tungsten and zirconium targets.

4.7 Normalised deposition rate

The ratio of the flux of sputtered species (ions and neutrals) that leave the ionization region (IR) towards the diffusion region (DR) Γ_{DR} and the total flux (atoms/s) of atoms sputtered from the target Γ_0, the useful fraction of the sputtered species, or the normalized deposition rate, can be approximated by (Bradley et al., 2015; Hajihoseini et al., 2019)

$$F_{dep} = \frac{\Gamma_{DR}}{\Gamma_0} = 1 - \alpha_t \beta_t. \tag{32}$$

This parameter is plotted versus the discharge voltage V_D for a discharge with 75 mm diameter tungsten target in Figure 4.9, where it is compared to the measured normalized deposition rate. The measured normalized deposition rate is the deposition rate for HiPIMS operation divided by the deposition rate determined from dc magnetron sputtering operated at the same average

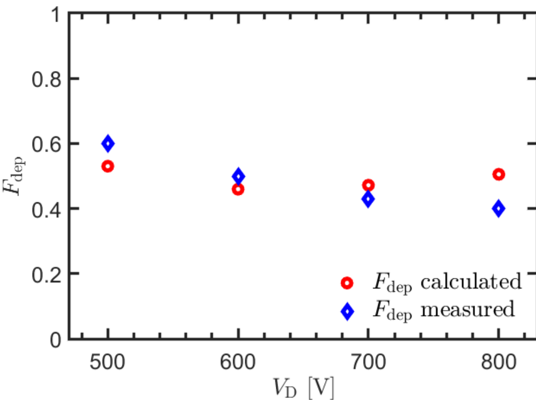

Figure 4.9. The measured normalized deposition rate and the normalized deposition rate determined from the IRM versus the discharge voltage V_D for a discharge with 75 mm diameter tungsten target.

power. We see that the normalized deposition rate calculated using the internal discharge parameters determined by the IRM agree well with the measured values. Keeping in mind that Eq. (32) does not take into account ion focusing (or spreading) en route towards the substrate (Butler et al., 2018; Rudolph et al., 2021). Eq. (32) says that this normalized deposition rate is reduced, and the fraction of the sputtered species reaching the substrate decreases, as the ionization of the sputtered material increases.

Figure 4.10 shows the measured normalized deposition rate for a zirconium target plotted against the peak discharge current density. The measured normalized deposition rate is

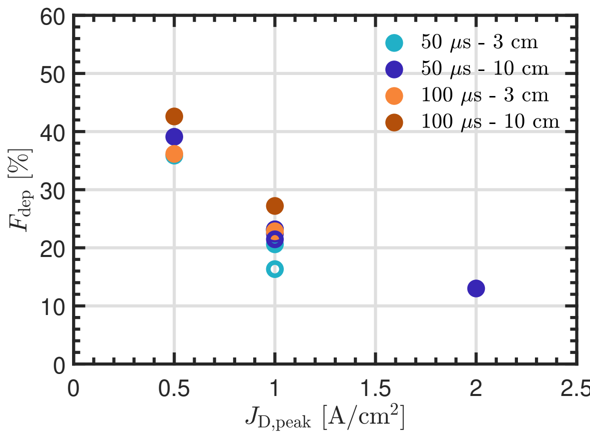

Figure 4.10. The measured normalized deposition rate versus the peak discharge current density for a 5.08 cm diameter zirconium target is shown. The working gas pressure was 0.5 Pa (open circles) and 1 Pa (solid dots) and the pulse length was 50 µs and 100 µs, measured 3 and 10 cm from the target surface.

the deposition rate for HiPIMS operation divided by the deposition rate determined from dc magnetron sputtering operated at the same average power. We see in figure 4.10 that the measured normalized deposition rate decreases with increased peak discharge current

density. This is commonly observed in HiPIMS operations. For a given pulse length and average power, the deposition rate decreases as the peak discharge current density increases (Tiron et al., 2015; Lundin et al., 2015; Shimizu et al., 2021; Suresh Babu et al., 2022). The normalized deposition rate for a given discharge current density is higher when measured 10 cm from the target surface than when measured at 3 cm. It can also be seen in Figure 4.10 that the normalized deposition rate is slightly lower for the lower working gas pressure (0.5 Pa) (open circles). The normalized deposition rate is also slightly higher for the longer pulse length (100 μs). This contradicts the findings of Shimizu et al. (2021) for a HiPIMS discharge with a titanium target as they observed a decrease in the normalized deposition rate as the pulse length was increased from 50 μs to 200 μs at $J_{\rm D,peak} = 1.1$ A/cm^2. In general, for a fixed peak discharge current density they found that the deposition rate increases with decreasing pulse length and reaches a maximum at around 25 – 50 μs, a trend that had been predicted earlier using the IRM (Rudolph et al., 2020). They also found that further shortening the pulse length decreases the deposition rate (Shimizu et al., 2021).

4.8 The potential drop across the IR

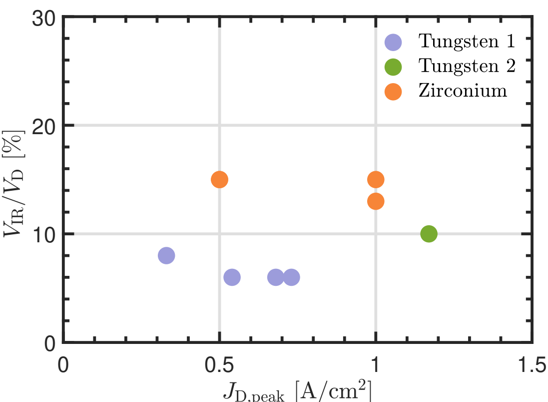

Figure 4.11. The fractional potential drop over the IR $f = V_{\rm IR}/V_{\rm D}$ versus the peak discharge current density for discharges with tungsten and zirconium targets. The pulse length was 100 μs.

The fraction of the discharge voltage that is dropped across the IR versus the peak discharge current density for tungsten and zirconium targets have been analyzed for pulse length of 100 μs. The fraction potential drop over the IR is shown versus the peak discharge current density for discharges with tungsten and zirconium targets in Figure 4.11. For a discharge with tungsten target this fraction was in the range 6 – 8 %, decreasing with increasing peak discharge current density (Suresh Babu et al., 2022, 2023). The fractional potential drop reported here for a discharge with zirconium target is higher or 12 – 15 % (Suresh Babu et al., 2024). For a copper target the fractional potential drop was found to lie in the range 14 – 17 % (Gudmundsson et al., 2022), and for a graphite target it was found to be 14 % (Eliasson et al., 2021), for a working gas pressure of $p_{\rm g} \sim 1$ Pa and $J_{\rm D,peak} \sim 1$ A/cm^2.

4.9 Ionized flux fraction

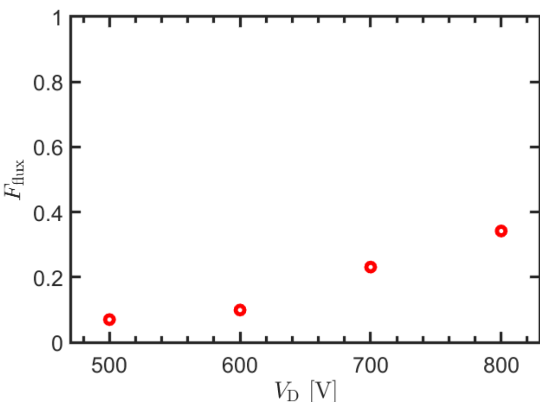

Figure 4.12. The ionized flux fraction versus the discharge voltage V_D determined by the IRM for a discharge with 75 mm diameter tungsten target.

We define the ionized flux fraction as

$$\frac{\Gamma_i}{\Gamma_i + \Gamma_n} \tag{33}$$

where Γ_i and Γ_n are the ion and neutral fluxes of the sputtered species arriving at the substrate, respectively. Figure 4.12 shows the ionized flux fraction F_{flux} determined by the IRM versus the discharge voltage V_D. It can be seen that the ionized flux fraction F_{flux} increases from 7 % for peak current density of 0.33 A/cm^2 to 34 % at 0.73 A/cm^2. For comparison, when operating a HiPIMS discharge with a copper target and peak current density $J_{D,peak} \sim 1$ A/cm^2, the ionized flux fraction is in the range 32 – 40 % (Gudmundsson et al., 2022), while when using a titanium target the ionized flux fraction is roughly 30 % for $J_{D,peak} \sim 1$ A/cm^2 and 14 – 20 % for $J_{D,peak} \sim 0.5$ A/cm^2 (Rudolph et al., 2021). The measured ionized flux fraction in HiPIMS operation, for various target materials, has been found to be in the range 10 – 80 % and it increases with increased peak current density and decreased working gas pressure (Lundin et al., 2015; Hajihoseini et al., 2019; Fischer et al., 2023; Kapran et al., 2024).

4.10 Gas rarefaction

The working gas rarefaction is either presented as a percentage of the total neutral argon density at the start of the pulse $n_{Ar}(t)/n_{Ar,0}$ or as a degree of working gas rarefaction

$$\text{degree of working gas rarefaction} = 1 - \frac{n_{Ar}(t)}{n_{Ar,0}}, \tag{34}$$

where $n_{Ar,0}$ is the total argon density at the start of the pulse and $n_{Ar}(t)$ is the temporal variation of the total argon density.

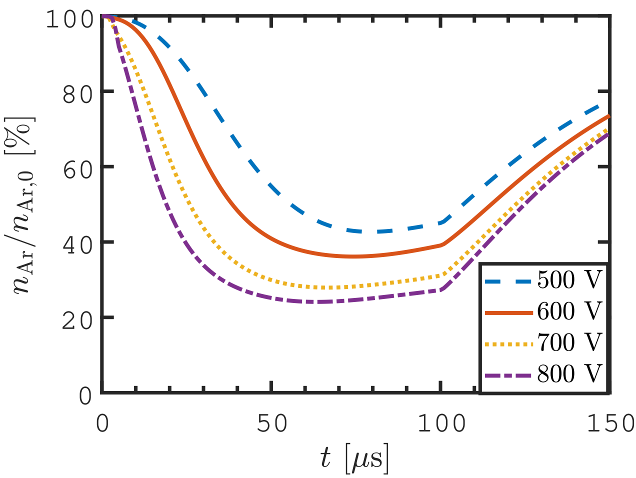

Figure 4.13. The temporal evolution of the total argon neutral density (ground state and excited states) as a percentage of the density at the start of the pulse for the various discharge voltages with 75 mm diameter tungsten target.

The temporal evolution of the total argon density as a percentage of the density at the start of the pulse ($n_{Ar}/n_{Ar,0}$), is shown in Figure 4.13 for all the discharge voltages explored for discharges with 75 mm tungsten target. With increased discharge voltage, the degree of rarefaction $1-(n_{Ar}/n_{Ar,0})$ increases from 57 % at 500 V (0.33 A/cm^2) to 76 % at 800 V (0.73 A/cm^2). There are several factors that contribute to working gas rarefaction, including electron impact ionization of argon atoms and kick-out of argon atoms by the sputter wind, which is then balanced by diffusional refill of cold argon from the bulk plasma, returning hot and warm argon atoms from the target, and charge exchange $Ar^+ + M \longrightarrow Ar + M^+$ (very small contribution) (Huo et al., 2012). We find that the kick-out of argon atoms by the sputter wind is the dominating process leading the working gas rarefaction for a HiPIMS discharge with tungsten target for peak current density $J_{D,peak}$ in the range 0.33 – 0.73 A/cm^2. For comparison, Huo et al. (2012) using the IRM observed reduction by up to 50 % for a 400 μs pulses with an aluminium target at 0.6 A/cm^2 and the dominating contributor to the working gas rarefaction is electron impact ionization of argon atoms. For a discharge with graphite target Eliasson et al. (2021) estimated up to 66 % rarefaction for 50 μs pulses and current density of 1 A/cm^2. The working gas rarefaction is explored in more details in Paper IV (Barynova et al., 2024) where it is demonstrated how the various contributions to working gas rarefaction depend on the sputter yield of the target material.

4.11 Sputter-rate-normalized deposition rate

Earlier Rudolph et al. (2021) have defined the sputter-rate-normalized deposition rate which is given by,

$$F_{sput} = (1-\alpha_t) + \left(\frac{\xi_{ti}}{\xi_{tn}}\right)\alpha_t(1-\beta_t) \tag{35}$$

where ξ_{ti} is the transport parameter for ions and ξ_{tn} is the transport parameter for neutrals of the sputtered species (Christie, 2005; Hajihoseini et al., 2022). Eq. (35) can be approximated

to become

$$F_{\text{sput}} = 1 - \alpha_{\text{t}}\beta_{\text{t}} = \frac{\Gamma^{\text{DR}}}{\Gamma_0} \tag{36}$$

for the special case when $\xi_{\text{ti}} = \xi_{\text{tn}}$ (Bradley et al., 2015; Hajihoseini et al., 2019). This is the ratio of the flux of sputtered species (ions and neutrals) out of the ionization region (IR) towards the diffusion region (DR) Γ^{DR} and the total flux of atoms sputtered from the target Γ_0 (atoms/s). Keeping in mind that Eq. (36) does therefore not take into account ion focusing (or spreading) en route towards the substrate (Butler et al., 2018; Rudolph et al., 2021; Hajihoseini et al., 2022). This equation states that the sputter-rate-normalized deposition rate is reduced as the ionization of the sputtered material increases (Brenning et al., 2020).

The relative ion-to-neutral transport parameter $\xi_{\text{ti}}/\xi_{\text{tn}}$ in Eq. (35), describes the relative deposited fractions of target material ions and neutrals onto a substrate. Experimentally, these parameters have been determined for HiPIMS of a titanium target to be roughly $\xi_{\text{ti}}/\xi_{\text{tn}} \approx 0.8$ for a substrate located 3 cm from the target surface and $\xi_{\text{ti}}/\xi_{\text{tn}} \approx 0.5$ for a substrate located 7 cm from the target surface (Hajihoseini et al., 2022). A value of $\xi_{\text{ti}}/\xi_{\text{tn}} < 1$ indicates a larger spread of metal ions compared to metal neutrals, which is explained by larger scattering cross sections of ions compared to neutrals, and by ions being subjected to electric fields (Rudolph et al., 2021). The sputter-rate-normalized deposition rate calculated using Eq. (35), using the measured relative ion-to-neutral transport factors for titanium (Hajihoseini et al., 2022), shows roughly the same behaviour as the normalized deposition rate but there is a slight difference in the value. This can be seen in Figure 4.14 where the sputter-rate-normalized deposition rate F_{sput} is shown versus the measured normalized deposition rate F_{dep}. We see that when the normalized deposition rate and the ionized flux fraction measured 10 cm from the target surface are used to lock the model the values fall approximately on a line with slope 1 that goes through the origin, while when the flux parameters measured at 3 cm are used to lock the model F_{sput} is slightly higher than the measured F_{dep}. When the flux parameters measured at 10 cm are used to lock the model we find the average value of the ratio $F_{\text{dep}}/F_{\text{sput}}$ to be 0.93 with a standard deviation of 0.17, while the measured values at 3 cm are used to lock the model we find it to be 0.71 with a standard deviation of 0.15.

The sputter-rate-normalized deposition rate F_{sput} and the experimentally determined normalized deposition rate F_{dep}, are related through the relative differences in the sputter rate $\Gamma_{\text{sput,HiPIMS}}/\Gamma_{\text{sput,dcMS}}$ and the neutral transport parameter ratio between HiPIMS and the corresponding (same pressure and average power) dcMS discharge $\xi_{\text{tn,HiPIMS}}/\xi_{\text{tn,dcMS}}$ needs to be taken into account as well or

$$F_{\text{dep}} = \frac{\Gamma_{\text{sput,HiPIMS}}}{\Gamma_{\text{sput,dcMS}}} \frac{\xi_{\text{tn,HiPIMS}}}{\xi_{\text{tn,dcMS}}} F_{\text{sput}}, \tag{37}$$

where (Hajihoseini et al., 2019; Rudolph et al., 2021; Fischer et al., 2023)

$$\frac{\Gamma_{\text{sput,HiPIMS}}}{\Gamma_{\text{sput,dcMS}}} = \frac{V_{\text{dcMS}}}{V_{\text{HiPIMS}}} \times \frac{\sum_i \zeta_i Y_i(z_i V_{\text{HiPIMS}})}{Y_{\text{Ar}^+\to\text{Zr}}(V_{\text{dcMS}})} \tag{38}$$

and $V_{\text{D,HiPIMS}}$ and $V_{\text{D,dcMS}}$ are the discharge voltages for the corresponding HiPIMS and dcMS discharges, respectively. The sum is taken over all the ions Ar^+, Zr^+, Zr^{2+}, and Ar^{2+}, which have sputter yields Y_i, and ζ_i is the fraction of the ion current at the target surface that is carried by a particular ion i and z_i is the charge state of that ion. The parameter $\sum_i \zeta_i Y_i(z_i V_{\text{HiPIMS}})/Y_{\text{Ar}^+\to\text{Zr}}(V_{\text{dcMS}})$ in Eq. (38) is fairly constant and does not vary much with

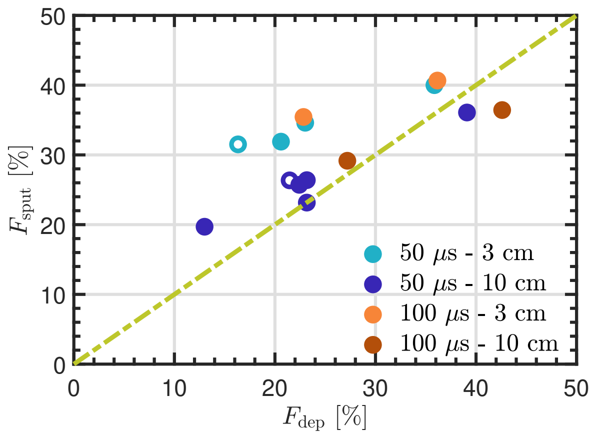

Figure 4.14. The sputter-rate-normalized deposition rate F_{sput} calculated using Eq. (35) versus the measured normalized deposition rate F_{dep} for a discharge with a 2 inch zirconium target for argon working gas pressure of 0.5 Pa (open circles) and 1 Pa (solid dots) and pulse lengths of 50 µs and 100 µs. The green dashed line has a slope of 1.

the varying ion fractions and pulse voltage. The average value is 1.67 with a standard deviation of 0.07. Due to a higher voltage applied cathode target, the average sputter yield is higher in HiPIMS than in dcMS.

5 Summary of Papers

5.1 Paper I: Modeling of high power impulse magnetron sputtering discharges with tungsten target

In Paper I (Suresh Babu et al., 2022), we modelled high power impulse magnetron sputtering (HiPIMS) discharges with tungsten target using an ionization region model (IRM). We explore the discharge behavior and the effects of varying discharge voltage on the sputtering process. The IRM is applied to understand the temporal variations in species concentrations, electron energy, and internal discharge parameters like ionization and back-attraction probabilities. The primary objectives in a high power impulse magnetron sputtering (HiPIMS) process are to maximize the ionized flux fraction of the sputtered target material while also achieving a high deposition rate.

The following are the main findings of the paper:

- The temporal evolution of the densities of the various species that constitute the discharge is reported and evaluated along with various plasma parameters.
- Ar^+ ions dominate the discharge current at the target surface in the beginning of the pulse, while later in the pulse W^+ ions dominate the discharge current for the remainder of the pulse duration.
- The ionization probability of tungsten increases by 39 %, while the back-attraction probability decreases by $\sim 25\%$, with increased discharge voltage.
- The working gas rarefaction towards the end of the pulse reaches values in the range 57 – 76 %.
- The findings, on the ionization probability and the back-attraction probability, were used as input into the generalized recycling model to estimate the peak discharge current.
- The results are in good agreement with experimental values. Furthermore, the measured normalized deposition rate is compared to values determined from the internal discharge parameters from the IRM, showing good agreement.

5.2 Paper II: High power impulse magnetron sputtering of tungsten: a comparison of experimental and modeling results

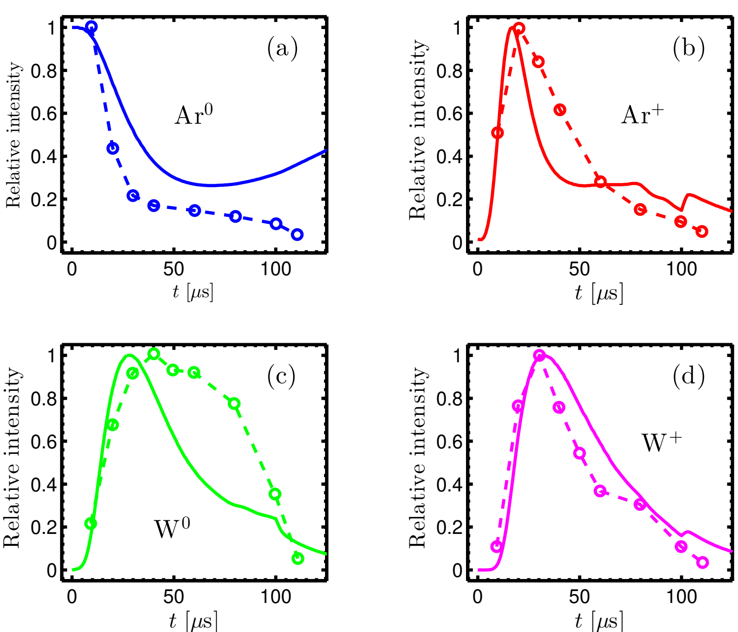

Figure 5.1. The temporal evolution of the relative optical emission from the various species (a) Ar^0, (b) Ar^+, (c) W^0, and (d) W^+, for 100 μs pulse length, argon working gas pressure of 1.6 Pa, and a discharge with 150 mm diameter tungsten target. The experimental data is from Ryan (2019), shown with dashed lines, and the IRM results are shown as solid lines.

The aim of Paper II (Suresh Babu et al., 2023) was to evaluate the performance of the ionization region model (IRM) to study high power impulse magnetron sputtering (HiPIMS) discharge using tungsten target and validate against experimental results obtained from Thomson scattering measurements and optical emission spectrometry (OES). The Thomson scattering measurements assess the electron density and temperature, and OES tracks the temporal evolution of heavy species.

- Figure 5.1 shows the temporal profiles of the intensity of line emission, normalised by the peak number of counts for each line in a profile, from various species in the plasma discharge (Ar^0, Ar^+, W^0 and W^+) (dashed lines).
- The intensity of the Ar^0 line decreases, while the Ar^+ emission intensity peaks at $t = 20$ μs, and the emission from both tungsten species increases. The figure also includes, for comparison and validation, the results of the model calculations (solid lines). The model results show a somewhat slower decay of the Ar^0 density than observed experimentally (Figure 5.1 (a)).
- The 751.5 nm argon emission line originates from the decay of the 13.48 eV (4p manifold) to the 11.83 eV (4s manifold). The assumption is that excitation process is primarily driven by electron impact excitation from the ground state, with a reaction rate of $k_{\rm exc}(T_{\rm e})n_{\rm e}n_{\rm Ar}$, where $k_{\rm exc}(T_{\rm e})$ depends on electron density, gas pressure, and electron temperature.

- We are aware that there is also some excitation from the metastable states into the 4s manifold. Earlier we have estimated the contribution of stepwise ionization from the metastable levels of the 4s manifold in HiPIMS operation to be as high as 15 % (Gudmundsson et al., 2015), and we would expect similar contribution to excitation to the 4p manifold. Also, keep mind that there can be a decay from the 13.48 eV level to other levels of the argon atom. Similar arguments apply for the other measured lines from the heavy species. The peak in the Ar^+ density appears roughly at the same time for the model calculation as determined experimentally, but the calculated Ar^+ density decays somewhat faster than the measured density (Figure 5.1 (b)).
- The calculated peak in the relative W^0 density occurs slightly earlier and declines more rapidly than the measured W^0 density. Experimental data suggest that W^0 remains elevated almost until the pulse terminates, a behavior that the model does not fully capture (Figure 5.1 (c)).
- The W^+ ion emission intensity peaks roughly 30 μs into the pulse, and the model calculations agree with the measurements (Figure 5.1 (d)).

5.3 Paper III: High power impulse magnetron sputtering of a zirconium target

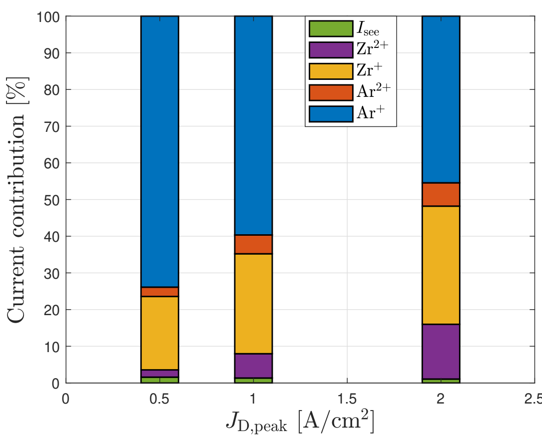

Figure 5.2. The discharge current composition within the ionization region versus the peak discharge current density for a discharge with 2 inch zirconium target for argon working gas pressure of 1 Pa and pulse length of 50 µs, and the ionized flux fraction used to lock the model was measured 10 cm from the target surface.

We explored experimentally the effect of the peak discharge current density on the ionized flux fraction and normalized deposition rate in a HiPIMS discharge with a zirconium target.

- The temporal evolution of the discharge current composition at the target surface is shown in figure 4.6 (b). The current composition is explored further in figure 5.2, we see that up to over 80 % of the discharge current is carried by Ar^+ ions while only about 20% is carried by Zr^+ ions for the lowest peak discharge current density explored. The contributions from Ar^{2+} and Zr^{2+} ions, and secondary electron emission are smaller.

- The current composition is explored further in figure 5.2, where the current composition is shown for three peak discharge current densities. We see that the fractional contribution of Zr^+ and Zr^{2+} ions increases, and the fractional contribution of Ar^+ ions decreases, with increased peak discharge current density. At $J_{D,peak} = 0.5$ A/cm^2 the Ar^+ ion contribution is roughly 74 %, at 1.0 A/cm^2 it is about 60 %, and roughly 45 % at $J_{D,peak} = 2$ A/cm^2.

- The Zr^+ ion contribution is 20 %, 27 %, and 32 %, and the Zr^{2+} contribution increases from 2 % to 6.6 %, to about 15 %, as the peak discharge current density is increased. The contribution of secondary electron current is always much smaller than the current carried by each of the ions.

- There is an upper limit on the current density that corresponds to where all the incoming argon atoms from the surrounding gas reservoir are ionized and drawn to the target. This upper limit defines the critical current density of $J_{crit} \approx 0.2$ A/cm^2 at 1 Pa and $T_g = 300$ K (Huo et al., 2014; Brenning et al., 2017). For all the cases discussed here, the discharge operates well above this limit and ion recycling has to take place to reach the high discharge current densities observed.

- As both argon and zirconium ions contribute significantly to the discharge current at the target surface the discharge operates on a combination of working gas recycling and self-sputter recycling (Brenning et al., 2017).

5.4 Paper IV: On working gas rarefaction in high power impulse magnetron sputtering

The various contributions to working gas rarefaction were explored in Paper IV (Barynova et al., 2024) utilizing the ionization region model (IRM). The rarefaction processes in high power impulse magnetron sputtering discharges were explored for targets made of graphite, aluminum, copper, titanium, zirconium, and tungsten. In all scenarios, significant rarefaction of the working gas is observed, with degrees of rarefaction reaching up to 83%.

- The various contributions to working gas rarefaction, including electron impact ionization, kick-out by the sputtered species or hot argon atoms, and diffusion, are evaluated and compared for the different target materials, and over a range of discharge current densities.
- The significance of each process varies with the type of target material. For instance, in setups using a graphite target with argon gas at 1 Pa, electron impact ionization (caused by both primary and secondary electrons) is the primary mechanism contributing to working gas rarefaction, accounting for over 90%, while the influence from sputter wind kick-out is minimal, less than 10%.
- In case of copper and tungsten targets, the kick-out mechanism dominates, contributing up to about 60% at the same pressure level 1 Pa. For metallic targets, this kick-out effect is largely due to metal atoms ejected from the target, whereas for graphite, it is mainly due to hot argon atoms and, to a lesser extent, carbon atoms.
- The sputter yield and the working gas pressure are critical factors determining the extent of contribution from the kick-out by sputtered species to working gas rarefaction.

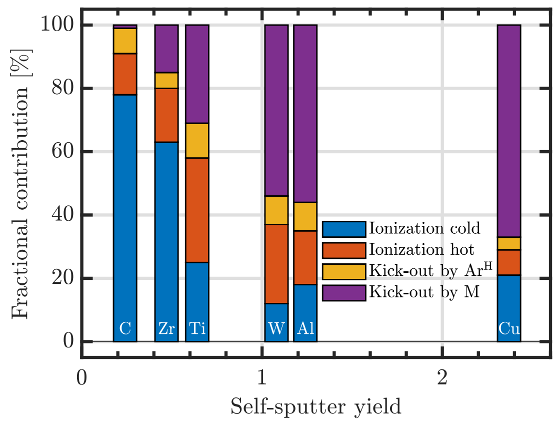

Figure 5.3. The fractional contribution of the various processes to working gas rarefaction within the ionization region versus self-sputter yield. The data is for C (0.24, 12 amu) ($J_{D,peak} = 1$ A/cm^2, $t_{pulse} = 50$ µs, $p_g = 1.0$ Pa), Zr (0.47, 91.2 amu) ($J_{D,peak} = 1$ A/cm^2, $t_{pulse} = 50$ µs, $p_g = 1.0$ Pa), Ti (0.64, 47.9 amu) ($J_{D,peak} = 1.0$ A/cm^2, $t_{pulse} = 100$ µs, $p_g = 1.0$ Pa), W (1.14, 183.8 amu) ($J_{D,peak} = 0.73$ A/cm^2 $t_{pulse} = 100$ µs, $p_g = 1.0$ Pa), Al (1.19, 27.0 amu) ($J_{D,average} = 1.0$ A/cm^2, $t_{pulse} = 100$ µs, $p_g = 2.0$ Pa), and Cu (2.37, 63.5 amu) ($J_{D,peak} = 1$ A/cm^2, $t_{pulse} = 40$ µs, $p_g = 1.0$ Pa). M denotes the target atom.

6 Conclusions

The research documented in this thesis is based on the use of the ionization region model to analyze high power impulse magnetron sputtering discharges with both zirconium and tungsten targets and to effectively determine various aspects of the plasma dynamics and discharge characteristics. Through experimental investigations and subsequent IRM simulations, the studies have offered insights into how different discharge parameters, particularly the peak discharge current density and the discharge voltage, and the sputter yield, significantly influence the behavior of the plasma discharge.

For the HiPIMS discharge employing the tungsten target, the Ar^+ ions initially dominate the discharge current at the onset of the pulse. However, as the pulse progresses, W^+ ions become the prevailing species affecting the discharge current for the rest of the pulse duration. The ionization probability of tungsten increases, while the back-attraction probability decreases, with increased discharge voltage. Furthermore, the measured normalized deposition rate is compared and corroborated with values derived from the internal discharge parameters of the IRM, showing good agreement.

Comparative analyses of a second set of tungsten target experiments between IRM predictions and experimental measurements such as electron density and temperature from Thomson scattering, alongside the densities of heavy species from optical emission spectrometry, were conducted. Although the IRM tended to underestimate electron density and overestimate electron temperature, it successfully captured the general temporal evolution of these plasma parameters. In particular the IRM results captured well the temporal evolution of the heavy species.

For the HiPIMS discharges using zirconium target, the results revealed that the ionized flux fraction notably increases, while the normalized deposition rate decreases as the peak discharge current density increases, confirming the so-called HiPIMS compromise. Detailed investigations into working gas rarefaction showed that electron impact ionization is the predominant factor contributing over 80%, with less significant contributions from zirconium and argon atom kick-out mechanisms.

Overall, this comprehensive application of the IRM across different target materials and discharge conditions has not only validated the model's robustness in simulating HiPIMS discharges but also enhanced our understanding of the underlying physical processes governing the behavior of the plasma discharge. These insights pave the way for optimizing HiPIMS processes and tailoring them for specific material deposition applications.

Paper I

Modeling of high power impulse magnetron sputtering discharges with tungsten target.

Swetha Suresh Babu, Martin Rudolph, Daniel Lundin, Tetsuhide Shimizu, Joel Fischer, Michael A Raadu, Nils Brenning and Jon Tomas Gudmundsson

Plasma Sources Science and Technology 31(6) (2022) 065009

OPEN ACCESS
IOP Publishing
Plasma Sources Science and Technology
Plasma Sources Sci. Technol. **31** (2022) 065009 (14pp)
https://doi.org/10.1088/1361-6595/ac774a

Modeling of high power impulse magnetron sputtering discharges with tungsten target

Swetha Suresh Babu[1], Martin Rudolph[2], Daniel Lundin[3], Tetsuhide Shimizu[4], Joel Fischer[3], Michael A Raadu[5], Nils Brenning[3,5] and Jon Tomas Gudmundsson[1,5,*]

[1] Science Institute, University of Iceland, Dunhaga 3, IS-107 Reykjavik, Iceland
[2] Leibniz Institute of Surface Engineering (IOM), Permoserstraße 15, 04318 Leipzig, Germany
[3] Plasma and Coatings Physics Division, IFM-Materials Physics, Linköping University, SE-581 83 Linköping, Sweden
[4] Department of Mechanical Systems Engineering, Graduate School of Systems Design, Tokyo Metropolitan University, 6-6, Asahigaoka, Hino-shi, 191-0065 Tokyo, Japan
[5] Space and Plasma Physics, School of Electrical Engineering and Computer Science, KTH Royal Institute of Technology, SE-10044 Stockholm, Sweden

E-mail: tumi@hi.is

Received 9 April 2022, revised 2 June 2022
Accepted for publication 9 June 2022
Published 29 June 2022

Abstract
The ionization region model (IRM) is applied to model a high power impulse magnetron sputtering discharge with a tungsten target. The IRM gives the temporal variation of the various species and the average electron energy, as well as internal discharge parameters such as the ionization probability and the back-attraction probability of the sputtered species. It is shown that an initial peak in the discharge current is due to argon ions bombarding the cathode target. After the initial peak, the W^+ ions become the dominating ions and remain as such to the end of the pulse. We demonstrate how the contribution of the W^+ ions to the total discharge current at the target surface increases with increased discharge voltage for peak discharge current densities $J_{D,peak}$ in the range 0.33–0.73 A cm^{-2}. For the sputtered tungsten the ionization probability increases, while the back-attraction probability decreases with increasing discharge voltage. Furthermore, we discuss the findings in terms of the generalized recycling model and compare to experimentally determined deposition rates and find good agreement.

Keywords: magnetron sputtering discharge, high power impulse magnetron sputtering, sputtering, tungsten

(Some figures may appear in colour only in the online journal)

1. Introduction

The magnetron sputtering discharge is a highly successful and widely used thin film deposition technique [1, 2] that falls into the category of physical vapor deposition processes. In the magnetron sputtering discharge a dense plasma is maintained in the cathode vicinity by a static magnetic field that traps the electrons. This is achieved by maintaining a relatively weak magnetic field (typically $B(z, r) < 100$ mTesla), and therefore electrons are the only magnetized species within the discharge [3]. In the dc magnetron sputtering (dcMS) discharge the film-forming material is mainly composed of neutral atoms, the ionization of the sputtered film-forming species is small, and the ions available in the discharge are ions of the noble working gas [4]. Often, it is desired to have a high degree of ionization in the flux of the film-forming material, as it gives overall improved thin film quality [5, 6]. This can be achieved by applying high power pulses at low repetition

[*] Author to whom any correspondence should be addressed.

Original content from this work may be used under the terms of the Creative Commons Attribution 4.0 licence. Any further distribution of this work must maintain attribution to the author(s) and the title of the work, journal citation and DOI.

 © 2022 The Author(s). Published by IOP Publishing Ltd

frequency and low duty cycle to the cathode target. This approach is referred to as high power impulse magnetron sputtering (HiPIMS) [2, 4, 5].

Tungsten (W) is a refractory metal with a range of diverse applications. It has the highest melting temperature ($T_m = 3695$ K) and the lowest thermal expansion coefficient (4.5×10^{-6} K^{-1}) among the elemental metals and has a low electrical resistivity. Therefore, tungsten is used for metallization in microelectronics, including as interconnects and contact plugs, and as a diffusion barrier [7, 8]. Currently, tungsten is considered as the most promising candidate as the divertor target material in thermonuclear fusion reactors due to its high threshold energy for sputtering by hydrogen and helium ions, high melting point, large thermal shock resistance, good handling with respect to machining, and low vapor pressure [9, 10]. Tungsten oxide (WO_3) thin films are of interest as electrochromic materials due to their chemical stability, strong adherence to a number of substrates, and high coloration efficiency [11]. Tungsten oxide films also have applications as the active layer in hydrogen gas sensors [12].

Deposition of tungsten thin films by dcMS and HiPIMS results in textured films that consists of two phases, the equilibrium α–W (A2 bcc) and the metastable β–W (A15 cubic). The HiPIMS-deposited films are denser, have smaller grains and better adhesion [13–15]. Furthermore, HiPIMS-deposited tungsten thin films exhibit enhanced properties, including smoother surfaces, higher hardness, and Young's modulus values [13, 16, 17]. In some of these studies an external magnetic field was added, by placing a toroidal-shaped permanent magnet in front of the cathode target [16, 17]. Recently, Shimizu *et al* [15] demonstrated stress-free, unstrained single phase α–W thin films, deposited without post-annealing, through synchronized pulsed substrate bias that selectively enhances the energy of the metal population of the ion bombardment. They also reported on the temporal behavior of ion and neutral species of the discharge determined by time-resolved optical emission spectrometry (OES). The OES measurements show that the emission from excited neutral argon increases rapidly at the beginning of the pulse and peaks at 4 μs into the 100 μs long pulse. The emission from the Ar^+ ions peaks a few microseconds into the pulse and then decays. This is followed by an increase in emission from atomic W and W^+ ions which indicates ejection of tungsten atoms from the target and subsequent ionization. The emission from the W^+ ions peaks at roughly 35 μs into the pulse and then it stabilizes at a level that remains constant until the end of the pulse.

The ionization region model (IRM) is a time-dependent volume-averaged plasma chemical model of the ionization region (IR), located in the close vicinity of the target racetrack, defined by the confining magnetic field. It was developed to study the discharge behavior during a HiPIMS pulse and the afterglow [18–20]. The IRM has been applied to study various processes, such as gas rarefaction and refill processes [18], and the electron heating mechanisms [21], in an argon HiPIMS discharge with an Al target, and the feasibility of ionizing carbon in a discharge with a graphite target [22]. Earlier we have demonstrated that in HiPIMS discharge operation a significant fraction of the discharge current is due to recycling, either working gas recycling or self-sputter (SS) recycling [23]. In what was coined as the generalized recycling model, a primary current acts as a seed that is amplified by the SS process and the working gas-recycling process. For a HiPIMS discharge with an aluminum [19, 23, 24] and a copper [25] target, the discharge reaches almost a complete SS recycle operation when operated in the HiPIMS regime, while a discharge with a graphite target [22] and reactive sputtering with a poisoned target [26, 27] operates in working gas recycling mode. However, so far the understanding of the plasma processes in a HiPIMS discharge with a tungsten target is limited. Here, we explore a HiPIMS discharge with a tungsten target using the IRM. Tungsten (7.98 V) has a higher ionization potential than Cu (7.73 V), Ti (6.83 V), and Al (5.99 V), and is therefore more difficult to ionize, while it has a sputter yield slightly higher than titanium, and has a higher atomic mass. Earlier, a volume-averaged model has been developed to describe a reactive HiPIMS discharge and to model the deposition of WO_3 films from a tungsten target in Ar/O_2 mixture [28]. The model results indicate that the degree of tungsten ionization increases from 50% to 80% as the power density is increased from 100–500 W cm^{-2}, and it also increases with increased pulse length. Furthermore, it is claimed that W^+ ions are re-implanted into the target which effectively decreases the target oxide coverage during reactive sputtering [28].

Here we extend the IRM to include a reaction set for a tungsten discharge. We apply the model to study a HiPIMS discharge formed with argon as the working gas and a tungsten cathode target in the discharge setup that was earlier explored experimentally by Shimizu *et al* [15] and used to deposit thin tungsten films. The IRM is described in section 2, where the reaction set for tungsten is also discussed. The experimental discharges that are to be analyzed are discussed in section 3. In section 4, the IRM is applied to discharges with a tungsten target to determine the temporal evolution of the particle densities, the ionization and back-attraction probabilities of the tungsten species, the working gas rarefaction, and the ionized flux fraction, as the discharge voltage is varied. In section 5, the findings are discussed in terms of the generalized recycling model. The results are summarized in section 6.

2. The ionization region model

The IRM is a plasma chemistry model that assumes volume-averaged values over the entire IR volume for the electron, ion and neutral densities and the electron temperature. Using the IRM, the time evolution of neutral and charged species and the electron temperature in pulsed magnetron sputtering discharges can be evaluated and explored further. This includes the temporal development of the electron energy and the particle densities for all the heavy particles, which are defined by a set of ordinary differential equations [19]. The IRM provides information on internal discharge properties including the ionization probability, the back-attraction probability, the voltage drop across the IR, and the electrical power transfer to the electrons. The model is limited to the IR, which is defined as an

annular cylinder with outer radius r_{c2}, and inner radius r_{c1} sitting above the racetrack, and a length $L = z_2 - z_1$, extending from z_1 to z_2 axially away from the target. Geometrical effects are included indirectly as loss and gain rates across the boundaries of this annular cylinder to the target and the bulk plasma (the diffusion region (DR)) [18]. The IRM allows us to determine the flux and ionization fraction as target species in the material flux from the IR to the DR that is deposited onto the substrate (located in the DR). The electron density is found by applying the quasi-neutrality condition.

The plasma-chemical reactions are described by two sets of rate coefficients, one for the cold and the other set for the hot electron population. The cold electrons are created by ionization of argon and tungsten atoms, while the hot electrons are ion-induced secondary electrons, emitted from the target surface, and consequently accelerated across the cathode sheath [29]. The majority of the electrons belong to the cold Maxwellian electron population, which therefore dictates the electron density and the effective electron temperature. The rate coefficients are calculated assuming a Maxwellian electron energy distribution function (EEDF) and fit in the range $T_e = 1$–7 eV for cold electrons, and in the range 200–1000 eV for hot electrons. A good agreement has been demonstrated between the bi-Maxwellian electron energy distribution assumed by the IRM and the electron energy distribution calculated by the Orsay Boltzmann equation for electrons coupled with ionization and excited states kinetics (OBELIX) model, a collisional-radiative model coupled with a Boltzmann solver [29]. The reaction set and the rate coefficients involving argon in the IRM are mostly the same as used in our earlier work on HiPIMS discharges with titanium target [26, 30, 31] with a few modifications of the rate coefficients involving the metastable argon atom [29], the consideration of the afterglow [20], and addition of Ar^{2+} ions [22]. Note that the argon atoms in the ground state are assumed to be split into three groups depending on their kinetic energy: cold argon atoms Ar^C are the atoms in the ground state in the feedstock gas at the gas temperature, hot argon Ar^H are atoms in the ground state which return from the target immediately after the argon ion impact event, with a typical sputter energy of a few eV, and warm argon Ar^W are atoms in the ground state that were implanted in the target at the location of ion impact, and return to the surface and leave with the target temperature, at most 0.1 eV [19, 24]. A detailed description of the IRM, including a discussion of the various generation and loss terms for each of the species, is given by Huo *et al* [19].

2.1. Reactions involving tungsten

The tungsten atoms enter the discharge as they are sputtered off the cathode target due to ion bombardment. The rate at which tungsten atoms are sputtered off the target is given by a generation term [19]

$$R_{\mathrm{W,sputt}} = \frac{\sum_i \Gamma_i^{\mathrm{RT}} S_{\mathrm{RT}} Y_i(\mathcal{E}_{\mathrm{i}})}{\mathcal{V}_{\mathrm{IR}}} \quad (\mathrm{m}^{-3}\ \mathrm{s}^{-1}), \tag{1}$$

where i stands for the ion involved in the process, here $i = W^+$, W^{2+}, Ar^+, or Ar^{2+}, and Γ_i^{RT} is the flux of ion i towards the target in ($\mathrm{m}^{-2}\ \mathrm{s}^{-1}$), S_{RT} is the area of the sputtered region (racetrack), $Y_i(\mathcal{E}_{\mathrm{i}})$ is the energy-dependent sputter yield for ion i bombarding the target, and $\mathcal{V}_{\mathrm{IR}}$ is the total volume of the IR. The sputter yield for each ion i is given by a fit following the general form

$$Y_i = a\mathcal{E}_{\mathrm{i}}^b, \tag{2}$$

where $\mathcal{E}_{\mathrm{i}}$ is the energy of the incoming ion and a and b are constants that depend on the ion target pair. For argon ions bombarding tungsten $a = 0.0429$ and $b = 0.521$, and for SS of tungsten $a = 0.0066$ and $b = 0.770$ [42] derived from fits to the sputter yields calculated using the TRansport of Ions in Matter code [43]. These parameters are valid in the ion energy range typical for magnetron sputtering or up to 2000 eV.

The atoms sputtered off the target are injected into the IR with a velocity corresponding to $1/2 \times \mathcal{E}_{\mathrm{cohesive}} = 1/2 \times 8.9$ eV $= 4.45$ eV [44, p 50], where $\mathcal{E}_{\mathrm{cohesive}}$ is the cohesive energy of the target material. These atoms participate in the discharge and are subject to collisions with other plasma species. This includes electron impact ionization and excitation of the tungsten atom. The ground state of the tungsten atom is denoted $[\mathrm{Xe}]4\mathrm{f}^{14}5\mathrm{d}^4 6\mathrm{s}^2\,{}^5\mathrm{D}_0$. The cross section for electron impact ionization of the tungsten atom is taken from the calculation by Deutsch *et al* [39] with an ionization potential of 7.864 eV. The cross section for electron impact ionization of singly charged tungsten ions is taken from the measurements by Montague and Harrison [40]. The rate coefficient for the charge transfer $Ar^+ + W$ is based on the value estimated for the same reaction with Cu [41]. For Penning ionization of tungsten through collisions with metastable argon atoms we use published cross sections [45–47] which were scaled by the square of the atomic radius, atom mass, and the number of valence electrons [48] and assume the sputtered species to have an average energy of 3 eV. All the reactions and rate coefficients included in the IRM for this current study are listed in table 1. To calculate the collisional energy loss per electron–tungsten ion pair created $\mathcal{E}_{\mathrm{c}}$, we use the electron impact ionization cross section from Deutsch *et al* [39]. Furthermore, we include the lowest excited levels of tungsten listed in table 2 and assume that each excitation cross section follows the Thomson cross section [49, p 70–72] with a peak at 1/10 of the peak of the ionization cross section. Note that these excited states of the tungsten atom are only included here to account for energy loss but are not treated as species. The cross section for electron elastic scattering with a tungsten atom is taken from the work of Blanco *et al* [50]. These cross sections are used to calculate the energy loss per electron–ion pair created for tungsten that is shown in figure 1. The figure also shows the energy loss per electron–ion pair created for ground state argon atom calculated as discussed elsewhere [26]. As expected the energy loss per electron–ion pair created for tungsten is lower than for argon.

For the secondary electron emission yield due to bombardment by argon ions we use the value of 0.094, which is taken from the measurements of Hagstrum [51], determined by averaging over all the values measured for ion bombarding energy in the range up to 1000 eV. In this ion energy

Table 1. The reactions and rate coefficients used in the IRM for a discharge with argon as the working gas and tungsten cathode target including both hot and cold electrons. The rate coefficients are calculated assuming a Maxwellian EEDF and fit in the range $T_e = 1$–7 eV for cold electrons and 200–1000 eV for hot electrons. The rate coefficients in the reaction set for argon are taken from earlier works [22, 29].

	Reaction	Threshold (eV)	Rate coefficient ($m^3\ s^{-1}$)	Electrons	References
(R1)	$e + Ar(3p^6) \rightarrow Ar^+ + e + e$	15.76	$2.34 \times 10^{-14} T_e^{0.59}\, e^{-17.44/T_e}$	Cold	[32]
			$8 \times 10^{-14} T_e^{0.16}\, e^{-27.53/T_e}$	Hot	
(R2)	$e + Ar(3p^6) \rightarrow Ar(4s[3/2]_2) + e$	11.548	$1.617 \times 10^{-14} T_e^{-0.8238} \exp(-14.1256/T_e)$	Cold	[33, 34]
			$1.1397 \times 10^{-22} T_e^2 - 1.8975 \times 10^{-19} T_e + 8.7910 \times 10^{-17}$	Hot	
(R3)	$e + Ar(3p^6) \rightarrow Ar(4s'[1/2]_0) + e$	11.723	$2.86 \times 10^{-15} T_e^{-0.8572} \exp(-14.6219/T_e)$	Cold	[33, 34]
			$1.8045 \times 10^{-23} T_e^2 - 2.9825 \times 10^{-20} T_e + 1.357 \times 10^{-17}$	Hot	
(R4)	$e + Ar(4s[3/2]_2) \rightarrow Ar(3p^6) + e$		$3.23 \times 10^{-15} T_e^{-0.8238} \exp(-2.578/T_e)$	Cold	Detailed
			$(1.1397 \times 10^{-22} T_e^2 - 1.8975 \times 10^{-19} T_e + 8.7910 \times 10^{-17})/5$	Hot	Balancing
(R5)	$e + Ar(4s'[1/2]_0) \rightarrow Ar(3p^6) + e$		$2.86 \times 10^{-15} T_e^{-0.8572} \exp(-2.8989/T_e)$	Cold	Detailed
			$1.8045 \times 10^{-23} T_e^2 - 2.9825 \times 10^{-20} T_e + 1.357 \times 10^{-17}$	Hot	Balancing
(R6)	$e + Ar(4s'[1/2]_0) \rightarrow Ar^+ + 2e$	4.21	$1.143\,56 \times 10^{-13} T_e^{0.2548} \exp(-4.4005/T_e)$	Cold	[35, 36]
			$1.5213 \times 10^{-19} T_e^2 - 2.9599 \times 10^{-16} T_e + 1.8155 \times 10^{-13}$	Hot	
(R7)	$e + Ar(4s[3/2]_2) \rightarrow Ar^+ + 2e$	4.21	$1.143\,56 \times 10^{-13} T_e^{0.2548} \exp(-4.4005/T_e)$	Cold	[35, 36]
			$1.5213 \times 10^{-19} T_e^2 - 2.9599 \times 10^{-16} T_e + 1.8155 \times 10^{-13}$	Hot	
(R8)	$e + Ar^+ \rightarrow Ar^{2+} + 2e$	27.63	$8.6365 \times 10^{-15} T_e^{0.6746} \exp(-24.3019/T_e)$	Cold	[37]
			$5.22 \times 10^{-14} - 4.943 \times 10^{-17} T_e$	Hot	[a]
(R9)	$e + Ar \rightarrow Ar^{2+} + 3e$		—	Cold	[38]
			$6.169 \times 10^{-15} - 1.6316 \times 10^{-17} T_e$	Hot	[b]
(R10)	$e + W \rightarrow W^+ + e$	7.864	$6.3966 \times 10^{-14} T_e^{0.4839} \exp(-8.221/T_e)$	Cold	[39]
			$4.2507 \times 10^{-10} T_e^{-1.1791} \exp(-256.38/T_e)$	Hot	
(R11)	$e + W^+ \rightarrow W^{2+} + e$	16.35	$1.446 \times 10^{-14} T_e^{0.7143} \exp(-14.5193/T_e)$	Cold	[40]
			$4.673 \times 10^{-10} T_e^{-1.3047} \exp(-273.55/T_e)$	Hot	
(R12)	$Ar^+ + W \rightarrow Ar + W^+$		2×10^{-16}		[41]
(R13)	$Ar(4s'[1/2]_0) + W \rightarrow Ar + W^+ + e$		5.3×10^{-15}		See text
(R14)	$Ar(4s[3/2]_2) + W \rightarrow Ar + W^+ + e$		5.3×10^{-15}		See text

[a] This is a fit for T_e in the range 200–700 eV.
[b] This is a fit for T_e in the range 100–200 eV.

Table 2. The reactions, threshold energies and references to cross sections used to calculate the collisional energy loss for tungsten.

	Reaction	$\mathcal{E}_{th}$ (eV)	Reference
(R15)	$e + W \rightarrow W^+ + e$	7.864	[39]
(R16)	$e + W \rightarrow W + e$	$3(m_e/M_W)T_e$	[50]
(R17)	$e + W(^5D_0) \rightarrow W(^5D_1) + e$	0.207	
(R18)	$e + W(^5D_0) \rightarrow W(^5D_2) + e$	0.412	
(R19)	$e + W(^5D_0) \rightarrow W(^5D_3) + e$	0.598	
(R20)	$e + W(^5D_0) \rightarrow W(^5D_4) + e$	0.771	
(R21)	$e + W(^5D_0) \rightarrow W(^7S) + e$	0.366	
(R22)	$e + W(^5D_0) \rightarrow W(^3P2_0) + e$	1.181	
(R23)	$e + W(^5D_0) \rightarrow W(^3P2_1) + e$	1.650	
(R24)	$e + W(^5D_0) \rightarrow W(^3P2_2) + e$	2.387	
(R25)	$e + W(^5D_0) \rightarrow W(^3H_4) + e$	1.508	
(R26)	$e + W(^5D_0) \rightarrow W(^3H_5) + e$	1.868	
(R27)	$e + W(^5D_0) \rightarrow W(^3H_6) + e$	2.109	
(R28)	$e + W(^5D_0) \rightarrow W(^3G) + e$	1.655	
(R29)	$e + W(^5D_0) \rightarrow W(^3F2) + e$	1.708	

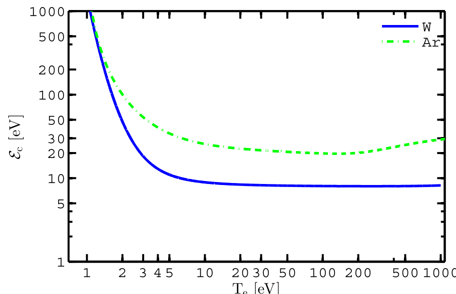

Figure 1. The collisional energy loss per electron–ion pair created, $\mathcal{E}_c$, as a function of the electron temperature for the ground state tungsten and argon atoms, calculated assuming a Maxwellian electron energy distribution.

range the electron emission is due to potential emission which appears to give roughly constant electron emission yield. For the tungsten ions bombarding the tungsten target the secondary electron emission yield is essentially zero. We neglect secondary electron emission due to bombardment of the target by W^{2+} ions.

3. Experimental apparatus and method

The IRM is a semi-empirical discharge model of a physical HiPIMS discharge and therefore requires input from an experiment. These inputs include the working gas pressure, the target material, discharge current and voltage waveforms, the dimensions of the target, and the dimensions of the IR. Here, the discharge voltage and current waveforms measured for a HiPIMS discharge in argon with a tungsten target are analyzed using the IRM. The discharge parameters were measured for a discharge with a planar circular unbalanced magnetron assembly with a tungsten (99.999% in purity) disk of diameter 75 mm, and a thickness of 5 mm, as the cathode target, and with argon working gas of purity of 99.997% at a constant flow rate of 100 sccm which was maintained at a constant working gas pressure of 1.0 Pa by adjusting the pumping speed via the main gate valve. Unipolar HiPIMS pulses, 100 μs in length, were supplied by a HiPSTER 1 pulsing unit fed by a 1 kW

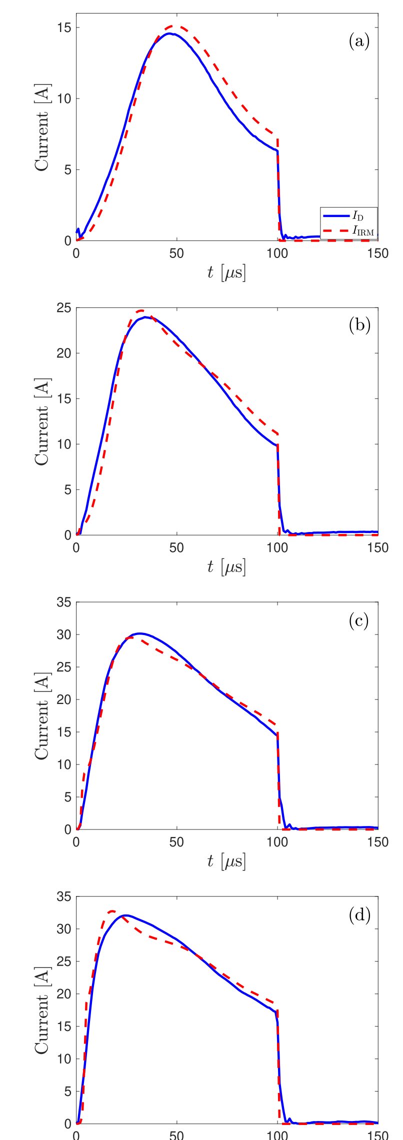

Figure 2. The measured temporal evolution of the discharge current (solid line) and the model fit (dashed line) for discharge voltages of (a) 500 V, (b) 600 V, (c) 700 V, and (d) 800 V, for a discharge with 75 mm diameter tungsten target.

HiPSTER 1-DCPSU DC power supply (Ionautics AB, Sweden) [15]. The details of the experimental setup and some measured discharge properties as well as the resulting thin tungsten films are discussed by Shimizu *et al* [15]. Based on the earlier work [15] the discharge current waveforms were measured for this current work for four different discharge voltages 500 V, 600 V, 700 V, and 800 V. There are slight differences in the discharge current characteristics compared to the earlier report as the target is somewhat more eroded. The measured discharge current waveforms for the various applied discharge voltages are shown in figure 2. The average power is maintained to be roughly the same for all cases by varying the repetition frequency. For each discharge voltage and current waveform pair in HiPIMS operation the deposition rate was determined. Furthermore, the deposition rate for a dcMS discharge operated at the same average power was determined. We assume the deposition rate from the dcMS operation to be proportional the total flux (atoms s^{-1}) of atoms sputtered from the target Γ_0, and the deposition rate in HiPIMS operation is assumed to be proportional to the flux of sputtered species (ions and neutrals) that leave the IR towards the DR Γ_{DR}. In this way the normalized deposition rate $F_{dep} = \Gamma_{DR}/\Gamma_0$ can be determined for each set of discharge voltage and discharge current waveforms.

4. Model results

The IRM is used to determine the temporal variation of the species densities along with a few internal discharge parameters for four different discharge voltages that exhibit the discharge current waveforms shown in figure 2. The volume parameters of the IR were set as follows: $r_{c1} = 8$ mm, $r_{c2} = 27$ mm, $z_1 = 2$ mm, and $z_2 = 22$ mm. Using the IRM, a best fit is determined where the experimentally determined discharge current waveform for each of the discharge voltages is best reproduced by the modeled discharge current. The IRM has three unknown fitting parameters: (i) the ion back-attraction probability for the metal ions $\beta_{t,pulse}$ and gas ions $\beta_{g,pulse}$ during the pulse on time (here we assume $\beta_{t,pulse} = \beta_{g,pulse}$ as in earlier studies [18, 19, 29, 52, 53]), (ii) the potential drop across the IR, V_{IR}, and (iii) the electron recapture probability r. The voltage drop across the IR is incorporated using the ratio $f = V_{IR}/V_D$ [19]. For a metal target the electron recapture probability r, can be varied in the range $0.25 \leqslant r \leqslant 0.9$ without influencing the model output much. For the cases presented here, the electron recapture probability r has been set to $r = 0.5$ [54]. This leaves the $(\beta_{t,pulse}, f)$ parameter space to be explored through the model fitting procedure. The best fit is found using a fitting map showing the fraction of the discharge voltage that drops across the IR $f = V_{IR}/V_D$ versus the back-attraction probability of an ion of the sputtered species during the pulse $\beta_{t,pulse}$ [53], and is shown in figure 3. In this figure the root mean square deviation between the modelled and the experimental peak discharge current is color-coded such that the blue zones in the fitting map indicate the combinations of $f = V_{IR}/V_D$ and $\beta_{t,pulse}$ where the least square error is the smallest and the modeled discharge current resembles the experimental waveform the best. The dark blue zones remain somewhat in the same region (combinations of f and $\beta_{t,pulse}$) for the varying discharge voltages but the area of the blue region decreases with increased discharge voltage.

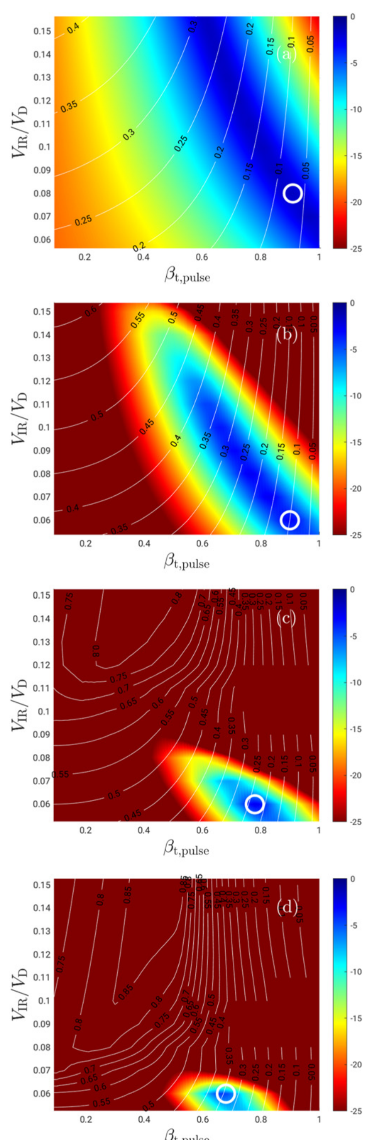

Figure 3. The fitting maps showing $f = V_{IR}/V_D$ versus the back attraction probability $\beta_{t,pulse}$ for discharge voltages of (a) 500 V, (b) 600 V, (c) 700 V, and (d) 800 V, for a discharge with 75 mm diameter tungsten target. The white circles indicate where a well fitted discharge current profile is observed. The white lines and the accompanying numbers indicate the ionized flux fraction.

Table 3. Parameters derived from the modeling of a HiPIMS discharges with tungsten target.

V_D (V)	$I_{D,peak}$ (A)	$J_{D,peak}$ (A cm^{-2})	Rarefaction (%)	α_t	$\beta_{t,pulse}$	β_t	$f = V_{IR}/V_D$	F_{flux}
500	14.56	0.33	57.3	0.54	0.91	0.87	0.08	0.07
600	23.96	0.54	63.8	0.62	0.90	0.87	0.06	0.09
700	30.14	0.68	72.1	0.70	0.78	0.75	0.06	0.23
800	32.06	0.73	75.9	0.75	0.68	0.66	0.06	0.34

Note that a larger blue area is apparent for the discharge with a discharge voltage of 500 V, which indicates that there are significantly higher uncertainties in the determined values for this case. The resulting best fits determined by the IRM for each of the discharge current waveforms are also shown with dashed lines in figure 2. The fits are generally very good for most of the pulse-on time.

The sputtered species are assumed to initially have a directional velocity away from the target. Consequently, the ions of the sputtered species are assumed to have the same directional velocity. In HiPIMS operation a significant fraction of the deposition flux is made of ionized tungsten, which we will confirm later is indeed the case. The potential drop across the IR constitutes a potential barrier, which prevents some of the tungsten ions from reaching the substrate, and therefore they do not contribute to the deposition rate. This potential barrier is eliminated after the pulse-on time. Therefore, we assume β_t to be zero in the afterglow and consequently the back-attraction probability is defined as [20]

$$\beta_t(t) = \begin{cases} \beta_{t,pulse} & \text{during the pulse} \\ 0 & \text{in the afterglow.} \end{cases} \quad (3)$$

The flux toward the DR is calculated from the flux toward the racetrack during the pulse [19, 55]. After the pulse has been switched off, the ions are assumed to have a velocity that is similar to that of the sputtered metal species. The back-attraction probability during the pulse is found to be in the range $\beta_{t,pulse} \approx 0.68$–$0.91$, decreasing with increasing peak discharge voltage. The overall back-attraction probability β_t is somewhat lower or in the range 66%–87%. The fraction of the discharge voltage that drops over the IR is rather low or in the range $f = V_{IR}/V_D = 6\%$–8%. Some of the key discharge parameters derived from the IRM, including the ionization probability, the back-attraction probability of the sputtered species, and the ionized flux fraction for the various discharge voltages are listed in table 3.

The temporal evolution of the neutral particle densities is shown in figure 4. Overall the temporal evolution of the neutral particle densities are similar for the various discharge voltages. The ground state working gas argon atoms dominate the discharge. The cold (or primary) argon ground state density (denoted $Ar^C(3p^6)$ in figure 4) decreases steadily to a minimum at the end of the pulse, which indicates working gas rarefaction [56]. Working gas rarefaction is known to occur and be rather significant in HiPIMS discharges as has been demonstrated experimentally [15, 57–59]. Actually, Shimizu *et al* [15] noted that the working gas rarefaction is particularly pronounced for the case of tungsten. Before the pulse initiation the density of cold ground state argon atoms at 1 Pa and $T_g = 500$ K is 1.4×10^{20} m^{-3}. Figure 4 shows that there is an increase in both the hot (Ar^H) and warm (Ar^W) argon atom densities to a peak, during the pulse, and then a slight decrease again. Note that the total argon ground state density is composed of the cold, warm and hot densities or $[Ar(3p^6)] = [Ar^C(3p^6)] + [Ar^W(3p^6)] + [Ar^H(3p^6)]$. The temporal evolution of the total argon density as a percentage of the density at the start of the pulse ($n_{Ar}/n_{Ar,0}$), is shown in figure 5 for all the discharge voltages explored. With increased discharge voltage, the degree of rarefaction $1 - (n_{Ar}/n_{Ar,0})$ increases from 57% at 500 V (0.33 A cm^{-2}) to 76% at 800 V (0.73 A cm^{-2}). Note that there are several factors that contribute to rarefaction, including electron impact ionization of argon atoms and kick-out of argon atoms by the sputter wind, which is then balanced by diffusional refill of cold argon from the bulk plasma, returning hot and warm argon atoms from the target, and charge exchange $Ar^+ + M \rightarrow Ar + M^+$ (very small contribution) [52].

We find that the kick-out of argon atoms by the sputter wind is the dominating process leading to working gas rarefaction for a HiPIMS discharge with a tungsten target for peak current densities $J_{D,peak}$ in the range 0.33–0.73 A cm^{-2}. For comparison, Huo *et al* [52] using the IRM observed a reduction by up to 50% for a 400 μs pulses with an aluminium target at 0.6 A cm^{-2} and the dominating contributor to the working gas rarefaction is electron impact ionization of argon atoms. For a discharge with graphite target Eliasson *et al* [22] estimated up to 66% rarefaction for 50 μs pulses and current density of 1 A cm^{-2}.

Figure 4 also shows that the tungsten atom density increases rapidly early in the pulse and remains stable throughout the pulse. After the end of the pulse when the sputtering by energetic ion bombardment comes to an end, the density of the ground state tungsten atoms decreases sharply at first and then more slowly.

The temporal evolution of the charged particle densities are shown in figure 6. Initially, the Ar^+ ion is the dominating ion but soon the W^+ ion takes over and remains the dominating ion towards the end of the pulse. The density of the doubly charged W^{2+} ions is always smaller than the density of the Ar^+ ions and the density of the Ar^{2+} ions significantly smaller. For comparison the total neutral argon density $[Ar^0]$ and the neutral tungsten density $[W^0]$ are shown as well in figure 6. Shimizu *et al* [15] applied time-resolved optical emission spectroscopy (OES) and mass spectrometry on a HiPIMS discharge with a tungsten target to monitor the time evolution of the plasma ion-composition reaching the substrate. The measurements show that the emission from excited neutral argon increases

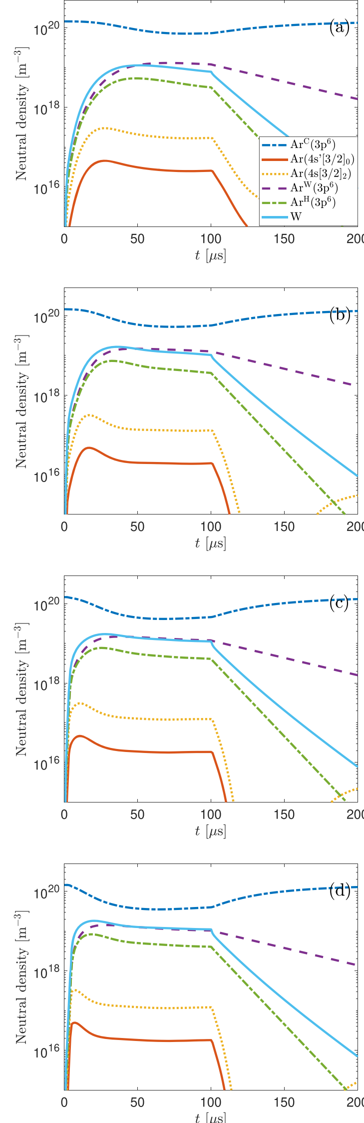

Figure 4. The temporal evolution of the neutral particle densities for discharge voltages of (a) 500 V, (b) 600 V, (c) 700 V, and (d) 800 V, for a discharge with 75 mm diameter tungsten target.

rapidly at the beginning of the pulse and peaks at 4 μs into the 100 μs long pulse. The emission from the Ar^+ ions peaks a few microseconds into the pulse and then decays. This is followed by an increase in emission from atomic W and W^+ ions which indicates ejection of tungsten atoms from the target and subsequent ionization. The emission from the W^+ ions peaks

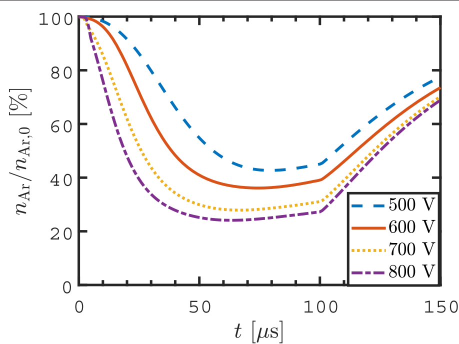

Figure 5. The temporal evolution of the total argon neutral density (ground state and excited states) as a percentage of the density at the start of the pulse for the various discharge voltages with 75 mm diameter tungsten target.

at roughly 35 μs into the pulse and then it stabilizes at a level that remains constant until the end of the pulse. They found the ion-composition to be initially working gas-dominated, but observed a window ranging from 30 to 120 μs from the pulse initiation when metal ions are dominating, having more than 50% of the total ion intensity. This they claim to be both due to efficient ionization of sputtered species during the pulse and a strong working gas rarefaction. After the end of the pulse duration the ions of the working gas dominate again. The emission intensity from the W^{2+} ions was always more than an order of magnitude weaker than from the W^+ ions. Therefore, the model results shown in figure 6 agree with the experimental findings. It should be noted that the measured time-averaged ion energy distributions for the W^+ ions exhibit a high energy tail [16], which is commonly observed in HiPIMS discharge operation [60, 61].

The temporal evolution of the discharge current composition at the target surface is shown in figure 7 for various discharge voltages. We see that the initial peak in the discharge current that was noted in figure 2 is due to Ar^+ ions, which dominate in the beginning of the pulse. For all cases the W^+ ions take over as dominating charged heavy species, as the initial Ar^+ peak decays. This is more pronounced for the higher discharge voltages as the contribution of the W^+ ions to the total discharge current at the target surface increases with increased discharge voltage. Therefore, in the beginning of the pulse the working gas ions bombard the target and sputter off metal atoms that are ionized and consequently return to the target, and constitute a SS recycling loop [23]. Consequently, tungsten atoms and ions, partially take over the role of the working gas argon atoms and ions as the pulse progresses. For a tungsten target Anders *et al* [62] observed an initial peak in the discharge current waveform and argued that the initial peak increases with increased argon pressure, whereas the level of the discharge current plateau later in the pulse is practically independent on the working gas pressure. Therefore, for the initial part of the pulse, working gas sputtering dominates, while the plateau is driven by self-sputtering. For a discharge voltage of 700 V or higher the W^+ ion contribution

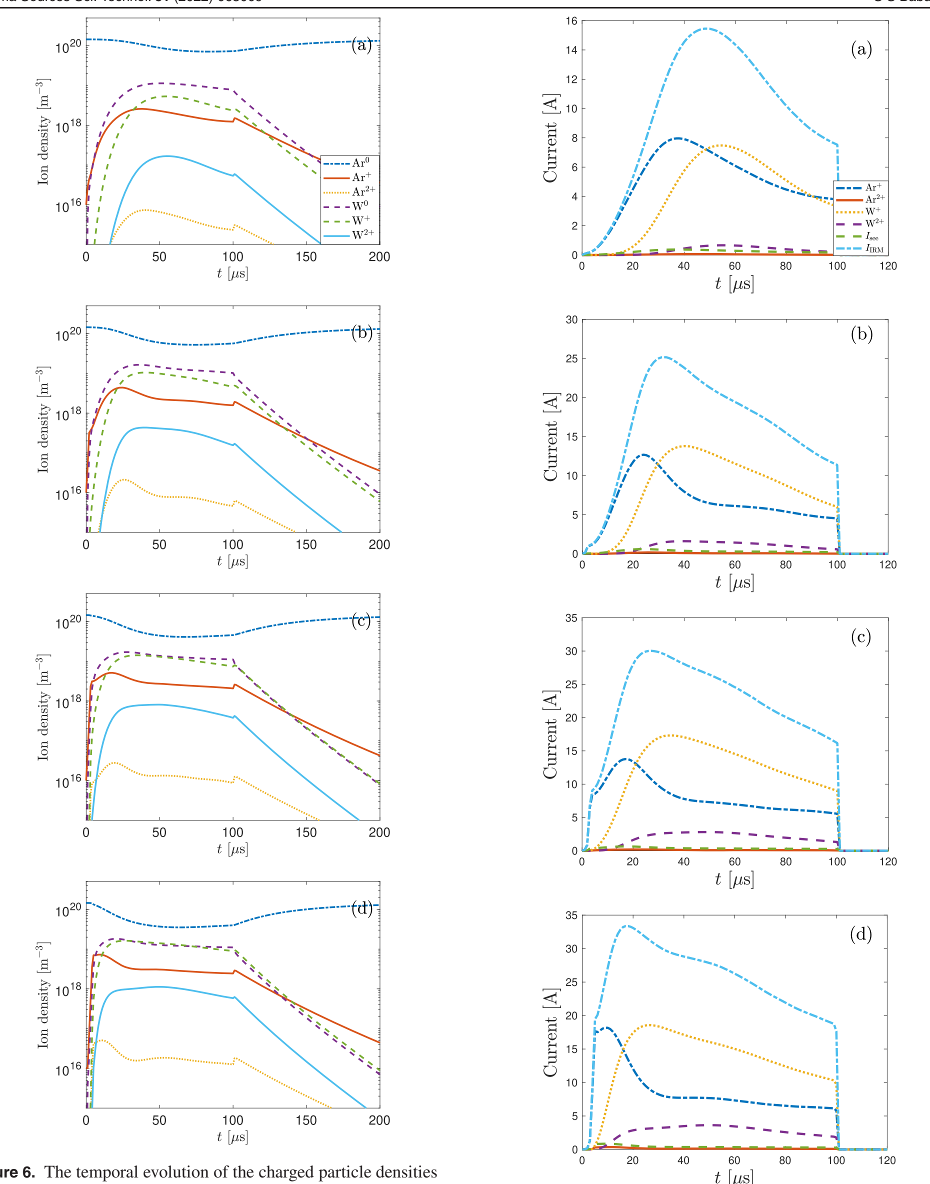

Figure 6. The temporal evolution of the charged particle densities for discharge voltages of (a) 500 V, (b) 600 V, (c) 700 V, and (d) 800 V, for a discharge with 75 mm diameter tungsten target. In addition we also show the total argon neutral density (ground state and excited states) [Ar^0] and the neutral tungsten density [W^0].

Figure 7. The temporal evolution of the discharge current composition at the target surface for discharge voltages of (a) 500 V, (b) 600 V, (c) 700 V, and (d) 800 V, for a discharge with 75 mm diameter tungsten target.

to the discharge current is much higher than the Ar^+ ion contribution. Our findings agree with the earlier work of Anders *et al* [62] who see an initial peak when the discharge voltage was 700 V or higher. They pointed out that the initial peak increases steeply indicating that the argon working gas is very efficiently ionized. There is some, but much smaller contribution, from W^{2+} ions to the discharge current while the contribution of Ar^{2+} ions and secondary electrons are negligible.

The temporal evolution of the electron density is shown in figure 8(a) and the temporal evolution of the electron temperature for the cold electron group is shown in figure 8(b). There is a peak in the electron density early in the pulse. It increases in value and peaks earlier in the pulse with increased discharge voltage. In the electron temperature, we observe a similar a sharp peak early in the pulse for all discharges. The electron temperature reaches a plateau in the range 3.59–5.03 eV as the pulse progresses. Similar spikes in the electron temperature in the beginning of the pulse were observed when modeling a discharge with a copper target operated with argon as working gas at 0.4 and 0.5 Pa [25]. It should also be noted that Pajdarová *et al* [63] experimentally observed a fast rise to high electron temperatures in the initial stages of the pulse, which is followed by a decrease to ∼1 eV, when operating a HiPIMS discharge with Cu target at 1 Pa, and measured outside the IR. Similarly, Poolcharuansin and Bradley [64] reported on three distinct groups of electrons which they referred to as 'super-thermal', 'hot' and 'cold' populations in the initial phase of the voltage pulse (1–4 μs) when operating with a titanium target. High electron temperatures in the beginning of a pulse observed in pulsed inductively coupled discharges were explained by fewer electrons available in the initial stages of the pulse [65, 66]. Therefore, in the initial stages of the pulse all the input power is absorbed by a limited number of electrons and it shows up as a spike in the electron temperature. The electron density and electron temperature have been determined experimentally for both dcMS [67] and HiPIMS [68] discharges with a tungsten target, using Langmuir probe and Thomson scattering. The electron density at the magnetic null point was found to peak at 5×10^{18} m^{-3} in a HiPIMS discharge at 50 μs into a 100 μs long pulse at working gas pressure of 1.6 Pa and peak discharge current density of 0.74 A cm^{-2}. At this time a local minimum in the electron temperature is observed which indicates cooling of the EEDF as the density of metallic species in the discharge increases. As the electrons cool down, the ion generation rate decreases and consequently the sputter rate is reduced. Consequently, the electron temperature rises again, decreasing the electron density [68]. It has been argued that for metals with high sputter yield, such as aluminum and copper, the HiPIMS discharge can be operated in the sustained SS mode and the discharge current is stabilized via a negative feedback mechanism [69]. Increased discharge current leads to increased sputtering, increased presence of metal atoms, and a lower effective electron temperature and, therefore, lower ionization. Furthermore, by comparing various target materials it has been suggested that the ionization fraction of the sputtered species is lower for materials with higher sputter yield as the electron

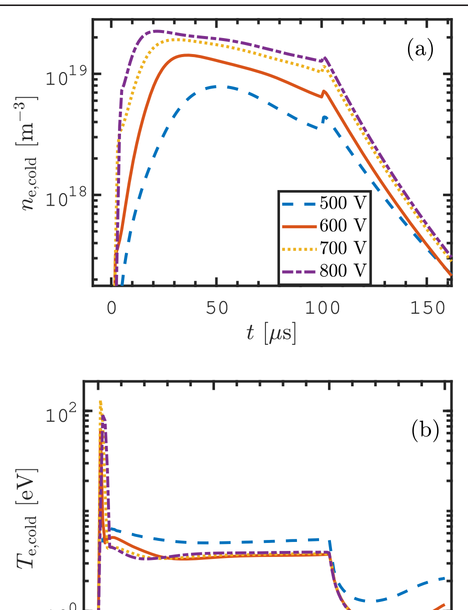

Figure 8. The temporal evolution of the (a) cold electron density and the (b) cold electron temperature for the various discharge voltages for a discharge with 75 mm diameter tungsten target.

temperature decreases due to increased number of sputtered species [69].

5. Discussion

The model results describe a discharge where the Ar^+ ions dominate in the beginning of the pulse and then few tens of μs into the pulse W^+ ions take over as the dominating ions as seen in figures 6 and 7. Here we explore how the internal discharge parameters vary with discharge voltage and resulting discharge current. Figure 9 shows the internal discharge parameters, the ionization probability α_t, the back-attraction probability during the pulse $\beta_{t,pulse}$, the overall back-attraction probability β_t, and the fractional potential drop over the IR $f = V_{IR}/V_D$ as a function of the discharge voltage. In figure 9(a) we see that the ionization probability α_t increases while the back-attraction probability $\beta_{t,pulse}$ decreases with increased discharge voltage. Earlier we have argued that the ionization probability depends only on the peak discharge current and increases with increased peak discharge current [70] and the decreasing back-attraction probability with increasing peak discharge current confirms the suggestion made by Brenning *et al* [71, 72]. Recall that the peak discharge current increases with increased discharge voltage (see figure 2), and the peak current density

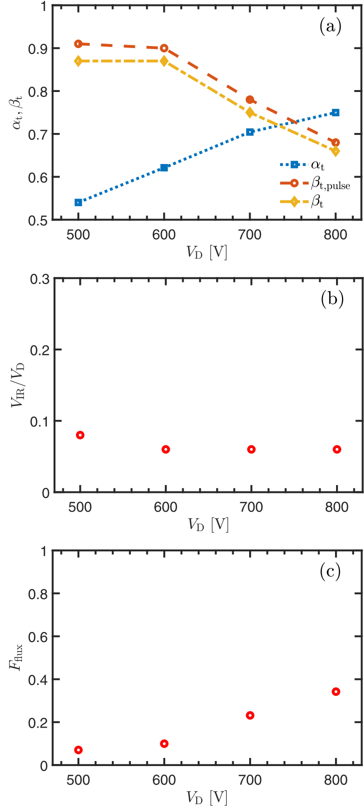

Figure 9. The (a) ionization probability α_t and the back-attraction probability $\beta_{t,pulse}$ and β_t, (b) the fractional potential drop over the IR $f = V_{IR}/V_D$, and (c) the ionized flux fraction versus the discharge voltage V_D determined by the IRM for a discharge with 75 mm diameter tungsten target.

$J_{D,peak}$ in this study is in the range 0.33–0.73 A cm^{-2}. The decrease of $\beta_{t,pulse}$ and β_t with increasing $J_{D,peak}$ can be understood when considering the ideal case of gas-less sputtering, in which there is no working gas. We consider a time span in a steady state discharge during which a number N_{W+} of W^+ ions hit the target. They sputter out a number $N_{W+}Y_{SS}$ tungsten atoms. The fraction α_t of the sputtered atoms will become ionized within the IR, and a fraction β_t of the ions will become back-attracted and hit the target. Each chain of events beginning with a W^+ ion hitting the target therefore ends with $\alpha_t\beta_t Y_{SS}$ target ions hitting the target. In steady state these two numbers of ions are identical and

$$N_{W+} = N_{W+}\alpha_t\beta_t Y_{SS} \tag{4}$$

giving

$$\beta_t = \frac{1}{\alpha_t Y_{SS}}. \tag{5}$$

As the ionization probability α_t increases with increased discharge current, and the SS yield Y_{SS} increases also slightly (from 0.8 to 1.1), the back-attraction probability has to decrease.

Figure 9(b) shows the fraction of the discharge voltage that drops over the IR versus the discharge voltage. It is 8% at 500 V and 6% at higher discharge voltage. Figure 9(c) shows that the ionized flux fraction F_{flux} increases from 7% for peak current density of 0.33 A cm^{-2} to 34% at 0.73 A cm^{-2}. For comparison, when operating a HiPIMS discharge with a copper target and peak current density $J_{D,peak} \sim 1$ A cm^{-2}, the ionized flux fraction is in the range 32%–40% [25], while when using a titanium target the ionized flux fraction is roughly 30% for $J_{D,peak} \sim 1$ A cm^{-2} and 14%–20% for $J_{D,peak} \sim 0.5$ A cm^{-2} [73].

The generalized recycling model combines the processes of SS-recycling and working gas recycling in HiPIMS discharges [23, 74] and can be used to explain the large discharge currents observed in HiPIMS. In the generalized recycling model it is assumed that a primary current acts as a seed that is amplified by both the SS recycling process and the working gas recycling process. A primary current I_{prim} is defined as a current, which is composed almost entirely of the ions of the working gas, here Ar^+ ions, that have been ionized for the first time and then drawn to the target (and maybe a very small contribution from secondary electrons, which we neglect) [24, 74]. This is the dominating current in dcMS discharge operation. However, there is a maximum steady state supply rate of argon atoms from the surrounding gas reservoir [19]. This current therefore has a critical upper limit that can be estimated using

$$I_{crit} = S_{RT} e p_g \sqrt{\frac{1}{2\pi m_g k_B T_g}} = S_{RT} e n_g \sqrt{\frac{k_B T_g}{2\pi m_g}}, \tag{6}$$

where p_g is the working gas pressure, T_g is the working gas temperature, n_g is the working gas density and S_{RT} is the racetrack area. For a gas temperature of 300 K, this gives an estimate of the maximum available discharge current due to working gas ions that are ionized for the first time and drawn to the target given in practical units as

$$I_{crit} \approx 0.38 p_g S_{RT}, \tag{7}$$

where S_{RT} is the racetrack area in cm^2, and p_g is the working gas pressure in Pa and here we assume $S_{RT} = 0.5 \times S_T$.

For our discharge conditions here, $I_{crit} = 8.4$ A. For discharge currents I_D larger than I_{crit} there has to be some kind of recycling of atoms that leave the target, subsequently become ionized and then are drawn back to the target [23]. This can be either SS recycling or working gas-recycling. For all the cases explored here the discharge current goes well above the critical current during the pulse. The lowest peak discharge current is $I_{D,peak} = 14.6$ A at 500 V and the discharge current increases with increased discharge voltage (see figure 2), and a bigger fraction of the discharge current is due to recycling.

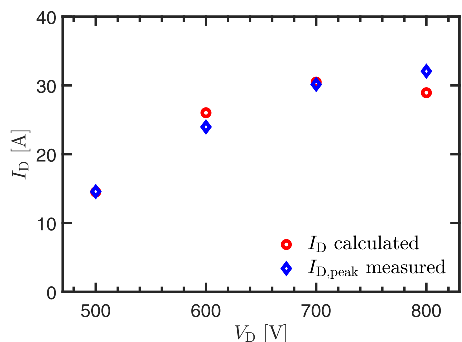

Figure 10. The measured peak discharge current and the discharge current calculated using the internal discharge parameters determined by IRM and equation (9), versus the discharge voltage V_D for a discharge with 75 mm diameter tungsten target.

Earlier we have shown that the discharge current in a HiPIMS discharge is the sum of the primary current, and contributions from working gas recycling and SS recycling, which can be written [23]

$$I_D \approx I_{prim} + I_{gas-recycle} + I_{SS}. \quad (8)$$

The discharge current can also be written as multiplication of the primary current I_{prim} that then acts as a seed [23], which in steady states gives

$$I_D \approx I_{prim}\left(1 + \frac{\pi_g}{1-\pi_g}\right)\left(1 + \frac{Y_g}{Y_{SS}}\frac{\pi_{SS}}{1-\pi_{SS}}\right), \quad (9)$$

where the working gas-sputtering parameter is $\pi_g = \alpha_g\beta_{g,pulse}\xi_{pulse}$ and the SS parameter is $\pi_{SS} = \alpha_t\beta_{t,pulse}Y_{SS}$ Here, $\xi_{pulse} = 1$ is the fraction of the recombined Ar^+ ions at the target that is assumed to return during the pulse as a hot argon atom Ar^H or warm argon atom Ar^W.

Figure 10 shows the measured peak discharge current and the discharge current calculated using equation (9) from the internal discharge parameters, that were determined by the IRM (and listed in table 3), versus the discharge voltage V_D. We see that the discharge current determined from the internal discharge parameters using the generalized recycling model agrees well with the measured peak discharge current.

The above discussion and in particular equation (9) is derived assuming that the primary current is at its critical upper limit, and that each subsequent cycle adds another contribution to the working gas and SS recycling current and, assuming a large number of such recycling loops, use the infinite sum $\sum_{n=1}^{\infty} a^n = a/(1-a)$ where $0 < a < 1$.

To verify the validity of this assumption we estimate the ion loss time based on average quantities. The complete sequence of events to reach equilibrium involves developing both a working gas recycling loop and a target species recycling loop. They come in a sequence of two loops. The working gas recycling loop initiates with an event of argon ionization and involves three steps (i) Ar^+ ion acceleration to the target (i.e., back-attraction), (ii) return to the IR either as a hot or a warm argon atom, and (iii) ionization. Similarly, the SS recycling loop starts with an event of tungsten ionization followed by (i) W^+ ion acceleration to the target, (ii) sputtering that creates a tungsten atom that enters the IR, and (iii) ionization of this atom. To estimate the time of step (i) we assume the average ion that ends up at the target was produced in the middle of the IR, at a distance $(z_2 - z_1)/2$ from the sheath edge, and that the potential difference from this position to the sheath edge is $V_{IR}/2$. The loss time in the IR for this average ion is under these assumptions [19]

$$t_{loss} = \frac{z_2 - z_1}{\sqrt{\frac{q_i V_{IR}}{m_i}}} \quad (10)$$

which for for Ar^+ ion is $t_{loss} \sim 2\ \mu s$ and for W^+ ions the loss time is $t_{loss} \sim 4\ \mu s$, using z_1 and z_2 assumed in the IRM. A different estimate is based on lateral imaging of a HiPIMS discharge by Anders *et al* [75]. They assume the atoms to only travel about 1–3 mm away from the target surface before they are ionized [76]. This leads to estimates for the residence time for Nb^+ ions in the range 0.2–0.3 μs. Scaling this with the square root of the ion mass ratio yields 0.3–0.4 μs for W^+ ions. For steps (ii) and (iii) we separate the time into a transit time t_{trans} and an ionization time t_{ion}. The transit time is the extent of the IR divided by the typical speed in the z-direction. It is longer for warm than for hot Ar atoms. Here we use the notation $\langle t_{trans}\rangle$ for a suitable average. The transit time $\langle t_{trans}\rangle$ is roughly 7.5 μs and 40 μs for hot and warm argon atoms, respectively, and about 13 μs for sputtered tungsten with energy of 4.45 eV. The ionization time for an atom is $t_{ion} = 1/(n_e \times k_{ioniz})$. The ionization time is about 1.5 ms for argon and about 30 μs for tungsten. A returning argon atom from the target can either be ionized in transit through the IR, or pass through it and escape to the DR and therefore the effective time for steps (ii) and (iii) can be approximated as the shorter of these: the time from target to ionization $t_{t,iz} = \min(\langle t_{trans}\rangle, t_{ion})$. The slower of the loops, the SS recycling loop, takes under 17 μs to complete. Therefore, the use of equation (9) is justified.

The ratio of the flux of sputtered species (ions and neutrals) that leave the IR towards the DR Γ_{DR} and the total flux (atoms s^{-1}) of atoms sputtered from the target Γ_0, the useful fraction of the sputtered species, or the normalized deposition rate, can be approximated by [77, 78]

$$F_{dep} = \frac{\Gamma_{DR}}{\Gamma_0} = 1 - \alpha_t\beta_t. \quad (11)$$

This parameter is plotted versus the discharge voltage V_D in figure 11, where it is compared to the measured normalized deposition rate. The measured normalized deposition rate is the deposition rate for HiPIMS operation divided by the deposition rate determined from dcMS operated at the same average power. We see that the normalized deposition rate calculated using the internal discharge parameters determined by the IRM agree well with the measured values. Keep in

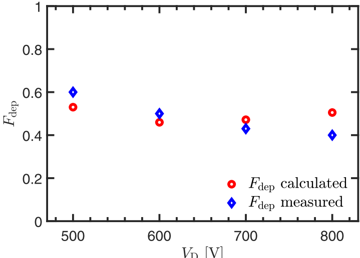

Figure 11. The measured normalized deposition rate and the normalized deposition rate determined from the IRM versus the discharge voltage V_D for a discharge with 75 mm diameter tungsten target.

mind that equation (11) does not take into account ion focusing (or spreading) en route towards the substrate [53, 73]. Equation (11) says that this normalized deposition rate is reduced, and the fraction of the sputtered species reaching the substrate decreases, as the ionization of the sputtered material increases.

6. Conclusions

We have explored the effect of the discharge voltage on the plasma parameters, including the internal discharge parameters, of a HiPIMS discharge in argon with tungsten target operated in the current density range 0.33–0.73 A cm^{-2}. The temporal evolution of the densities of the various species that constitute the discharge is reported and evaluated along with various plasma parameters. Ar^+ ions dominate the discharge current at the target surface in the beginning of the pulse, while later in the pulse W^+ ions dominate the discharge current for the remainder of the pulse duration. The ionization probability of tungsten increases, while the back-attraction probability decreases, with increased discharge voltage. The gas rarefaction toward the end of the pulse reaches values in the range 57%–76%. The findings, on the ionization probability and the back-attraction probability, were used as an input into the generalized recycling model to estimate the peak discharge current. The results are in good agreement with experimental values. Furthermore, the measured normalized deposition rate is compared to values determined from the internal discharge parameters from the IRM, with good agreement.

Acknowledgments

This work was partially supported by the Icelandic Research Fund Grant No. 196141, by the Free State of Saxony and the European Regional Development Fund (Grant No. 100336119), and the Swedish Government Strategic Research Area in Materials Science on Functional Materials at Linköping University (Faculty Grant SFO-Mat-LiU No. 2009-00971).

Data availability statement

The data that support the findings of this study are available upon reasonable request from the authors.

ORCID iDs

Swetha Suresh Babu https://orcid.org/0000-0001-5360-5562
Martin Rudolph https://orcid.org/0000-0002-0854-6708
Daniel Lundin https://orcid.org/0000-0001-8591-1003
Tetsuhide Shimizu https://orcid.org/0000-0002-7810-3777
Joel Fischer https://orcid.org/0000-0001-9116-6302
Michael A Raadu https://orcid.org/0000-0002-1299-5039
Nils Brenning https://orcid.org/0000-0003-1308-9270
Jon Tomas Gudmundsson https://orcid.org/0000-0002-8153-3209

References

[1] Waits R K 1978 *J. Vac. Sci. Technol.* **15** 179
[2] Gudmundsson J T 2020 *Plasma Sources Sci. Technol.* **29** 113001
[3] Krüger D, Köhn K, Gallian S and Brinkmann R P 2018 *Phys. Plasmas* **25** 061207
[4] Gudmundsson J T and Lundin D 2020 *High Power Impulse Magnetron Sputtering: Fundamentals, Technologies, Challenges and Applications* ed D ed Lundin, T Minea and J T Gudmundsson (Amsterdam: Elsevier) pp 1–48
[5] Helmersson U, Lattemann M, Bohlmark J, Ehiasarian A P and Gudmundsson J T 2006 *Thin Solid Films* **513** 1
[6] Greczynski G, Petrov I, Greene J E and Hultman L 2019 *J. Vac. Sci. Technol.* A **37** 060801
[7] Rossnagel S M, Noyan I C and Cabral C 2002 *J. Vac. Sci. Technol.* B **20** 2047
[8] Choi D *et al* 2011 *J. Vac. Sci. Technol.* A **29** 051512
[9] Naujoks D *et al* 1996 *Nucl. Fusion* **36** 671
[10] Pitts R A *et al* 2013 *J. Nucl. Mater.* **438** S48
[11] Najafi-Ashtiani H, Akhavan B, Jing F and Bilek M M 2019 *ACS Appl. Mater. Interfaces* **11** 14871
[12] Haviar S, Čapek J, Batková Š, Kumar N, Dvořák F, Duchoň T, Fialová M and Zeman P 2018 *Int. J. Hydrog. Energy* **43** 22756
[13] Engwall A M, Shin S J, Bae J and Wang Y M 2019 *Surf. Coat. Technol.* **363** 191
[14] Roychowdhury T, Shah D, Jain V, Patel D I, Dodson B, Skinner W, Hilfiker J N, Smith S J and Linford M R 2020 *Surf. Interface Anal.* **52** 433
[15] Shimizu T, Takahashi K, Boyd R, Viloan R P, Keraudy J, Lundin D, Yang M and Helmersson U 2021 *J. Appl. Phys.* **129** 155305
[16] Velicu I-L, Tiron V, Porosnicu C, Burducea I, Lupu N, Stoian G, Popa G and Munteanu D 2017 *Appl. Surf. Sci.* **424** 397
[17] Velicu I-L, Tiron V, Mihaila I and Costin C 2018 Pulsed magnetron sputtering: the role of the applied power on W coatings properties *Recent Advances in Technology Research and Education Advances in Intelligent Systems and Computing* vol 660 ed D Luca, L Sirghi and C Costin (Berlin: Springer) pp 183–90
[18] Raadu M A, Axnäs I, Gudmundsson J T, Huo C and Brenning N 2011 *Plasma Sources Sci. Technol.* **20** 065007
[19] Huo C, Lundin D, Gudmundsson J T, Raadu M A, Bradley J W and Brenning N 2017 *J. Phys. D: Appl. Phys.* **50** 354003
[20] Rudolph M, Brenning N, Raadu M A, Hajihoseini H, Gudmundsson J T, Anders A and Lundin D 2020 *Plasma Sources Sci. Technol.* **29** 05LT01

[21] Huo C, Lundin D, Raadu M A, Anders A, Gudmundsson J T and Brenning N 2013 *Plasma Sources Sci. Technol.* **22** 045005
[22] Eliasson H *et al* 2021 *Plasma Sources Sci. Technol.* **30** 115017
[23] Brenning N, Gudmundsson J T, Raadu M A, Petty T J, Minea T and Lundin D 2017 *Plasma Sources Sci. Technol.* **26** 125003
[24] Huo C, Lundin D, Raadu M A, Anders A, Gudmundsson J T and Brenning N 2014 *Plasma Sources Sci. Technol.* **23** 025017
[25] Gudmundsson J T, Fischer J, Hinriksson B P, Rudolph M and Lundin D 2022 *Surf. Coat. Technol.* **442** 128189
[26] Gudmundsson J T, Lundin D, Brenning N, Raadu M A, Huo C and Minea T M 2016 *Plasma Sources Sci. Technol.* **25** 065004
[27] Lundin D, Gudmundsson J T, Brenning N, Raadu M A and Minea T M 2017 *J. Appl. Phys.* **121** 171917
[28] Rezek J, Kozák T, Kumar N and Haviar S 2021 *J. Phys. D: Appl. Phys.* **54** 125202
[29] Rudolph M, Revel A, Lundin D, Hajihoseini H, Brenning N, Raadu M A, Anders A, Minea T M and Gudmundsson J T 2021 *Plasma Sources Sci. Technol.* **30** 045011
[30] Stancu G D, Brenning N, Vitelaru C, Lundin D and Minea T 2015 *Plasma Sources Sci. Technol.* **24** 045011
[31] Gudmundsson J T, Lundin D, Stancu G D, Brenning N and Minea T M 2015 *Phys. Plasmas* **22** 113508
[32] Gudmundsson J T and Thorsteinsson E G 2007 *Plasma Sources Sci. Technol.* **16** 399
[33] Alves L L 2014 *J. Phys.: Conf. Ser.* **565** 012007
[34] Alves L L and Guerra V 2020 IST-Lisbon database www.lxcat.net/ist-lisbon retrieved on (18 May 2020)
[35] Dixon A J, Harrison M F A and Smith A C H 1973 *8th Int. Conf. Physics of Electronic and Atomic Collisions (VIII ICPEAC)* ed B C ed Cobić and M V Kurepa (Beograd: Institute of Physics) pp 405–6
[36] Freund R S 1987 *Swarm Studies and Inelastic Electron–Molecule Collisions Proc. Meeting of the 4th Int. Swarm Seminar and the Inelastic Electron–Molecule Collisions Symp.* (Tahoe City, California, USA 19–23 July 1985) ed L C Pitchford, B V McKoy, A Chutjian and S Trajmar (New York: Springer) pp 329–46
[37] Müller A, Salzborn E, Frodl R, Becker R, Klein H and Winter H 1980 *J. Phys. B: At. Mol. Opt. Phys.* **13** 1877
[38] Stephan K, Helm H and Märk T D 1980 *J. Chem. Phys.* **73** 3763
[39] Deutsch H, Hilpert K, Becker K, Probst M and Märk T D 2001 *J. Appl. Phys.* **89** 1915
[40] Montague R G and Harrison M F A 1984 *J. Phys. B: At. Mol. Opt. Phys.* **17** 2707
[41] Rae S C and Tobin R C 1988 *J. Appl. Phys.* **64** 1418
[42] Anders A 2010 *J. Vac. Sci. Technol.* A **28** 783
[43] Biersack J P and Haggmark L G 1980 *Nucl. Instrum. Methods* **174** 257
[44] Kittel C 2005 *Introduction to Solid State Physics* 8th edn (New York: Wiley)
[45] Riseberg L A, Parks W F and Schearer L D 1973 *Phys. Rev.* A **8** 1962
[46] Inaba S, Goto T and Hattori S 1983 *J. Phys. Soc. Japan* **52** 1164
[47] Bogaerts A, Gijbels R and Carman R J 1998 *Spectrochim. Acta* B **53** 1679
[48] Hotop H and Niehaus A 1969 *Z. Phys.* A **228** 68
[49] Lieberman M A and Lichtenberg A J 2005 *Principles of Plasma Discharges and Materials Processing* 2nd edn (New York: Wiley)
[50] Blanco F, da Silva F F, Limão-Vieira P and García G 2017 *Plasma Sources Sci. Technol.* **26** 085004
[51] Hagstrum H D 1956 *Phys. Rev.* **104** 317
[52] Huo C, Raadu M A, Lundin D, Gudmundsson J T, Anders A and Brenning N 2012 *Plasma Sources Sci. Technol.* **21** 045004
[53] Butler A, Brenning N, Raadu M A, Gudmundsson J T, Minea T and Lundin D 2018 *Plasma Sources Sci. Technol.* **27** 105005
[54] Thornton J A 1978 *J. Vac. Sci. Technol.* **15** 171
[55] Brenning N, Huo C, Lundin D, Raadu M A, Vitelaru C, Stancu G D, Minea T and Helmersson U 2012 *Plasma Sources Sci. Technol.* **21** 025005
[56] Rossnagel S M 1988 *J. Vac. Sci. Technol.* A **6** 19
[57] Alami J, Sarakinos K, Mark G and Wuttig M 2006 *Appl. Phys. Lett.* **89** 154104
[58] Vlček J, Pajdarová A D and Musil J 2004 *Contrib. Plasma Phys.* **44** 426
[59] Vitelaru C, Lundin D, Stancu G D, Brenning N, Bretagne J and Minea T 2012 *Plasma Sources Sci. Technol.* **21** 025010
[60] Bohlmark J, Lattemann M, Gudmundsson J T, Ehiasarian A P, Aranda Gonzalvo Y, Brenning N and Helmersson U 2006 *Thin Solid Films* **515** 1522
[61] Greczynski G and Hultman L 2010 *Vacuum* **84** 1159
[62] Anders A, Andersson J and Ehiasarian A 2007 *J. Appl. Phys.* **102** 113303
[63] Pajdarová A D, Vlček J, Kudláček P and Lukáš J 2009 *Plasma Sources Sci. Technol.* **18** 025008
[64] Poolcharuansin P and Bradley J W 2010 *Plasma Sources Sci. Technol.* **19** 025010
[65] Ashida S, Lee C and Lieberman M A 1995 *J. Vac. Sci. Technol.* A **13** 2498
[66] Ashida S, Shim M R and Lieberman M A 1996 *J. Vac. Sci. Technol.* A **14** 391
[67] Ryan P J, Bradley J W and Bowden M D 2019 *Phys. Plasmas* **26** 073515
[68] Ryan P J, Bradley J W and Bowden M D 2019 *Phys. Plasmas* **26** 040702
[69] Zheng B *et al* 2019 *IEEE Trans. Plasma Sci.* **47** 193
[70] Rudolph M, Brenning N, Hajihoseini H, Raadu M A, Minea T M, Anders A, Gudmundsson J T and Lundin D 2022 *J. Phys. D: Appl. Phys.* **55** 015202
[71] Brenning N, Butler A, Hajihoseini H, Rudolph M, Raadu M A, Gudmundsson J T, Minea T and Lundin D 2020 *J. Vac. Sci. Technol.* A **38** 033008
[72] Brenning N, Hajihoseini H, Rudolph M, Raadu M A, Gudmundsson J T, Minea T M and Lundin D 2021 *Plasma Sources Sci. Technol.* **30** 015015
[73] Rudolph M, Hajihoseini H, Raadu M A, Gudmundsson J T, Brenning N, Minea T M, Anders A and Lundin D 2021 *J. Appl. Phys.* **129** 033303
[74] Anders A, Čapek J, Hála M and Martinu L 2012 *J. Phys. D: Appl. Phys.* **45** 012003
[75] Anders A, Ni P and Rauch A 2012 *J. Appl. Phys.* **111** 053304
[76] Anders A 2012 *Appl. Phys. Lett.* **100** 224104
[77] Bradley J W, Mishra A and Kelly P J 2015 *J. Phys. D: Appl. Phys.* **48** 215202
[78] Hajihoseini H, Čada M, Hubička Z, Ünaldi S, Raadu M A, Brenning N, Gudmundsson J T and Lundin D 2019 *Plasma* **2** 201

Paper II

High power impulse magnetron sputtering of tungsten: a comparison of experimental and modelling results

Swetha Suresh Babu, Martin Rudolph, Peter John Ryan, Joel Fischer, Daniel Lundin, James W Bradley and Jon Tomas Gudmundsson

Plasma Sources Science and Technology 32(3) (2023) 034003

OPEN ACCESS
IOP Publishing

Plasma Sources Science and Technology

Plasma Sources Sci. Technol. 32 (2023) 034003 (10pp) https://doi.org/10.1088/1361-6595/acc12f

High power impulse magnetron sputtering of tungsten: a comparison of experimental and modelling results

Swetha Suresh Babu[1], **Martin Rudolph**[2], **Peter John Ryan**[3], **Joel Fischer**[4], **Daniel Lundin**[4], **James W Bradley**[3] **and Jon Tomas Gudmundsson**[1,5,*]

[1] Science Institute, University of Iceland, Dunhaga 3, IS-107 Reykjavik, Iceland
[2] Leibniz Institute of Surface Engineering (IOM), Permoserstraße 15, 04318 Leipzig, Germany
[3] Department of Electrical Engineering and Electronics, University of Liverpool, Brownlow Hill, Liverpool L69 3GJ, United Kingdom
[4] Plasma and Coatings Physics Division, IFM-Materials Physics, Linköping University, SE-581 83 Linköping, Sweden
[5] Division of Space and Plasma Physics, School of Electrical Engineering and Computer Science, KTH Royal Institute of Technology, Stockholm SE-10044, Sweden

E-mail: tumi@hi.is

Received 30 November 2022, revised 11 February 2023
Accepted for publication 3 March 2023
Published 20 March 2023

Abstract

Here, we compare the ionization region model (IRM) against experimental measurements of particle densities and electron temperature in a high power impulse magnetron sputtering discharge with a tungsten target. The semi-empirical model provides volume-averaged temporal variations of the various species densities as well as the electron energy for a particular cathode target material, when given the measured discharge current and voltage waveforms. The model results are compared to the temporal evolution of the electron density and the electron temperature determined by Thomson scattering measurements and the temporal evolution of the relative neutral and ion densities determined by optical emission spectrometry. While the model underestimates the electron density and overestimates the electron temperature, the temporal trends of the species densities and the electron temperature are well captured by the IRM.

Keywords: high power impulse magnetron sputtering, tungsten, magnetron sputtering, HiPIMS, plasma chemistry

(Some figures may appear in colour only in the online journal)

1. Introduction

Magnetron sputtering [1] is a physical vapor deposition technique [2] that has become the deposition process of choice for a wide range of industrially relevant coatings [3, 4]. This technique has developed rapidly over the past decades, driven by an increasing demand for high-quality functional thin films and coatings for an ever-increasing range of applications [1, 3]. In the magnetron sputtering discharge a dense plasma is trapped in the cathode target vicinity by a static magnetic field forming an ionization region (IR). When driven by dc voltage or current, the sputtered species that reach the substrate constitute almost only neutral atoms. However, it can be beneficial for the resulting deposited films to have the flux onto the substrate to also contain ions of the sputtered species. Therefore, among the important advances of the magnetron sputtering technique in recent decades, is the possibility of increased

* Author to whom any correspondence should be addressed.

Original Content from this work may be used under the terms of the Creative Commons Attribution 4.0 licence. Any further distribution of this work must maintain attribution to the author(s) and the title of the work, journal citation and DOI.

 © 2023 The Author(s). Published by IOP Publishing Ltd

ionization of the sputtered film-forming species [4–6], which has turned out to become a game-changer for thin-film deposition by magnetron sputtering [7].

High power impulse magnetron sputtering (HiPIMS) is one approach to create a highly ionized flux of the film-forming material onto the substrate. High voltage pulses of short duty cycle (typically 0.5%–5%) are applied to the cathode target and lead to a high peak discharge current density (0.5–10 A cm^{-2}) and therefore to a high electron density ($\sim 10^{19}$ cm^{-3}) within the magnetic trap [8–10]. Consequently, the species sputtered from the target are ionized as they pass through the dense plasma of the IR. When the film-forming material is ionized, the ion bombarding energy can be controlled by biasing the substrate [6, 7], which provides an additional parameter for process development. The metal ions provide efficient energy and momentum transfer to the growing film surface which makes a deposition at lower substrate temperatures possible, while still achieving the desired film properties [11]. The film-forming species are then primarily incorporated at lattice sites resulting in films exhibiting much lower compressive stress, while noble gas trapping at the interstitial sites is avoided [7, 12].

One application for magnetron sputtering is the fabrication of tungsten thin films. Sputter-deposited tungsten thin films exhibit two phases, the equilibrium $\alpha-$W (A2 bcc) and the metastable $\beta-$W (A15 cubic) phases. HiPIMS-deposited tungsten films are denser, exhibit smaller grains and better adhesion [13–15] in addition to higher hardness, higher Young's modulus values, and smoother surfaces [13, 16, 17]. This is well demonstrated by Shimizu *et al* [15] who reported stress-free, unstrained single phase $\alpha-$W thin films, deposited by applying a synchronized substrate bias to selectively increase the energy of the metal population of the ion bombardment.

To understand the discharge processes that lead to the desired film properties in deposition experiments, one can resort to plasma characterization. For example, Ryan *et al* employed Thomson scattering measurements, to resolve the temporal evolution of the electron density and electron temperature in a HiPIMS discharge with a tungsten target [18, 19]. In addition, Ryan *et al* measured the electron densities and temperatures using a Langmuir probe, which showed a good agreement with before-mentioned results from the Thomson scattering measurements [20]. Furthermore, the temporal evolution of certain emission lines from the heavy species were recorded using optical emission spectrometry (OES) [19].

A different methodology to characterize plasma discharges is by modelling. The IR model (IRM) is a semi-empirical volume-averaged global model of the plasma chemistry of a pulsed magnetron sputtering discharge [21, 22]. Recently, a tungsten reaction set and related surface processes were incorporated in the IRM and applied to study a HiPIMS discharge with a tungsten target as the discharge voltage was varied [23]. It was seen that the contribution of the W^{+} ions to the total discharge current at the target surface increases with increased discharge voltage for peak current densities $J_{\mathrm{D,peak}}$ in the range from 0.33 to 0.73 A cm^{-2} [23]. Furthermore, the ionization probability of the sputtered tungsten increases, while the back-attraction probability decreases, with increased discharge voltage and peak current density.

Here, the objective is to compare the calculated IRM results with measurements. For this, we model three discharges that were characterized experimentally by Ryan *et al* [18, 19]. This allows us to compare the measured plasma parameters, in particular the temporal evolution of the electron temperature and electron density (from Thomson scattering measurements) and the temporal evolution of the neutral and ion densities of the working gas and sputtered species (from OES), to the model results.

In section 2 a brief overview of the experimental setup is given followed by a brief summary of the IRM in section 3. The results of the IRM calculations are discussed and compared to the experimental findings in section 4. A summary is given in section 5.

2. Experimental apparatus and method

The experiments were carried out in a custom-built cylindrical vacuum chamber (height 500 mm and diameter 450 mm) made of stainless steel. The discharge was driven by a SINEX 3 pulser unit (Chemfilt Ionsputtering A.B., Sweden). A 150 mm diameter tungsten target was mounted on a VTech 150 series unbalanced magnetron assembly (Gencoa Ltd., United Kingdom). Argon at a pressure of 1.6 Pa was used as the working gas. This is a somewhat higher working gas pressure than typically used in HiPIMS operation, but high density and low electron temperature conditions are favourable for the (peak) signal-to-noise ratio of the Thomson scattering spectrum. The pulses were 50 μs, 100 μs, and 200 μs long, and the repetition frequency was 50 Hz. For the three cases, an average discharge power (P_{D}) was maintained at 400 W. The discharge voltage and current waveforms measured for the three cases are shown in figure 1. Note that both the discharge voltage and the discharge current vary with time as the SINEX 3 pulser unit has a smaller storage capacitor compared to more modern pulser units [24, 25]. Figure 1(a) shows that the discharge voltage exhibits a similar temporal behavior regardless of the pulse length. The discharge current waveform (figure 1(b)) exhibits a spike in the beginning of the pulse followed by a monotonic decrease until the voltage is cut off. The discharge voltage is slightly higher (about 11% higher 10 μs into the pulse) when the pulse length is shorter. We see in figure 1(b) that the peak discharge current is higher for the shortest pulse length of 50 μs, while the discharge current for the longer pulses (100 μs and 200 μs) exhibits the same peak current and are almost identical until they are cut off.

Thomson scattering measurements were applied on the discharges to determine the temporal variation of the electron temperature and the electron density. A Nd:YAG laser operated at the second-harmonic wavelength (532 nm) was the radiation source. The laser energy per pulse was $\leqslant$240 mJ, the pulse duration 5 ns, the repetition rate 10 Hz, and the beam divergence 0.5 mrad. The laser beam was focused by a 1 m

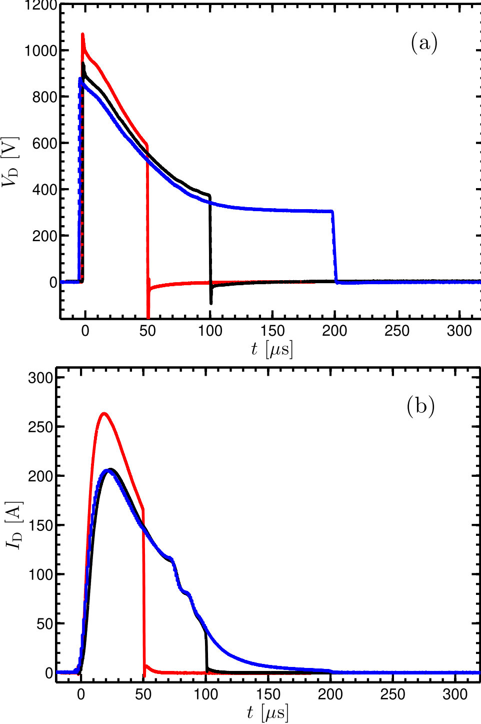

Figure 1. The temporal evolution of the discharge (a) voltage $V_D(t)$ and (b) current $I_D(t)$. The argon working gas pressure was 1.6 Pa and the target was made of tungsten 150 mm in diameter.

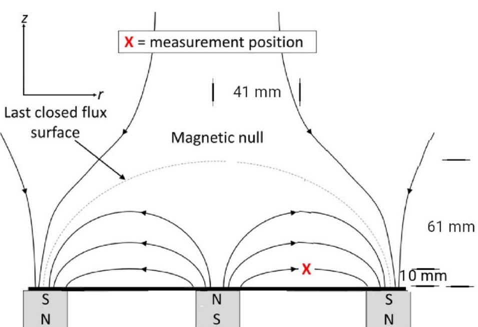

Figure 2. A schematic showing the magnetic field from an unbalanced planar magnetron assembly with a 150 mm diameter tungsten target, and the measurement position above the racetrack ($r = 41$ mm and $z = 10$ mm). The magnetic null position is $r = 0$ mm and $z = 61$ mm.

focal length lens to create a beam diameter of ∼0.25 mm at the measurement location, on a spot 10 mm above the racetrack, in the magnetic trap region ($r = 41$ mm, $z = 10$ mm), where the magnetic field strength was 33 mT [19], as shown schematically in figure 2. The beam path was in the plane of the target surface and the laser electric field was linearly polarized in the direction perpendicular to the plane of the target surface. The scattering volume was 0.15 mm in diameter and 3 mm long. The scattered light was collected by a lens (75 mm in diameter and focal length $f = 200$ mm) positioned at 90° with respect to both the laser propagation and polarisation axes in order to maximise the Thomson scattering differential cross-section. An image of the detection volume was presented onto the entrance slit (0.30 mm × 6 mm (the slit length was parallel to the laser propagation axis)) of a triple-grating spectrometer (TGS (Horiba T64000)). The spectrometer was configured in the double-subtractive configuration to attenuate the wavelength region 531.5–532.5 nm using a mask, a notch filter, to remove the stray laser light and Rayleigh scattering signals. An intensified charge-coupled device camera (Andor iStar DH320T-18U-A3) was used to record the spectra in two-dimensions. The wings of the Thomson spectra were fitted by either a single or double-Gaussian curve, corresponding to a Maxwellian or bi-Maxwellian electron velocity distribution function, respectively, to obtain the electron density and electron temperature. The system was calibrated for absolute density measurements using Rayleigh scattering from room temperature argon gas after each Thomson scattering measurement. The Thomson scattering signal was accumulated from 600 pulses for each time-resolved data point. From the Thomson scattering measurement, the temporal evolution of the absolute electron density and electron temperature was constructed.

Time-resolved OES measurements were performed in the magnetic trap region ($r = 41$ mm, $z = 10$ mm (see figure 2)) by Ryan [19] to provide information on the species composition in the discharge. This involved measuring the intensity of selected line emissions. These lines represent the various species: Ar I (751.47 nm), Ar II (480.60 nm), W I (361.75 nm), and W II (361.38 nm). The lines were chosen based on their relatively strong intensity and their large Einstein coefficient for spontaneous emission. Moreover, care was taken that they did not overlap with other significant transition lines. Therefore, the emission intensity is assumed to be representative of the instantaneous density of the upper excited level of the transition. The OES results presented in this article are displayed as relative intensities, where each data point in a temporal profile of line emission intensity is normalised by the maximum intensity measured in that particular time series. For each time-resolved data point the acquisition time was 10–20 s (500–1000 pulses). The line emission intensity was calculated by fitting a Gaussian curve to the peak and then calculating the area under the curve. More details of the experimental setup and methods are given elsewhere [19].

Table 1. The reactions and rate coefficients used in the IRM involving tungsten, determined for both hot and cold electrons. The rate coefficients are calculated assuming a Maxwellian electron energy distribution function and fit in the range $T_e = 1$–7 eV for cold electrons and 200–1000 eV for hot electrons.

Reaction	Threshold (eV)	Rate coefficient ($m^3 s^{-1}$)	electrons	Reference
(R1) $e + W \rightarrow W^+ + e$	7.864	$6.397 \times 10^{-14} T_e^{0.4839} \exp(-8.221/T_e)$	cold	[28]
		$4.251 \times 10^{-10} T_e^{-1.1791} \exp(-256.38/T_e)$	hot	
(R2) $e + W^+ \rightarrow W^{2+} + e$	16.35	$1.446 \times 10^{-14} T_e^{0.7143} \exp(-14.5193/T_e)$	cold	[29]
		$4.673 \times 10^{-10} T_e^{-1.3047} \exp(-273.55/T_e)$	hot	
(R3) $Ar^+ + W \rightarrow Ar + W^+$		2×10^{-16}		[30]
(R4) $Ar(4s'[1/2]_0) + W \rightarrow Ar + W^+ + e$		5.3×10^{-15}		
(R5) $Ar(4s[3/2]_2) + W \rightarrow Ar + W^+ + e$		5.3×10^{-15}		

3. The IRM

The IRM is a semi-empirical volume-averaged discharge model that requires inputs from an experimental discharge. These inputs are the discharge voltage and current waveforms, as well as the working gas pressure, and an estimated size of the IR [21, 22]. The IRM has been under development for well over a decade and has been applied in a number of studies to reveal the processes within a HiPIMS discharge [21–23, 26].

The IR in the model is assumed to be an annular cylinder with outer radius r_{c2}, and inner radius r_{c1}. It resides on top of the circular racetrack and has a height of $L = z_2 - z_1$, extending axially away from the target surface. For the studied discharges the parameters for the size of the IR are assumed to be: $r_{c1} = 12$ mm, $r_{c2} = 57$ mm, $z_1 = 2$ mm, $z_2 = 33$ mm. We explore how this choice of the dimensions of the IR influences the results in appendix.

In the model, we assume two electron populations, one cold population and one hot population. The majority of the electrons in the discharge are members of the cold electron population. They are created through volume reactions within the IR. This population essentially determines the electron density and the effective electron temperature. Hot electrons stem from secondary electron emission created by the ion bombardment of the cathode target. The electrons can gain energy either by being accelerated in the sheath or by Ohmic heating [22]. In each part, a fraction of the discharge power is dissipated [10], that is fed into the model via the discharge current and voltage waveforms. At the start of the simulation, we add an initial electron density of $1 \times 10^{18}\ m^{-3}$. In the appendix we show that the exact choice of the initial electron density does not influence the results.

The temporal development of the heavy species densities is defined by a set of ordinary differential equations [22], involving rate coefficients for each of the electron populations. The rate coefficients are calculated assuming a Maxwellian electron energy distribution function [22]. The rate coefficients for the cold electron population are valid in a range from $T_e = 1$–7 eV. The rate coefficients for the hot electron population are valid in a range from 200 to 1000 eV. This was shown to be a good approximation by comparison to the electron energy distribution calculated by the Orsay Boltzmann equation for ELectrons coupled with Ionization and EXcited states kinetics (OBELIX) model, which includes a Boltzmann solver [27]. The complete reaction set for the argon working gas and the tungsten discharge is listed in an earlier work [23], where the reaction set involving the tungsten discharge was discussed in detail, but the rate coefficients involving tungsten species are also listed in table 1.

Not every necessary model parameter is possible to obtain experimentally. There are three parameters that are unknown *a priori*: (i) the ion back-attraction probability for the metal ions $\beta_{t,pulse}$ and gas ions $\beta_{g,pulse}$ (it is assumed that $\beta_{t,pulse} = \beta_{g,pulse}$ as in previous studies [21–23]), (ii) the potential drop across the IR, V_{IR}, and (iii) the electron recapture probability r. For the latter, we assume $r = 0.7$, as it has been suggested by Buyle *et al* [31] that the electron recapture probability is typically between 65% and 75% for a planar magnetron sputtering discharge. This leaves two remaining parameters, that are found in a model fitting procedure. The best fit to the measured discharge current is determined by varying the fraction of the discharge voltage that drops across the IR f (with a resolution of $\Delta f = 0.01$) and the back-attraction probability of an ion of the sputtered species during the pulse $\beta_{t,pulse}$ (resolution $\Delta\beta_{t,pulse} = 0.025$). The model chooses values for the two parameters for which the discharge currents between the experiment and the model matches best.

An example fitting map is shown in figure 3 for the discharge with a 200 μs-long pulse. The blue zones in the fitting map (figure 3) indicate the combinations of $f = V_{IR}/V_D$ and $\beta_{t,pulse}$ where the weighted square deviation of the discharge current is smallest, which is where the modeled discharge current resembles the experimental discharge current best. The resulting best fits to the discharge current waveform determined by the IRM ($I_{D,IRM}(t)$) for the 200 μs long pulse is shown with dashed lines along with the measured discharge current ($I_D(t)$) shown by solid lines in figure 4.

4. Results and discussion

The internal discharge parameters derived from the IRM for the HiPIMS discharges with a tungsten target are given in table 2. The ionization probability of the sputtered species α_t is in the range from 0.89 to 0.81, the back-attraction probability

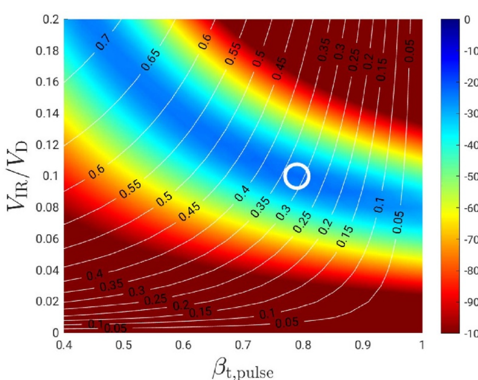

Figure 3. A fitting map showing the back attraction probability $\beta_{t,pulse}$ versus $f = V_{IR}/V_D$ for a discharge with a 150 mm diameter tungsten target, argon working gas pressure of 1.6 Pa, and pulse length of 200 μs. The white circles show where a well fitted discharge current waveform is observed. The white lines and the accompanying numbers indicate the ionized flux fraction.

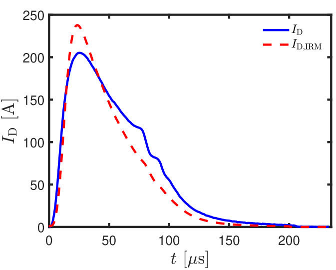

Figure 4. The temporal evolution of the measured discharge current (I_D) and the model calculated discharge current ($I_{D,IRM}$) for a 150 mm diameter tungsten target, argon working gas pressure of 1.6 Pa, and 200 μs long pulse.

$\beta_{t,pulse}$ increases from 0.54 to 0.79, and the ionized flux fraction decreases from 0.65 to 0.32, as the pulse length is increased from 50 μs to 200 μs. Shorter pulse length increases the ionized flux fraction and lowers the back-attraction probability.

The temporal evolution of the neutral particle densities for the 200 μs-long pulse is shown in figure 5. The cold ground state working gas argon atoms (denoted $Ar^C(3p^6)$) dominate the discharge. However, their density decreases steadily with increased discharge current during the pulse, exhibiting a minimum which coincides with the peak in the discharge current. This is an indication of working gas rarefaction, a phenomena that has been observed experimentally to be rather significant in HiPIMS operation [32–36]. It is also seen that there is a sharp increase in the density of both the warm and hot argon atoms in the initial stages of the pulse. The maximum degree of working gas rarefaction, determined by adding all neutral argon atoms within the IR, and comparing them to the initial cold Ar density, is in the range 65%–69%. Figure 5 also shows that the ground state tungsten atom W^0 density increases early in the pulse and becomes the second highest density species in the discharge for a short time early in the pulse. The metastable argon atoms exhibit more than an order of magnitude lower density.

Figure 6 shows the temporal evolution of the ion densities. The Ar^+ ions dominate the ion densities only during the first few microseconds of the pulse. Early in the pulse the W^+ ions take over as the dominating ions and remain dominating until the termination of the pulse. For much of the pulse duration and the afterglow the W^+ ions exhibit roughly an order of magnitude higher density than the Ar^+ ions. At the peak in the discharge current, the density of tungsten ions reaches a value of around 2×10^{19} m^{-3} versus $8 \times 10^{18} - 10^{19}$ m^{-3} for the argon ion density. For all cases investigated, the Ar^{2+} ion density peaks around 2×10^{16} m^{-3}, which is more than three orders of magnitude smaller than the W^+ ion density. The W^{2+} ion density is roughly two orders of magnitude smaller than the W^+ ion density. Note that the small bump seen in all ion densities at pulse-end in figure 6 is not due to a sudden increase in ion gain rates, but instead a result of a reduced ion loss rate from the back-attraction β_t, becoming zero in the pulse afterglow, which consequently leads to a jump in ion density in the IR [37]. The model results for the temporal evolution for both neutrals and ions agree with the findings from our earlier modeling of a HiPIMS discharge with a tungsten target [23] as well as experimental observations [15]. Note that for the discharges explored in earlier studies the discharge voltage was maintained throughout the pulse, while in this current work the discharge voltage varies greatly through the pulse, as can be seen in figure 1(a).

The temporal evolution of the discharge current composition at the target surface is shown in figure 7 for a 200 μs long pulse. The other pulse lengths have very similar compositions (not shown). Early in the pulse Ar^+ ions dominate the heavy charged species in the discharge, before it is taken over by W^+ ions. Initially argon ions bombard the target and sputter off metal atoms that are ionized and consequently return to the target and sputter off metal atoms again, and therefore, constitute a self-sputter recycling loop [38], where the tungsten atoms and ions, partially take over the role of the working gas argon atoms and ions as the pulse progresses. The fact that W^+ ions dominate the discharge causes the secondary electron emission from the target to become very small (see $I_{sec}(t)$ in figure 7), as the secondary electron emission yield is zero for W^+ ions bombarding tungsten target.

Figure 8 shows the temporal profiles of the intensity of line emission, normalised by the peak number of counts for each line in a profile, from various species in the plasma discharge (Ar^0, Ar^+, W^0 and W^+) (dashed lines). The measurement was performed on a discharge formed with a 100 μs-long pulse and the average power was 400 W with a 50 Hz repetition rate, and the working gas pressure was 1.6 Pa. The intensity of the Ar^0 line decreases, while the Ar^+ emission intensity peaks at $t = 20$ μs, and the emission from both tungsten species increases. The figure also includes, for comparison and validation, the results of the model calculations (solid

Table 2. Operation parameters, the pulse length t_{pulse} and the peak discharge current $I_{\text{D,peak}}$, and parameters derived from the modeling of a HiPIMS discharges with a tungsten target, the working gas rarefaction, the ionization probability α_{t}, the back-attraction probability β_{t}, the fractional voltage drop across the ionization region f, and the ionized flux fraction F_{flux}.

t_{pulse} (μs)	$I_{\text{D,peak}}$ (A)	$J_{\text{D,peak}}$ (A cm^{-2})	maximum degree of rarefaction (%)	α_{t}	$\beta_{\text{t,pulse}}$	β_{t}	$f = V_{\text{IR}}/V_{\text{D}}$	F_{flux}
50	263.2	1.49	69.4	0.89	0.61	0.54	0.10	0.65
100	206.5	1.17	65.1	0.83	0.76	0.74	0.10	0.39
200	205.2	1.16	64.8	0.81	0.79	0.79	0.10	0.32

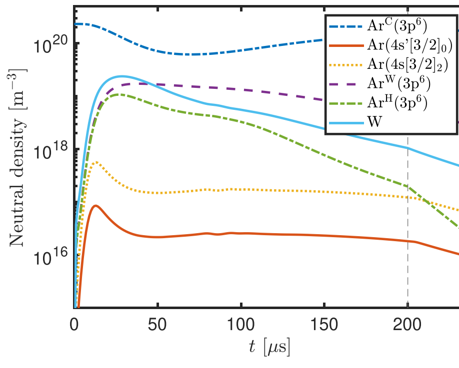

Figure 5. The temporal evolution of the neutral particle densities for a discharge with a 150 mm diameter tungsten target, argon working gas pressure of 1.6 Pa, and 200 μs long pulse. The dashed vertical line indicates the termination of the pulse.

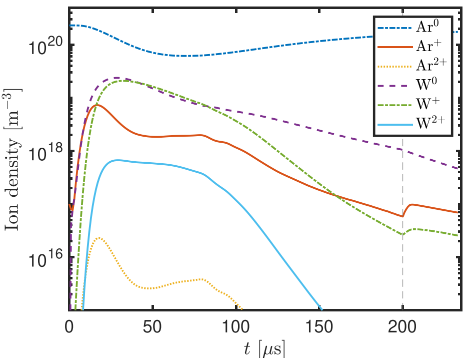

Figure 6. The temporal evolution of the charged particle densities for a discharge with a 150 mm diameter tungsten target, argon working gas pressure of 1.6 Pa, and a 200 μs-long pulse. For comparison the total argon neutral density (ground state and excited states) Ar^0 and the neutral tungsten density W^0 is also shown. The dashed vertical line indicates the termination of the pulse.

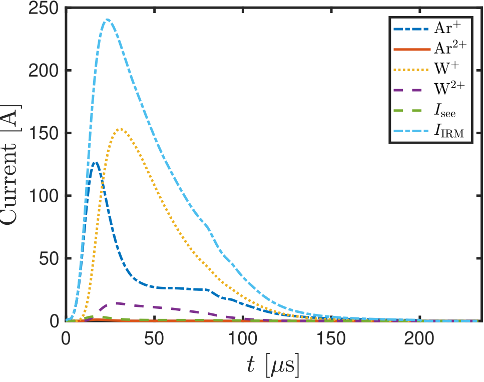

Figure 7. The temporal evolution of the discharge current composition at the target surface for a discharge with a 150 mm diameter tungsten target, argon working gas pressure of 1.6 Pa, and 200 μs long pulse.

lines). The model results show a somewhat slower decay of the Ar^0 density than observed experimentally (figure 8(a)). The 751.5 nm emission line from an argon atom is due to the decay from the 13.48 eV level in the 4p manifold to the 11.83 eV radiative level in the 4s manifold. We assume that electron impact excitation from the ground state dominates the excitation process. The reaction rate for electron impact excitation of the ground state argon atom is $k_{\text{exc}}(T_{\text{e}})n_{\text{e}}n_{\text{Ar}}$, where $k_{\text{exc}}(T_{\text{e}})$ is the excitation rate coefficient to the particular 4p state, which depends both on the electron density, the working gas pressure, and the electron temperature. We are aware that there is also some excitation from the metastable states into the 4s manifold. Earlier we have estimated the contribution of stepwise ionization from the metastable levels of the 4s manifold in HiPIMS operation to be as high as 15% [39], and we would expect a similar contribution to the excitation to the 4p manifold. Also, keep mind that there can be a decay from the 13.48 eV level to other levels of the argon atom. Similar arguments apply for the other measured lines from the heavy species used in this study. The peak in the Ar$^+$ density appears roughly at the same time for the model calculation as determined experimentally, but the calculated Ar$^+$ density decays somewhat faster than the measured density (figure 8(b)). The peak in the calculated relative W^0 density appears somewhat earlier and decays much faster than the measured W^0 density peak, as the measurements indicate that the W^0 density remains high almost to the termination of the pulse, which is something that the model does not capture (figure 8(c)). The W$^+$ ion emission intensity peaks roughly 30 μs into the

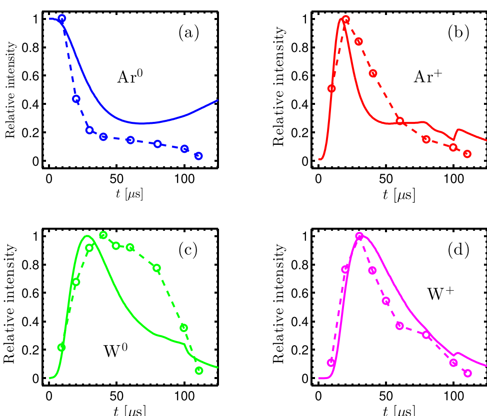

Figure 8. The temporal evolution of the relative optical emission from the various species (a) Ar^0, (b) Ar^+, (c) W^0, and (d) W^+, for 100 μs pulse length, argon working gas pressure of 1.6 Pa, and a discharge with a 150 mm diameter tungsten target. The experimental data is from Ryan [19], shown with dashed lines, and the IRM results are shown as solid lines.

pulse, and the model calculations agree with the measurements (figure 8(d)).

The temporal evolution of the electron density and the electron temperature in a HiPIMS discharge with a tungsten target was determined experimentally using Thomson scattering [18–20]. The measured temporal evolution of the electron density from the Thomson scattering measurements is shown in figure 9. For the 50 μs long pulse the measured maximum electron density is $(1.15 \pm 0.07) \times 10^{20}$ m^{-3} [18] (figure 9(a)), while for the longer pulses the measured peak value is $\sim 7 \times 10^{19}$ m^{-3} (figures 9(b) and (c)).

The measured temporal evolution of the electron density is compared to the calculated primary electron density in figure 9. Clearly, there is a discrepancy between the experimental and modelled electron density. The calculated electron density is always lower than the measured electron density. This discrepancy is up to a factor 4 during the peak for the 50 μs pulse length and somewhat smaller for 100 μs and 200 μs pulse length. However, it should be taken into account that the IRM is a simple global model with densities averaged over the entire IR volume, which is here assumed to extend 33 mm away from the cathode target, while the measurement is taken 10 mm from the target surface. Therefore, if we assume the electron (and ion) density to decrease with distance from the target surface, it is expected that the model calculations yield a smaller electron density than what is measured close to the target surface. Recent study by Dubois *et al* [40] determined, using Thomson scattering measurements, the variation in the electron density and electron temperature with distance from the target surface above the race track. The electron density was found to drop with distance from the target surface following a bi-exponential dependence. For pulse length of

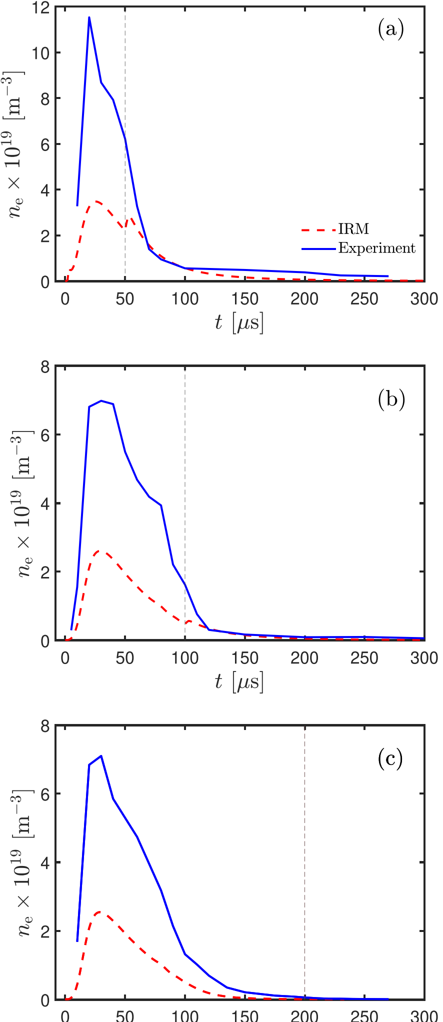

Figure 9. The measured temporal evolution of the electron density and the calculated electron density for pulse length of (a) 50 μs, (b) 100 μs, and (c) 200 μs for a discharge with a 150 mm diameter tungsten target and argon working gas pressure of 1.6 Pa. The dashed vertical line indicates the termination of the pulse.

70 μs, an argon working gas pressure of 1 Pa, a titanium target, and a peak discharge current of 40 A, the electron density 6 mm above the target surface was 1.81×10^{19} m^{-3} and had fallen to half this value roughly 15 mm, and by about 70% roughly 25 mm above the target surface. This shows that a significant variation in electron density is to be expected within the IR.

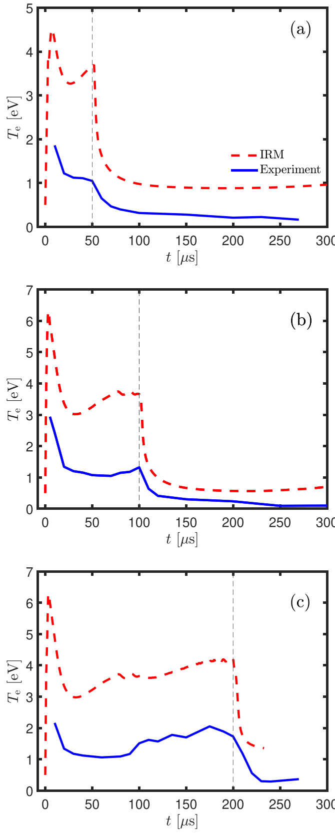

Figure 10. The measured temporal evolution of the electron temperature and the calculated primary electron temperature for pulse length of (a) 50 μs, (b) 100 μs, and (c) 200 μs for a discharge with argon working gas pressure of 1.6 Pa and a 150 mm diameter tungsten target. The dashed vertical line indicates the termination of the pulse.

Figure 10 shows the temporal profiles of the electron temperature within the magnetic trap for pulse lengths of 50 μs, 100 μs, and 200 μs. The electron temperature for the three discharges is similar during the overlapping pulse-on periods. The direct comparison of the calculated and measured electron temperature shows a discrepancy (figure 10). The calculated electron temperature is always significantly higher than the measured electron temperature. This again can be explained by the extension of the modelled IR, and the location of the measured volume, as the study by Dubois *et al* [40] indicates an exponential drop in the electron temperature with distance from the target surface. However, we like to point out that the features in the temporal evolution of the electron temperature are mostly captured by the model.

Despite the explainable differences between the experimental results and the model, we consider the model to reproduce the important trends in the electron temperature and the species density temporal evolution. Note that the objective of the IRM is to describe exactly these trends in HiPIMS discharges [21, 22]. The assumptions and necessary simplifications (e.g. it neglects spatial variation and uses an assumed EEDF) render the IRM considerably more efficient compared to e.g. particle-in-cell Monte Carlo collision simulations. This makes it possible to use the IRM for e.g. deposition process optimization [37, 41, 42], not possible with other modeling methodologies.

5. Summary

We have applied the IRM to explore a HiPIMS discharge with a tungsten target. Applying the IRM, the temporal evolution of the species densities and the internal discharge properties of the HiPIMS discharge can be determined. It is shown that Ar^+ ions dominate the discharge current at the target surface in the initial stages of the pulse, but W^+ ions take over early in the pulse and dominate the discharge current for the remainder of the pulse duration. The IRM calculation were compared to the experimentally determined temporal evolution of the electron density and electron temperature from Thomson scattering measurements and the temporal evolution of the heavy species determined by OES. The IRM captures the relative temporal evolution of the ions and neutrals of the working gas and sputtered species. However, we find that the model underestimates the electron density and overestimates the electron temperature, but captures well the trends of the temporal evolution of the electron temperature and density.

Data availability statement

All data that support the findings of this study are included within the article (and any supplementary files).

Acknowledgments

This work was partially funded by the Icelandic Research Fund (Grant No. 196141), the Swedish Research Council (Grant No. VR 2018-04139), the Swedish Government Strategic Research Area in Materials Science on Functional Materials at Linköping University (Faculty Grant SFO-Mat-LiU No. 2009-00971).

Appendix. Sensitivity analysis

The question that remains is if the discrepancy in the electron density and the electron temperature values is due to the choice of initial values or the assumption of the size of the IR, which is a somewhat arbitrary. Figure 11 shows a sensitivity analysis of the effect of the initial electron density on the temporal evaluation of the electron temperature. We compare the calculated

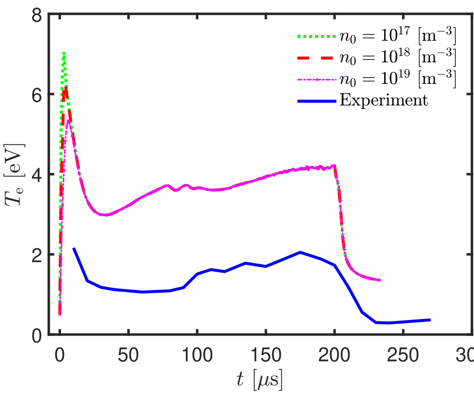

Figure 11. The temporal evolution of the electron temperature for pulse length of 200 μs for a discharge with a 150 mm diameter tungsten target and argon working gas of 1.6 Pa. The model results for the electron temperature are calculated assuming varying initial electron density.

Figure 13. The temporal evolution of the electron temperature for pulse length of 200 μs for a discharge with a 150 mm diameter tungsten target and argon working gas pressure of 1.6 Pa. Sensitivity analysis where the electron temperature is calculated while varying the size of the IR, $z_2 = 33$ mm and $z_2 \pm 20\%$.

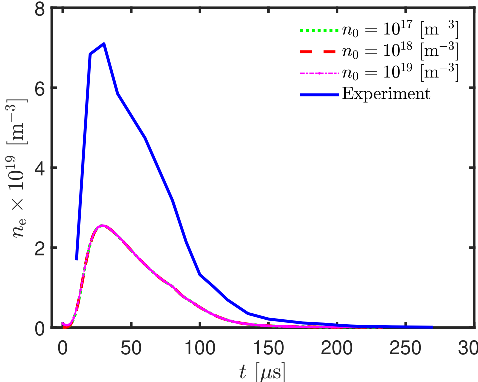

Figure 12. The temporal evolution of the electron density for pulse length of 200 μs, for a discharge with a 150 mm diameter tungsten target and argon working gas pressure of 1.6 Pa. The model results for the electron density are calculated assuming varying initial electron density.

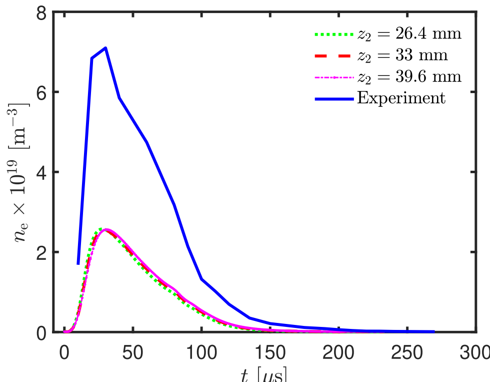

Figure 14. The temporal evolution of the electron density for pulse length of 200 μs for a discharge with a 150 mm diameter tungsten target and argon working gas pressure of 1.6 Pa. Sensitivity analysis where the electron temperature is calculated while varying the size of the IR, $z_2 = 33$ mm and $z_2 \pm 20\%$.

electron temperature assuming initial electron density of $n_0 = 10^{17}$ m^{-3}, 10^{18} m^{-3}, and 10^{19} m^{-3}. For a lower initial electron density the initial peak in the electron temperature is somewhat higher, but after the initial peak the electron temperature is the same regardless of the initial value. For all cases the calculated electron temperature is well above the measured value. Therefore, the initial electron density does not have much influence on the calculated value of the electron temperature. A sensitivity analysis of the effect of the initial electron density on the temporal evaluation of the electron density is shown in figure 12. In all cases the calculated electron density is well below the measured value and the initial electron density does not have much influence on the overall results, except that a too high value can create an overshot in the first few μs. Figure 13 shows a sensitivity analysis of the effect of the size of the IR on the temporal evaluation of the electron temperature. We compare the calculated electron temperature for $z_2 = 33$ mm and $z_2 \pm 20\%$. In all cases the calculated electron temperature is well above the measured value. Therefore, the size of the IR does not have much influence of the calculated value of the electron temperature. Figure 14 shows a sensitivity analysis of the effect of the size of the IR on the temporal evaluation of the electron density. We show the results for $z_2 = 33$ mm and then when $z_2 \pm 20\%$. In all cases the calculated electron density is

well below the measured value. Therefore, the size of the IR does not have much influence of the overall results. The choice of initial electron density or the size of the IR does not have a major influence on the overall results.

ORCID iDs

Swetha Suresh Babu https://orcid.org/0000-0001-5360-5562
Martin Rudolph https://orcid.org/0000-0002-0854-6708
Peter John Ryan https://orcid.org/0000-0002-7133-6156
Joel Fischer https://orcid.org/0000-0001-9116-6302
Daniel Lundin https://orcid.org/0000-0001-8591-1003
James W Bradley https://orcid.org/0000-0002-8833-0180
Jon Tomas Gudmundsson https://orcid.org/0000-0002-8153-3209

References

[1] Gudmundsson J T 2020 *Plasma Sources Sci. Technol.* **29** 113001
[2] Gudmundsson J T, Anders A and von Keudell A 2022 *Plasma Sources Sci. Technol.* **31** 083001
[3] Kelly P J and Arnell R D 2000 *Vacuum* **56** 159
[4] Rossnagel S M 1999 *IBM J. Res. Dev.* **43** 163
[5] Hopwood J 1998 *Phys. Plasmas* **5** 1624
[6] Helmersson U, Lattemann M, Bohlmark J, Ehiasarian A P and Gudmundsson J T 2006 *Thin Solid Films* **513** 1
[7] Greczynski G, Petrov I, Greene J E and Hultman L 2019 *J. Vac. Sci. Technol.* A **37** 060801
[8] Gudmundsson J T, Brenning N, Lundin D and Helmersson U 2012 *J. Vac. Sci. Technol.* A **30** 030801
[9] Lundin D, Minea T and Gudmundsson J T (eds) 2020 *High Power Impulse Magnetron Sputtering: Fundamentals, Technologies, Challenges and Applications* (Amsterdam: Elsevier)
[10] Rudolph M, Brenning N, Hajihoseini H, Raadu M A, Minea T M, Anders A, Lundin D and Gudmundsson J T 2022 *J. Phys. D: Appl. Phys.* **55** 015202
[11] Anders A 2010 *Thin Solid Films* **518** 4087
[12] Greczynski G, Mráz S, Schneider J M and Hultman L 2020 *J. Appl. Phys.* **127** 180901
[13] Engwall A M, Shin S J, Bae J and Wang Y M 2019 *Surf. Coat. Technol.* **363** 191
[14] Roychowdhury T, Shah D, Jain V, Patel D I, Dodson B, Skinner W, Hilfiker J N, Smith S J and Linford M R 2020 *Surf. Interface Anal.* **52** 433
[15] Shimizu T, Takahashi K, Boyd R, Viloan R P, Keraudy J, Lundin D, Yang M and Helmersson U 2021 *J. Appl. Phys.* **129** 155305
[16] Velicu I-L, Tiron V, Porosnicu C, Burduce I, Lupu N, Stoian G, Popa G and Munteanu D 2017 *Appl. Surf. Sci.* **424** 397
[17] Velicu I L, Tiron V, Mihaila I and Costin C 2018 *Recent Advances in Technology Research and Education* (*Advances in Intelligent Systems and Computing* vol 660) ed D Luca, L Sirghi and C Costin (Cham: Springer) pp 183–90
[18] Ryan P J, Bradley J W and Bowden M D 2019 *Phys. Plasmas* **26** 040702
[19] Ryan P J 2019 Electron diagnostics of magnetron discharges *PhD Thesis* University of Liverpool, Liverpool, England
[20] Ryan P J, Bradley J W and Bowden M D 2019 *Phys. Plasmas* **26** 073515
[21] Raadu M A, Axnäs I, Gudmundsson J T, Huo C and Brenning N 2011 *Plasma Sources Sci. Technol.* **20** 065007
[22] Huo C, Lundin D, Gudmundsson J T, Raadu M A, Bradley J W and Brenning N 2017 *J. Phys. D: Appl. Phys.* **50** 354003
[23] Babu S S, Rudolph M, Lundin D, Shimizu T, Fischer J, Raadu M A, Brenning N and Gudmundsson J T 2022 *Plasma Sources Sci. Technol.* **31** 065009
[24] Hubička Z, Gudmundsson J T, Larsson P and Lundin D 2020 Hardware and power management for high power impulse magnetron sputtering *High Power Impulse Magnetron Sputtering: Fundamentals, Technologies, Challenges and Applications* (eds) D Lundin, T Minea and J T Gudmundsson (Amsterdam: Elsevier) pp 49–80
[25] Gudmundsson J T, Fischer J, Hinriksson B P, Rudolph M and Lundin D 2022 *Surf. Coat. Technol.* **442** 128189
[26] Huo C, Lundin D, Raadu M A, Anders A, Gudmundsson J T and Brenning N 2013 *Plasma Sources Sci. Technol.* **22** 045005
[27] Rudolph M, Revel A, Lundin D, Hajihoseini H, Brenning N, Raadu M A, Anders A, Minea T M and Gudmundsson J T 2021 *Plasma Sources Sci. Technol.* **30** 045011
[28] Deutsch H, Hilpert K, Becker K, Probst M and Märk T D 2001 *J. Appl. Phys.* **89** 1915
[29] Montague R G and Harrison M F A 1984 *J. Phys. B: At. Mol. Opt. Phys.* **17** 2707
[30] Rae S C and Tobin R C 1988 *J. Appl. Phys.* **64** 1418
[31] Buyle G, Depla D, Eufinger K and De Gryse R 2004 *J. Phys. D: Appl. Phys.* **37** 1639
[32] Vlček J, Pajdarová A D and Musil J 2004 *Contrib. Plasma Phys.* **44** 426
[33] Alami J, Sarakinos K, Mark G and Wuttig M 2006 *Appl. Phys. Lett.* **89** 154104
[34] Palmucci M, Britun N, Konstantinidis S and Snyders R 2013 *J. Appl. Phys.* **114** 113302
[35] Liebig B, Braithwaite N S J, Kelly P J and Bradley J W 2010 *Thin Solid Films* **519** 1699
[36] Kanitz A, Hecimovic A, Böke M and Winter J 2016 *J. Phys. D: Appl. Phys.* **49** 125203
[37] Rudolph M, Brenning N, Raadu M A, Hajihoseini H, Gudmundsson J T, Anders A and Lundin D 2020 *Plasma Sources Sci. Technol.* **29** 05LT01
[38] Brenning N, Gudmundsson J T, Raadu M A, Petty T J, Minea T and Lundin D 2017 *Plasma Sources Sci. Technol.* **26** 125003
[39] Gudmundsson J T, Lundin D, Stancu G D, Brenning N and Minea T M 2015 *Phys. Plasmas* **22** 113508
[40] Dubois T, Tsikata S and Minea T 2022 *Plasma Sources Sci. Technol.* **31** 115018
[41] Brenning N, Butler A, Hajihoseini H, Rudolph M, Raadu M A, Gudmundsson J T, Minea T and Lundin D 2020 *J. Vac. Sci. Technol.* A **38** 033008
[42] Brenning N, Hajihoseini H, Rudolph M, Raadu M A, Gudmundsson J T, Minea T M and Lundin D 2021 *Plasma Sources Sci. Technol.* **30** 015015

Paper III

High power impulse magnetron sputtering of a zirconium target.

Swetha Suresh Babu, Joel Fischer, Kateryna Barynova, Martin Rudolph, Daniel Lundin, Jon Tomas Gudmundsson

Journal of Vacuum Science and Technology A 42(4) (2024) 043007

JVST A
Journal of Vacuum Science & Technology A

ARTICLE pubs.aip.org/avs/jva

High power impulse magnetron sputtering of a zirconium target

Cite as: J. Vac. Sci. Technol. A **42**, 043007 (2024); doi: 10.1116/6.0003647
Submitted: 25 March 2024 · Accepted: 30 May 2024 ·
Published Online: 25 June 2024

View Online Export Citation CrossMark

Swetha Suresh Babu,[1] Joel Fischer,[2] Kateryna Barynova,[1] Martin Rudolph,[3] Daniel Lundin,[2] and Jon Tomas Gudmundsson[1,4]

AFFILIATIONS

[1] Science Institute, University of Iceland, Dunhaga 3, Reykjavik IS-107, Iceland
[2] Plasma and Coatings Physics Division, IFM-Materials Physics, Linköping University, Linköping SE-581 83, Sweden
[3] Leibniz Institute of Surface Engineering (IOM), Permoserstraße 15, Leipzig 04318, Germany
[4] Division of Space and Plasma Physics, School of Electrical Engineering and Computer Science, KTH Royal Institute of Technology, Stockholm SE-10044, Sweden

ABSTRACT

High power impulse magnetron sputtering (HiPIMS) discharges with a zirconium target are studied experimentally and by applying the ionization region model (IRM). The measured ionized flux fraction lies in the range between 25% and 59% and increases with increased peak discharge current density ranging from 0.5 to 2 A/cm^2 at a working gas pressure of 1 Pa. At the same time, the sputter rate-normalized deposition rate determined by the IRM decreases in accordance with the HiPIMS compromise. For a given discharge current and voltage waveform, using the measured ionized flux fraction to lock the model, the IRM provides the temporal variation of the various species and the average electron energy within the ionization region, as well as internal discharge parameters such as the ionization probability and the back-attraction probability of the sputtered species. The ionization probability is found to be in the range 73%–91%, and the back-attraction probability is in the range 67%–77%. Significant working gas rarefaction is observed in these discharges. The degree of working gas rarefaction is in the range 45%–85%, higher for low pressure and higher peak discharge current density. We find electron impact ionization to be the main contributor to working gas rarefaction, with over 80% contribution, while kick-out by zirconium atoms and argon atoms from the target has a smaller contribution. The dominating contribution of electron impact ionization to working gas rarefaction is very similar to other low sputter yield materials.

© 2024 Author(s). All article content, except where otherwise noted, is licensed under a Creative Commons Attribution (CC BY) license (https://creativecommons.org/licenses/by/4.0/). https://doi.org/10.1116/6.0003647

27 June 2024 10:24:25

I. INTRODUCTION

The magnetron sputtering discharge[1–3] is a highly successful and widely used thin film deposition technique that belongs to the group of physical vapor deposition methods.[4] The source of the film-forming material is a solid target out of which the atoms are released by ion bombardment. The magnetron sputtering discharge is based on forming a dense plasma in the target vicinity by a static magnetic field that traps the electrons.[1,2,5] This dense plasma is easily observable and appears as a brightly glowing torus located adjacent to the target surface. This brightly glowing region is referred to as the ionization region (IR).[6] Ions accelerated from this dense plasma sputter the film-forming material from the cathode target.

When operated as a dc magnetron sputtering (dcMS) discharge, the ions of the working gas bombard the target and the sputtered species that reach the substrate are mostly neutral atoms. The ions bombarding the substrate are ions of the working gas. By applying high voltage pulses of low duty cycle to the cathode target, the discharge current density in the pulse can become high, and therefore, a high electron density is created in the IR.[7–12] Consequently, a significant fraction of the sputtered atoms coming off the target becomes ionized as they pass through the dense plasma of the ionization region. In this case, ions of both the working gas and the target material bombard the target. This also makes ions of the film-forming material available for deposition onto the substrate. This variant of magnetron sputtering is referred to as high power impulse magnetron sputtering (HiPIMS).[7,10] It is one approach to create a highly ionized flux of the film-forming material.[7,13] When the atoms of the film-forming material in the deposition flux are ionized, the energy and direction of the ions

© Author(s) 2024

bombarding the substrate can be controlled by biasing the substrate.[13–15] Control of the ion bombarding energy means that the need for external substrate heating can be significantly reduced or even eliminated.[16–18] Furthermore, selective microstructural texturing is made possible.[18–20]

Zirconium (Zr([Kr]4d^{2}s^2)) is a group-IV transition metal element. The stable crystalline state of zirconium at room temperature and ambient pressure is a hexagonal close-packed (hcp) structure (α-Zr phase). With increased temperature, it transforms martensitically into the body-centered cubic (bcc) structure (β-Zr phase) at 1136 K.[21] In comparison with other elemental metals, zirconium in solid form exhibits good thermal conductivity, high melting point, low thermal expansion, and good mechanical strength. Furthermore, zirconium has a very low neutron scattering cross section and a high solid solubility of oxygen and hydrogen. Therefore, zirconium and its alloys in bulk and thin film forms are widely used in the nuclear industry.[22,23] Furthermore, as zirconium has excellent corrosion resistance and acceptable biocompatibility, titanium–zirconium (Ti–Zr) binary alloys have been proposed for biomedical applications.[24,25]

Zirconium thin films with hexagonal close packed crystal structure (α-Zr) have been deposited by dc magnetron sputtering,[26–28] asymmetric bipolar pulsed magnetron sputtering,[29,30] and HiPIMS.[19,20] Noteworthy is the work of Fankhauser *et al.*[28] which deposited epitaxial Zr(0001) thin films onto Al_2O_3(0001) using dc magnetron sputtering. When deposited by HiPIMS, at substrate temperature in the range 300–873 K, Kuo *et al.*[20] find zirconium films to be polycrystalline and exhibit predominantly [0 0 0 1] texture. The crystallite size is found to increase with increasing substrate temperature during deposition.[29,30] Kuo *et al.*[20] also explored the influence of the pulse width and substrate bias on the properties of zirconium films deposited by HiPIMS and showed that the predominant texture can become [1 0 $\bar{1}$ 1] by synchronizing bias on the substrate and longer pulse lengths. Lustosa *et al.*[25] deposited Ti-Zr alloy using HiPIMS, exploring how the hardness varied with pulsing frequency. The hardness decreased and lower contact angles and better hydrophilic properties were observed when the alloy was deposited at lower pulsing frequencies.

Here, we develop an ionization region model (IRM) of a HiPIMS discharge with argon as the working gas and a zirconium target. The model provides insights into the discharge physics and chemistry, notably the temporal evolution of the species densities and the discharge current composition, a voltage drop across the IR, the ionization probability, as well as the back-attraction probability of the sputtered species.[31] Earlier, the IRM has been applied to study discharges with graphite,[32] aluminum,[31,33] titanium,[31,34] copper,[35] and tungsten[36,37] targets. These studies indicate that the process that dominates working gas rarefaction depends strongly on the sputter yield and/or self-sputter yield,[38] with little dependence on the mass of the target atoms, contrary to reports by other authors.[39,40] For example, rarefaction in a discharge with a tungsten target, having a high atomic mass and a moderate sputter yield, behaves very similar to a discharge using an aluminum target, having a low atomic mass and a similar sputter yield to tungsten.[38] Similarly, the back-attraction probability appears to depend on the sputter yield of the target material.[35] To fully disentangle the effect of mass and sputter yield, we here develop a model of a HiPIMS discharge with a zirconium target and apply it to a few discharges with experimentally determined discharge voltage and current waveforms and measured ionized flux fraction. Zirconium has a moderate atomic mass, lower than tungsten and higher than copper, and a low sputter yield. Therefore, it is important to understand a HiPIMS discharge with a zirconium target to provide a piece of the puzzle on how working gas rarefaction, the deposition rate, and the back-attraction probability depend on the atom mass and the sputter yield of the target material.

The paper is structured as follows: In Sec. II A, we discuss the experimental setup. The basics of the ionization region model and the addition of the zirconium reaction set are reviewed in Sec. II B. Section III A discusses the experimental findings and Sec. III B the results of the model studies. The findings of this work are summarized in Sec. IV.

II. EXPERIMENTAL APPARATUS AND METHOD

A. Experimental setup

The sputter target was a 2 in. zirconium disk mounted on an unbalanced magnetron assembly. The base pressure was maintained below 2×10^{-4} Pa by a turbomolecular pump backed by a roughing pump. The working gas pressure was set to 0.5 and 1 Pa by regulating the argon gas flow. A dc power supply together with a HiPSTER 6 pulsing unit (Ionautics, Sweden) was used to apply voltage pulses to the cathode target. The peak discharge current was kept fixed and an average discharge power $\langle P_D \rangle$ was maintained at 60 W by varying the repetition frequency. The pulse was kept at a constant length of either 50 or 100 μs. For comparison, measurements were also made for a dcMS discharge at the same pressures and average power and a discharge voltage of $V_{D,dcMS} = 255$ V.

The flux parameters were determined using an ion meter, which consisted of a magnetic schielding, a grounded casing, and a quartz crystal micro-balance (QCM) sensor which could be biased to achieve charge selectivity. The ion meter could measure either the deposition rate from ions and neutrals or from neutrals only by varying the voltage applied to the biased top QCM electrode. The ion meter (or gridless QCM/m-QCM) and its design and operation principles are described in detail elsewhere.[41,42] For the measurements, the ion meter was placed at distances of 3, 4, 6, 8, and 10 cm above the racetrack and facing the target surface.

B. Ionization region model

The IRM of a high power impulse magnetron sputtering discharge is a volume-averaged plasma chemistry model that provides the temporal variation of the various species densities and the electron energy. It is a semi-empirical model that requires experimentally determined discharge voltage and current waveforms, the working gas pressure, the target and its dimensions, and the dimensions of the ionization region as input. The IRM only covers the target and the ionization region, which is defined as an annular cylinder of width $w_{RT} = r_{c2} - r_{c1}$ positioned above the racetrack, and a length $L = z_2 - z_1$, extending from z_1 to z_2 axially away from the target.

The IRM, originally described by Raadu *et al.*[43] in 2011, has been under constant development ever since, and its main features

27 June 2024 10:24:25

© Author(s) 2024

are summarized by Huo *et al.*[31] In the IRM, the temporal development of the species densities and electron temperature is defined by a set of ordinary differential equations.[31,43] The electron density is found by applying the quasineutrality condition. The details of the IRM, including the reaction rates for the various surface and volume processes that are taken into account, are summarized by Huo *et al.*[31] More recent modifications concerning the treatment of the afterglow[44] and updated reaction rates[45] have been made, as well as a modification to the term that describes the kick-out by the sputtered species and contributes to working gas rarefaction as discussed by Barynova *et al.*.[38] This last modification is needed to analyze the contributions from electron impact ionization and kick-out to working gas rarefaction. The updated IRM is applied for this current study.

There are three free parameters or fitting parameters that are adjusted in the IRM: (i) the ion back-attraction probability for the metal ions $\beta_{\rm t,pulse}$ and gas ions $\beta_{\rm g,pulse}$; (ii) the potential drop across the IR, $V_{\rm IR}$; and (iii) the electron recapture probability r. In practice, $V_{\rm IR}$ is determined using the ratio $f = V_{\rm IR}/V_{\rm D}$, where $V_{\rm D}$ is the discharge voltage.[31] For the cases presented here, we assume $r = 0.7$, since it has been suggested by Buyle *et al.*,[46] based on a Monte Carlo model calculations, that the electron recapture probability is typically between 65% and 75% for a planar magnetron sputtering discharge. Note that for a metal target, the value of the electron recapture probability r does not influence the model results significantly. Furthermore, we assume $\beta_{\rm t,pulse} = \beta_{\rm g,pulse}$ as in previous studies.[31,36,43] It has been argued, based on the direct simulation Monte Carlo calculation, that this may be a rough approximation and that the back-attraction probability for the ions of the working gas is close to unity.[47] This will not have much influence on the overall findings reported in this current work.

We can lock the model and confine the two fitting parameters, using the experimentally measured discharge current waveform and the measured ionized flux fraction as discussed by Butler *et al.*.[48] The ionized flux fraction onto a given surface facing the discharge is related to the time-integrated total number of metal atoms and metal ions leaving the IR for the diffusion region (DR) during the discharge pulse through

$$F_{\rm flux} = \left(1 + \left(\frac{\xi_{\rm tn}}{\xi_{\rm ti}}\right)\frac{\int_T \tilde{\Gamma}_{\rm M}^{\rm DR}(t){\rm d}t}{\int_T \tilde{\Gamma}_{\rm M^+}^{\rm DR}(t){\rm d}t}\right)^{-1}, \qquad (1)$$

where $\tilde{\Gamma}_{\rm M}(t)$ is the total flux of metal neutrals and $\tilde{\Gamma}_{\rm M^+}(t)$ is the total flux of metal ions into the diffusion region, T is the pulse period, and the collection of metal neutrals and ions on the given surface is described through the ratio of the transport parameters $\xi_{\rm tn}/\xi_{\rm ti}$, where $\xi_{\rm ti}$ is the transport parameter for ions, and $\xi_{\rm tn}$ is the transport parameter for neutrals, of the sputtered species[49,50] (see, in particular, Fig. 1 of Rudolph *et al.*[34]). The transport parameter ratio has been determined experimentally for a HiPIMS discharge with a titanium target to be roughly $\xi_{\rm tn}/\xi_{\rm ti} \approx 1.25$ for a substrate located 3 cm from the target surface and $\xi_{\rm tn}/\xi_{\rm ti} \approx 2$ for a substrate located 7 cm from the target surface.[50] We use these values and assume a value of 2 for flux measurements made in the range 7–10 cm from the target surface and use a linear fit to determine values for 4 and 6 cm distance.

As discussed above, the model results include the back-attraction probability during the pulse from a potential drop across the IR, $V_{\rm IR}$. This potential barrier prevents some of the ions in the IR from reaching the substrate, lowering the deposition rate. This potential barrier is eliminated when the pulse is shut off. Therefore, we assume $\beta_{\rm t}$ to be zero in the afterglow and consequently the back-attraction probability is defined as[44]

$$\beta_{\rm t}(t) = \begin{cases} \beta_{\rm t,pulse} & \text{during the pulse,} \\ 0 & \text{in the afterglow.} \end{cases} \qquad (2)$$

After the pulse is switched off, the metal ions are assumed to have a velocity that is similar to that of the sputtered metal species.

1. Species considered and reactions involving zirconium

The discharge formed is composed of the argon working gas atoms and ions, the sputtered zirconium species and their ions, as well as electrons. The working gas species included in the model for the argon discharge are cold argon atoms in the ground state $\rm Ar^C$, metastable argon atoms [both $\rm Ar(4s[3/2]_2)$ and $\rm Ar(4s'[1/2]_0)$], $\rm Ar^+$ and $\rm Ar^{2+}$ ions, and warm $\rm Ar^W$ and hot $\rm Ar^H$ argon atoms. The latter two populations of argon atoms originate from argon ions that bombard the target and then return to the discharge as neutrals. The hot argon population represents reflected argon atoms at the target.[51,52] They are assumed to have an average energy of 2 eV as motivated by Raadu *et al.*[43] The warm population $\rm Ar^W$, which is assumed to have energy similar to the thermal energy of the surface, with about 0.1 eV (∼1000 K),[53] is due to argon ions that penetrate the target surface and then slowly diffuse back as atoms. The argon discharge, the reaction set, and rate coefficients can be found in recent publications.[32,36]

For the zirconium discharge, we include zirconium atoms in the ground state and the ions $\rm Zr^+$ and $\rm Zr^{2+}$. The sputtered zirconium atoms enter the IR with a velocity corresponding to the energy of $1/2 \times \mathcal{E}_{\rm cohesive} = 1/2 \times 6.25\,{\rm eV} = 3.125\,{\rm eV}$,[54] (p. 50), where $\mathcal{E}_{\rm cohesive}$ is the cohesive energy of the target material. We note here that the cohesive energy of zirconium is almost as high as that of graphite.[32] For a HiPIMS discharge using a graphite target, we have partially attributed the low ionized flux fraction to the high cohesive energy of graphite, resulting in a low residence time of the carbon atoms within the ionization region. Here, in the case of zirconium, the velocity with which the atoms leave the target remains moderate, as the mass of zirconium is high with $91 m_{\rm p}$, where $m_{\rm p}$ is the proton mass. Therefore, the probability of ionization of zirconium is expected to be higher than that of carbon. Consequently, we expected a substantial density of both zirconium atoms and ions in the discharge, in particular, late in the pulse.

Due to this composition of the discharge, we need to calculate and account for the collisional loss for each electron-ion pair created $\mathcal{E}_{\rm c}$ for zirconium in the electron energy balance. For this purpose, we use the electron impact ionization cross section calculated by Deutsch *et al.*[55] with an ionization potential of 6.63 V. Our calculations of the collisional energy loss also include the seven lowest excited levels of the atom listed in Table II. As the electron impact excitation cross sections for the zirconium atom

27 June 2024 10:24:25

© Author(s) 2024

are mostly unknown, we assume that each excitation cross section follows the Thomson cross section[56] (p. 71) with a peak at 1/5 of the peak of the ionization cross section. If the electron impact excitation cross sections are overestimated (underestimated), the collisional energy loss per electron-ion pair created from Zr atoms is overestimated (underestimated) slightly, and the Zr^+ ion density and the electron density are underestimated (overestimated). However, as we will see later that the Zr^+ ion is not the dominating ion in the discharge, so this assumption does not have much influence on the overall results. We assume the cross section for electron elastic scattering on Zr atoms to be the same as for tungsten.[57] For electron energies above 50 eV, the total electron elastic cross section agrees well with the elastic cross section for zirconium calculated using the NIST Electron Elastic-Scattering Cross-Section Database SRD 64.[58] To find an electron impact ionization cross section for Zr^+ to create the doubly ionized Zr^{2+}, we use the cross section for the first ionization of the zirconium atom from Deutsch *et al.*[55] and scale it down by a factor of 10 and shift the energy axis by the difference in ionization energy between Zr^+ and Zr^{2+}. The reactions and the rate coefficients for electron impact ionization of Zr and Zr^+ by both primary (cold) and secondary (hot) electrons are listed in Table III. The rate coefficients for electron impact collisions are calculated assuming a Maxwellian EEDF. The fits are valid in the range 1–7 eV for the cold electrons and in the range 200–1000 eV for the hot electrons.

The sputter yield for Ar^+ and Zr^+ ions bombarding a zirconium target was estimated using the TU Wien Sputter Yield Calculator,[59] which is based on the empirical equations for sputter yields at normal incidence developed by Matsunami *et al.*[60] The calculated sputter yields were fitted using a power-law equation

$$Y = a\mathcal{E}_i^b, \tag{3}$$

where a and b are the fitting parameters. Here, $a = 0.003538$ and $b = 0.7936$ for Ar^+ sputtering of zirconium and for self-sputtering of zirconium $a = 0.001896$ and $b = 0.9316$.

For the secondary electron emission yield due to bombardment of the target by argon ions, we use the fit given for clean metals by Phelps and Petrović.[61] For the zirconium ions bombarding the zirconium target, the secondary electron emission yield is essentially zero. Furthermore, we neglect secondary electron emission due to the bombardment of the target by Zr^{2+} ions.

III. RESULTS AND DISCUSSION

A. Experimental results

Figure 1 shows the measured ionized flux fraction vs the discharge current density at a working gas pressure of 0.5 and 1 Pa. We see that at 1 Pa the ionized flux fraction is in the range 25%–61% and increases with increased discharge current density in the range 0.5–2.0 A/cm^2. The ionized flux fraction was measured at 3 cm from the target surface, facing the race track, representing the edge of the ionization region,[6] and 10 cm from the target surface, representing a typical substrate distance. The ionized flux fraction was also measured at 4, 6, and 8 cm from the target surface for $J_{D,peak} = 1$ A/cm^2. All the measured ionized flux fraction values are listed in Table I and shown in Fig. 1. We see that the ionized flux fraction is slightly higher when measured at 3 cm from the target than when measured at 10 cm from the target surface. This can be understood from a larger ion sputter cone compared to the neutral sputter cone.[34,50] The lower pressure (0.5 Pa) delivers a slightly higher ionized flux fraction as shown by the open circles in Fig. 1. Furthermore, longer pulses (100 μs) also give higher ionized flux fraction, except at the lowest peak discharge current density (0.5 A/cm^2). This contradicts the recent findings of Shimizu *et al.*[63] that observed, while studying a HiPIMS discharge with titanium target, that there is an increase in the ionized flux fraction for decreasing pulse length for peak discharge current density $J_{D,peak} = 1.1$ A/cm^2 and that there is a small decrease in the ionized flux fraction with decreasing pulse length for low $J_{D,peak} = 0.37$ A/cm^2. In their study, the ionized flux fraction was measured to be in the range ∼20 to ∼40% and increased with increased peak discharge current density.

For comparison, measurements with a copper target find the ionized flux fraction to be in the range of 31%–62% at the substrate position (9 cm from the target) and increase with increased peak discharge current density in a discharge operated at 1 Pa for a 50 μs long pulse and $J_{D,peak}$ in the range 1–1.5 A/cm^2.[64] For aluminum and titanium targets, Lundin *et al.*[65] measured the ionized flux fraction to increase from about 20% to roughly 70% as the average discharge current density $J_{D,average}$ was varied from 0.5 to 2.0 A/cm^2, for working gas pressure of 0.5 and 2.0 Pa, and 100 μs long pulses 4 cm from the target surface. Lower working gas pressure resulted in a slightly higher ionized flux fraction, a trend that has also been observed for a discharge with a copper target,[64] as well as titanium and aluminum targets.[65] This latter effect is also seen for the zirconium target in Fig. 1.

The measured normalized deposition rate vs the peak discharge current density is shown in Fig. 2. The measured normalized deposition rate is the deposition rate for HiPIMS operation divided by the deposition rate determined from dc magnetron sputtering operated at the same average power. We see in Fig. 2 that the measured normalized deposition rate decreases with increased peak discharge current density. This is commonly observed in HiPIMS operations. For a given pulse length and average power, the deposition rate decreases as the peak discharge current density increases.[36,63,65,66] The normalized deposition rate for a given discharge current density is higher when measured 10 cm from the target surface than when measured at 3 cm. It can also be seen in Fig. 2 that the normalized deposition rate is slightly lower for the lower working gas pressure (0.5 Pa) (open circles). The normalized deposition rate is also slightly higher for the longer pulse length (100 μs). This again contradicts the findings of Shimizu *et al.*[63] for a HiPIMS discharge with a titanium target as they observed a decrease in the normalized deposition rate as the pulse length was increased from 50 μs at $J_{D,peak} = 1.1$ A/cm^2. In general, for a fixed peak discharge current density, they found that the deposition rate increases with decreasing pulse length and reaches a maximum at around 25–50 μs, a trend that had been predicted earlier using the IRM.[44] They also found that further shortening the pulse length decreases the deposition rate.[63]

Overall, we observe that the ionized flux fraction increases (Fig. 1) and the normalized deposition rate decreases (Fig. 2) as the peak discharge current density is increased. This is a manifestation

27 June 2024 10:24:25

© Author(s) 2024

TABLE I. Discharge parameters, the measured ionized flux fraction F_{flux}, and the measured deposition rate normalized to the deposition rate in a dcMS, operated at the same power and pressure, F_{dep}, at the axial position z_{QCM}, and the internal discharge parameters ionization probability α_t, the back-attraction probability β_t and the peak in the degree of working gas rarefaction derived from the modeling of HiPIMS discharges with zirconium target for 0.5 and 1 Pa pressure.

t_{pulse} (μs)	Pressure (Pa)	$J_{D,\ peak}$ (A/cm^2)	V_D (V)	z_{QCM} (cm)	α_t (%)	$\beta_{t,\ pulse}$ (%)	β_t (%)	F_{flux} (%)	F_{dep} (%)	$1 - n_{Ar}/n_{Ar,\ 0}$ (%)
50	1	1	550	10	86	73	71	45	23	72
100	1	1	549	10	85	68	67	48	27	78
100	1	0.5	485	10	73	76	75	25	43	49
50	1	0.5	485	10	75	73	71	31	39	50
50	1	2	575	10	91	79	76	59	13	80
50	0.5	1	488	10	88	70	68	54	21	85
50	1	1	548	10	88	78	76	46	23	72
50	1	1	538	10	85	76	74	43	22	67
50	1	1	535	8	85	74	72	46	—[a]	68
50	1	1	534	6	86	70	68	53	—[a]	74
50	1	1	529	4	86	75	73	54	—[a]	69
50	1	1	529	3	85	78	75	52	21	65
100	1	1	536	3	84	73	72	53	23	71
50	1	0.5	467	3	73	80	77	34	36	45
100	1	0.5	488	3	75	75	74	38	36	52
50	1	1	488	3	86	73	71	58	23	70
50	0.5	1	488	3	88	75	72	61	16	81

[a]No dcMS reference measurements were made.

of the HiPIMS compromise, which states that the increased ionized flux fraction comes at the cost of a lower deposition rate.[67]

B. Modeling results

As discussed in Sec. II B, the IRM is a semi-empirical model and has three unknown fitting parameters: the ion back-attraction probability, the potential drop across the IR, and the electron recapture probability. The last parameter is given a fixed value as discussed above. This leaves the ($\beta_{t,pulse}$, $f = V_{IR}/V_D$) parameter space as the one to be explored through a model fitting procedure, where we find the best fit to the experimentally determined discharge current waveform. The best fit is determined using a fitting map showing the fraction of the discharge voltage that drops across the ionization region f, vs the back-attraction probability of an ion of the sputtered species $\beta_{t,pulse}$ during the pulse. The fitting procedure is shown in Fig. 3 for one particular discharge with a zirconium target for a 50 μs long pulse with peak discharge current density $J_{D,peak} = 1$ A/cm^2, and working gas pressure of 1 Pa, and the ionized flux fraction used to lock the model was measured 10 cm from the target surface (the discharge parameters listed in the first line of Table I). The parameters that define the size of the IR were set as follows: $r_{c1} = 6$ mm, $r_{c2} = 19$ mm, $z_1 = 2$ mm, and $z_2 = 13$ mm. The figure of merit (FOM), shown in Fig. 3, is calculated as the weighted sum of square residuals normalized by the weighted total sum of squares (see Gudmundsson *et al.*[35]). The regions on the fitting map where the modeled discharge current matches the experimental discharge current the best is shown as a yellow zone. This yellow zone indicates the combination of $f = V_{IR}/V_D$ and $\beta_{t,pulse}$ where the weighted square deviation of the discharge current is the smallest. The ionized flux fraction is shown as black contour lines. As this yellow zone is large, an additional constraint from an experimentally determined quantity is necessary. This is done by using the measured ionized flux fraction to lock the model as suggested by Butler *et al.*[48] [see Eq. (1)]. We use the ionized flux fraction measured (45%) at 10 cm from the target surface over the racetrack to lock the model. The measured discharge current waveform and the measured discharge voltage waveform are shown by solid lines in Fig. 4. The resulting best fit determined by the IRM for the discharge current waveform and the measured ionized flux fraction is shown with a dashed line in Fig. 4. The modeled discharge current matches the experimental discharge current very well.

TABLE II. Lowest few excited states of the zirconium atom that are used to calculate the collisional loss per electron-ion pair created.

Configuration	Term	Threshold (eV)
$4d^2 5s^2$	a ^{3}F	0–0.15
$4d^2 5s^2$	a ^{3}P	0.52–0.54
$4d^3(^4F)5s$	a ^{5}F	0.60–0.73
$4d^2 5s^2$	a ^{1}D	0.63
$4d^2 5s^2$	a ^{1}G	1.00
$4d^3(^4F)5s$	a ^{1}G	1.44–1.53
$4d^3(^3G)5s$	a ^{1}G	1.55–1.58

The temporal evolution of the species densities calculated by the IRM for the discharge fitted in Fig. 3 is shown in Fig. 5, the neutral species densities in Fig. 5(a) and the ions in Fig. 5(b). As to be expected, the ground state working gas argon atoms dominate the discharge. The cold argon ground state density [denoted $Ar^C(3p^6)$ in Fig. 5(a)] decreases steadily to a minimum and then

27 June 2024 10:24:25

© Author(s) 2024

TABLE III. Reactions and rate coefficients used in the IRM involving zirconium determined for both hot and cold electrons. The rate coefficients are calculated assuming a Maxwellian electron energy distribution function and fit in the range $T_e = 1 - 7$ eV for cold electrons and 200–1000 eV for hot electrons.

	Reaction	Threshold (eV)	Rate coefficient (m^3/s)	Electron group	Reference
(R1)	e + Zr → Zr$^+$ + e	6.63	$1.69 \times 10^{-13} T_e^{0.171} \exp(-7.825/T_e)$	Cold	55
			$3.04 \times 10^{-13} - 2.18 \times 10^{-16} \times T_e$	Hot	
(R2)	e + Zr$^+$ → Zr^{2+} + e	13.13	$3.06 \times 10^{-14} T_e^{0.042} \exp(-14.39/T_e)$	Cold	
			$3.09 \times 10^{-14} - 2.21 \times 10^{-17} \times T_e$	Hot	
(R3)	Ar$^+$ + Zr → Ar + Zr$^+$		2×10^{-16}		62
(R4)	Ar(4s'[1/2]$_0$) + Zr → Ar + Zr$^+$ + e		5.3×10^{-15}		
(R5)	Ar(4s[3/2]$_2$) + Zr → Ar + Zr$^+$ + e		5.3×10^{-15}		

rises slightly to the end of the pulse. The minimum in Ar^C density appears close to the maximum in the discharge current. We see that there is an increase in the density of both the hot (Ar^H) and warm (Ar^W) argon atoms, during the pulse, followed by a decay in the afterglow. Furthermore, the warm argon atom density approaches the cold argon density during its minimum. We also see in Fig. 5(a) that the zirconium atom density increases rapidly early in the pulse and then decays slowly to the end of the pulse, when the sputtering by energetic ion bombardment comes to an end. In the afterglow, the density of the ground state zirconium atoms decreases sharply at first and then slower. As seen in Fig. 5(a) toward the end of the pulse the working gas is rarefied, and the zirconium atoms pass through at high speed, while after the pulse is off there is back diffusion of argon that shortens the mean free path of the zirconium atoms and slows them down which appears as a slower decay of the zirconium atom density. Recall that the zirconium atoms enter the IR with a velocity that is directed away from the target surface and this dictates the decay rate in the afterglow. We note that the hot argon atoms, which also have a directed velocity away from the target surface, have a similar decay rate, while warm argon atoms that have lower velocity decay slower in the afterglow. The temporal behavior of the densities of the metastable argon atoms show an increase in the beginning of the pulse a drop and a peak at the end of the pulse and then a much slower decay in the afterglow, but the densities are much lower. As mentioned, the temporal evolution of the neutral argon density in Fig. 5(a) shows a significant drop toward the end of the pulse. This is what is referred to as working gas rarefaction. Working gas rarefaction is known to occur in magnetron sputtering discharges[68,69] and has been observed experimentally in HiPIMS operation.[70–72] Note that the total neutral argon density within the IR is the sum of the cold, warm, and hot argon atoms in the ground state, and the two metastable states. Hence, working gas rarefaction is not only the drop in the cold argon atom density shown in Fig. 5(a), it is the drop in the total neutral argon density. The calculated values for the degree of working gas rarefaction, including all the neutral argon atom populations, are listed in Table I for all the cases explored.

27 June 2024 10:24:25

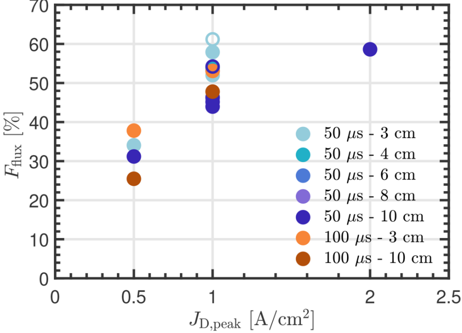

FIG. 1. Measured ionized flux fraction vs the peak discharge current density. The working gas pressure was 0.5 Pa (open circles) and 1 Pa (solid dots), and the pulse length was 50 and 100 μs and the ionized flux fraction was measured 3, 4, 6, 8, and 10 cm from the target surface.

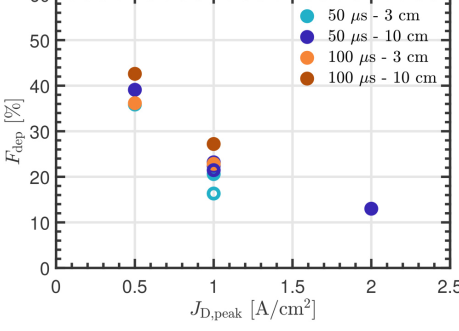

FIG. 2. Measured normalized deposition rate vs the peak discharge current density. The working gas pressure was 0.5 Pa (open circles) and 1 Pa (solid dots) and the pulse length was 50 and 100 μs, measured 3 and 10 cm from the target surface.

© Author(s) 2024

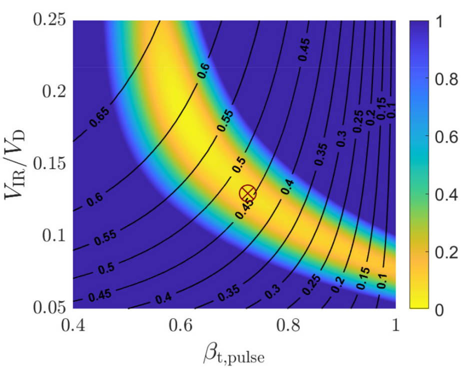

FIG. 3. FOM and the ionized flux fraction F_{flux}, displayed as a color map and contour lines, respectively, for a grid scan over $\beta_{t,pulse}$ and $f = V_{IR}/V_D$ for a zirconium target, a 50 μs long pulse, peak discharge current density $J_{D,peak} = 1$ A/cm^2, working gas pressure of 1 Pa, and the ionized flux fraction used to lock the model was measured 10 cm from the target surface. The parameter combination giving the best fit while meeting the F_{flux} constraint is highlighted with a red × inside a circle.

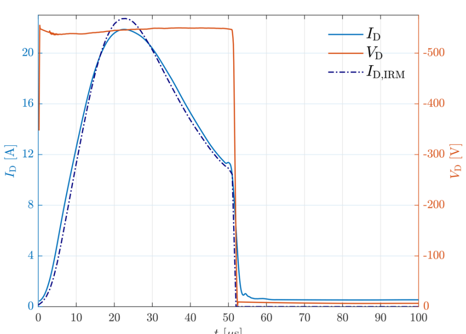

FIG. 4. Measured temporal evolution of the cathode voltage (solid red line and the right y-axis) and the discharge current (solid blue line and the left y-axis) as well as the model fit (purple dash dot line and the left y-axis) for the discharge current with a zirconium target, a 50 μs long pulse, a peak discharge current density $J_{D,peak} = 1$ A/cm^2, working gas pressure of 1 Pa, and the ionized flux fraction used to lock the model was measured 10 cm from the target surface.

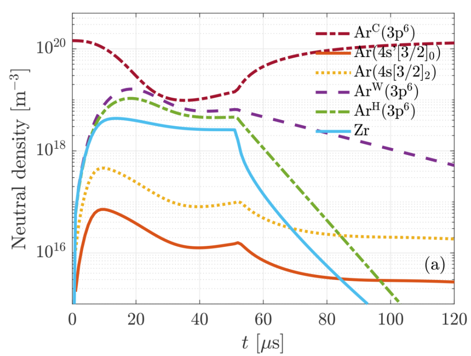

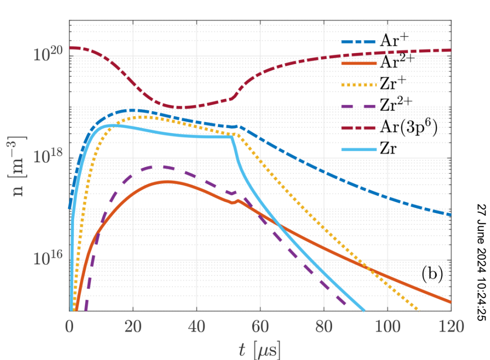

FIG. 5. Temporal evolution of the (a) neutral particle densities and (b) the ion densities for a zirconium target, a 50 μs long pulse, with peak discharge current density $J_{D,peak} = 1$ A/cm^2, working gas pressure of 1 Pa, and the ionized flux fraction used to lock the model was measured 10 cm from the target surface.

The degree of working gas rarefaction is defined as

$$\text{degree of working gas rarefaction} = 1 - \frac{n_{Ar}(t)}{n_{Ar,0}}, \quad (4)$$

where $n_{Ar,0}$ is the total argon density at the start of the pulse and $n_{Ar}(t)$ is the temporal variation of the total argon density. The peak in the degree of working gas rarefaction at $p_g = 1$ Pa and $J_{D,peak} = 1$ A/cm^2 for a 50 μs long pulse is roughly 70%, and at $J_{D,peak} = 2$ A/cm^2, it is roughly 80%. At 0.5 Pa, the peak in the degree of working gas rarefaction for $J_{D,peak} = 1$ A/cm^2 is 81%–85%. Lower working gas pressure and high peak discharge current density leads to a higher degree of working gas rarefaction. Keep in mind that the value of the degree of working gas

27 June 2024 10:24:25

© Author(s) 2024

rarefaction depends on the volume size of the IR, so the values given are estimates.

In a separate study, we have applied the ionization region model to determine the various contributions to working gas rarefaction in HiPIMS discharges with several different cathode targets.[38] This study revealed that working gas rarefaction is driven by electron impact ionization by both primary (or cold) and hot electrons as well as by kick-out by fast neutrals coming from the target. The fast neutral species coming from the target can be either the sputtered target species or hot argon atoms. Charge exchange was found to have a negligible contribution to working gas rarefaction for all the target materials. The role of kick-out increases and the role of electron impact ionization decreases with increased sputter yield of the target material. When comparing the various contributions to working gas rarefaction for different target materials, we observed that the sputter yield is the determining factor regarding which process contributes the most to working gas rarefaction in HiPIMS operation.[38]

For the zirconium target, the contributions of the various processes to working gas rarefaction in a HiPIMS discharge vs the peak discharge current density are shown in Fig. 6. When comparing the relative contributions of each of the processes to working gas rarefaction, they are all determined by integrating the contribution of each term throughout the entire pulse and the afterglow. We see that ionization by cold primary electrons is the dominating process at all discharge current densities with a contribution in the range of 63%–65%, while ionization by secondary electrons has 14%–19% contribution, the contribution of kick-out by Zr atoms decreases from 16% to 12% and the contribution of hot argon atoms decreases from 7% to 4%, with increasing peak discharge current density in the range 0.5–2.0 A/cm^2. In this case, the location of the ionized flux fraction measurement used to lock the model was 10 cm from the target surface. We see that the peak discharge current density does not have much influence on the relative contribution of the various terms. Zirconium has a rather low sputter yield and, therefore, electron impact ionization is expected to be the most important process.[38] This confirms our expectation that the sputter yield is the primary factor in determining the dominating mechanism for argon gas rarefaction among the kick-out mechanism and the ionization by the cold and hot electron population.

The temporal evolution of the charged particle densities is shown in Fig. 5(b). The Ar^+ ion is always the dominating ion and the Zr^+ ion has always a smaller density. The densities of the doubly charged Zr^{2+} and Ar^{2+} ions are always more than an order of magnitude smaller than the density of the singly charged ions. The temporal evolution of the cold argon atoms and zirconium atoms is also shown in Fig. 5(b) to ease comparison. For most of the pulse duration, the density of Ar^+ and Zr^+ ions surpasses the density of zirconium atoms.

The temporal evolution of the discharge current composition at the target surface is shown in Fig. 7. We see that roughly 2/3 of the discharge current is carried by Ar^+ ions while only 1/3 is carried by Zr^+ ions. The contributions from Ar^{2+} and Zr^{2+} ions and secondary electron emission are smaller. The current composition is explored further in Fig. 8 where the current composition is shown for three peak discharge current densities. We see that the fractional contribution of Zr^+ and Zr^{2+} ions increases, and the

27 June 2024 10:24:25

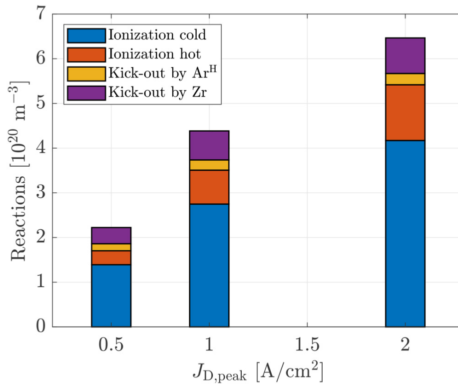

FIG. 6. Contribution of the various processes to working gas rarefaction within the ionization region for a discharge with 2 in. zirconium target vs the peak discharge current density for argon working gas pressure of 1 Pa and pulse length of 50 μs, and the ionized flux fraction used to lock the model was measured 10 cm from the target surface. Ionization cold and hot refers to electron impact ionization of argon atoms by the cold and hot electron populations, respectively.

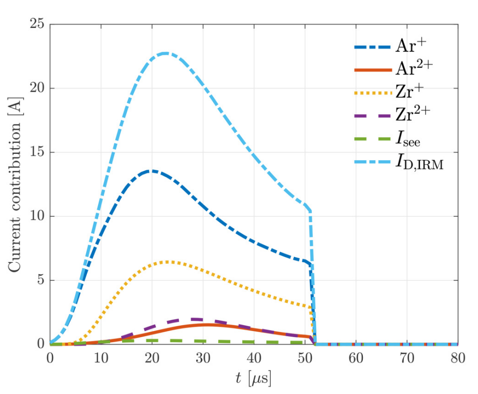

FIG. 7. Temporal evolution of the discharge current composition at the target surface for a zirconium target, for a 50 μs long pulse, with peak discharge current density $J_{D,peak} = 1$ A/cm^2, working gas pressure of 1 Pa, and the ionized flux fraction used to lock the model was measured 10 cm from the target surface.

© Author(s) 2024

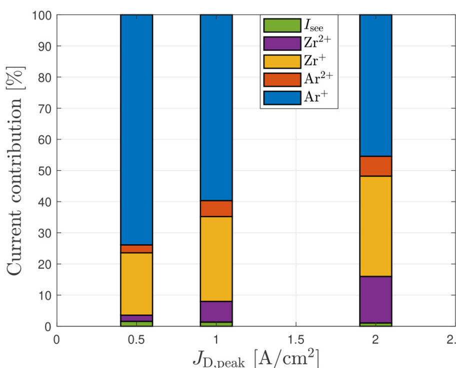

FIG. 8. Discharge current composition within the ionization region vs the peak discharge current density for a discharge with 2 in. zirconium target for argon working gas pressure of 1 Pa and pulse length of 50 μs, and the ionized flux fraction used to lock the model was measured 10 cm from the target surface.

fractional contribution of Ar^+ ions decreases, with increased peak discharge current density. At $J_{D,peak} = 0.5$ A/cm^2, the Ar^+ ion contribution is roughly 74%, at 1.0 A/cm^2 it is about 60%, and roughly 45% at $J_{D,peak} = 2$ A/cm^2. The Zr^+ ion contribution is 20%, 27%, and 32%, and the Zr^{2+} contribution increases from 2% to 6.6%, to about 15%, as the peak discharge current density is increased. The contribution of secondary electron current is always much smaller than the current carried by each of the ions. There is an upper limit on the current density that corresponds to where all the incoming argon atoms from the surrounding gas reservoir are ionized and drawn to the target. This upper limit defines the critical current density of $J_{crit} \approx 0.2$ A/cm^2 at 1 Pa and $T_g = 300$ K.[73,74] For all the cases discussed here, the discharge operates well above this limit and ion recycling has to take place to reach the high discharge current densities observed. As both argon and zirconium ions contribute significantly to the discharge current at the target surface, the discharge operates on a combination of working gas recycling and self-sputter recycling.[74]

The IRM calculations provide, in addition to the temporal variation of the species densities, various other information and discharge parameters. This includes the internal discharge parameters such as the ionization probability α_t, the back-attraction probability β_t, and the voltage drop across the IR. Earlier, we applied the IRM to study a HiPIMS discharge with 75 mm diameter tungsten target as the discharge voltage was varied.[36] There, the peak discharge current density $J_{D,peak}$ increases in the range 0.33–0.73 A/cm^2, with increased discharge voltage in the range 500–800 V. For the sputtered tungsten atoms, the ionization probability was found to increase with increased peak discharge current density and be in the range 54%–75%. For a titanium target, the ionization probability was found to increase from 45% to 84% as the peak discharge current density was varied from 0.15 to 1 A/cm^2.[11,34]

Another important internal discharge parameter is the back-attraction probability for the sputtered species after they have been ionized within the IR. The back-attraction probability β_i for an ion species i relates the ion fluxes out of the IR toward the diffusion region and the flux toward the racetrack during the pulse. The ion flux out of the IR toward the diffusion region is calculated from the flux toward the racetrack during the pulse,[31,75]

$$\int_T \tilde{\Gamma}_i^{DR}(t)\mathrm{d}t = \left(\frac{1}{\beta_i} - 1\right)\frac{S_{RT}}{S_{DR}}\int_T \tilde{\Gamma}_i^{RT}(t)\mathrm{d}t, \qquad (5)$$

where $\int_T \tilde{\Gamma}_i^{RT}(t)\mathrm{d}t$ is the ion flux toward the racetrack which has a surface area of S_{RT} and T is the pulse period, $\int_T \tilde{\Gamma}_i^{DR}(t)\mathrm{d}t$ is the ion flux toward the diffusion region, and S_{DR} is the surface area of the ionization region facing the diffusion region. Here, i denotes the ion, which can be Ar^+, Zr^+, Ar^{2+}, or Zr^{2+}. A significant fraction of the ion flux onto the racetrack is made up of ionized zirconium as can be seen in Figs. 7 and 8. These are zirconium atoms that were sputtered off the target and ionized within the IR and then return to the target. For the target material, we write t as a subscript. Figure 9(b) shows the target metal ion back-attraction probability β_t vs the peak discharge current density for a HiPIMS discharge with a zirconium target. The back-attraction probability during the pulse is found to be in the range $\beta_{t,pulse} \approx 68\%–80\%$. The overall back-attraction probability β_t is somewhat lower or in the range 67%–77%. There is clearly some uncertainty or scatter in the calculated back-attraction probability values. This uncertainty is at least partially due to the uncertainty in the values of the transport parameters, used in Eq. (1) to determine the flux of ions and neutrals, to lock the model. Recall that we used values that were determined experimentally for a discharge with titanium target over a limited range.[50] The back-attraction probability β_t for zirconium is higher than for copper, which was found to be in the range 44%–50%,[35] but lower than for titanium target which was determined to be 83%–87%.[34] For the sputtered tungsten, the back-attraction probability β_t decreases from 87% to 67% with increasing discharge voltage or increasing discharge current density.[36]

Figure 10 shows the fractional potential drop over the IR $f = V_{IR}/V_D$ vs the peak discharge current density. The fractional potential drop is in the range 10%–16% of the applied discharge voltage. The fractional potential drop is slightly lower at 0.5 Pa than at 1 Pa and appears to decrease slightly as the peak current density is increased. The fractional potential drop reported here for a discharge with zirconium target is higher than what was determined for a discharge with tungsten target which was in the range 6%–8%, decreasing with increasing peak discharge current density.[36] For a copper target, the fractional potential drop was found to lie in the range 14%–17%,[4] and for a graphite target it was found to be 14%,[32] for a working gas pressure of $p_g \sim 1$ Pa and $J_{D,peak} \sim 1$ A/cm^2.

Figure 2 shows how the measured normalized deposition rate decreases as the peak discharge current is increased. Earlier we have defined the sputter-rate-normalized deposition rate, which is

27 June 2024 10:24:25

© Author(s) 2024

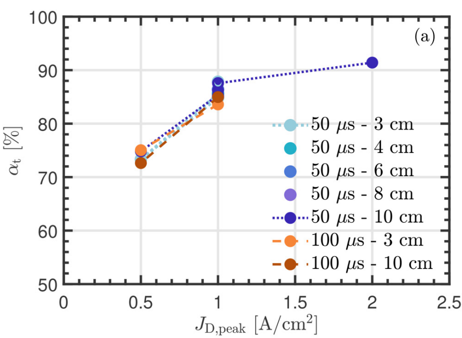

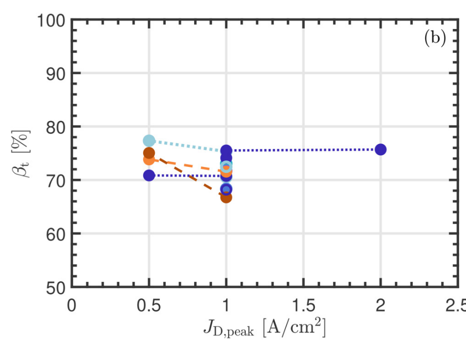

FIG. 9. (a) Ionization probability α_t and (b) the back-attraction probability β_t vs the peak discharge current density determined by the IRM for a discharge with a 2 in. zirconium target for argon working gas pressure of 0.5 Pa (open circles) and 1 Pa (solid dots) and pulse length of 50 and 100 μs and the ionized flux fraction measured 3, 4, 6, 8, and 10 cm from the target surface was used to lock the model.

given by[34]

$$F_{sput} = (1-\alpha_t) + \left(\frac{\xi_{ti}}{\xi_{tn}}\right)\alpha_t(1-\beta_t), \tag{6}$$

where ξ_{ti} is the transport parameter for ions and ξ_{tn} is the transport parameter for neutrals of the sputtered species.[49,50] Equation (6) can be approximated to become

$$F_{sput} = 1 - \alpha_t\beta_t = \frac{\Gamma^{DR}}{\Gamma_0}, \tag{7}$$

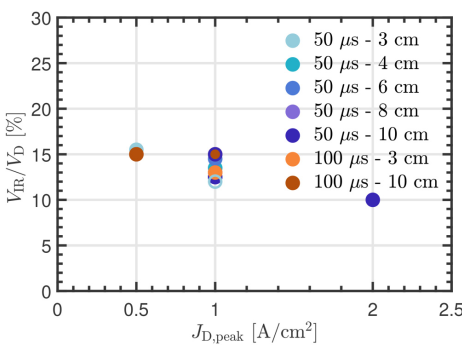

FIG. 10. Fractional potential drop over the IR $f = V_{IR}/V_D$ vs the peak discharge current density. The working gas pressure was 0.5 Pa (open circles) and 1 Pa (solid dots), the pulse length was 50 and 100 μs, and the ionized flux fraction measured 3, 4, 6, 8, and 10 cm from the target surface was used to lock the model.

for the special case when $\xi_{ti} = \xi_{tn}$.[76,77] This is the ratio of the flux of sputtered species (ions and neutrals) out of the IR toward the DR Γ^{DR} and the total flux of atoms sputtered from the target Γ_0 (atoms/s). Keep in mind that Eq. (7) does therefore not take into account ion focusing (or spreading) *en route* toward the substrate.[34,48,50] This equation states that the sputter-rate-normalized deposition rate is reduced as the ionization of the sputtered material increases.[67]

The relative ion-to-neutral transport factors ξ_{ti}/ξ_{tn} in Eq. (6) describe the relative deposited fractions of target material ions and neutrals onto a substrate. Experimentally, these parameters have been determined for HiPIMS of a titanium target to be roughly $\xi_{ti}/\xi_{tn} \approx 0.8$ for a substrate located 3 cm from the target surface and $\xi_{ti}/\xi_{tn} \approx 0.5$ for a substrate located 7 cm from the target surface.[50] A value of $\xi_{ti}/\xi_{tn} < 1$ indicates a larger spread of metal ions compared to metal neutrals, which is explained by larger scattering cross sections of ions compared to neutrals and by ions being subjected to electric fields.[34] The sputter rate-normalized deposition rate calculated using Eq. (6), using the measured relative ion-to-neutral transport factors for titanium,[50] shows roughly the same behavior as the experimentally determined normalized deposition rate but there is a slight difference in the value. This can be seen in Fig. 11 where the sputter rate-normalized deposition rate F_{sput} vs the measured normalized deposition rate F_{dep} is shown. We see that when the normalized deposition rate and the ionized flux fraction are measured 10 cm from the target surface are used to lock the model the values fall approximately on a line with slope 1 that goes through the origin, while when the flux parameters measured at 3 cm are used to lock the model F_{sput} is slightly higher than the measured F_{dep}. When the flux parameters measured at 10 cm are used to lock the model, we find the average value of the ratio F_{dep}/F_{sput} to be 0.93 with a standard deviation of 0.17, while

27 June 2024 10:24:25

© Author(s) 2024

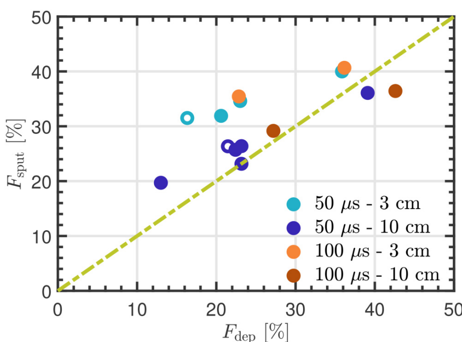

FIG. 11. Sputter-rate-normalized deposition rate $F_{\rm sput}$ calculated using Eq. (6) vs the measured normalized deposition rate $F_{\rm dep}$ for a discharge with a 2 in. zirconium target for argon working gas pressure of 0.5 Pa (open circles) and 1 Pa (solid dots) and pulse lengths of 50 and 100 μs. The dashed line has a slope of 1.

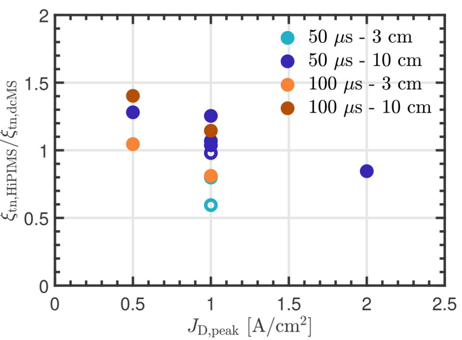

FIG. 12. Ratio of the neutral transport parameters in a HiPIMS discharge to dcMS discharge $\xi_{\rm tn,HiPIMS}/\xi_{\rm tn,dcMS}$ vs the peak discharge current density determined by the IRM for a discharge with a 2 in. zirconium target for argon working gas pressure of 0.5 Pa (open circles) and 1 Pa (solid dots) and pulse lengths of 50 and 100 μs.

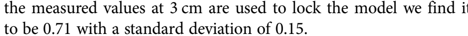

the measured values at 3 cm are used to lock the model we find it to be 0.71 with a standard deviation of 0.15.

The sputter rate-normalized deposition rate $F_{\rm sput}$ and the experimentally determined normalized deposition rate $F_{\rm dep}$ are related through the relative differences in the sputter rate $\Gamma_{\rm sput,HiPIMS}/\Gamma_{\rm sput,dcMS}$ and the neutral transport parameter ratio between HiPIMS and the corresponding (same pressure and average power) dcMS discharge $\xi_{\rm tn,HiPIMS}/\xi_{\rm tn,dcMS}$ needs to be taken into account as well or

$$F_{\rm dep} = \frac{\Gamma_{\rm sput,HiPIMS}}{\Gamma_{\rm sput,\,dcMS}}\frac{\xi_{\rm tn,HiPIMS}}{\xi_{\rm tn,dcMS}}F_{\rm sput}, \tag{8}$$

where[34,64,77]

$$\frac{\Gamma_{\rm sput,HiPIMS}}{\Gamma_{\rm sput,\,dcMS}} = \frac{V_{\rm D,dcMS}}{V_{\rm D,HiPIMS}} \times \frac{\sum_i \zeta_i Y_i(z_i V_{\rm D,HiPIMS})}{Y_{\rm Ar^+\to Zr}(V_{\rm D,dcMS})}, \tag{9}$$

and $V_{\rm D,HiPIMS}$ and $V_{\rm D,dcMS}$ are the discharge voltages for the corresponding HiPIMS and dcMS discharges, respectively. The sum is taken over all the ions $\rm Ar^+$, $\rm Zr^+$, $\rm Zr^{2+}$, and $\rm Ar^{2+}$, which have sputter yields Y_i, and ζ_i is the fraction of the ion current at the target surface that is carried by a particular ion i and z_i is the charge state of that ion. The parameter $\sum_i \zeta_i Y_i(z_i V_{\rm D,HiPIMS})/Y_{\rm Ar^+\to Zr}(V_{\rm D,dcMS})$ in Eq. (9) is fairly constant and does not vary much with the varying ion fractions and pulse voltage. The average value is 1.67 with a standard deviation of 0.07. Due to a higher voltage, the average sputter during the pulse higher in HiPIMS than in dcMS. As mentioned, Eq. (8) relates the measured normalized deposition rate $F_{\rm dep}$ and the sputter rate-normalized deposition rate $F_{\rm sput}$. This information can be used to estimate the unknown neutral transport parameter ratio.[34]

The ratios of the neutral transport parameters in a HiPIMS discharge to dcMS discharge $\xi_{\rm tn,HiPIMS}/\xi_{\rm tn,dcMS}$, estimated from the measured $F_{\rm sput}$, and the calculated $F_{\rm sput}$, are shown vs the peak discharge current density, for argon working gas pressure of 0.5 and 1 Pa and pulse lengths of 50 and 100 μs, in Fig. 12. It can be seen that the ratio $\xi_{\rm tn,HiPIMS}/\xi_{\rm tn,dcMS}$ decreases slightly with increased peak discharge current density for a given pulse length and distance from the target surface. We see that the ratio $\xi_{\rm tn,HiPIMS}/\xi_{\rm tn,dcMS}$ is slightly higher if the flux parameters measured at 10 cm from the target surface are used to lock the model, compared to when they are measured 3 cm from the target surface. The ratios are smaller if we assume $\xi_{\rm ti} = \xi_{\rm tn}$ and use Eq. (7) to calculate the sputter-rate normalized deposition rate $F_{\rm sput}$ (not shown). Earlier we estimated the ratio $\xi_{\rm tn,HiPIMS}/\xi_{\rm tn,dcMS}$ to be roughly 1.9 for discharges with titanium target and justified this value by a simple estimate involving the difference in argon gas temperature in HiPIMS and dcMS operation that influences the mean free path of the sputtered Ti neutrals.[34] Note also that working gas rarefaction due to ionization losses in the HiPIMS process will add to this factor.

27 June 2024 10:24:25

IV. SUMMARY

We have explored experimentally the effect of the peak discharge current density on the ionized flux fraction and normalized deposition rate in a HiPIMS discharge with a zirconium target. The ionized flux fraction increases and the normalized deposition rate decreases as the peak discharge current density increases, in accordance with the HiPIMS compromise. The measured discharge current and voltage waveforms were fed into the IRM to determine the temporal evolution of the plasma parameters and the internal discharge properties, the ionization and back-attraction probabilities. At a working gas pressure of 1 Pa, the ionization probability

© Author(s) 2024

was found to be in the range 73%–91% and the overall back-attraction probability to be in the range 67%–77% for a peak discharge current density in the range 0.5–2.0 A/cm^2. We explored the processes contributing to working gas rarefaction and found electron impact ionization to be the main contributor to working gas rarefaction, with over 80% contribution, while kick-out by zirconium atoms and argon atoms has a smaller contribution.

ACKNOWLEDGMENTS

This work was partially supported by the Icelandic Research Fund under Grant Nos. 196141 and 217999, the University of Iceland Research Fund under Grant No. 93940, the University of Iceland Research Fund for Doctoral Students, and the Swedish Government Strategic Research Area in Materials Science on Functional Materials at Linköping University (Faculty Grant SFO-Mat-LiU No. 2009-00971).

AUTHOR DECLARATIONS

Conflict of Interest

The authors have no conflicts to disclose.

Author Contributions

Swetha Suresh Babu: Data curation (equal); Formal analysis (equal); Investigation (equal); Methodology (equal); Software (equal); Validation (equal); Visualization (equal); Writing – review & editing (equal). **Joel Fischer:** Conceptualization (equal); Data curation (equal); Formal analysis (equal); Investigation (equal); Methodology (equal); Resources (equal); Writing – review & editing (equal). **Kateryna Barynova:** Data curation (equal); Formal analysis (equal); Investigation (equal); Methodology (equal); Software (equal); Writing – review & editing (equal). **Martin Rudolph:** Formal analysis (equal); Investigation (equal); Methodology (equal); Software (equal); Validation (equal); Writing – original draft (equal); Writing – review & editing (equal). **Daniel Lundin:** Conceptualization (equal); Funding acquisition (equal); Methodology (equal); Project administration (equal); Resources (equal); Supervision (equal); Validation (equal); Writing – review & editing (equal). **Jon Tomas Gudmundsson:** Conceptualization (equal); Data curation (equal); Formal analysis (equal); Funding acquisition (equal); Investigation (equal); Methodology (equal); Project administration (equal); Supervision (equal); Writing – original draft (equal); Writing – review & editing (equal).

DATA AVAILABILITY

The data that support the findings of this study are available within the article.

REFERENCES

[1] J. T. Gudmundsson, Plasma Sources Sci. Technol. **29**, 113001 (2020).
[2] R. K. Waits, J. Vac. Sci. Technol. **15**, 179 (1978).
[3] P. J. Kelly and R. D. Arnell, Vacuum **56**, 159 (2000).
[4] J. T. Gudmundsson, A. Anders, and A. von Keudell, Plasma Sources Sci. Technol. **31**, 083001 (2022).
[5] D. Krüger, K. Köhn, S. Gallian, and R. P. Brinkmann, Phys. Plasmas **25**, 061207 (2018).
[6] V. G. Antunes, M. Rudolph, A. Kapran, H. Hajihoseini, M. A. Raadu, N. Brenning, J. T. Gudmundsson, D. Lundin, and T. Minea, Plasma Sources Sci. Technol. **32**, 075016 (2023).
[7] J. T. Gudmundsson, N. Brenning, D. Lundin, and U. Helmersson, J. Vac. Sci. Technol. A **30**, 030801 (2012).
[8] A. Hecimovic, J. Held, V. Schulz-von der Gathen, W. Breilmann, C. Maszl, and A. von Keudell, J. Phys. D: Appl. Phys. **50**, 505204 (2017).
[9] F. Lockwood Estrin, S. K. Karkari, and J. W. Bradley, J. Phys. D: Appl. Phys. **50**, 295201 (2017).
[10] *High Power Impulse Magnetron Sputtering: Fundamentals, Technologies, Challenges and Applications*, edited by D. Lundin, T. Minea, and J. T. Gudmundsson (Elsevier, Amsterdam, 2020).
[11] M. Rudolph, N. Brenning, H. Hajihoseini, M. A. Raadu, T. M. Minea, A. Anders, D. Lundin, and J. T. Gudmundsson, J. Phys. D: Appl. Phys. **55**, 015202 (2022).
[12] M. Rudolph, N. Brenning, H. Hajihoseini, M. A. Raadu, J. Fischer, J. T. Gudmundsson, and D. Lundin, J. Vac. Sci. Technol. A **40**, 043005 (2022).
[13] U. Helmersson, M. Lattemann, J. Bohlmark, A. P. Ehiasarian, and J. T. Gudmundsson, Thin Solid Films **513**, 1 (2006).
[14] G. Greczynski, I. Petrov, J. E. Greene, and L. Hultman, J. Vac. Sci. Technol. A **37**, 060801 (2019).
[15] Z. Hubička, J. T. Gudmundsson, P. Larsson, and D. Lundin, in *High Power Impulse Magnetron Sputtering: Fundamentals, Technologies, Challenges and Applications*, edited by D. Lundin, T. Minea, and J. T. Gudmundsson (Elsevier, Amsterdam, 2020), pp. 49–80.
[16] A. Anders, Thin Solid Films **518**, 4087 (2010).
[17] B. Wicher, O. V. Pshyk, X. Li, B. Bakhit, V. Rogoz, I. Petrov, L. Hultman, and G. Greczynski, Mater. Des. **238**, 112727 (2024).
[18] G. Greczynski, L. Hultman, and I. Petrov, J. Appl. Phys. **134**, 140901 (2023).
[19] H. Luo, F. Gao, and A. Billard, Surf. Coat. Technol. **374**, 822 (2019).
[20] C.-C. Kuo, C.-H. Lin, J.-T. Chang, and Y.-T. Lin, Coatings **11**, 7 (2021).
[21] I. Schnell and R. C. Albers, J. Phys.: Condens. Matter **18**, 1483 (2006).
[22] D. R. Olander, *Fundamental Aspects of Nuclear Reactor Fuel Elements* (Technical Information Center, Office of Public Affairs Energy Research and Development Administration, Springfield, VA, 1976).
[23] *The Metallurgy of Zirconium*, edited by C. E. Coleman (International Atomic Energy Agency, Vienna, 2022).
[24] M. Niinomi, Sci. Technol. Adv. Mater. **4**, 445 (2003).
[25] C. J. R. Lustosa, J. Stryhalski, R. L. P. Gonçalves, E. Bonturim, O. Florêncio, and M. Massi, Mater. Res. **26**, e20220566 (2023).
[26] J. Chakraborty, K. K. Kumar, S. Mukherjee, and S. K. Ray, Thin Solid Films **516**, 8479 (2008).
[27] D. Pilloud, J. F. Pierson, C. Rousselot, and F. Palmino, Scr. Mater. **53**, 1031 (2005).
[28] J. Fankhauser, M. Sato, D. Yu, A. Ebnonnasir, M. Kobashi, M. S. Goorsky, and S. Kodambaka, J. Vac. Sci. Technol. A **34**, 050616 (2016).
[29] A. Singh, P. Kuppusami, R. Thirumurugesan, R. Ramaseshan, M. Kamruddin, S. Dash, V. Ganesan, and E. Mohandas, Appl. Surf. Sci. **257**, 9909 (2011).
[30] A. Singh, P. Kuppusami, R. Thirumurugesan, V. Ganesan, and E. Mohandas, Int. J. Des. Manuf. Technol. **8**, 5 (2014).
[31] C. Huo, D. Lundin, J. T. Gudmundsson, M. A. Raadu, J. W. Bradley, and N. Brenning, J. Phys. D: Appl. Phys. **50**, 354003 (2017).
[32] H. Eliasson *et al.*, Plasma Sources Sci. Technol. **30**, 115017 (2021).
[33] C. Huo, M. A. Raadu, D. Lundin, J. T. Gudmundsson, A. Anders, and N. Brenning, Plasma Sources Sci. Technol. **21**, 045004 (2012).
[34] M. Rudolph, H. Hajihoseini, M. A. Raadu, J. T. Gudmundsson, N. Brenning, T. M. Minea, A. Anders, and D. Lundin, J. Appl. Phys. **129**, 033303 (2021).
[35] J. T. Gudmundsson, J. Fischer, B. P. Hinriksson, M. Rudolph, and D. Lundin, Surf. Coat. Technol. **442**, 128189 (2022).
[36] S. Suresh Babu, M. Rudolph, D. Lundin, T. Shimizu, J. Fischer, M. A. Raadu, N. Brenning, and J. T. Gudmundsson, Plasma Sources Sci. Technol. **31**, 065009 (2022).

27 June 2024 10:24:25

© Author(s) 2024

[37]S. Suresh Babu, M. Rudolph, P. J. Ryan, J. Fischer, D. Lundin, J. W. Bradley, and J. T. Gudmundsson, Plasma Sources Sci. Technol. **32**, 034003 (2023).
[38]K. Barynova, S. Suresh Babu, M. Rudolph, J. Fischer, D. Lundin, M. A. Raadu, N. Brenning, and J. T. Gudmundsson, "On working gas rarefaction in high power impulse magnetron sputtering," Plasma Sources Sci. Technol. (to be published) (2024).
[39]G. Greczynski, I. Zhirkov, I. Petrov, J. E. Greene, and J. Rosen, J. Vac. Sci. Technol. A **35**, 060601 (2017).
[40]X. Li, B. Bakhit, M. P. Johansson Jõesaar, L. Hultman, I. Petrov, and G. Greczynski, Surf. Coat. Technol. **415**, 127120 (2021).
[41]Z. Hubička, Š. Kment, J. Olejníček, M. Čada, T. Kubart, M. Brunclíková, P. Kšírová, P. Adámek, and Z. Remeš, Thin Solid Films **549**, 184 (2013).
[42]T. Kubart, M. Čada, D. Lundin, and Z. Hubička, Surf. Coat. Technol. **238**, 152 (2014).
[43]M. A. Raadu, I. Axnäs, J. T. Gudmundsson, C. Huo, and N. Brenning, Plasma Sources Sci. Technol. **20**, 065007 (2011).
[44]M. Rudolph, N. Brenning, M. A. Raadu, H. Hajihoseini, J. T. Gudmundsson, A. Anders, and D. Lundin, Plasma Sources Sci. Technol. **29**, 05LT01 (2020).
[45]M. Rudolph, A. Revel, D. Lundin, H. Hajihoseini, N. Brenning, M. A. Raadu, A. Anders, T. M. Minea, and J. T. Gudmundsson, Plasma Sources Sci. Technol. **30**, 045011 (2021).
[46]G. Buyle, D. Depla, K. Eufinger, and R. De Gryse, J. Phys. D: Appl. Phys. **37**, 1639 (2004).
[47]T. Kozák, Plasma Sources Sci. Technol. **32**, 035007 (2023).
[48]A. Butler, N. Brenning, M. A. Raadu, J. T. Gudmundsson, T. Minea, and D. Lundin, Plasma Sources Sci. Technol. **27**, 105005 (2018).
[49]D. J. Christie, J. Vac. Sci. Technol. A **23**, 330 (2005).
[50]H. Hajihoseini, N. Brenning, M. Rudolph, M. A. Raadu, D. Lundin, J. Fischer, T. M. Minea, and J. T. Gudmundsson, J. Vac. Sci. Technol. A **41**, 013002 (2022).
[51]Y. Yamamura and M. Ishida, J. Vac. Sci. Technol. A **13**, 101 (1995).
[52]M. Rudolph, D. Lundin, E. Foy, M. Debongnie, M.-C. Hugon, and T. Minea, Thin Solid Films **658**, 46 (2018).
[53]A. Anders, J. Čapek, M. Hála, and L. Martinu, J. Phys. D: Appl. Phys. **45**, 012003 (2012).
[54]C. Kittel, *Introduction to Solid State Physics*, 8th ed. (John Wiley & Sons, Hoboken, NJ, 2005).
[55]H. Deutsch, K. Becker, and T. Märk, Int. J. Mass Spectrom. **271**, 58 (2008).
[56]M. A. Lieberman and A. J. Lichtenberg, *Principles of Plasma Discharges and Materials Processing*, 2nd ed. (John Wiley & Sons, New York, 2005).
[57]F. Blanco, F. Ferreira da Silva, P. Limão-Vieira, and G. García, Plasma Sources Sci. Technol. **26**, 085004 (2017).
[58]NIST electron elastic-scattering cross-section database, SRD 64, version 5.0.
[59]M. Schmid, "A simple sputter yield calculator," Surface Physics, Institute of Applied Physics, Technischen Universität Wien, https://www2.iap.tuwien.ac.at/www/surface/sputteryield.
[60]N. Matsunami, Y. Yamamura, Y. Itikawa, N. Itoh, Y. Kazumata, S. Miyagawa, K. Morita, R. Shimizu, and H. Tawara, "Energy dependence of the yields of ion-induced sputtering of monatomic solids," Technical Report IPPJ-AM-32, Institute of Plasma Physics, Nagoya University, 1983.
[61]A. V. Phelps and Z. L. Petrović, Plasma Sources Sci. Technol. **8**, R21 (1999).
[62]S. C. Rae and R. C. Tobin, J. Appl. Phys. **64**, 1418 (1988).
[63]T. Shimizu, M. Zanáška, R. P. Villoan, N. Brenning, U. Helmersson, and D. Lundin, Plasma Sources Sci. Technol. **30**, 045006 (2021).
[64]J. Fischer, M. Renner, J. T. Gudmundsson, M. Rudolph, H. Hajihoseini, N. Brenning, and D. Lundin, Plasma Sources Sci. Technol. **32**, 125006 (2023).
[65]D. Lundin, M. Čada, and Z. Hubička, Plasma Sources Sci. Technol. **24**, 035018 (2015).
[66]V. Tiron, I.-L. Velicu, O. Vasilovici, and G. Popa, J. Phys. D: Appl. Phys. **48**, 495204 (2015).
[67]N. Brenning, A. Butler, H. Hajihoseini, M. Rudolph, M. A. Raadu, J. T. Gudmundsson, T. Minea, and D. Lundin, J. Vac. Sci. Technol. A **38**, 033008 (2020).
[68]S. M. Rossnagel, J. Vac. Sci. Technol. A **6**, 19 (1988).
[69]S. M. Rossnagel, J. Vac. Sci. Technol. A **6**, 1821 (1988).
[70]J. Alami, K. Sarakinos, G. Mark, and M. Wuttig, Appl. Phys. Lett. **89**, 154104 (2006).
[71]J. Vlček, A. D. Pajdarová, and J. Musil, Contrib. Plasma Phys. **44**, 426 (2004).
[72]M. Palmucci, N. Britun, S. Konstantinidis, and R. Snyders, J. Appl. Phys. **114**, 113302 (2013).
[73]C. Huo, D. Lundin, M. A. Raadu, A. Anders, J. T. Gudmundsson, and N. Brenning, Plasma Sources Sci. Technol. **23**, 025017 (2014).
[74]N. Brenning, J. T. Gudmundsson, M. A. Raadu, T. J. Petty, T. Minea, and D. Lundin, Plasma Sources Sci. Technol. **26**, 125003 (2017).
[75]N. Brenning, D. Lundin, M. A. Raadu, C. Huo, C. Vitelaru, G. D. Stancu, T. Minea, and U. Helmersson, Plasma Sources Sci. Technol. **21**, 025005 (2012).
[76]J. W. Bradley, A. Mishra, and P. J. Kelly, J. Phys. D: Appl. Phys. **48**, 215202 (2015).
[77]H. Hajihoseini, M. Čada, Z. Hubička, S. Ünaldi, M. A. Raadu, N. Brenning, J. T. Gudmundsson, and D. Lundin, Plasma **2**, 201 (2019).

27 June 2024 10:24:25

© Author(s) 2024

Paper IV

On working gas rarefaction in high power impulse magnetron sputtering

Kateryna Barynova, Martin Rudolph, Swetha Suresh Babu, Joel Fischer, Daniel Lundin, Michael A Raadu, Nils Brenning, and Jon Tomas Gudmundsson

Plasma Sources Science and Technology 33(6) (2024) 065010

OPEN ACCESS
IOP Publishing
Plasma Sources Science and Technology
Plasma Sources Sci. Technol. **33** (2024) 065010 (17pp)
https://doi.org/10.1088/1361-6595/ad53fe

On working gas rarefaction in high power impulse magnetron sputtering

Kateryna Barynova[1], **Martin Rudolph**[2], **Swetha Suresh Babu**[1], **Joel Fischer**[3], **Daniel Lundin**[3], **Michael A Raadu**[4], **Nils Brenning**[3,4] and **Jon Tomas Gudmundsson**[1,4,*]

[1] Science Institute, University of Iceland, Dunhaga 3, IS-107 Reykjavik, Iceland
[2] Leibniz Institute of Surface Engineering (IOM), Permoserstraße 15, 04318 Leipzig, Germany
[3] Plasma and Coatings Physics Division, IFM-Materials Physics, Linköping University, SE-581 83 Linköping, Sweden
[4] Division of Space and Plasma Physics, School of Electrical Engineering and Computer Science, KTH Royal Institute of Technology, SE-10044 Stockholm, Sweden

E-mail: tumi@hi.is

Received 19 February 2024, revised 26 April 2024
Accepted for publication 4 June 2024
Published 18 June 2024

Abstract

The ionization region model (IRM) is applied to explore working gas rarefaction in high power impulse magnetron sputtering discharges operated with graphite, aluminum, copper, titanium, zirconium, and tungsten targets. For all cases the working gas rarefaction is found to be significant, the degree of working gas rarefaction reaches values of up to 83%. The various contributions to working gas rarefaction, including electron impact ionization, kick-out by the sputtered species or hot argon atoms, and diffusion, are evaluated and compared for the different target materials, and over a range of discharge current densities. The relative importance of the various processes varies between different target materials. In the case of a graphite target with argon as the working gas at 1 Pa, electron impact ionization (by both primary and secondary electrons) is the dominating contributor to working gas rarefaction, with over 90% contribution, while the contribution of sputter wind kick-out is small $<$10%. In the case of copper and tungsten targets, the kick-out dominates, with up to $\sim$60% contribution at 1 Pa. For metallic targets the kick-out is mainly due to metal atoms sputtered from the target, while for the graphite target the small kick-out contribution is mainly due to kick-out by hot argon atoms and to a smaller extent by carbon atoms. The main factors determining the relative contribution of the kick-out by the sputtered species to working gas rarefaction appear to be the sputter yield and the working gas pressure.

Keywords: magnetron sputtering, high power impulse magnetron sputtering (HiPIMS), sputter yield, sputtering

* Author to whom any correspondence should be addressed.

Original Content from this work may be used under the terms of the Creative Commons Attribution 4.0 licence. Any further distribution of this work must maintain attribution to the author(s) and the title of the work, journal citation and DOI.

© 2024 The Author(s). Published by IOP Publishing Ltd

1. Introduction

Magnetron sputtering [1–3] is a versatile and widely applied physical vapor deposition technique [4], in which the film-forming material is sputtered from a cathode target by ion bombardment. A discharge is formed in a working gas, preferentially constituting heavy noble atoms, most often argon. The ions for the sputter process are accelerated from a dense plasma region created near the target and confined there by a static magnetic field, that traps the electrons. Often, the discharge is driven by a dc voltage or current, in particular when depositing metallic films. In that case the sputtered species are mainly neutral atoms, and the ions available in the discharge are the ions of the working gas [3].

A variation of the magnetron sputtering technique is high power impulse magnetron sputtering (HiPIMS), where the discharge is driven by high power pulses delivered at a low repetition frequency, and with low duty cycle [5–7]. As a result of the HiPIMS process, the discharge is composed of atoms and ions of both the working gas and target material. Pulsing the discharge at high peak power results in a high peak discharge current density, increased electron density [3, 8], increased ionization of the sputtered species [9], and higher ionization fraction in the flux of film-forming species to the substrate [6, 10, 11], which ultimately leads to denser deposited films [12], that exhibit better crystallinity [13], and overall improved film properties [14, 15].

The sputter process releases atoms of the film-forming species from the target, and the sputtered species enter the discharge volume with considerable energy, which, as a first approximation, can be described by the Thompson distribution [16–18]. The most probable energy of the Thompson distribution corresponds to roughly half the cohesive energy of the solid target [17, 18]. The interaction between the energetic sputtered particles and the working gas atoms not only influences the momentum of the sputtered species, but also the discharge properties as it leads to a reduction in the working gas density, and increase in the working gas temperature, in front of the cathode target. The pressure drop was first identified in a dc magnetron sputtering (dcMS) discharge, in the cylindrical configuration, by Hoffman [19], who referred to the observed phenomena as 'sputtering wind', as he argued this to be a pressure variation resulting from collisions between the sputtered particles and the working gas atoms. This phenomena was further explored experimentally in a planar dcMS discharge by Rossnagel [20–22] and Drüsedau [23], who observed a pressure drop just in front of the cathode target and referred to it as working gas rarefaction or gas heating. Rossnagel [20, 21] found the working gas rarefaction to depend on the discharge current, sputter yield, sputtered species type (velocity and collision cross section) and the mass of the sputtered species and the working gas atoms. They further argued that the reduction in working gas density drives up the plasma impedance. Therefore, the discharge requires a higher discharge voltage to operate at the same discharge current, as the resulting current density is determined by the reduced concentration of the working gas species in the target vicinity. These studies were followed by a development of analytical models to describe the working gas rarefaction process [20, 23–26]. The occurrence of rarefaction has also been observed using the direct simulation Monte Carlo (DSMC) method [27] and particle-in-cell Monte Carlo simulations [28, 29] of dc magnetron sputtering discharges. In fact, it has been suggested that working gas rarefaction improves both the deposition rate and the coverage in sub-micron sized holes [27].

The HiPIMS discharge is operated at much higher peak discharge current densities than the dcMS discharge, and therefore, working gas rarefaction could be expected to be even more significant. However, as the duty cycle in HiPIMS operation is short, the gas refill during the off-times could result in lower working gas rarefaction on average. A brief discussion on how the rarefaction influences the discharge current waveform in HiPIMS operation was given by Lundin [30], where it was observed that several mechanisms lead to working gas rarefaction—not only sputter wind. Experimentally, using optical emission spectroscopy (OES) [31–36], measuring time-resolved ion saturation currents by a probe array [37], and mass spectrometry [38, 39], it has been demonstrated that working gas rarefaction occurs and can indeed be rather significant in HiPIMS discharges, and be even more pronounced for longer pulses [38]. Alami *et al* [31] observed almost an order of magnitude drop in the Ar^0 emission intensity when operating with a chromium target, 50 μs long pulses, an average current density of 2.8 A cm^{-2} and a working gas pressure of 0.8 Pa. Palmucci *et al* [33] also observed a strong gas rarefaction, which significantly reduces the sputtered species energy dissipation during a certain time interval at the end of a 20 μs long pulse, when operating with a titanium target. They referred to this phenomena as 'rarefaction window'. Incidentally, recent studies seem to indicate that working gas rarefaction may be a desired property of the discharge process in the case of HiPIMS operation and have some benefits for the deposition process [40, 41]. Using mass spectrometry, Greczynski *et al* [39] observed that the time- and energy integrated metal-ion-to-gas-ion ratio increases when the peak discharge current density is increased during HiPIMS operation. This, they claim to be due to working gas rarefaction. Also, they find this effect to become even stronger with increasing atom mass of the sputtered species. Vitelaru *et al* [42] applied time-resolved tunable diode-laser absorption spectroscopy measurements on the argon metastable (Ar^m) level $3s^2 3p^5(^2P^\circ_{3/2})4s$ excited by 801.478 nm photons, in the dense plasma region in front of the titanium cathode target in a HiPIMS discharge. From the Doppler profile they determined the temporal evolution of the working gas temperature and the metastable argon Ar^m density during the pulse as well as during the plasma afterglow. They showed that the metastable argon Ar^m density sharply increases at the beginning of the discharge pulse, followed by a severe Ar^m density depletion, along with increasing working gas temperature around the peak in the discharge current. The working gas temperature was found to increase during the pulse and more so with increased discharge current. This is in agreement with the increased sputtering of metal particles resulting in more

metal-argon collisions, and thus increased momentum transfer to the neutral working gas atoms, and increased density of hot working gas neutrals, due to recombination of Ar^+ ions.

Working gas rarefaction in HiPIMS operation has also been explored through modeling. Kadlec [43] studied the behavior of the neutral argon working gas atoms during a HiPIMS pulse by the three-dimensional DSMC method, assuming a titanium target. When the discharge current density reached the 2.2 A cm^{-2} range very strong gas rarefaction was observed. The volume density of sputtered metal exceeded the working gas density several times and the working gas atoms moved rapidly away from the target as a shock wave a few microseconds into the pulse. Note that in the DSMC simulations the ionization of the working gas is neglected. In a more recent study Kozák and Lazar [44] investigated working gas rarefaction in HiPIMS operation using a three-dimensional DSMC simulation and compared the findings to results from volume-averaged models. The DSMC results indicate that the working gas rarefaction is only slightly more pronounced for target atoms with higher mass and that the rarefied region extends much further from the target than the extent of the ionization region (IR), that is typically defined for volume-averaged modeling. They found that volume-averaged models provide good approximation for the temporal evolution of the target material density in front of the target compared to the DSMC simulation. However, they found the volume-averaged models underestimate the magnitude of the rarefaction during the pulse-on time, and predict faster return to equilibrium during the pulse-off time compared to the DSMC simulation. This is because the size of the IR assumed in volume-averaged modeling of the HiPIMS discharge is small and in reality the region where the working gas density is significantly reduced extends somewhat farther from the target surface than the extent of the high plasma density region that is maintained by the magnetic confinement. More recently the DSMC model has been updated to simulate the dynamics of both atoms and ions in an HiPIMS discharge [45].

The ionization region model (IRM) is a semi-empirical time-dependent volume-averaged plasma chemical model of the IR of the HiPIMS discharge. It provides the temporal evolution of the densities of ions, neutrals and electrons with known discharge current and voltage waveforms [46]. The IRM has been applied to model HiPIMS discharges in argon with aluminum [46–48], titanium [46, 49–51], copper [52], tungsten [53, 54], graphite [55], and zirconium [56] targets. From the IRM studies, using various target materials, it has been observed that there is indeed a significant working gas rarefaction. The IRM results have furthermore verified that several rarefaction mechanisms are involved [47]. When operating a HiPIMS discharge with an aluminum target it has been shown that electron impact ionization has the largest contribution to working gas rarefaction [47], while when operating with a tungsten target the sputter wind appears to have the largest contribution [53].

Here, using the IRM, we explore the relative contributions of the various mechanisms that contribute to the working gas rarefaction in HiPIMS discharges with a few different target materials, in the order of increasing atomic mass, graphite, aluminum, copper, titanium, zirconium, and tungsten. This we do by reevaluating the IRM results for discharges studied in the past, while focusing on the rarefaction processes. In section 2 we give an introduction to the IRM and the various terms that contribute to working gas rarefaction. There we also introduce an updated kick-out term into the IRM. The temporal evolution of the gain and loss processes of argon atoms within the IR, as well as diffusion of argon atoms in and out of the IR, for the six target materials, spanning a wide range in atomic mass and sputter yield, is evaluated in section 3. The results are discussed in section 4, where we determine the main contributor for working gas rarefaction and how they depend on the target material and which parameter determines which contributor is the most important. The main findings are summarized in section 5.

2. The IRM

The IRM is a global plasma chemistry model of the IR of a pulsed magnetron sputtering discharge. The IR is taken to be an annular cylinder with outer radius r_2, and inner radius r_1 sitting above the race track of width $w_{RT} = r_2 - r_1$, and height $L = z_2 - z_1$, extending from z_1 to z_2 axially away from the target surface [46, 57]. The loss and gain rates across the boundaries of this annular cylinder to the target on one side, and the bulk plasma on the other side, account for the geometry of the IR [57]. To determine the electron density the quasi-neutrality condition is applied. The model gives the temporal variation of the various species, electrons, ions, and neutrals, that constitute the discharge for a given discharge setup and experimentally determined discharge voltage and current waveforms. The IRM is therefore a tool that allows us to explore, among other processes, the mechanisms responsible for working gas rarefaction.

The plasma chemistry is introduced through two sets of rate coefficients that are calculated using an assumed electron energy distribution function (EEDF), one set for cold, or primary electrons, and another set for the secondary electrons, emitted from the target due to ion bombardment. This assumption has been tested against a kinetic Boltzmann solver and a good agreement has been achieved [58]. The cold electrons are created through the ionization processes within the IR volume and are referred to as primary electrons in the discussion below. The majority of the electrons are primary electrons and belong to the cold Maxwellian electron population which therefore dictates the electron density and the effective electron temperature. The rate coefficients are calculated assuming Maxwellian EEDFs and fit in the range $T_e = 1 - 7$ eV for the primary electrons, and in the range 200 – 1000 eV for secondary electrons. The reaction set and the rate coefficients involving argon in the IRM are described in our earlier works on HiPIMS discharges with titanium target [49, 59], with a few modifications of the rate coefficients involving the metastable argon atom [58] and addition of Ar^{2+} to the reaction set [55]. The reaction set and the parameters that describe the

plasma surface interactions, such as sputter yields, and secondary electron emission, involving the various target materials are given in respective publications, for graphite [55], aluminum [46], copper [52], titanium [59], zirconium [56], and tungsten [53] targets.

2.1. The model implementation

To further explore working gas rarefaction we look at the processes that are involved in the gain and loss of argon atoms within the IR. There are a number of processes that contribute to working gas rarefaction in the magnetron sputtering discharge. Below we discuss these processes and how they are implemented in the IRM, following the discussion given by Huo *et al* [46], which also provides a more detailed discussion of the IRM in general. We also discuss a number of modifications to the IRM made for this current study.

The film-forming species are sputtered out of the cathode target by ion bombardment. The rate at which the sputtered species enter the discharge is given by

$$R_{\mathrm{n,sputt}} = \frac{\sum_i \Gamma_i^{\mathrm{RT}} S_{\mathrm{RT}} Y_i(\mathcal{E}_i)}{\mathcal{V}_{\mathrm{IR}}} \tag{1}$$

where n stands for neutral atom sputtered off the target and i stands for the ion species involved in the process, Γ_i^{RT} is the flux of ion species i towards the target in [ions/m^2 s], S_{RT} is the area of the sputtered region (racetrack area), $Y_i(\mathcal{E}_i)$ is the energy-dependent sputter yield for ion species i bombarding the target, and $\mathcal{V}_{\mathrm{IR}}$ is the total volume of the IR. The sum is taken over all the positive ion species in the discharge, and each ion species i has its energy-dependent sputter yield. The sputter yields for most of the various targets are taken from fits suggested by Anders [60], but for titanium the sputter yields are taken from fits provided by Tomas Kubart at Uppsala University [59]. For a zirconium target the sputter yield was estimated using the TU Wien Sputter Yield Calculator [61], which is based on the empirical equations for sputter yields at normal incidence developed by Matsunami *et al* [62]. The sputter yields depend on the ion energy $\mathcal{E}_i(t)$ which we take to be the energy equivalent of the discharge voltage $V_{\mathrm{D}}(t)$.

In addition to cold argon neutrals in ground state Ar^{C} with density $n_{\mathrm{Ar}}^{\mathrm{C}}$, and metastable argon (the densities of both $\mathrm{Ar(4s[3/2]_2)}$ and $\mathrm{Ar(4s'[1/2]_0)}$), the model considers two additional populations of argon atoms originating from argon ions that bombard the target and then return to the discharge volume as neutrals. These are warm argon atoms with density $n_{\mathrm{Ar}}^{\mathrm{W}}$ and hot argon atoms with density $n_{\mathrm{Ar}}^{\mathrm{H}}$. The hot argon population originates from argon species that are reflected from the target [63, 64]. They are assumed to have an average energy of 2 eV [47]. The warm population Ar^{W} is due to argon ions that penetrate the target surface, and then slowly diffuse back as atoms. Their energy is taken to be the thermal energy of the surface, with about 0.1 eV ($\sim$1000 K) as an upper bound [65]. We assume that a fraction ξ_{H} of the recombined Ar^+ ions return as hot neutrals Ar^{H} during the pulse, and a fraction $(1-\xi_{\mathrm{H}})$ return as warm neutrals Ar^{W} during the pulse. We further assume that all target-implanted argon atoms leave the target during the pulse [47, 66]. Of importance for the working gas rarefaction are the hot argon atoms, as they have a considerable momentum. They are incorporated in the IRM as a generation term for hot argon neutrals Ar^{H}

$$R_{\mathrm{Ar^H,return}} = \xi_{\mathrm{H}}\left(\Gamma_{\mathrm{Ar^+}}^{\mathrm{RT}} + \Gamma_{\mathrm{Ar^{2+}}}^{\mathrm{RT}}\right)\frac{S_{\mathrm{RT}}}{\mathcal{V}_{\mathrm{IR}}} \tag{2}$$

where $\Gamma_{\mathrm{Ar^+}}^{\mathrm{RT}}$ is the flux of Ar^+ ions and $\Gamma_{\mathrm{Ar^{2+}}}^{\mathrm{RT}}$ is the flux of Ar^{2+} ions towards the target racetrack. For the generation of warm neutrals ξ_{H} in equation (2) is replaced by $(1-\xi_{\mathrm{H}})$. Coming from the target, the hot argon neutrals Ar^{H} and the warm argon neutrals Ar^{W} have a directed flux away from the target, giving a loss out of the IR at random velocity defined by

$$v_{\mathrm{ran}} = \sqrt{\frac{2eT_{\mathrm{n}}}{\pi m_{\mathrm{n}}}} \tag{3}$$

where T_{n} is the temperature and m_{n} is the mass of the neutral species and thus the loss rate is

$$R_{\mathrm{Ar}^Z,\mathrm{loss}} = v_{\mathrm{ran}} n_{\mathrm{Ar}^Z}\frac{S_{\mathrm{DR}}}{\mathcal{V}_{\mathrm{IR}}} \tag{4}$$

where the superscript Z stands for hot (H) and warm (W) argon atoms. For this current study we assume $\xi_{\mathrm{H}} = 0.5$ i.e. 50% are Ar^{W}, with $T_{\mathrm{Ar}}^{\mathrm{W}} = 0.1$ eV, and 50% are Ar^{H} with $T_{\mathrm{Ar}}^{\mathrm{H}} = 2$ eV for all the target materials studied. This choice is arbitrary and has been motivated in earlier studies [47, 66]. However, ξ_{H} will possibly vary with the mass of the target element, and for heavier target elements the fraction of Ar^{W} is expected to be higher (see Rudolph *et al* [64]), which we neglect in this current study.

Neutral atoms created through volume reactions within the IR along with atoms sputtered or released from the target are lost as they diffuse out of the IR, described by a loss term

$$R_{\mathrm{n,diff}} = \Gamma_{\mathrm{n,diff}}\frac{S_{\mathrm{DR}}}{\mathcal{V}_{\mathrm{IR}}}, \tag{5}$$

where $\Gamma_{\mathrm{n,diff}}$ is the flux of neutral atoms or molecules through the border of the IR with the diffusion region (DR), S_{DR} is the surface area of the IR facing the DR, and $S_{\mathrm{DR}}/\mathcal{V}_{\mathrm{IR}}$ is the distance through the IR, which represents the typical length that species with a directed flow from the target travel when diffusing out of the IR. The atom flux is

$$\Gamma_{\mathrm{n,diff}} = \Gamma_{\mathrm{n,0}}\exp\left(\frac{-L}{\lambda_{\mathrm{n,Ar}}}\right), \tag{6}$$

where $\lambda_{\mathrm{n,Ar}} = 1/(\sigma_{\mathrm{m}} n_{\mathrm{Ar}})$ is the mean free path for target atoms colliding with argon atoms and σ_{m} is the momentum transfer cross section for collisions between atoms. For the cold working gas atoms $\Gamma_{\mathrm{n,0}}$ is the random atom flux governed by the thermal energy. For the species coming off the target, the sputtered species and warm and hot argon atoms, the flux $\Gamma_{\mathrm{n,0}}$ is governed by the velocity of the particle coming off the target, directed away from the target surface. For the sputtered species the flux is dictated by the cohesive energy of the target.

The cross section σ_{m} for collisions of sputtered metal atoms and argon atoms is based on the momentum-exchange

Table 1. Selected atomic data for the various target atoms. The values for the cohesive energy $\mathcal{E}_{\rm cohesive}$ are taken from Kittel [69] and the atomic radius is from Clementi *et al* [68].

Atom	$\mathcal{E}_{\rm iz}[eV]$	$\mathcal{E}_{\rm cohesive}[eV]$	Atomic mass [amu]	Atomic radius [pm]	$\sigma_{\rm m}$ [10^{-19} m^2]	$Y_{\rm SS}$	$V_{\rm D}[V]$
C	11.26	7.37	12.0	67	1.2	0.24	611
Al	6.0	3.39	27.0	118	2.6	1.19	730
Ti	6.8	4.85	47.9	176	4.1	0.64	625
Cu	7.73	3.49	63.5	145	3.4	2.37	575
Ar	15.76		39.95	71	1.2–1.5		
Zr	6.63	6.25	91.2	206	4.9	0.47	550
Mo	7.09	6.82	95.9	190	4.2	0.51	450
W	7.98	8.90	183.8	193	4.0	1.14	800

cross section calculated for the Ar–Ar interaction by Phelps *et al* [67]. As pointed out by Rossnagel [22], it has to be noted that the momentum transfer cross section for the sputtered atoms, with energy of few eVs, is up to a factor 10 larger than the momentum transfer cross section for the energetic reflected neutrals with energy of few hundred eVs (see also Phelps *et al* [67]). To get a more reasonable value for the momentum-exchange between the sputtered species and the argon atoms we approximate this to be a billiard-ball collision, and assume that the momentum-exchange cross section scales as $\pi(a_1+a_2)^2$, where a_1 is the atomic radius of the sputtered species and a_2 is the atomic radius of the argon atom. The velocity of the particle coming off the target is assumed to be the most probable velocity from the Thompson distribution [16, 17] or $\frac{1}{2}\mathcal{E}_{\rm cohesive}$. The Ar–Ar cross section is determined at the most probable energy for each metal atom using the fit given in Phelps *et al* [67]. This value is then multiplied by the ratio $((a_1+a_2)/(a_2+a_2))^2$ to get the momentum exchange cross section for each argon-metal atom pair. The values used to calculate the cross sections and the calculated momentum transfer cross sections are given in table 1. The values for the atomic radius are taken from the work of Clementi *et al* [68] and the values for the cohesive energy are from the textbook by Kittel [69]. This is a revision from our earlier works where we assumed the metal–Ar momentum transfer cross section to be 2×10^{-19} m^2 as a typical cross section for all neutral-neutral collisions [46, 47, 57].

For this study the working gas temperature (cold argon atoms) is assumed to be 500 K. At a gas temperature of 500 K and using the cross sections in table 1 the mean free path for the sputtered atoms is roughly 8–30 mm at 1 Pa and 2–8 mm at 4 Pa. Due to the energy transfer from the sputter process and heat conduction from the cathode target the effective gas temperature is high. We will see later (section 3) that late in the pulse a significant fraction of the argon atoms within the IR are warm and hot atoms. Therefore, the effective working gas temperature can be significantly higher, and argon gas a temperature above 1200 K has been measured for a 200 μs long pulse [42].

In the IRM, gas rarefaction by the effect of the sputter wind [19] is implemented as an argon kick-out term due to collisions with fast sputtered particles [46, 57]. Here, we slightly modify the model from our previous studies to also include the hot argon atoms $\rm Ar^H$ species that originate from the target with a considerable energy. The warm argon species $\rm Ar^W$ on the other hand, also originating from the target, are still neglected in the model, as their energy of 0.1 eV is too low to have a significant impact on gas rarefaction by kicking out argon species. Also, we neglect kick-out by the metal ions.

For this current study we significantly revise the kick-out term in the IRM code from our earlier studies [46, 47, 57]. For the derivation of a kick-out term, we denote the kicking-out species by an X, and those that are kicked-out by a Y. Here, $\rm X = \{M, Ar^H\}$, where M stands for the target atoms, and $\rm Y = \{Ar^C, Ar(4s[3/2]_2), Ar(4s'[1/2]_0)\}$. In the model, we assume that a collision of a species X with a species Y leads to the instantaneous loss of species Y from the IR. This is acceptable if two conditions are met: (i) The momentum of species X is always higher than the average momentum of the cold Ar species (species Y) at an assumed working gas temperature of 500 K. The lightest target atom studied here, carbon, has the mass $M = 12M_{\rm p}$, where $M_{\rm p}$ is the proton mass, and an ejection energy $\mathcal{E}_{\rm ejection} = \frac{1}{2}\mathcal{E}_{\rm cohesive} = 3.7$ eV [55]. This yields a momentum of 10^{-22} kg m s^{-1} which is higher than the momentum of an average argon species at $T_{\rm g} = 500$ K which is $\sim 10^{-23}$ kg m s^{-1}. We therefore consider the first condition to be fulfilled. (ii) The length of a HiPIMS pulse is longer than the typical loss time of species Y out of the IR after the collision. For example, a collision in the middle of the IR with a typical height $h = 2$ cm and a post-collision velocity of $v = 1000$ m s^{-1}, results in a loss of species Y within $t = h/2v = 10\,\mu$s. The pulse lengths of the HiPIMS discharges investigated in this study are longer by a factor of 4 to 20, which is why the assumed instantaneous loss is an acceptable assumption. We neglect that this assumption underestimates the momentary argon density. This approximation of instant loss of species from the IR is therefore acceptable for the discharges studied in this work. Furthermore, for collisions between $\rm Ar^H$ and $\rm Ar^C$, we neglect the effect that head-on collisions would simply result in the exhange of velocity vectors with no net change in the argon density in the IR. Collisions under an angle result in both particles to be lost out of the IR. As collisions under an angle are much more probable compared to head-on collisions, also this is an acceptable assumption.

For each species X, we assume that there is a certain probability for these particles to collide with particles of the species Y. This is given by

$$F_{\text{coll,X}\to\text{Y}} = 1 - \exp\left(-L/\lambda_{\text{X}\to\text{Y}}\right), \tag{7}$$

where L is the height of the IR and the mean free path $\lambda_{\text{X}\to\text{Y}}$ of a species X in a background gas composed of species Y is given by

$$\lambda_{\text{X}\to\text{Y}} = \frac{1}{\sigma_{\text{X}\to\text{Y}} n_{\text{Y}}}. \tag{8}$$

where the cross sections $\sigma_{\text{X}\to\text{Y}}$ are the momentum transfer cross sections, as discussed above for each pair of X and Y, and n_{Y} is the density of species Y.

Note that $F_{\text{coll,X}\to\text{Y}}$ is the fraction of the momentum carried by the sputtered species that is transferred to the kicked-out species Y. We can therefore link the sputter flux Γ_{sputter} (in m^{-2} s^{-1}) to the kick-out flux Γ_{kickout} out of the IR by

$$R_{\text{kickout, X}\to\text{Y}} = F_{\text{coll,X}\to\text{Y}} \Gamma_{\text{sputter,X}} \frac{S_{\text{RT}}}{\mathcal{V}_{\text{IR}}} = \Gamma_{\text{kickout}} \frac{S_{\text{DR}}}{\mathcal{V}_{\text{IR}}}, \tag{9}$$

where S_{RT} is the surface area of the IR facing the racetrack, and S_{DR} is the surface area of the IR facing the DR [57]. The sputtered flux is

$$\Gamma_{\text{sputter,X}} = \sum_i \Gamma_i^{\text{RT}} Y_i\left(\mathcal{E}_i\right) \tag{10}$$

where $Y_i(\mathcal{E}_i)$ is the sputter yield for an ion species i bombarding the target. Note that equation (9) represents 6 equations, representing each pair (X,Y) of kicking-out species X and species Y that are kicked-out. Note that this model assumes that there is at most one collision between a sputtered species and a gas species. Based on the long mean free path of sputtered species in the IR compared to the typical height of the IR (see above), this is acceptable assumption.

A second loss mechanism is the ionization of the argon atoms followed by attraction to the target. The argon atoms within the IR are lost through electron impact ionization

$$\text{e} + \text{Ar} \longrightarrow \text{Ar}^+ + 2\text{e}$$

where the argon atom can be in the ground state or in an excited state. This includes cold, warm and hot argon atoms. The electrons that drive the reaction can be from either the cold (primary) or hot (secondary) population. In addition charge exchange

$$\text{Ar}^+ + \text{M} \longrightarrow \text{Ar} + \text{M}^+$$

contributes to adding argon atoms to the IR, however the contribution is expected to be very small. Due to the electric fields within the IR, most of these gas ions are drawn toward the target and are lost from the IR.

As discussed above, gas rarefaction lowers the density of the working gas (the neutral argon atoms) within the IR below the density value in the surrounding gas reservoir, $n_{\text{g,0}}$ [19, 20, 29, 30]. This leads to back-diffusion (gain) that is modeled by the term

$$R_{\text{g,refill}} = \frac{1}{2} v_{\text{g,ran}} \frac{\left(n_{\text{g,0}} - n_{\text{g}}\right) S_{\text{DR}}}{\mathcal{V}_{\text{IR}}} \tag{11}$$

where the subscript g stands for the atoms of the working gas and $v_{\text{g,ran}}$ is their random thermal velocity as defined by equation (3). The argon gas diffusional refill term is determined by the gas temperature and the gas density difference $(n_{\text{Ar,0}} - n_{\text{Ar}})$ between the IR and the surrounding volume. By definition, only atoms moving towards the boundary are involved so that the densities are taken to be one half of the volume densities.

2.2. The degree of working gas rarefaction

The working gas rarefaction is either presented as a percentage of the total neutral argon density at the start of the pulse $n_{\text{Ar}}(t)/n_{\text{Ar,0}}$ or as a degree of working gas rarefaction

$$\text{degree of working gas rarefaction} = 1 - \frac{n_{\text{Ar}}(t)}{n_{\text{Ar,0}}}, \tag{12}$$

where $n_{\text{Ar,0}}$ is the total argon density at the start of the pulse and $n_{\text{Ar}}(t)$ is the temporal variation of the total argon density. As discussed in section 2.1 there are several factors that contribute to working gas rarefaction, including electron impact ionization of argon atoms and kick-out of argon atoms by the sputter wind, which is then balanced by diffusion (refill) of cold argon atoms from the bulk plasma, returning hot and warm argon atoms from the target, and charge-exchange collisions [47]. When we compare the relative contribution of each of the processes to working gas rarefaction they are all determined by integrating the contribution of each term throughout the entire pulse and the afterglow.

3. Results

3.1. Overview

As mentioned in section 1 the IRM has been applied to study HiPIMS discharges using a number of different target materials including graphite [55], aluminum [46, 47], copper [52], titanium [51], and tungsten [53]. For all the target materials the IRM calculations have shown that the cold (or primary) argon ground state density (denoted $\text{Ar}^{\text{C}}(3\text{p}^6)$) decreases steadily to a minimum close to the peak in the discharge current and then it increases again. The question that we will answer with this work is: What processes contribute to working gas rarefaction in the HiPIMS discharge? Is the sputter wind important? In the following, we will re-analyze some of these discharges in terms of working gas rarefaction.

In the following we explore how much each of the four terms described in section 2.1 contributes to working gas rarefaction for a few target materials, from low atom mass (graphite) to high atom mass (tungsten). For this we model discharges with targets of various materials and of varying sizes. For the various target sizes the dimensions of the IR for the IRM calculations are listed in table 2. Note that in some cases we use different dimensions for the size of the IR in this current study than in the original study of that particular target material. However, all the dimensions are within ± 1 mm from the earlier assumed dimensions. The size of the IR is chosen rather

Table 2. The dimensions of the ionization region used in the model calculations for the different targets and target sizes.

Target	Target diameter [mm]	z_1 [mm]	z_2 [mm]	r_1 [mm]	r_2 [mm]
C	50	2	13	6	20
Al, Zr	50	2	20	6	20
Cu	50	2	28	6	20
W	75	2	22	8	28
Ti	100	2	25	11	39

arbitrary. Also, it has been observed experimentally that the size of the IR varies with the magnetic field strength among other operating parameters [70]. In fact the absolute value of the degree of rarefaction scales with the size of the IR. Electron impact ionization scales with $1/\mathcal{V}_{\mathrm{IR}}$, while kick-out scales as $1/L$, and therefore the absolute values mentioned in the text for the degree of working gas rarefaction are just rough estimates. Also keep in mind that as mentioned in section 1 that the size of the IR is small compared to the actual extent of the working gas rarefaction in the discharge [44], which also influences the absolute value of the degree of working gas rarefaction. Working gas rarefaction is therefore expected to be less pronounced when modeling with volume average models compared to DSMC simulations. Furthermore, Kozák and Lazar [44] point out that volume-averaged models do not take into account the spatial distribution of the neutral Ar and M densities, and therefore the velocity and angular distribution of the sputtered atoms [71, 72], and secondary M–Ar and Ar–Ar collisions are neglected. The latter is justified by a mean free path of a few tens of mm as discussed in section 2.1 and given the extension of the IR it means that only a single collision occurs.

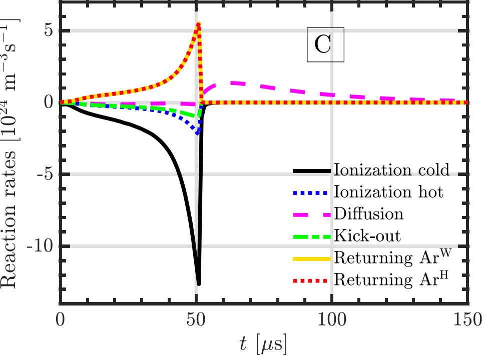

Figure 1. The reaction rates for the argon atom loss and argon atom gain within the ionization region for a discharge with 50 mm diameter graphite target operated at working gas pressure of 1 Pa, with a peak discharge current $I_{\mathrm{D,peak}}$ of 20 A ($J_{\mathrm{D,peak}} = 1\ \mathrm{A\,cm^{-2}}$) and 50 μs long pulse.

3.2. *Graphite target*

In a recent study we applied the IRM to analyze HiPIMS discharges with a 50 mm diameter graphite target and argon working gas at a pressure of 1 Pa [55]. It was observed that the discharge operates on working gas recycling and most of the discharge current at the cathode target surface is composed of $\mathrm{Ar^+}$ ions, which constitute over 90% of the discharge current, while the contribution of the $\mathrm{C^+}$ ions is always small (<5%). The ion back-attraction probability during the pulse β_{t} is high (>83%), and the ionized flux fraction is low, or in the range 2%–4%. The maximum in the degree of working gas rarefaction derived from the IRM is 45%, 51%, and 55%, for peak discharge current densities of 1, 2, and 3 $\mathrm{A\,cm^{-2}}$, respectively. These values are determined from the maximum drop in the total argon atom density within the IR, calculated using equation (12), by adding the densities of all the neutral argon atom species densities within the IR. Earlier we reported a maximum in the degree of cold argon atom rarefaction of 66%, 74%, and 81% for discharge current densities of 1, 2, and 3 $\mathrm{A\,cm^{-2}}$, respectively [55]. The difference in the degree of working gas rarefaction values, reported here, compared to the earlier published values, is mainly due to warm and hot argon atoms that enter the IR during the pulse, which have influence on the rarefaction, and were not taken into account when the degree of working gas rarefaction was evaluated in the earlier study. Note, that the various values we report here for the discharge with graphite target have changed slightly as we discovered a few minor errors in the calculations published earlier [55], that have now been corrected, in addition to the modifications of the kick-out term discussed in section 2.1. Also, note that this does not affect the key results of that study concerning the reasons for low carbon ionization in HiPIMS. Furthermore, we have adjusted the size of the IR.

Here, we analyze the contributions of the various processes to rarefaction for a HiPIMS discharge with a graphite target in more detail. Figure 1 shows the temporal evolution of the reaction rates for the loss and gain of argon atoms within the IR for the $J_{\mathrm{D,peak}} = 1\ \mathrm{A\,cm^{-2}}$ and 50 μs long pulse case explored earlier by Eliasson *et al* [55]. The main contributor to the loss of argon atoms is electron impact ionization of the argon atoms by primary electrons (referred to as ionization cold), and the second most important loss process is electron impact ionization by secondary electrons (referred to as ionization hot) has much smaller contribution. This is the case even though both argon ions and carbon ions contribute to the creation of secondary electrons as they bombard the cathode target. Warm and hot argon atoms released from the target enter the IR and constitute the main contribution to the gain of argon atoms within the IR. The reaction gain rates for the warm and hot

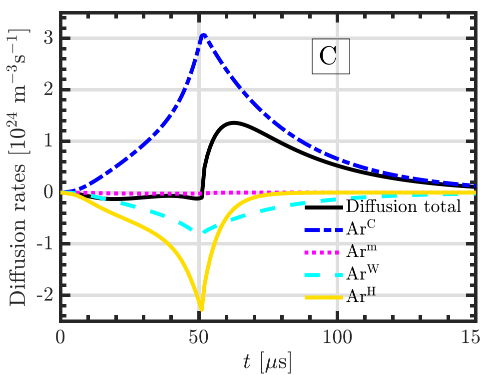

Figure 2. The reaction rates for the cold argon atom diffusion and warm and hot argon atom escaping from the ionization region for a discharge with 50 mm diameter graphite target operated at working gas pressure of 1 Pa, with a peak discharge current $I_{\mathrm{D,peak}}$ of 20 A ($J_{\mathrm{D,peak}} = 1$ A cm^{-2}) and 50 μs long pulse.

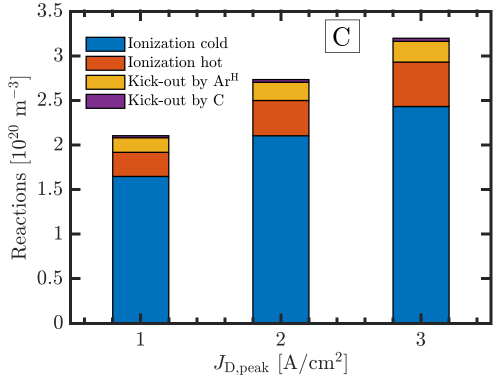

Figure 3. The contribution of the various processes to working gas rarefaction within the ionization region for a discharge with 50 mm diameter graphite target versus the peak discharge current density for argon at 1 Pa, pulse length of 50 μs and average discharge power $\langle P_{\mathrm{D}} \rangle$ of 80 W.

argon atoms in figure 1 are assumed to be the same and overlap, due to the assumption that equal number of argon atoms leaves the target during one pulse [47]. We see in figure 1 that when operating with a graphite target the contributions of kick-out is small and charge-exchange is negligible (not shown). We note that diffusion contributes to a net loss of argon atoms during the pulse, but to a flow into the IR after the pulse is off.

We explore the diffusion terms more closely in figure 2. The main contribution to the diffusion is the refill of cold argon atoms into the IR, while the warm and hot argon atoms escape out of the IR, and the hot argon atoms are lost faster than the warm atoms. The total diffusion (the dashed pink line in figure 1), i.e. the sum of the diffusion terms for $\mathrm{Ar^C}$, $\mathrm{Ar^m}$, $\mathrm{Ar^W}$, and $\mathrm{Ar^H}$, is also shown in figure 2. During the pulse-on time the escape of warm and hot argon atoms out of the IR is larger than the refill by cold argon atoms, this is the reason why the total diffusion term appears negative during the pulse. This reverses after the pulse is off. Almost a fifth of the warm and hot argon atoms that are released from the target escape out of the IR without being ionized. For $J_{\mathrm{D,peak}} = 1$ A cm^{-2}, at the peak in the degree of working gas rarefaction cold argon atoms in ground state account for 42%, metastable argon atoms 0.5%, warm argon atoms 37%, and hot argon atoms 21% of the argon atoms within the IR. So a substantial portion of the argon atoms within the IR, during the pulse, consists of warm and hot atoms.

Figure 3 shows the contribution of each of the terms to the working gas rarefaction versus the peak discharge current density for discharges with graphite target. We see that electron impact ionization by primary and secondary electrons has over 90% contribution and its role increases with increased peak discharge current density, and is the dominating process. Electron impact ionization by hot secondary electrons has about $\sim$10% overall contribution. Kick-out by the sputtered species, the sputter wind, has small ($<$10%) contribution on working gas rarefaction when operating with graphite target at a working gas pressure of 1 Pa, and 87% is due to kick-out by hot argon atoms and 13% is due to sputtered carbon atoms. The discharge current density does not have much influence on the relative contribution of the various terms. From the above discussion we see that the composition of the argon atoms within the IR changes during the pulse.

3.3. *Aluminum target*

The early development of the IRM [57] was based around HiPIMS discharges with an aluminum target, that were studied experimentally by Anders *et al* [73], and included studies of the discharge composition at the target surface [46], working gas rarefaction [47], and electron heating mechanisms [46, 66]. When the discharge enters the HiPIMS operating regime the $\mathrm{Al^+}$ ions dominate the discharge current at the target surface, while the contribution of $\mathrm{Ar^+}$ ions is low [46] and the discharge operates in the self-sputter regime to reach the high discharge currents [74]. When operating with aluminum target, electron impact ionization of argon atoms was determined to be the biggest contributor to working gas rarefaction, when the degree of working gas rarefaction was determined to be about 50%, for $J_{\mathrm{D,peak}} \approx 0.6$ A cm^{-2} and $t_{\mathrm{pulse}} = 400\,\mu$s at $p_{\mathrm{g}} = 1.8$ Pa [47].

Here, we analyze a few discharges that were explored experimentally by Lundin *et al* [10], who measured the electron density and the ionized flux fraction as the working gas pressure, pulse length, and discharge current density was varied. The aluminum target was 50 mm in diameter and the working gas pressure was 0.5 and 2.0 Pa. At average current density $J_{\mathrm{D,average}} \approx 1.4$ A cm^{-2} the measured ionized flux fraction was 50% at 0.5 Pa and at $J_{\mathrm{D,average}} \approx 1.2$ A cm^{-2} the ionized flux fraction was 38% at 2 Pa for a 100 μs long pulse. Here, we further explore these discharges with the help of the IRM. For the IRM calculations the rate coefficients for

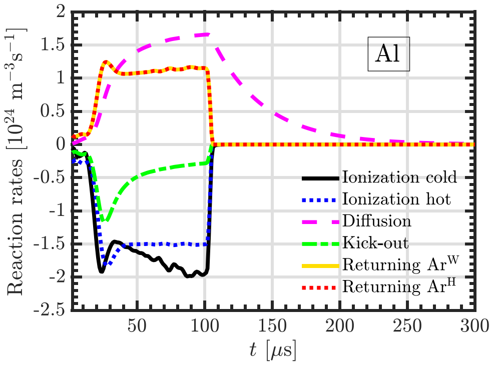

Figure 4. The reaction rates for the argon atom loss and argon atom gain within the ionization region for a discharge with 50 mm aluminum target operated at working gas pressure of 0.5 Pa, with a discharge voltage of $V_D = 730$ V giving average discharge current $I_{D,average}$ of 27 A ($J_{D,average} = 1.4$ A cm^{-2}) for 100 μs long pulse.

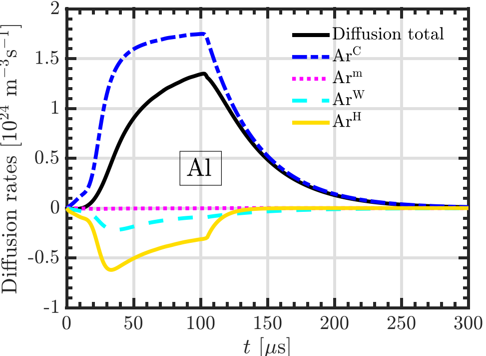

Figure 5. The reaction rates for the cold argon atom diffusion and warm and hot argon atom escaping the ionization region for a discharge with 50 mm aluminum target operated at working gas pressure of 0.5 Pa, with a discharge voltage of $V_D = 730$ V giving average discharge current $I_{D,average}$ of 27 A ($J_{D,average} = 1.4$ A cm^{-2}) for 100 μs long pulse.

reactions involving aluminum atoms and ions are the same as given by Huo *et al* [46]. When applying the IRM we use the measured ionized flux fraction to lock the model as proposed by Butler *et al* [75]. The maximum degree of working gas rarefaction derived from the IRM calculations is 83% at 0.5 Pa and 57% at 2 Pa close to the end of the pulse. The working gas rarefaction is much more significant for the lower pressure. The back-attraction probability of the ionized aluminum is 70% at 0.5 Pa and 75% at 2.0 Pa.

The reaction rates for the argon atom loss and argon atom gain within the IR for a discharge with a 50 mm aluminum target operated at a working gas pressure of 0.5 Pa are shown in figure 4. We see that the loss of argon atoms is mainly due to electron impact ionization of the argon atom, while kick-out also has 14% contribution. Electron impact ionization by the primary electrons has 46% contribution, and the secondary electrons 40% contribution, to the loss of argon atoms from the IR. The diffusion processes (figure 5) are dominated by refill of cold argon atoms, while the warm and hot argon atoms escape out of the IR. At 2 Pa (figure 6) kick-out has similar contribution to the loss of argon atoms from the IR as does electron impact ionization. Electron impact ionization by the primary electrons and secondary electrons have each similar contributions.

The contribution of kick-out increases significantly (from 14% to 53%) with increasing working gas pressure from 0.5 to 2 Pa. At 0.5 Pa the kick-out is 83% due to aluminum atoms and 17% due to hot argon atoms, while at 2 Pa 86% is due to aluminum atoms and 14% due to hot argon atoms. As before, argon atoms enter the IR as returning warm and hot atoms from the target and by diffusion of cold argon atoms. Huo *et al* [47] pointed out that the long mean free path is the reason why rarefaction by electron impact ionization losses dominate over the sputter wind in the discharge. Therefore, for higher working gas pressures the sputter wind contribution would become

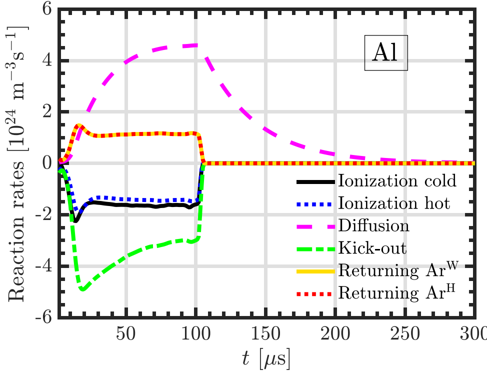

Figure 6. The reaction rates for the argon atom loss and argon atom gain within the ionization region for a discharge with 50 mm aluminum target operated at working gas pressure of 2.0 Pa, with a discharge voltage of $V_D = 540$ V giving average discharge current $I_{D,average}$ of 23 A ($J_{D,average} = 1.2$ A cm^{-2}) for 100 μs long pulse.

more significant, which is indeed what is observed here. At the peak in the degree of working gas rarefaction (for 0.5 Pa) cold argon atoms in the ground state are 44%, metastable argon atoms 0.5%, warm argon atoms 31%, and hot argon atoms 25% of the argon atoms within the IR. Again, more than half the argon atoms within the IR are warm and hot atoms.

3.4. Copper target

In a recent study the IRM was applied to study a few historical HiPIMS discharges operated with a copper target [52].

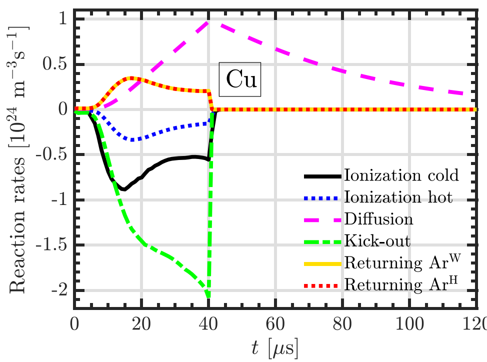

Figure 7. The reaction rates for the argon atom loss and argon atom gain within the ionization region for a discharge with 50 mm diameter copper target operated at working gas pressure of 0.5 Pa, with a peak discharge current density of $J_{D,peak} = 1.0$ A cm^{-2} for 40 μs long pulse.

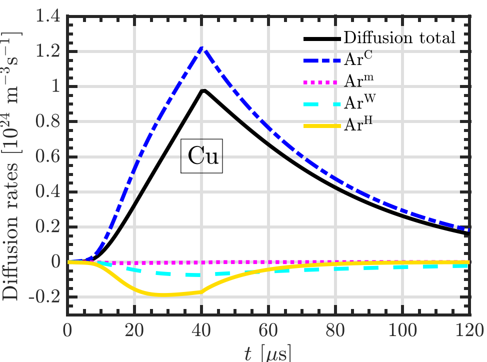

Figure 8. The reaction rates for the cold argon atom diffusion and warm and hot argon atom escaping the ionization region for a discharge with 50 mm diameter copper target operated at working gas pressure of 0.5 Pa, with a peak discharge current density of $J_{D,peak} = 1.0$ A cm^{-2} for 40 μs long pulse.

It was observed that Cu^+ ions dominate the total ion current at the target surface. This indicates that the discharge is dominated by self-sputter recycling in order to reach the high discharge currents [74]. For peak discharge current densities in the range 0.9–1.3 A cm^{-2} the back-attraction probability was found to be in the range 44%–50%, while the ionization probability was in the range 61%–69%, and the ionized flux fraction was in the range 32%–40% [52]. The model results showed that copper ions dominate the ion flux out of the IR, with about ∼77%–88% contribution, in agreement with experimental observations [32]. Recall that for a HiPIMS discharge with copper target, the ionized flux fraction was early on determined experimentally to be as high 70% [76] and more recently an ionized flux fraction up to 80% has been measured experimentally [77]. Gas compression and rarefaction have been observed in a HiPIMS discharge with a copper target by measuring time-resolved ion saturation currents from probe array [37]. It was observed as an onset of the sputter flux that causes a transient densification of the working gas, followed by rarefaction.

Here, we explore reaction rates for the gain and loss of argon atoms within the IR for a discharge created with a 50 mm diameter copper target operated at a working gas pressure of 0.5 Pa, with a peak discharge current density of $J_{D,peak} = 1.0$ A cm^{-2} and 40 μs long pulse. The discharge current and voltage waveforms were recorded by Cemin *et al* [78] and explored in an earlier work as Case I [52]. The degree of working gas rarefaction was determined to reach 60% toward the end of the pulse.

The reaction rates for the loss and gain of argon atoms within the IR are shown in figure 7. The main contributor to the loss of argon atoms is kick-out by the sputtered copper atoms while kick-out by the hot argon atoms has rather small contribution. Electron impact ionization of the argon atoms by primary and secondary electrons have smaller contributions. Warm and hot argon atoms released from the target and diffusion adds argon atoms to the IR. The diffusion terms are explored more closely in figure 8. The main contribution to the diffusion is the refill of cold argon atoms into the IR, while the warm and hot argon atoms escape out of the IR. The hot argon atoms are lost faster than the warm atoms as to be expected. At the peak in the degree of working gas rarefaction, the cold argon atoms in ground state constitute 75%, metastable argon atoms 0.5%, warm argon atoms 16%, and hot argon atoms 8%, of the argon atoms within the IR.

3.5. Titanium target

For a HiPIMS discharge with a titanium target the IRM results have shown that the ion composition at the target surface is composed of both argon and titanium ions in roughly equal numbers, and roughly a third of the titanium ions are the doubly ionized Ti^{2+}, depending on the peak discharge current [46]. In this case, as the self-sputter yield is somewhat below unity, a combination of self-sputter recycling and working gas-recycling is necessary to maintain the high discharge currents.

Here, we model discharges that were explored experimentally by Hajihoseini *et al* [11]. As the magnet configuration was varied, the deposition rate and the ionized flux fraction was determined, while maintaining fixed averaged power by varying the repetition frequency as either the discharge current or discharge voltage was kept fixed. The titanium target was 100 mm in diameter, the working gas pressure 1 Pa, and the average power 300 W. These discharges have been analyzed extensively in order to gain understanding on how the magnetic field strength and topology influence the discharge parameters and operation, including the ionization probability [9], the deposition rate and ionized flux fraction [11, 79, 80], the size of the IR [70], and transport parameters for both ions and neutrals [72], as well as modeling by the IRM [51] and DSMC simulations [45] to determine the ionization and the target ion back-attraction probabilities. The IRM studies

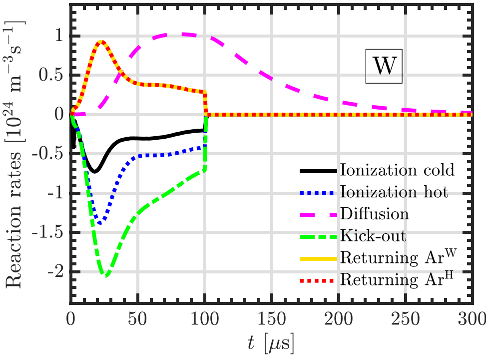

Figure 9. The reaction rates for the argon atom loss and argon atom gain within the ionization region for a discharge with 100 mm diameter Ti target operated at working gas pressure of 1 Pa, with a discharge voltage $V_D = 625$ V giving peak discharge current $I_{D,peak}$ of 80 A ($J_{D,peak} = 1.0\,A\,cm^{-2}$) and 100 μs long pulse.

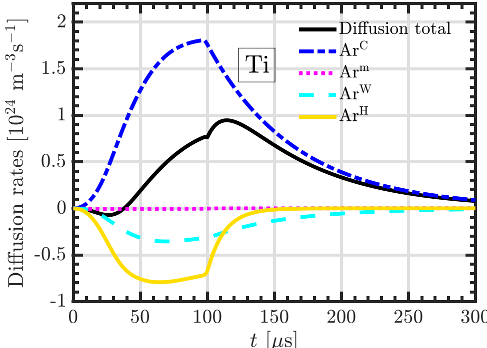

Figure 10. The reaction rates for the cold argon atom diffusion and warm and hot argon atom escaping the ionization region for a discharge with 100 mm diameter Ti target operated at working gas pressure of 1 Pa, with a discharge voltage $V_D = 625$ V giving peak discharge current $I_{D,peak}$ of 80 A ($J_{D,peak} = 1.0\,A\,cm^{-2}$) and 100 μs long pulse.

showed that the back-attraction probability is high > 0.8 [51]. Here, we explore the various contributions to rarefaction in the discharge operated with the strongest magnetic field, referred to as C0E0 by Hajihoseini *et al* [11]. The peak discharge current density was $J_{D,peak} = 1.0\,A\,cm^{-2}$ and the argon working gas pressure $p_g = 1$ Pa. The IRM calculations give a peak in the degree of working gas rarefaction of 77%. For comparison for this particular discharge the DSMC simulations give the maximum in the degree of working gas rarefaction of 53% shortly after the end of the pulse [45]. The various contributions to rarefaction are shown in figure 9. The loss of argon atoms is due to a combination of electron impact ionization by primary electrons and ionization by hot electrons, as well as kick-out, all with similar contributions. Charge-exchange has negligible contribution as before (not shown). The kick-out is split up in 74% contribution due to titanium atoms and 26% due to hot argon atoms. The large fraction of Ar^+ and Ti^{2+} ions at the target surface lead to a high contribution of secondary electrons in the ionization process. Hot and cold argon atoms as well as diffusion of argon atoms into the IR add to the argon atom density within the IR. The contribution of diffusion is explored further in figure 10, and it is seen that diffusion of cold argon atoms into the IR is the most important factor. At maximum degree of working gas rarefaction the cold ground state argon atoms constitute 42%, metastable argon atoms 0.3%, warm argon atoms 36%, and hot argon atoms 22% of the argon atoms within the IR.

3.6. Zirconium target

We apply the IRM to a discharge operated with a 50 mm diameter zirconium disk. The discharge voltage V_D was kept at 550 V, the pulse was kept at constant length of 50 μs and the argon working gas pressure was kept at 1 Pa [56]. The ionized flux fraction and the normalized deposition rate was measured as the peak discharge current density was varied in the range 0.5 – 2.0 $A\,cm^{-2}$. We use the ionized flux fraction measured at 30 mm (45%) to lock the model. We apply the IRM to study a discharge operated with peak current density of $J_{D,peak} = 1\,A\,cm^{-2}$. The back-attraction probability is determined by the IRM to be 73% and the peak in the degree of working gas rarefaction was determined to be 70%. We also note that aproximately 2/3 of the discharge current at the target surface is carried by Ar^+ ions [56]. This discharge therefore operates on combination of working gas recycling and self-sputter recycling to reach the high discharge currents [74].

The reaction rates for loss and gain of argon atoms within the IR are shown in figure 11. Electron impact ionization by primary electrons contributes 67% to the total rarefaction, while secondary electron ionization contributes 18% to the loss of argon atoms and kick-out contributes 15%. The kick-out is 74% due to zirconium atoms sputtered from the targets and 26% due to hot argon atoms. The diffusion term is analyzed further in figure 12 and shows a refill by cold argon atoms and loss due to diffusion of warm and hot argon atoms out of the IR. At the peak in the degree of working gas rarefaction cold argon atoms in the ground state constitute 50%, metastable argon atoms 0.4%, warm argon atoms 32%, and hot argon atoms 18% of the argon atoms within the IR.

3.7. Tungsten target

Earlier, we applied the IRM to study a HiPIMS discharge with 75 mm diameter tungsten target as the discharge voltage was varied [53]. The peak discharge current and the peak discharge current density $J_{D,peak}$ increases in the range 0.33 – 0.73 $A\,cm^{-2}$, with increased discharge voltage in the range 500 – 800 V. The details of the experiment, experimental setup, and method can be found elsewhere [36]. The model results show that when operating with a tungsten target an initial peak appears in the discharge current, which is due to argon ions

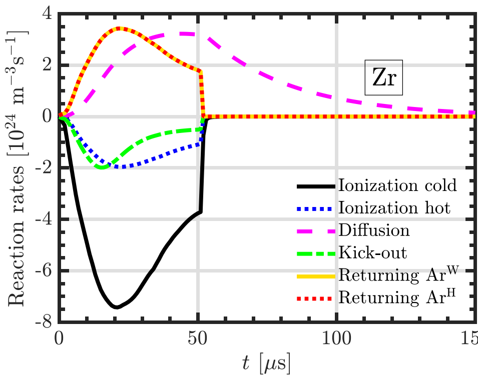

Figure 11. The reaction rates for the argon atom loss and argon atom gain within the ionization region for a discharge with 50 mm diameter Zr target operated at working gas pressure of 1 Pa, with a discharge voltage $V_D = 550$ V giving peak discharge current density of $J_{D,peak} = 1.0$ A cm^{-2} and 50 μs long pulse.

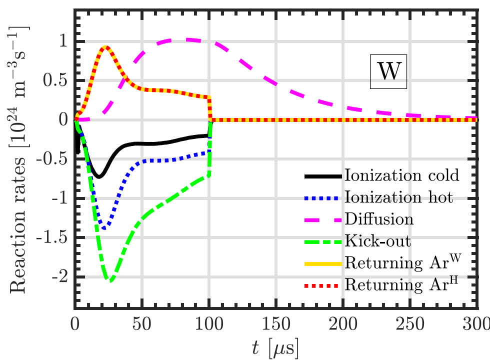

Figure 13. The reaction rates for the argon atom loss and argon atom gain within the ionization region for a discharge with 75 mm tungsten target operated at working gas pressure of 1 Pa, with a discharge voltage of $V_D = 600$ V giving peak discharge current $I_{D,peak}$ of 24 A ($J_{D,peak} = 0.54$ A cm^{-2}) for 100 μs long pulse.

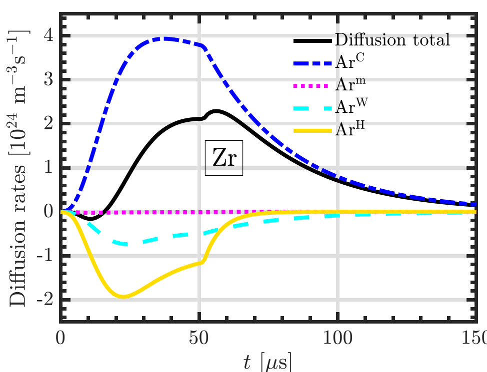

Figure 12. The reaction rates for the cold argon atom diffusion and warm and hot argon atom escaping the ionization region for a discharge with 50 mm diameter Zr target operated at working gas pressure of 1 Pa, with a discharge voltage $V_D = 550$ V giving peak discharge current density of $J_{D,peak} = 1.0$ A cm^{-2} and 50 μs long pulse.

bombarding the cathode target [53]. After this initial peak W^+ ions become the dominating ions and remain as such to the end of the pulse, and the role of W^+ ions increases with increased discharge voltage [53]. However, there is always a rather significant contribution from the Ar^+ ions, which contribute to the creation of secondary electrons. For the sputtered tungsten the back-attraction probability β_t decreases from 91% to 68% with increasing discharge voltage. With increased discharge voltage, the degree of working gas rarefaction increases from 34% at 500 V ($J_{D,peak} = 0.33$ A cm^{-2}) to 64% at 800 V ($J_{D,peak} = 0.73$ A cm^{-2}), when all the neutral argon species are included in the calculation. These are somewhat lower values than we reported in the earlier work [53] as there the degree of rarefaction was calculated assuming only cold argon atoms in the ground state when reporting the degree of working gas rarefaction.

Figure 13 shows the reaction rates for the loss and gain of argon atoms within the IR for the 600 V ($J_{D,peak} = 0.54$ A cm^{-2}) case explored earlier by Suresh Babu *et al* [53]. The degree of working gas rarefaction peaked at 46% when all the argon atoms are taken into account. We see that the main contributor to the loss of argon atoms from the IR is kick-out of the argon atoms by tungsten atoms sputtered from the target. The second most important loss process is electron impact ionization by secondary electrons followed by electron impact ionization by the primary electrons. Charge exchange has negligible contribution (not shown). Diffusional refill of argon atoms is the main contributor to adding argon to the IR, while warm and hot argon atoms released from the target also have a contribution to add argon atoms to the IR. The reaction rates for the warm and hot argon atoms are the same and overlap, due to the assumption that an equal number of argon atoms leaves the target during one pulse [47]. The diffusion of argon atoms is explored further in figure 14, where it is seen that the main contribution to the diffusion is the refill of cold argon atoms into the IR, while the warm and hot argon atoms escape out of the IR, and as expected that the hot argon atoms are lost faster than the warm atoms. The total diffusion is also shown in figure 14. At the peak in the degree of working gas rarefaction cold argon atoms in the ground state constitute 78%, warm argon atoms 17%, and hot argon atoms 5% of the argon atoms within the IR.

Figure 15 shows the contribution of each of the terms to the working gas rarefaction versus the peak current density. We see that kick-out has 49%–56% contribution to working gas rarefaction and is the dominating process, and its relative contribution increases with increased discharge current density.

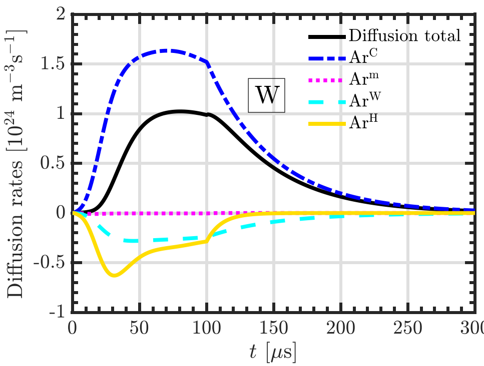

Figure 14. The reaction rates for the argon atom diffusion and hot and warm argon atoms escaping out of the ionization region for a discharge with 75 mm tungsten target operated at working gas pressure of 1 Pa, with a discharge voltage of $V_D = 600$ V giving peak discharge current $I_{D,peak}$ of 24 A ($J_{D,peak} = 0.54$ A cm^{-2}) for 100 μs long pulse.

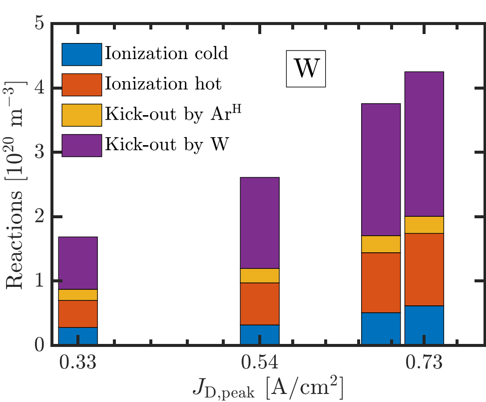

Figure 15. The contribution of the various processes to working gas rarefaction within the ionization region for a discharge with 75 mm tungsten target versus the discharge current density for argon working gas pressure of 1 Pa and pulse length of 100 μs.

The kick-out is mostly due to tungsten atoms sputtered out of the target. The second most important process is electron impact ionization by secondary electrons, which has about 30% contribution, and its role also increases with increased discharge current density. The contributions of electron impact ionization by primary electrons is always smaller.

4. Discussion

We have applied the IRM to determine the various contributions to working gas rarefaction in HiPIMS discharges with a number of different cathode targets, spanning a wide range

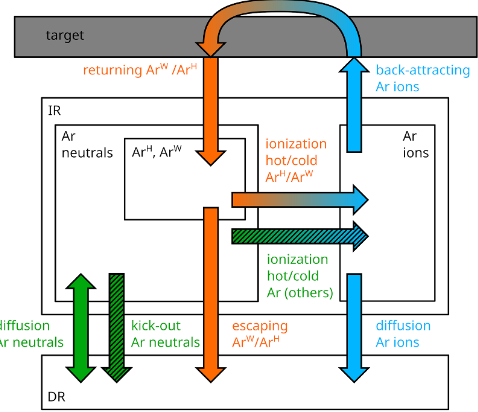

Figure 16. A schematic showing the processes involved in working gas rarefaction. The green arrows denote the neutrals, orange the hot (Ar^H) and warm (Ar^W) argon atoms, and blue arrows denote the ions. Metal sputtering and its influence on working gas rarefaction is omitted in this sketch for clarity.

in atomic mass and sputter yield. We have observed that the working gas rarefaction is driven by electron impact ionization by both primary and hot electrons as well as by kick-out by fast neutrals coming from the target. We observed charge-exchange to have a negligible contribution to working gas rarefaction for all the target materials.

Figure 16 shows the different pathways for argon atoms within the IR and how they enter and are lost from the IR. The green arrows denote the neutrals, orange the hot and warm argon atoms (Ar^H and Ar^W), and blue arrows denote the ions. The argon ions that bombard the target return to the IR as hot (Ar^H) and warm (Ar^W) argon atoms. The argon atoms can be kicked out into the DR by hot argon atoms Ar^H and by sputtered metal neutrals M (not shown in figure 16) and cold argon neutrals can be re-filled from the DR. We see that diffused Ar^W and Ar^H can be ionized and back-attracted again. This loop can proceed several times and appears as a working gas recycling loop [74]. Eventually, these particles escape from the IR. To not overestimate the contribution of ionization to the overall rarefaction, in the following we count only the first ionization of the argon species (hatched horizontal arrow). This can then be compared to the kick-out of argon neutrals by sputtered species and hot argon atoms (vertical hatched arrow). These are the two principal processes that lead to working gas rarefaction.

Figure 17 shows the various contributions to rarefaction, versus the atomic mass of the target material for discharges operated at discharge current densities close to 1 A cm^{-2} and working gas pressures close to 1 Pa. The results show that the processes that are responsible for working gas rarefaction and their relative contributions vary greatly depending on the target material. The relative contribution is determined by integrating the reaction rate for each process throughout the entire

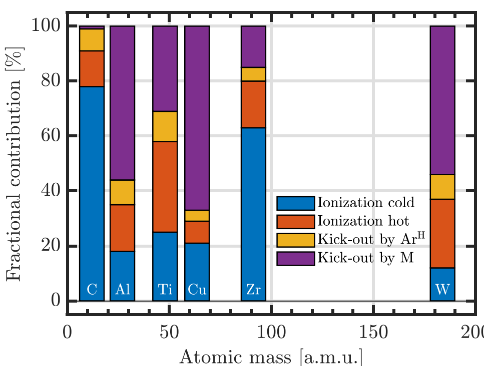

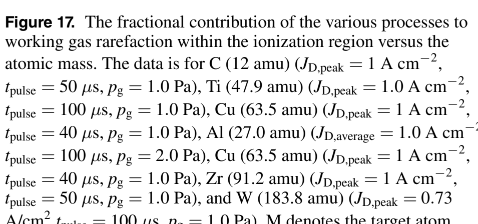

Figure 17. The fractional contribution of the various processes to working gas rarefaction within the ionization region versus the atomic mass. The data is for C (12 amu) ($J_{\mathrm{D,peak}} = 1$ A cm^{-2}, $t_{\mathrm{pulse}} = 50$ μs, $p_{\mathrm{g}} = 1.0$ Pa), Ti (47.9 amu) ($J_{\mathrm{D,peak}} = 1.0$ A cm^{-2}, $t_{\mathrm{pulse}} = 100$ μs, $p_{\mathrm{g}} = 1.0$ Pa), Cu (63.5 amu) ($J_{\mathrm{D,peak}} = 1$ A cm^{-2}, $t_{\mathrm{pulse}} = 40$ μs, $p_{\mathrm{g}} = 1.0$ Pa), Al (27.0 amu) ($J_{\mathrm{D,average}} = 1.0$ A cm^{-2}, $t_{\mathrm{pulse}} = 100$ μs, $p_{\mathrm{g}} = 2.0$ Pa), Cu (63.5 amu) ($J_{\mathrm{D,peak}} = 1$ A cm^{-2}, $t_{\mathrm{pulse}} = 40$ μs, $p_{\mathrm{g}} = 1.0$ Pa), Zr (91.2 amu) ($J_{\mathrm{D,peak}} = 1$ A cm^{-2}, $t_{\mathrm{pulse}} = 50$ μs, $p_{\mathrm{g}} = 1.0$ Pa), and W (183.8 amu) ($J_{\mathrm{D,peak}} = 0.73$ A/cm^2 $t_{\mathrm{pulse}} = 100$ μs, $p_{\mathrm{g}} = 1.0$ Pa). M denotes the target atom.

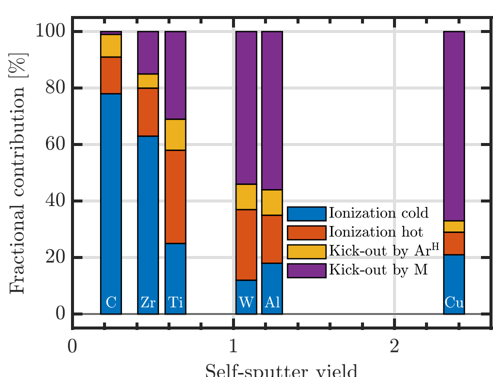

Figure 18. The fractional contribution of the various processes to working gas rarefaction within the ionization region versus self-sputter yield. The data is for C (0.24, 12 amu) ($J_{\mathrm{D,peak}} = 1$ A cm^{-2}, $t_{\mathrm{pulse}} = 50$ μs, $p_{\mathrm{g}} = 1.0$ Pa), Zr (0.47, 91.2 amu) ($J_{\mathrm{D,peak}} = 1$ A cm^{-2}, $t_{\mathrm{pulse}} = 50$ μs, $p_{\mathrm{g}} = 1.0$ Pa), Ti (0.64, 47.9 amu) ($J_{\mathrm{D,peak}} = 1.0$ A cm^{-2}, $t_{\mathrm{pulse}} = 100$ μs, $p_{\mathrm{g}} = 1.0$ Pa), W (1.14, 183.8 amu) ($J_{\mathrm{D,peak}} = 0.73$ A/cm^2 $t_{\mathrm{pulse}} = 100$ μs, $p_{\mathrm{g}} = 1.0$ Pa), Al (1.19, 27.0 amu) ($J_{\mathrm{D,average}} = 1.0$ A cm^{-2}, $t_{\mathrm{pulse}} = 100$ μs, $p_{\mathrm{g}} = 2.0$ Pa), and Cu (2.37, 63.5 amu) ($J_{\mathrm{D,peak}} = 1$ A cm^{-2}, $t_{\mathrm{pulse}} = 40$ μs, $p_{\mathrm{g}} = 1.0$ Pa). M denotes the target atom.

pulse and the afterglow. Table 1 summarizes the atomic properties, for the six target atoms explored. The role of electron impact ionization by primary electrons is significant for most of the target materials explored, while its contribution is however smaller for a discharge with copper and tungsten targets. Electron impact ionization by hot (secondary) electrons has ∼10% contribution when operating with a graphite target while for titanium and tungsten targets the contribution is ∼30%. We also note, for the zirconium case that the role of electron impact ionization is large, or well over 80%, when both primary and secondary electrons are taken into account, while kick-out has only a small contribution. For titanium the overall contribution of electron impact ionization is high or almost 60%. The role of kick-out, or sputter wind, plays a significant role in a discharge with target made of the heaviest target atom, tungsten (183.8 amu), and a larger and indeed rather significant role for a discharge with a copper (63.5 amu) target, while for a discharge with a zirconium (91.2 amu) target the contribution is small. There is therefore no apparent dependence of the various contributions on the target atom mass as can be seen in figure 17.

The missing correlation between target material mass and the contribution to the overall gas rarefaction by the kick-out mechanism is to be expected, as our kick-out model does not explicitly depend on the mass ratios. The justification is based on the fact that argon species are quickly lost on time scales that are short compared to typical pulse lengths (see section 2.1). This short residence time of an argon species in the IR after a collision is in our model therefore approximated by zero. In addition there is at most one collision between a sputtered species from the target and an argon species, due to the long mean free path compared to typical heights of the IR (see section 2.1). The momentum of a sputtered species is therefore unlikely to be shared between more than one argon species. This leads us to the conclusion that the mass ratio is only of secondary importance for determining the contribution of kick-out to the overall gas rarefaction.

Figure 18 shows the fractional contributions of the various processes to working gas rarefaction versus the self-sputter yield of the various target ions. Note that we have chosen to plot the data versus the self-sputter yield, although for argon-dominated discharges, the sputter yield would be the more relevant parameter. For the materials under investigation here, the numerical value of both is very similar, which is why the plot and the conclusions drawn from it would not change if we had used the sputter yield instead of the self-sputter yield. We see that the fractional contribution of kick-out increases with increased self-sputter yield. The total contribution of electron impact ionization decreases with increased self-sputter yield. The sputter yield or the self-sputter yield appears to be the primary factor for which process is the dominating contributor to working gas rarefaction. This is the reason why kick-out is so significant for copper, which has high sputter yield, even though the mass ratio and cohesive energy are smaller than for Zr. In general we see that for the metal targets the kick-out is mainly due to metal atoms sputtered from the target and that kick-out by hot argon atoms has smaller contribution. This is different for the graphite target where hot argon atoms are the dominant contributor by far and carbon atoms only have a small contribution due to its low sputter yield.

A secondary trend is visible in the data in figure 18. From copper with a high sputter yield, to titanium with a moderate sputter yield, the contribution of electron impact ionization increases as discussed in the preceding paragraph. At the same time the share of electron impact ionization from the hot electron population increases. This is due to the IR becoming more argon-dominated as opposed to metal-dominated. As the bombardment of a metal target with argon ions produces secondary electrons, while the bombardment of singly ionized metal ions does not, there is a higher density of hot electrons in these discharges, explaining the stronger contribution of ionization from this electron population for titanium compared to copper. The continuation of this trend cannot be seen for zirconium, nor for graphite.

The above observations, and the discussion above on the working gas rarefaction, highlights its importance for the deposition processes based on magnetron sputtering. In some of the earlier studies of working gas rarefaction [27, 33, 81] the deposition flux is suggested to be influenced in both its magnitude and kinetic energy by the working gas rarefaction. On the one hand, the reduced density of heavy species in a pronounced rarefaction window decreases the energy dissipation of sputtered species on their path through the IR and to the substrate [33], while on the other hand, fewer particles are scattered, possibly increasing the deposition rate in the axial direction [27, 81]. Finally, the reduction of heavy species in front of the target also reduces electron-neutral collision frequency and, therefore, reduces classical (collisional) diffusion of electrons across the magnetic field lines, which is suggested to promote the appearance of plasma instabilities, termed spokes, to provide an alternative path for electron transport across the magnetic field lines [82–85]. These spokes have been suggested to positively influence the release of target ions toward the substrate [86]. Studying the effect of the degree of gas rarefaction on the thin film deposition process is left for the future.

5. Conclusion

The IRM has been applied to determine the degree of working gas rarefaction and the relative contribution of various processes to working gas rarefaction in HiPIMS discharges with different target materials. The dominating contribution of the various processes to working gas rarefaction varies between the different target materials. For targets with low sputter yield electron impact ionization is the dominating process, while for high sputter yield target materials, tungsten as well as copper targets, kick-out of argon atoms by the metal atoms is the dominating process, with over 60% contribution. For the metal targets the magnitude of the kick-out is mainly due to metal atoms sputtered from the target and kick-out by hot argon atoms has a smaller contribution. For the graphite target, the small kick-out contribution is dominated by a kick-out by the hot argon atoms, while carbon atoms only have a small contribution. The sputter yield is the primary factor that dictates which process is the most important when it comes to working gas rarefaction. We also see that the degree of working gas rarefaction depends on the working gas pressure as demonstrated for a discharge with an aluminum target. Working gas rarefaction is much more significant for the lower pressures and the kick-out mechanism is a much more important at higher working gas pressure. Furthermore, we note that in most cases there is a significant fraction of hot and warm argon atoms within the IR. This value is highest or 67% when operating with the graphite target. However, this fraction is smaller for the copper target (16%) and the tungsten target (26%), as much of the sputtering is self-sputtering. This may explain the high neutral gas temperature that has been observed experimentally [42].

Data availability statement

All data that support the findings of this study are included within the article (and any supplementary files).

Acknowledgments

This work was partially supported by the University of Iceland Research Fund for Doctoral students, the Icelandic Research Fund Grant Nos. 196141 and 217999, the University of Iceland Research Fund Grant No. 93940 and the Swedish Government Strategic Research Area in Materials Science on Functional Materials at Linköping University (Faculty Grant SFO-Mat-LiU No. 2009-00971).

ORCID iDs

Kateryna Barynova https://orcid.org/0009-0009-0894-6160
Martin Rudolph https://orcid.org/0000-0002-0854-6708
Swetha Suresh Babu https://orcid.org/0000-0001-5360-5562
Joel Fischer https://orcid.org/0000-0001-9116-6302
Daniel Lundin https://orcid.org/0000-0001-8591-1003
Michael A Raadu https://orcid.org/0000-0002-1299-5039
Nils Brenning https://orcid.org/0000-0003-1308-9270
Jon Tomas Gudmundsson https://orcid.org/0000-0002-8153-3209

References

[1] Rossnagel S M 1999 *IBM J. Res. Dev.* **43** 163
[2] Kelly P J and Arnell R D 2000 *Vacuum* **56** 159
[3] Gudmundsson J T 2020 *Plasma Sources Sci. Technol.* **29** 113001
[4] Gudmundsson J T, Anders A and von Keudell A 2022 *Plasma Sources Sci. Technol.* **31** 083001
[5] Gudmundsson J T 2010 *Vacuum* **84** 1360
[6] Gudmundsson J T, Brenning N, Lundin D and Helmersson U 2012 *J. Vac. Sci. Technol.* A **30** 030801
[7] D Lundin, T Minea and J T Gudmundsson ed 2020 *High Power Impulse Magnetron Sputtering: Fundamentals, Technologies, Challenges and Applications* (Elsevier)
[8] Cada M, Gudmundsson J T and Lundin D 2020 Electron dynamics in high power impulse magnetron sputtering discharges *High Power Impulse Magnetron Sputtering: Fundamentals, Technologies, Challenges and Applications*

ed D Lundin, T Minea and J T Gudmundsson (Elsevier) pp 81–110
[9] Rudolph M, Brenning N, Hajihoseini H, Raadu M A, Minea T M, Anders A, Lundin D and Gudmundsson J T 2022 *J. Phys. D: Appl. Phys.* **55** 015202
[10] Lundin D, Cada M and Hubicka Z 2015 *Plasma Sources Sci. Technol.* **24** 035018
[11] Hajihoseini H, Cada M, Hubicka Z, Ünaldi S, Raadu M A, Brenning N, Gudmundsson J T and Lundin D 2019 *Plasma* **2** 201
[12] Samuelsson M, Lundin D, Jensen J, Raadu M A, Gudmundsson J T and Helmersson U 2010 *Surf. Coat. Technol.* **202** 591
[13] Alami J, Petersson P O Å, Music D, Gudmundsson J T, Bohlmark J and Helmersson U 2005 *J. Vac. Sci. Technol.* A **23** 278
[14] Helmersson U, Lattemann M, Bohlmark J, Ehiasarian A P and Gudmundsson J T 2006 *Thin Solid Films* **513** 1
[15] Greczynski G, Mráz S, Schneider J M and Hultman L 2020 *J. Appl. Phys.* **127** 180901
[16] Thompson M W 1968 *Phil. Mag.* **18** 377
[17] Hofer W O 1991 Angular, energy, and mass distribution of sputtered particles *Sputtering by Particle Bombardment III: Characteristics of Sputtered Particles, Technical Applications* (*Topics in Applied Physics* vol 64) ed R Behrisch and K Wittmaack (Springer) pp 15–90
[18] Gnaser H 2007 Energy and angular distributions of sputtered species *Sputtering by Particle Bombardment: Experiments and Computer Calculations From Threshold to MeV Energies* (*Topics in Applied Physics* vol 110) ed R Behrisch and W Eckstein (Springer) ch 5, pp 231–328
[19] Hoffman D W 1985 *J. Vac. Sci. Technol.* A **3** 561
[20] Rossnagel S M 1988 *J. Vac. Sci. Technol.* A **6** 19
[21] Rossnagel S M and Kaufman H R 1988 *J. Vac. Sci. Technol.* A **6** 223
[22] Rossnagel S M 1988 *J. Vac. Sci. Technol.* A **6** 1821
[23] Drüsedau T P 2002 *J. Vac. Sci. Technol.* A **20** 459
[24] Palmero A, Rudolph H and Habraken F H P M 2005 *Appl. Phys. Lett.* **87** 071501
[25] Palmero A, Rudolph H and Habraken F H P M 2006 *Thin Solid Films* **515** 631
[26] Palmero A, Rudolph H and Habraken F H P M 2006 *Appl. Phys. Lett.* **89** 211501
[27] Kobayashi T 2001 *Appl. Surf. Sci.* **169–170** 405
[28] Serikov V V, Kawamoto S and Nanbu K 1999 *IEEE Trans. Plasma Sci.* **27** 1389
[29] Kolev I and Bogaerts A 2008 *J. Appl. Phys.* **104** 093301
[30] Lundin D, Brenning N, Jadernas D, Larsson P, Wallin E, Lattemann M, Raadu M A and Helmersson U 2009 *Plasma Sources Sci. Technol.* **18** 045008
[31] Alami J, Sarakinos K, Mark G and Wuttig M 2006 *Appl. Phys. Lett.* **89** 154104
[32] Vlcek J, Pajdarová A D and Musil J 2004 *Contrib. Plasma Phys.* **44** 426
[33] Palmucci M, Britun N, Konstantinidis S and Snyders R 2013 *J. Appl. Phys.* **114** 113302
[34] Hecimovic A, de los Arcos T, Schulz-von der Gathen V, Böke M and Winter J 2012 *Plasma Sources Sci. Technol.* **21** 035017
[35] Liebig B, Braithwaite N S J, Kelly P J and Bradley J W 2010 *Thin Solid Films* **519** 1699
[36] Shimizu T, Takahashi K, Boyd R, Viloan R P, Keraudy J, Lundin D, Yang M and Helmersson U 2021 *J. Appl. Phys.* **129** 155305
[37] Horwat D and Anders A 2010 *J. Appl. Phys.* **108** 123306
[38] Ferrec A, Kéraudy J and Jouan P-Y 2016 *Appl. Surf. Sci.* **390** 497
[39] Greczynski G, Zhirkov I, Petrov I, Greene J E and Rosen J 2017 *J. Vac. Sci. Technol.* A **35** 060601
[40] Greczynski G, Zhirkov I, Petrov I, Greene J E and Rosen J 2018 *J. Vac. Sci. Technol.* A **36** 020602
[41] Li X, Bakhit B, Johansson Jõesaar M P, Hultman L, Petrov I and Greczynski G 2021 *Surf. Coat. Technol.* **415** 127120
[42] Vitelaru C, Lundin D, Stancu G D, Brenning N, Bretagne J and Minea T 2012 *Plasma Sources Sci. Technol.* **21** 025010
[43] Kadlec S 2007 *Plasma Process. Polym.* **4** S419
[44] Kozák T and Lazar J 2018 *Plasma Sources Sci. Technol.* **27** 115012
[45] Kozák T 2023 *Plasma Sources Sci. Technol.* **32** 035007
[46] Huo C, Lundin D, Gudmundsson J T, Raadu M A, Bradley J W and Brenning N 2017 *J. Phys. D: Appl. Phys.* **50** 354003
[47] Huo C, Raadu M A, Lundin D, Gudmundsson J T, Anders A and Brenning N 2012 *Plasma Sources Sci. Technol.* **21** 045004
[48] Huo C, Lundin D, Raadu M A, Anders A, Gudmundsson J T and Brenning N 2014 *Plasma Sources Sci. Technol.* **23** 025017
[49] Gudmundsson J T, Lundin D, Stancu G D, Brenning N and Minea T M 2015 *Phys. Plasmas* **22** 113508
[50] Stancu G D, Brenning N, Vitelaru C, Lundin D and Minea T 2015 *Plasma Sources Sci. Technol.* **24** 045011
[51] Rudolph M, Hajihoseini H, Raadu M A, Gudmundsson J T, Brenning N, Minea T M, Anders A and Lundin D 2021 *J. Appl. Phys.* **129** 033303
[52] Gudmundsson J T, Fischer J, Hinriksson B P, Rudolph M and Lundin D 2022 *Surf. Coat. Technol.* **442** 128189
[53] Suresh Babu S, Rudolph M, Lundin D, Shimizu T, Fischer J, Raadu M A, Brenning N and Gudmundsson J T 2022 *Plasma Sources Sci. Technol.* **31** 065009
[54] Suresh Babu S, Rudolph M, Ryan P J, Fischer J, Lundin D, Bradley J W and Gudmundsson J T 2023 *Plasma Sources Sci. Technol.* **32** 034003
[55] Eliasson H, Rudolph M, Brenning N, Hajihoseini H, Zanáska M, Adriaans M J, Raadu M A, Minea T M, Gudmundsson J T and Lundin D 2021 *Plasma Sources Sci. Technol.* **30** 115017
[56] Suresh Babu S, Fischer J, Rudolph M, Lundin D and Gudmundsson J T 2024 *J. Vac. Sci. Technol.* A **42** accepted
[57] Raadu M A, Axnäs I, Gudmundsson J T, Huo C and Brenning N 2011 *Plasma Sources Sci. Technol.* **20** 065007
[58] Rudolph M, Revel A, Lundin D, Hajihoseini H, Brenning N, Raadu M A, Anders A, Minea T M and Gudmundsson J T 2021 *Plasma Sources Sci. Technol.* **30** 045011
[59] Gudmundsson J T, Lundin D, Brenning N, Raadu M A, Huo C and Minea T M 2016 *Plasma Sources Sci. Technol.* **25** 065004
[60] Anders A 2010 *J. Vac. Sci. Technol.* A **28** 783
[61] Schmid M 2024 A simple sputter yield calculator (Surface Physics, Institute of Applied Physics, Technischen Universität Wien) (available at: www2.iap.tuwien.ac.at/www/surface/sputteryield)
[62] Matsunami N, Yamamura Y, Itikawa Y, Itoh N, Kazumata Y, Miyagawa S, Morita K, Shimizu R and Tawara H 1983 Energy dependence of the yields of ion-induced sputtering of monatomic solids *Technical Report* IPPJ-AM-32 (Institute of Plasma Physics, Nagoya University)
[63] Yamamura Y and Ishida M 1995 *J. Vac. Sci. Technol.* A **13** 101
[64] Rudolph M, Lundin D, Foy E, Debongnie M, Hugon M-C and Minea T 2018 *Thin Solid Films* **658** 46
[65] Anders A, Capek J, Hála M and Martinu L 2012 *J. Phys. D: Appl. Phys.* **45** 012003
[66] Huo C, Lundin D, Raadu M A, Anders A, Gudmundsson J T and Brenning N 2013 *Plasma Sources Sci. Technol.* **22** 045005
[67] Phelps A V, Greene C H, Burke J P and Phelps A V 2000 *J. Phys. B: At. Mol. Opt. Phys.* **33** 2965

[68] Clementi E, Raimondi D L and Reinhardt W P 1967 *J. Chem. Phys.* **47** 1300
[69] Kittel C 2005 *Introduction to Solid State Physics* 8th edn (Wiley)
[70] Antunes V G, Rudolph M, Kapran A, Hajihoseini H, Raadu M A, Brenning N, Gudmundsson J T, Lundin D and Minea T 2023 *Plasma Sources Sci. Technol.* **32** 075016
[71] Renner M, Fischer J, Hajihoseini H, Gudmundsson J T, Rudolph M and Lundin D 2023 *J. Vac. Sci. Technol.* A **41** 033009
[72] Hajihoseini H, Brenning N, Rudolph M, Raadu M A, Lundin D, Fischer J, Minea T M and Gudmundsson J T 2022 *J. Vac. Sci. Technol.* A **41** 013002
[73] Anders A, Andersson J and Ehiasarian A 2007 *J. Appl. Phys.* **102** 113303
[74] Brenning N, Gudmundsson J T, Raadu M A, Petty T J, Minea T and Lundin D 2017 *Plasma Sources Sci. Technol.* **26** 125003
[75] Butler A, Brenning N, Raadu M A, Gudmundsson J T, Minea T and Lundin D 2018 *Plasma Sources Sci. Technol.* **27** 105005
[76] Kouznetsov V, Macák K, Schneider J M, Helmersson U and Petrov I 1999 *Surf. Coat. Technol.* **122** 290
[77] Fischer J, Renner M, Gudmundsson J T, Rudolph M, Hajihoseini H, Brenning N and Lundin D 2023 *Plasma Sources Sci. Technol.* **32** 125006
[78] Cemin F, Lundin D, Cammilleri D, Maroutian T, Lecoeur P and Minea T 2016 *J. Vac. Sci. Technol.* A **34** 051506
[79] Hajihoseini H, Cada M, Hubicka Z, Ünaldi S, Raadu M A, Brenning N, Gudmundsson J T and Lundin D 2020 *J. Vac. Sci. Technol.* A **38** 033009
[80] Rudolph M, Brenning N, Hajihoseini H, Raadu M A, Fischer J, Gudmundsson J T and Lundin D 2022 *J. Vac. Sci. Technol.* A **40** 043005
[81] Drüsedau T P, Löhmann M and Garke B 1998 *J. Vac. Sci. Technol.* A **16** 2728
[82] Lundin D, Helmersson U, Kirkpatrick S, Rohde S and Brenning N 2008 *Plasma Sources Sci. Technol.* **17** 025007
[83] Anders A, Ni P and Rauch A 2012 *J. Appl. Phys.* **111** 053304
[84] Hecimovic A and von Keudell A 2018 *J. Phys. D: Appl. Phys.* **51** 453001
[85] Rudolph M, Kalanov D, Diyatmika W and Anders A 2021 *J. Appl. Phys.* **130** 243301
[86] Biskup B, Maszl C, Breilmann W, Held J, Böke M, Benedikt J and von Keudell A 2018 *J. Phys. D: Appl. Phys.* **51** 115201

References

Abroyan, I. A., M. A. Eremeev, and N. N. Petrov (1967). Excitation of electrons in solids by relatively slow atomic particles. *Physics–Uspekhi 10*(3), 332–367.

Alami, J., P. O. Å. Petersson, D. Music, J. T. Gudmundsson, J. Bohlmark, and U. Helmersson (2005). Ion-assisted physical vapor deposition for enhanced film deposition on non-flat surfaces. *Journal of Vacuum Science and Technology A 23*(2), 278–280.

Alami, J., K. Sarakinos, G. Mark, and M. Wuttig (2006). On the deposition rate in a high power pulsed magnetron sputtering discharge. *Applied Physics Letters 89*(15), 154104.

Alami, J., K. Sarakinos, F. Uslu, and M. Wuttig (2009). On the relationship between the peak target current and the morphology of chromium nitride thin films deposited by reactive high power pulsed magnetron sputtering. *Journal of Physics D: Applied Physics 42*(1), 015304.

Alves, L. L. (2014). The IST-LISBON database on LXCat. *Journal of Physics: Conference Series 565*, 012007.

Anders, A. (2010). Deposition rates of high power impulse magnetron sputtering: Physics and economics. *Journal of Vacuum Science and Technology A 28*(4), 783–790.

Anders, A. (2012). Self-organization and self-limitation in high power impulse magnetron sputtering. *Applied Physics Letters 100*(22), 224104.

Anders, A., J. Čapek, M. Hála, and L. Martinu (2012). The 'recycling trap': a generalized explanation of discharge runaway in high-power impulse magnetron sputtering. *Journal of Physics D: Applied Physics 45*(1), 012003.

Anders, A., P. Ni, and A. Rauch (2012). Drifting localization of ionization runaway: Unraveling the nature of anomalous transport in high power impulse magnetron sputtering. *Journal of Applied Physics 111*(5), 053304.

Antunes, V. G., M. Rudolph, A. Kapran, H. Hajihoseini, M. A. Raadu, N. Brenning, J. T. Gudmundsson, D. Lundin, and T. Minea (2023). Influence of the magnetic field on the dimension of the ionization region in high power impulse magnetron sputtering discharges. *Plasma Sources Science and Technology 32*(7), 075016.

Ashida, S., C. Lee, and M. A. Lieberman (1995). Spatially averaged (global) model of time modulated high density argon plasma. *Journal of Vacuum Science and Technology A 13*(5), 2498–2507.

Barynova, K., S. Suresh Babu, M. Rudolph, J. Fischer, D. Lundin, M. A. Raadu, N. Brenning, and J. T. Gudmundsson (2024). On working gas rarefaction in high power impulse magnetron sputtering. *Plasma Sources Science and Technology 33*(6), 065010.

Biersack, J. P. and L. G. Haggmark (1980). A Monte Carlo computer program for the transport of energetic ions in amorphous targets. *Nuclear Instruments and Methods 174*(1–2), 257–269.

Bird, G. A. (1994). *Gas Dynamics and The Direct Simulation of Gas Flows*, Volume 42 of *Oxford Engineering Science Series*. Oxford: Oxford University Press.

Birdsall, C. (1991). Particle-in-cell charged-particle simulations, plus Monte Carlo collisions with neutral atoms, PIC-MCC. *IEEE Transactions on Plasma Science 19*(2), 65–85.

Bohlmark, J., J. Alami, C. Christou, A. P. Ehiasarian, and U. Helmersson (2005). Ionization of sputtered metals in high power pulsed magnetron sputtering. *Journal of Vacuum Science and Technology A 23*(1), 18–22.

Bohlmark, J., J. T. Gudmundsson, J. Alami, M. Lattemann, and U. Helmersson (2005). Spatial electron density distribution in a high-power pulsed magnetron discharge. *IEEE Transactions on Plasma Science 33*(2), 346–347.

Bohlmark, J., M. Lattemann, J. T. Gudmundsson, A. P. Ehiasarian, Y. A. Gonzalvo, N. Brenning, and U. Helmersson (2006). The ion energy distributions and ion flux composition from a high power impulse magnetron sputtering discharge. *Thin Solid Films 515*(5), 1522–1526.

Bradley, J. W., A. Mishra, and P. J. Kelly (2015). The effect of changing the magnetic field strength on HiPIMS deposition rates. *Journal of Physics D: Applied Physics 48*(21), 215202.

Brenning, N., I. Axnäs, M. A. Raadu, D. Lundin, and U. Helmerson (2008). A bulk plasma model for dc and HiPIMS magnetrons. *Plasma Sources Science and Technology 17*(4), 045009.

Brenning, N., A. Butler, H. Hajihoseini, M. Rudolph, M. A. Raadu, J. T. Gudmundsson, T. Minea, and D. Lundin (2020). Optimization of HiPIMS discharges: The selection of pulse power, pulse length, gas pressure, and magnetic field strength. *Journal of Vacuum Science and Technology A 38*(3), 033008.

Brenning, N., J. T. Gudmundsson, M. A. Raadu, T. J. Petty, T. Minea, and D. Lundin (2017). A unified treatment of self-sputtering, process gas recycling, and runaway for high power impulse sputtering magnetrons. *Plasma Sources Science and Technology 26*(12), 125003.

Brenning, N., H. Hajihoseini, M. Rudolph, M. A. Raadu, J. T. Gudmundsson, T. M. Minea, and D. Lundin (2021). HiPIMS optimization by using mixed high-power and low-power pulsing. *Plasma Sources Science and Technology 30*(1), 015015.

Brenning, N., D. Lundin, M. A. Raadu, C. Huo, C. Vitelaru, G. D. Stancu, T. Minea, and U. Helmersson (2012). Understanding deposition rate loss in high power impulse magnetron sputtering: I. Ionization-driven electric fields. *Plasma Sources Science and Technology 21*(2), 025005.

Bugaev, S., V. G. Podkovyrov, K. V. Oskomov, S. Smaykina, and N. S. Sochugov (2001). Ion-assisted pulsed magnetron sputtering deposition of ta-C films. *Thin Solid Films 389*(1-2), 16–26.

Bugaev, S. P., N. N. Koval, N. S. Sochugov, and A. N. Zakharov (Berkeley, California, July 21–26, 1996). Investigation of a high-current pulsed magnetron discharge initiated in the low-pressure diffuse arc plasma. In *XVIIth International Symposium on Discharges and Electrical Insulation in Vacuum, 1996*, pp. 1074–1076.

Butler, A., N. Brenning, M. A. Raadu, J. T. Gudmundsson, T. Minea, and D. Lundin (2018). On three different ways to quantify the degree of ionization in sputtering magnetrons. *Plasma Sources Science and Technology 27*(10), 105005.

Buyle, G., D. Depla, K. Eufinger, and R. De Gryse (2004). Calculation of the effective gas interaction probabilities of the secondary electrons in a dc magnetron discharge. *Journal of Physics D: Applied Physics 37*(12), 1639–1647.

Cemin, F., D. Lundin, D. Cammilleri, T. Maroutian, P. Lecoeur, and T. Minea (2016). Low electrical resistivity in thin and ultrathin copper layers grown by high power impulse magnetron sputtering. *Journal of Vacuum Science and Technology A 34*(5), 051506.

Chakraborty, J., K. K. Kumar, S. Mukherjee, and S. K. Ray (2008). Stress, texture and microstructure of zirconium thin films probed by X-ray diffraction. *Thin Solid Films 516*(23), 8479–8486.

Christie, D. J. (2005). Target material pathways model for high power pulsed magnetron sputtering. *Journal of Vacuum Science and Technology A 23*(2), 330–335.

Coleman, C. E. (Ed.) (2022). *The Metallurgy of Zirconium*. Vienna, Austria: International Atomic Energy Agency.

DeKoven, B. M., P. R. Ward, R. E. Weiss, D. J. Christie, R. A. Scholl, W. D. Sproul, F. Tomasel, and A. Anders (2003). Carbon thin film deposition using high power pulsed magnetron sputtering. In *Society of Vacuum Coaters 46th Annual Technical Conference Proceedings, May 3 – 8, 2003, San Francisco, California*, Albuquerque, New Mexico, pp. 158–165. Society of Vacuum Coaters.

Deutsch, H., K. Becker, and T. Märk (2008). Calculated absolute cross-sections for the electron-impact ionization of atoms with atomic numbers between 20 and 56 using the Deutsch-Märk (DM) formalism. *International Journal of Mass Spectrometry 271*(1-3), 58–62.

Deutsch, H., K. Hilpert, K. Becker, M. Probst, and T. D. Märk (2001). Calculated absolute electron-impact ionization cross sections for AlO, Al_2O, and WO_x ($x = 1 - -3$). *Journal of Applied Physics 89*(3), 1915–1921.

Dixon, A. J., M. F. A. Harrison, and A. C. H. Smith (1973). Ionization of metastable rare gas atoms by electron impact. In B. C. Cobić and M. V. Kurepa (Eds.), *8th International Conference on the Physics of Electronic and Atomic Collisions (VIII ICPEAC)*, Belgrade, Yugoslavia, pp. 405–406. Institute of Physics.

Ehiasarian, A. P., P. Hovsepian, L. Hultman, and U. Helmersson (2004). Comparison of microstructure and mechanical properties of chromium nitride-based coatings deposited by high power impulse magnetron sputtering and by the combined steered cathodic arc/unbalanced magnetron technique. *Thin Solid Films 457*(2), 270–277.

Ehiasarian, A. P., J. G. Wen, and I. Petrov (2007). Interface microstructure engineering by

high power impulse magnetron sputtering for the enhancement of adhesion. *Journal of Applied Physics 101*(5), 054301.

Eliasson, H., M. Rudolph, N. Brenning, H. Hajihoseini, M. Zanáška, M. J. Adriaans, M. A. Raadu, T. M. Minea, J. T. Gudmundsson, and D. Lundin (2021). Modeling of high power impulse magnetron sputtering discharges with graphite target. *Plasma Sources Science and Technology 30*(11), 115017.

Emmerlich, J., S. Mráz, R. Snyders, K. Jiang, and J. M. Schneider (2008). The physical reason for the apparently low deposition rate during high power pulsed magnetron sputtering. *Vacuum 82*(8), 867–870.

Engwall, A. M., S. J. Shin, J. Bae, and Y. M. Wang (2019). Enhanced properties of tungsten films by high-power impulse magnetron sputtering. *Surface and Coatings Technology 363*, 191–197.

Fankhauser, J., M. Sato, D. Yu, A. Ebnonnasir, M. Kobashi, M. S. Goorsky, and S. Kodambaka (2016). Growth and characterization of epitaxial Zr(0001) thin films on Al_2O_3(0001). *Journal of Vacuum Science and Technology A 34*(5), 050616.

Fetisov, I. K., A. A. Filippov, G. V. Khodachenko, D. V. Mozgrin, and A. A. Pisarev (1999). Impulse irradiation plasma technology for film deposition. *Vacuum 53*(1-2), 133–136.

Fischer, J., M. Renner, J. T. Gudmundsson, M. Rudolph, H. Hajihoseini, N. Brenning, and D. Lundin (2023). Insights into the copper HiPIMS discharge: Deposition rate and ionised flux fraction. *Plasma Sources Science and Technology 32*(12), 125006.

Freund, R. S. (1987). Electron impact ionization cross-sections for atoms, radicals, and metastables. In L. C. Pitchford, B. V. McKoy, A. Chutjian, and S. Trajrnar (Eds.), *Swarm Studies and Inelastic Electron-Molecule Collisions Proceedings of the Meeting of the Fourth International Swarm Seminar and the Inelastic Electron-Molecule Collisions Symposium, July 19–23, 1985, Tahoe City, California, USA*, pp. 329–346. New York: Springer-Verlag.

Gudmundsson, J. T. (2006). The high power impulse magnetron sputtering discharge: Ionization mechanism. In *49th Annual Technical Conferenece Proceedings, April 22-27, 2006, Washington, D.C. USA*, Albuquerque, New Mexico, pp. 329 – 333. Society of Vacuum Coaters.

Gudmundsson, J. T. (2008). Ionization mechanism in the high power impulse magnetron sputtering (HiPIMS) discharge. *Journal of Physics: Conference Series 100*, 082013.

Gudmundsson, J. T. (2010). The high power impulse magnetron sputtering discharge as an ionized physical vapor deposition tool. *Vacuum 84*(12), 1360–1364.

Gudmundsson, J. T. (2020). Physics and technology of magnetron sputtering discharges. *Plasma Sources Science and Technology 29*(11), 113001.

Gudmundsson, J. T., J. Alami, and U. Helmersson (2002). Spatial and temporal behavior of the plasma parameters in a pulsed magnetron discharge. *Surface and Coatings Technology 161*(2-3), 249–256.

Gudmundsson, J. T., A. Anders, and A. von Keudell (2022). Foundations of physical vapor deposition with plasma assistance. *Plasma Sources Science and Technology 31*(8), 083001.

Gudmundsson, J. T., N. Brenning, D. Lundin, and U. Helmersson (2012). The high power impulse magnetron sputtering discharge. *Journal of Vacuum Science and Technology A 30*(3), 030801.

Gudmundsson, J. T., J. Fischer, B. P. Hinriksson, M. Rudolph, and D. Lundin (2022). Ionization region model of a high power impulse magnetron sputtering discharge of copper. *Surface and Coatings Technology 442*, 128189.

Gudmundsson, J. T., D. Lundin, N. Brenning, M. A. Raadu, C. Huo, and T. M. Minea (2016). An ionization region model of the reactive Ar/O_2 high power impulse magnetron sputtering discharge. *Plasma Sources Science and Technology 25*(6), 065004.

Gudmundsson, J. T., D. Lundin, G. D. Stancu, N. Brenning, and T. M. Minea (2015). Are the argon metastables important in high power impulse magnetron sputtering discharges ? *Physics of Plasmas 22*(11), 113508.

Gudmundsson, J. T., P. Sigurjonsson, P. Larsson, D. Lundin, and U. Helmersson (2009). On the electron energy in the high power impulse magnetron sputtering discharge. *Journal of Applied Physics 105*(12), 123302.

Gudmundsson, J. T. and E. G. Thorsteinsson (2007). Oxygen discharges diluted with argon: dissociation processes. *Plasma Sources Science and Technology 16*(2), 399–412.

Hagstrum, H. D. (1954). Auger ejection of electrons from tungsten by noble gas ions. *Physical Review 96*(2), 325–335.

Hagstrum, H. D. (1956). Auger ejection of electrons from tungsten by noble gas ions. *Physical Review 104*(2), 317–318.

Hajihoseini, H., N. Brenning, M. Rudolph, M. A. Raadu, D. Lundin, J. Fischer, T. M. Minea, and J. T. Gudmundsson (2022). Target ion and neutral spread in high power impulse magnetron sputtering. *Journal of Vacuum Science and Technology A 41*(1), 013002.

Hajihoseini, H., M. Čada, Z. Hubička, S. Ünaldi, M. A. Raadu, N. Brenning, J. T. Gudmundsson, and D. Lundin (2019). The effect of magnetic field strength and geometry on the deposition rate and ionized flux fraction in the HiPIMS discharge. *Plasma 2*(2), 201–221.

Held, J., V. Schulz-von der Gathen, and A. von Keudell (2023). Ionization of sputtered material in high power impulse magnetron sputtering plasmas – comparison of titanium, chromium and aluminum. *Plasma Sources Science and Technology 32*(6), 065006.

Helmersson, U., M. Lattemann, J. Bohlmark, A. P. Ehiasarian, and J. T. Gudmundsson (2006). Ionized physical vapor deposition (IPVD): A review of technology and applications. *Thin Solid Films 513*(1-2), 1–24.

Hopwood, J. (1998). Ionized physical vapor deposition of integrated circuit interconnects. *Physics of Plasmas 5*(5), 1624–1631.

Hubička, Z., J. T. Gudmundsson, P. Larsson, and D. Lundin (2020). Hardware and power management for high power impulse magnetron sputtering. In D. Lundin, T. Minea, and J. T. Gudmundsson (Eds.), *High Power Impulse Magnetron Sputtering: Fundamentals, Technologies, Challenges and Applications*, pp. 49–80. Amsterdam, The Netherlands: Elsevier.

Hubička, Z., Š. Kment, J. Olejníček, M. Čada, T. Kubart, M. Brunclíková, P. Kšírová, P. Adámek, and Z. Remeš (2013). Deposition of hematite Fe_2O_3 thin film by DC pulsed magnetron and DC pulsed hollow cathode sputtering system. *Thin Solid Films 549*, 184–191.

Huo, C. (2013). *Modeling and Experimental Studies of High Power Impulse Magnetron Sputtering Discharges*. Ph. D. thesis, KTH Royal Institute of Technology, Stockholm.

Huo, C., D. Lundin, J. T. Gudmundsson, M. A. Raadu, J. W. Bradley, and N. Brenning (2017). Particle-balance models for pulsed sputtering magnetrons. *Journal of Physics D: Applied Physics 50*(35), 354003.

Huo, C., D. Lundin, M. A. Raadu, A. Anders, J. T. Gudmundsson, and N. Brenning (2013). On sheath energization and ohmic heating in sputtering magnetrons. *Plasma Sources Science and Technology 22*(4), 045005.

Huo, C., D. Lundin, M. A. Raadu, A. Anders, J. T. Gudmundsson, and N. Brenning (2014). On the road to self-sputtering in high power impulse magnetron sputtering: particle balance and discharge characteristics. *Plasma Sources Science and Technology 23*(2), 025017.

Huo, C., M. A. Raadu, D. Lundin, J. T. Gudmundsson, A. Anders, and N. Brenning (2012). Gas rarefaction and the time evolution of long high-power impulse magnetron sputtering pulses. *Plasma Sources Science and Technology 21*(4), 045004.

Kadlec, S. (2007). Simulation of neutral particle flow during high power magnetron impulse. *Plasma Processes and Polymers 4*(S1), S419–S423.

Kapran, A., C. Ballage, Z. Hubička, and T. Minea (2024). 2D analysis of sputtered species transport in high-power impulse magnetron sputtering (HiPIMS) discharge. *Journal of Applied Physics 135*(17), 173302.

Kelly, P. J. and R. D. Arnell (2000). Magnetron sputtering: a review of recent developments and applications. *Vacuum 56*(3), 159–172.

Konstantinidis, S., A. Hemberg, J. P. Dauchot, and M. Hecq (2007). Deposition of zinc oxide layers by high-power impulse magnetron sputtering. *Journal of Vacuum Science and Technology B 25*(3), L19–L21.

Kouznetsov, V., K. Macák, J. M. Schneider, U. Helmersson, and I. Petrov (1999). A novel pulsed magnetron sputter technique utilizing very high target power densities. *Surface and Coatings Technology 122*(2-3), 290–293.

Kozák, T. (2023). Particle-based simulation of atom and ion transport in HiPIMS: effect of the plasma potential distribution on the ionized flux fraction. *Plasma Sources Science and Technology 32*(3), 035007.

Kozák, T. and J. Lazar (2018). Gas rarefaction in high power impulse magnetron sputtering: comparison of a particle simulation and volume-averaged models. *Plasma Sources Science and Technology 27*(11), 115012.

Kozák, T. and A. D. Pajdarová (2011). A non-stationary model for high power impulse magnetron sputtering discharges. *Journal of Applied Physics 110*(10), 103303.

Kubart, T., M. Čada, D. Lundin, and Z. Hubička (2014). Investigation of ionized metal flux fraction in HiPIMS discharges with Ti and Ni targets. *Surface and Coatings Technology 238*, 152–157.

Kuo, C.-C., C.-H. Lin, J.-T. Chang, and Y.-T. Lin (2021). Synchronized substrate bias in high-power impulse magnetron sputtering of zirconium films. *Coatings 11*(1), 7.

Lundin, D. (2010). *The HiPIMS Process*. Ph. D. thesis, Linköping University, Sweden.

Lundin, D., N. Brenning, D. Jadernas, P. Larsson, E. Wallin, M. Lattemann, M. A. Raadu, and U. Helmersson (2009). Transition between the discharge regimes of high power impulse magnetron sputtering and conventional direct current magnetron sputtering. *Plasma Sources Science and Technology 18*(4), 045008.

Lundin, D., M. Čada, and Z. Hubička (2015). Ionization of sputtered Ti, Al, and C coupled with plasma characterization in HiPIMS. *Plasma Sources Science and Technology 24*(3), 035018.

Lundin, D., J. T. Gudmundsson, N. Brenning, M. A. Raadu, and T. M. Minea (2017). A study of the oxygen dynamics in a reactive Ar/O_2 high power impulse magnetron sputtering discharge using an ionization region model. *Journal of Applied Physics 121*(17), 171917.

Lundin, D. and K. Sarakinos (2012). An introduction to thin film processing using high power impulse magnetron sputtering. *Journal of Materials Research 27*(5), 780–792.

Luo, H., F. Gao, and A. Billard (2019). Tunable microstructures and morphology of zirconium films via an assist of magnetic field in HiPIMS for improved mechanical properties. *Surface and Coatings Technology 374*, 822–832.

Magnus, F., A. S. Ingason, S. Olafsson, and J. T. Gudmundsson (2012). Nucleation and resistivity of ultrathin TiN films grown by high power impulse magnetron sputtering. *IEEE Electron Device Letters 33*(7), 1045–1047.

Magnus, F., A. S. Ingason, O. B. Sveinsson, S. Olafsson, and J. T. Gudmundsson (2011). Morphology of TiN thin films grown on SiO_2 by reactive high power impulse magnetron sputtering. *Thin Solid Films 520*(5), 1621–1624.

Matsunami, N., Y. Yamamura, Y. Itikawa, N. Itoh, Y. Kazumata, S. Miyagawa, K. Morita, R. Shimizu, and H. Tawara (1983, September). Energy dependence of the yields of ion-induced sputtering of monatomic solids. Technical Report IPPJ-AM-32, Institute of Plasma Physics, Nagoya University.

Metropolis, N., A. W. Rosenbluth, M. N. Rosenbluth, A. H. Teller, and E. Teller (1953). Equation of state calculations by fast computing machines. *Journal of Chemical Physics 21*(6), 1087–1092.

Metropolis, N. and S. Ulam (1949). The Monte Carlo method. *Journal of the American Statistical Association 44*(247), 335–341.

Minea, T., T. Kozák, C. Costin, J. T. Gudmundsson, and D. Lundin (2020). Modeling the high power impulse magnetron sputtering discharge. In D. Lundin, T. Minea, and J. T. Gudmundsson (Eds.), *High Power Impulse Mangetron Sputtering: Fundamentals, Technologies, Challenges and Applications*, pp. 159–221. Amsterdam, The Netherlands: Elsevier.

Minea, T. M., C. Costin, A. Revel, D. Lundin, and L. Caillault (2014). Kinetics of plasma species and their ionization in short-HiPIMS by particle modeling. *Surface and Coatings Technology 255*, 52–61.

Möller, W. and W. Eckstein (1984). TRIDYN - a TRIM simulation code including dynamic composition changes. *Nuclear Instruments and Methods in Physics Research Section B: Beam Interactions with Materials and Atoms 2*(1-3), 814–818.

Möller, W., W. Eckstein, and J. Biersack (1988). TRIDYN - binary collision simulation of atomic collisions and dynamic composition changes in solids. *Computer Physics Communications 51*(3), 355–368.

Montague, R. G. and M. F. A. Harrison (1984). A measurement of the cross section for electron impact ionisation of singly charged tungsten ions. *Journal of Physics B: Atomic, Molecular and Optical Physics 17*(13), 2707–2711.

Mozgrin, D. V. (1994). *High-current low-pressure quasi-stationary discharge in a magnetic field: Experimental research.* Ph. D. thesis, Moscow Egineering Physics Institute (MEPhi), Moscow, Russian Federation.

Mozgrin, D. V., I. K. Fetisov, and G. V. Khodachenko (1995). High-current low-pressure quasi-stationary discharge in a magnetic field: Experimental research. *Plasma Physics Reports 21*(5), 400–409.

Müller, A., E. Salzborn, R. Frodl, R. Becker, H. Klein, and H. Winter (1980). Absolute ionisation cross sections for electrons incident on O^+, Ne^+, Xe^+ and $Ar^{i+}(i = 1,...,5)$ ions. *Journal of Physics B: Atomic, Molecular and Optical Physics 13*(9), 1877–1899.

Ohring, M. (2002). *Materials Science of Thin Films* (2 ed.). San Diego, California: Academic Press.

Olander, D. R. (1976). *Fundamental Aspects of Nuclear Reactor Fuel Elements*. Springfield, Virginia: Technical Information Center, Office of Public Affairs Energy Research and Development Administration.

Palmucci, M., N. Britun, S. Konstantinidis, and R. Snyders (2013). Rarefaction windows in a high-power impulse magnetron sputtering plasma. *Journal of Applied Physics 114*(11), 113302.

Paulitsch, J., M. Schenkel, T. Zufraß, P. Mayrhofer, and W.-D. Münz (2010). Structure and properties of high power impulse magnetron sputtering and DC magnetron sputtering CrN and TiN films deposited in an industrial scale unit. *Thin Solid Films 518*(19), 5558–5564.

Petrov, I., P. B. Barna, L. Hultman, and J. E. Greene (2003). Microstructural evolution during film growth. *Journal of Vacuum Science and Technology A 21*(5), S117–S128.

Phelps, A. V. and Z. L. Petrović (1999). Cold-cathode discharges and breakdown in argon: surface and gas phase production of secondary electrons. *Plasma Sources Science and Technology 8*(3), R21–R44.

Pilloud, D., J. F. Pierson, C. Rousselot, and F. Palmino (2005). Substrate effect on the formation of ω-phase in sputtered zirconium films. *Scripta Materialia 53*(9), 1031–1036.

Raadu, M. A., I. Axnäs, J. T. Gudmundsson, C. Huo, and N. Brenning (2011). An ionization region model for high power impulse magnetron sputtering discharges. *Plasma Sources Science and Technology 20*(6), 065007.

Rae, S. C. and R. C. Tobin (1988). Sputtering in the presence of a rapid gas flow. *Journal of Applied Physics 64*(3), 1418–1424.

Revel, A., T. Minea, and C. Costin (2018). 2D PIC-MCC simulations of magnetron plasma in HiPIMS regime with external circuit. *Plasma Sources Science and Technology 27*(10), 105009.

Rezek, J., T. Kozák, N. Kumar, and S. Haviar (2021). Synergy of experiment and model for reactive HiPIMS: effect of discharge parameters on WO_x composition and deposition rate. *Journal of Physics D: Applied Physics 54*(12), 125202.

Rossnagel, S. M. (1988). Gas density reduction effects in magnetrons. *Journal of Vacuum Science and Technology A 6*(1), 19–24.

Rossnagel, S. M. and J. Hopwood (1994). Metal ion deposition from ionized mangetron sputtering discharge. *Journal of Vacuum Science and Technology B 12*(1), 449–453.

Roychowdhury, T., D. Shah, V. Jain, D. I. Patel, B. Dodson, W. Skinner, J. N. Hilfiker, S. J. Smith, and M. R. Linford (2020). Multy-instrument characterization of HiPIMS and DC magnetron sputtered tungsten and copper films. *Surface and Interface Analysis 52*(7), 433–441.

Rudolph, M., N. Brenning, H. Hajihoseini, M. A. Raadu, T. M. Minea, A. Anders, D. Lundin, and J. T. Gudmundsson (2022). Influence of the magnetic field on the discharge physics of a high power impulse magnetron sputtering discharge. *Journal of Physics D: Applied Physics 55*(1), 015202.

Rudolph, M., N. Brenning, M. A. Raadu, H. Hajihoseini, J. T. Gudmundsson, A. Anders, and D. Lundin (2020). Optimizing the deposition rate and ionized flux fraction by tuning the pulse length in high power impulse magnetron sputtering. *Plasma Sources Science and Technology 29*(5), 05LT01.

Rudolph, M., H. Hajihoseini, M. A. Raadu, J. T. Gudmundsson, N. Brenning, T. M. Minea, A. Anders, and D. Lundin (2021). On how to measure the probabilities of target atom ionization and target ion back-attraction in high-power impulse magnetron sputtering. *Journal of Applied Physics 129*(3), 033303.

Rudolph, M., D. Lundin, E. Foy, M. Debongnie, M.-C. Hugon, and T. Minea (2018). Influence of backscattered neutrals on the grain size of magnetron-sputtered TaN thin films. *Thin Solid Films 658*, 46–53.

Rudolph, M., A. Revel, D. Lundin, H. Hajihoseini, N. Brenning, M. A. Raadu, A. Anders, T. M. Minea, and J. T. Gudmundsson (2021). On the electron energy distribution function in the high power impulse magnetron sputtering discharge. *Plasma Sources Science and Technology 30*(4), 045011.

Ryan, P. J. (2019). *Electron diagnostics of magnetron discharges*. Ph. D. thesis, University of Liverpool, Liverpool, England.

Ryan, P. J., J. W. Bradley, and M. D. Bowden (2019). Comparison of Langmuir probe and laser Thomson scattering for plasma density and electron temperature measurements in HiPIMS plasma. *Physics of Plasmas 26*(4), 040702.

Samuelsson, M., D. Lundin, J. Jensen, M. A. Raadu, J. T. Gudmundsson, and U. Helmersson (2010). On the film density using high power impulse magnetron sputtering. *Surface and Coatings Technology 202*(2), 591–596.

Sarakinos, K., J. Alami, and S. Konstantinidis (2010). High power pulsed magnetron sputtering: Scientific and engineering state of the art. *Surface and Coatings Technology 204*(11), 1661–1684.

Schmid, M. (2024). A simple sputter yield calculator. Surface Physics, Institute of Applied Physics, Technischen Universität Wien.

Schnell, I. and R. C. Albers (2006). Zirconium under pressure: phase transitions and thermodynamics. *Journal of Physics: Condensed Matter 18*(5), 1483–1494.

Sheridan, T. E., M. J. Goeckner, and J. Goree (1990). Pressure dependence of ionization efficiency in sputtering magnetrons. *Applied Physics Letters 57*(20), 2080–2082.

Shimizu, T., K. Takahashi, R. Boyd, R. P. Viloan, J. Keraudy, D. Lundin, M. Yang, and U. Helmersson (2021). Low temperature growth of stress-free single phase α-W films using HiPIMS with synchronized pulsed substrate bias. *Journal of Applied Physics 129*(15), 155305.

Shimizu, T., M. Zanáška, R. P. Villoan, N. Brenning, U. Helmersson, and D. Lundin (2021). Experimental verification of deposition rate increase, with maintained high ionized flux fraction, by shortening the HiPIMS pulse. *Plasma Sources Science and Technology 30*(4), 045006.

Singh, A., P. Kuppusami, R. Thirumurugesan, V. Ganesan, and E. Mohandas (2014). Development of zirconium thin films by pulsed direct current magnetron sputtering: Effect of pulsed parameters. *International Journal on Design & Manufacturing Technologies 8*(1), 5–14.

Singh, A., P. Kuppusami, R. Thirumurugesan, R. Ramaseshan, M. Kamruddin, S. Dash, V. Ganesan, and E. Mohandas (2011). Study of microstructure and nanomechanical properties of Zr films prepared by pulsed magnetron sputtering. *Applied Surface Science 257*(23), 9909–9914.

Snyders, R., D. Hegemann, D. Thiry, O. Zabeida, J. Klemberg-Sapieha, and L. Martinu (2023). Foundations of plasma enhanced chemical vapor deposition of functional coatings. *Plasma Sources Science and Technology 32*(7), 074001.

Stancu, G. D., N. Brenning, C. Vitelaru, D. Lundin, and T. Minea (2015). Argon metastables in HiPIMS: Validation of the ionization region model by direct comparison to time resolved tunable diode-laser diagnostics. *Plasma Sources Science and Technology 24*(4), 045011.

Stephan, K., H. Helm, and T. D. Märk (1980). Mass spectrometric determination of partial electron impact ionization cross sections of He, Ne, Ar and Kr from threshold up to 180 eV. *Journal of Chemical Physics 73*(8), 3763–3778.

Suresh Babu, S., J. Fischer, K. Barynova, M. Rudolph, D. Lundin, and J. T. Gudmundsson (2024). High power impulse magnetron sputtering of a zirconium target. *Journal of Vacuum Science and Technology A 42*(4), 043007.

Suresh Babu, S., M. Rudolph, D. Lundin, T. Shimizu, J. Fischer, M. A. Raadu, N. Brenning, and J. T. Gudmundsson (2022). Ionization region model of a high power impulse magnetron sputtering of tungsten. *Plasma Sources Science and Technology 31*(6), 065009.

Suresh Babu, S., M. Rudolph, P. J. Ryan, J. Fischer, D. Lundin, J. W. Bradley, and J. T. Gudmundsson (2023). High power impulse magnetron sputtering of tungsten: A comparison of experimental and modelling results. *Plasma Sources Science and Technology 32*(3), 034003.

Thornton, J. A. (1978). Magnetron sputtering: basic physics and application to cylindrical magnetrons. *Journal of Vacuum Science and Technology 15*(2), 171–177.

Tiron, V., I.-L. Velicu, O. Vasilovici, and G. Popa (2015). Optimization of deposition rate in HiPIMS by controlling the peak target current. *Journal of Physics D: Applied Physics 48*(49), 495204.

Vavassori, D., F. Mirani, F. Gatti, D. Dellasega, and M. Passoni (2023). Role of magnetic field and bias configuration on HiPIMS deposition of W films. *Surface and Coatings Technology 458*, 129343.

Velicu, I. L., V. Tiron, I. Mihaila, and C. Costin (2018). Pulsed magnetron sputtering: The role of the applied power on W coatings properties. In D. Luca, L. Sirghi, and C. Costin (Eds.), *Recent Advances in Technology Research and Education*, Volume 660 of *Advances in Intelligent Systems and Computing*, pp. 183–190. Cham, Switzerland: Springer International Publishing.

Velicu, I.-L., V. Tiron, C. Porosnicu, I. Burduce, N. Lupu, G. Stoian, G. Popa, and D. Munteanu (2017). Enhanced properties of tungsten thin films deposited with a novel HiPIMS approach. *Applied Surface Science 424*(Part 3), 397–406.

Vitelaru, C., D. Lundin, G. D. Stancu, N. Brenning, J. Bretagne, and T. Minea (2012). Argon metastables in HiPIMS: time-resolved tunable diode-laser diagnostics. *Plasma Sources Science and Technology 21*(2), 025010.

Vlček, J. and K. Burcalová (2010). A phenomenological equilibrium model applicable to high-power pulsed magnetron sputtering. *Plasma Sources Science and Technology 19*(6), 065010.

Vlček, J., A. D. Pajdarová, and J. Musil (2004). Pulsed dc magnetron discharges and their utilization in plasma surface engineering. *Contributions to Plasma Physics 44*(5-6), 426–436.

Waits, R. K. (1978). Planar magnetron sputtering. In J. L. Vossen and W. Kern (Eds.), *Thin Film Processes*, Volume 4, pp. 131–173. New York, New York: Academic Press.

Window, B. and N. Savvides (1986). Charged particle fluxes from planar magnetron sputtering sources. *Journal of Vacuum Science and Technology A 4*(2), 196–202.

Yamamura, Y. and M. Ishida (1995). Monte Carlo simulation of the thermalization of

sputtered atoms and reflected atoms in the magnetron sputtering discharge. *Journal of Vacuum Science and Technology A 13*(1), 101–112.

Yamamura, Y. and H. Tawara (1996). Energy dependence of ion-induced sputtering yields from monoatomic solids at normal incidence. *Atomic Data and Nuclear Data Tables 62*(2), 149–253.

Ziegler, J. F., J. P. Biersack, and M. D. Ziegler (2008). *SRIM–The Stopping and Range of Ions in Matter*. Chester, Maryland: SRIM Co.

Ziegler, J. F., M. D. Ziegler, and J. P. Biersack (2010). SRIM – the stopping and range of ions in matter (2010). *Nuclear Instruments and Methods in Physics Research Section B: Beam Interactions with Materials and Atoms 268*(11-12), 1818–1823.